Surface photovoltage phenomena: theory, experiment, and applications

Leeor Kronik,* Yoram Shapira
Department of Physical Electronics, Tel-Aviv University, Ramat-Aviv 69978, Israel

ELSEVIER
Amsterdam–Lausanne–New York–Oxford–Shannon–Tokyo

Contents

- 1. Introduction 5
- 2. General theory 7
  - 2.1. Electrical properties of semiconductor surfaces 7
    - 2.1.1. Fundamental concepts 7
    - 2.1.2. Gap states 9
    - 2.1.3. Surface space charge region 13
    - 2.1.4. Surface dipoles 16
    - 2.1.5. Interface space charge regions 19
  - 2.2. Surface photovoltage (SPV) 24
    - 2.2.1. Basic concepts 24
    - 2.2.2. Super-bandgap SPV 25
    - 2.2.3. Sub-bandgap SPV 38
    - 2.2.4. The Dember potential 45
    - 2.2.5. Effect of buried interfaces 47
- 3. Experimental methods 49
  - 3.1. The Kelvin probe 49
    - 3.1.1. Principles of operation 49
    - 3.1.2. Practical considerations 51
    - 3.1.3. Limitations and solutions 57
    - 3.1.4. Scanning Kelvin probes 61
  - 3.2. MIS structures 64
  - 3.3. Other methods 68
    - 3.3.1. E-beam analysis 68
    - 3.3.2. Photoelectron spectroscopy 71
  - 3.4. High resolution scanning techniques 73
    - 3.4.1. Kelvin probe force microscopy 73
    - 3.4.2. Scanning tunneling microscopy 79
- 4. Basic surface photovoltage spectroscopy 84
  - 4.1. Bandgap energy and semiconductor type 85
  - 4.2. Gap state spectroscopy 92
  - 4.3. Points of importance 106
- 5. Advanced analyses 111
  - 5.1. Carrier diffusion length 111
    - 5.1.1. Analysis principles 111
    - 5.1.2. Practical considerations 116
    - 5.1.3. Limitations and solutions 119
  - 5.2. Surface band bending and dipole 128
    - 5.2.1. Surface band bending – photosaturation 128
    - 5.2.2. Surface band bending – other methods 138
    - 5.2.3. Surface dipole 143
  - 5.3. Recombination rates 148
  - 5.4. Surface states 153
    - 5.4.1. Energy distribution 153
    - 5.4.2. Properties 160
    - 5.4.3. Distinction between surface and bulk states 168

  5.5. Thin films and heterstructures 170
    5.5.1. Spectroscopy of multilayer structures 171
    5.5.2. Spectroscopy of quantum structures 179
    5.5.3. Construction of band diagrams 183
6. Concluding remarks 188
Acknowledgements 189
References 189

ELSEVIER

Surface Science Reports 37 (1999) 1–206

surface science reports

www.elsevier.nl/locate/surfrep

Surface photovoltage phenomena: theory, experiment, and applications

Leeor Kronik,* Yoram Shapira

Department of Physical Electronics, Tel-Aviv University, Ramat-Aviv 69978, Israel

Manuscript received in final form 18 May 1999

Abstract

The theoretical concepts, experimental tools, and applications of surface photovoltage (SPV) techniques are reviewed in detail. The theoretical discussion is divided into two sections. The first reviews the electrical properties of semiconductor surfaces and the second discusses SPV phenomena. Next, the most common tools for SPV measurements and their relative advantages and disadvantages are reviewed. These include the Kelvin probe and the use of MIS structures, as well as other less used techniques. Recent novel high-spatial-resolution SPV measurement techniques are also presented. Applications include surface photovoltage spectroscopy (SPS) which is a very effective tool for gap state spectroscopy. An in-depth review of quantitative analyses, which permit the extraction of various important surface and bulk parameters, follows. These analyses include: carrier diffusion length; surface band bending, charge, and dipole; surface and bulk recombination rates; surface state distribution and properties; distinction between surface and bulk states; spectroscopy of thin films, heterostructures and quantum structures; and construction of band diagrams. Finally, concluding remarks are given. © 1999 Elsevier Science B.V. All rights reserved.

---

1. Introduction

The surface photovoltage (SPV) method is a well-established contactless technique for the characterization of semiconductors, which relies on analyzing illumination-induced changes in the surface voltage. For five decades, it has been used as an extensive source of surface and bulk information on various semiconductors and semiconductor interfaces. During that time, the SPV technique has continuously evolved: newer, better and more diverse experimental tools have emerged. Simultaneously, more sophisticated methods and algorithms for data analysis have also appeared.

---

*Corresponding author. Present address: Department of Chemical Engineering and Materials Science, University of Minnesota, Minneapolis, MN 55455, USA. Fax: +1-612-626-7246
E-mail address: leeork@msi.umn.edu

0167-5729/99/$ – see front matter © 1999 Elsevier Science B.V. All rights reserved.
PII: S0167-5729(99)00002-3

Studies of the effects of illumination on the surface voltage had begun in the late 1940s and early 1950s with the classical articles of Nobel prize laureates Brattain and Bardeen [1–3]. Consequently, Johnson has shown that surface photovoltage measurements may yield minority carrier lifetimes [4] and Goodman has developed an algorithm for easy extraction of the minority carrier diffusion length [5]. The next major breakthrough in SPV methods took place in the early 1970s, when systematic research on the effects of sub-bandgap illumination on the surface voltage took place by Gatos et al. [6]. These researchers realized that they had invented a powerful tool for surface state characterization and also coined the term 'surface photovoltage spectroscopy' (SPS).

Brillson used SPS extensively throughout much of the 1970s and 1980s to study a great variety of semiconductor surfaces [7]. In many of his works, he has shown that the simultaneous use of SPS with 'main stream' analytical surface techniques makes it possible to obtain an unequivocal correlation between the chemical/structural and electronic properties of the surface. Mönch, Heiland, and Lüth were also among the first outside Gatos' group to realize the potential of SPS and have utilized it for studying Ge, Si, GaAs, and ZnO [8–10]. Specifically, Mönch has been an active user and developer of work function techniques in general, and SPV methods in particular [11].

The 1990s have seen a renewed vigor in the development of SPV related techniques. Lagowski et al. have scanned the SPV across an entire Si wafer, relating areas of different voltage to areas of heavy metal contamination or to surface defects [12]. Several groups have applied scanning tunneling microscopy (STM) [13,14] and atomic force microscopy (AFM) [15] tips for obtaining SPV measurements with a greatly improved lateral resolution. The importance of the surface photovoltaic effect in photoemission measurements has been pointed out [16–18], leading to both a renewed interest in SPV and an extensive re-examination of the interpretation of many previous photoemission experiments. Finally, the authors of this treatise have systematically applied SPV methods for the quantitative study of *buried* interfaces at semiconductor heterojunctions [19–21].

Despite the great body of work, of which only the 'tip of the iceberg' has been mentioned in the preceding discussion, no single treatise devoted solely to an in-depth description of the SPV technique has appeared. The present manuscript is intended to provide a tutorial review of both theory and applications of SPV methods in general, and SPS in particular. We have tried to cover all aspects of the technique, from the earliest theoretical and experimental achievements to the latest developments.

Following this brief introduction of the SPV technique and its uses, the second chapter is devoted to a structured presentation of the physical and mathematical groundwork necessary for a comprehensive understanding of the method. The chapter is divided into two sections. The first reviews the electrical properties of semiconductor surfaces, including gap states, surface dipoles and the surface space charge region (SCR). These concepts are immediately put to use in the following section, devoted to principles of the surface photovoltaic effect.

The third section of the review is devoted to a survey of the experimental methods available for carrying out SPV experiments. It begins with a detailed discussion of the two most important SPV measurement methods, namely, the Kelvin probe and the capacitive pick-up technique. Other techniques are then reviewed, including high lateral resolution STM- and AFM-based approaches.

Having laid down both the theoretical and experimental groundwork of the SPV technique, the fourth chapter deals with fundamentals of SPS experiments. It describes the most basic analyses of SPV spectra, namely, the determination of semiconductor type (p or n) and bandgap energy, and the identification of gap states. Various applications of the basic analysis are reviewed. A special section is devoted to the analysis of potential artifacts and to means of avoiding them.

The fifth section of this review article describes advanced analyses of SPV experiments. These analyses offer detailed quantitative information about semiconductor surface, interface, and bulk properties, including: carrier diffusion length; surface band bending, charge, and dipole; surface and bulk carrier recombination rates; surface state distribution and properties; distinction between surface and bulk states; band-bending and defects in thin films and heterostructures; heterojunction band offsets and band diagrams; and energy levels in quantum structures.

The sixth and final section of this review is devoted to concluding remarks.

2. General theory

2.1. Electrical properties of semiconductor surfaces

2.1.1. Fundamental concepts

This section is aimed to serve as a brief introduction to the electrical properties of semiconductor surfaces, as well as to lay a solid foundation of definitions, concepts, and equations for the subsequent sections. For our introductory purposes, we loosely rely mostly on the excellent books by Many et al. [22], Mönch [23], Lüth [24], and Sze [25]. The reader is referred to these books for a more detailed discussion.

In general, a surface is defined as a boundary of media with different physical properties. For example, the surface between a semiconductor and vacuum or gas is referred to as a 'free surface', or just a 'surface'. The surface between a semiconductor and another solid is usually referred to as an 'interface'. However, we shall sometimes use the term 'surface' to denote any boundary.

The termination of the periodic structure of a semiconductor at its free surface may form surface-localized electronic states within the semiconductor bandgap and/or a double layer of charge, known as a surface dipole (see Sections 2.1.2 and 2.1.4 below, respectively). The appearance of surface-localized states induces charge transfer between bulk and surface in order to establish thermal equilibrium between the two. The charge transfer results in a non-neutral region (with a non-zero electric field) in the semiconductor bulk, usually referred to as the surface space charge region (SCR). This region may extend quite deeply into the bulk. Similar considerations apply to a semiconductor interface.

For a mathematical analysis, we assume that the lateral dimensions are much larger than the vertical ones. We therefore adopt a one-dimensional analysis. First, we solve the Poisson equation, which relates the electric potential to the electric charge:

$$\frac{\mathrm{d}}{\mathrm{d}x}\left(\epsilon_{\mathrm{s}}(x)\frac{\mathrm{d}V(x)}{\mathrm{d}x}\right) = -\rho(x), \tag{2.1}$$

where x is the coordinate, $V(x)$ is the electric potential, $\rho(x)$ is the charge density in the SCR, and $\epsilon_{\mathrm{s}}(x)$ is the dielectric permittivity of the semiconductor. The 'physics' in Eq. (2.1) rests in the proper identification of the static charge density and the dependence of the mobile charge on the electric potential.

To understand non-equilibrium phenomena, one must additionally solve the continuity equations for electrons and holes:

$$\frac{\partial n}{\partial t} = \frac{1}{e}\frac{\mathrm{d}J_n}{\mathrm{d}x} + G_n - R_n, \tag{2.2a}$$

$$\frac{\partial p}{\partial t} = -\frac{1}{e}\frac{\mathrm{d}J_p}{\mathrm{d}x} + G_p - R_p, \tag{2.2b}$$

where $n(p)$ is the electron (hole) density, $J_n(J_p)$ is the electron (hole) current density, $G_n(G_p)$ is the net electron (hole) generation rate per unit volume, $R_n(R_p)$ is the net electron (hole) recombination rate per unit volume, and e is the (absolute value of the) electron charge. All variables are, in general, functions of time and coordinate. Eqs. (2.2), as such, are merely mathematical formalisms which express the law of charge conservation. In order for the equations to lead to meaningful physical information, one must have sufficient knowledge of generation, recombination, and current mechanisms. Generation/recombination mechanisms are discussed in subsequent sections. The electron and hole currents are typically expressed in terms of the drift–diffusion approximation:

$$J_n = -e\mu_n n \frac{\mathrm{d}V}{\mathrm{d}x} + eD_n \frac{\mathrm{d}n}{\mathrm{d}x}, \tag{2.3a}$$

$$J_p = -e\mu_p p \frac{\mathrm{d}V}{\mathrm{d}x} - eD_p \frac{\mathrm{d}p}{\mathrm{d}x}, \tag{2.3b}$$

where $\mu_n(\mu_p)$ is the electron (hole) mobility and $D_n(D_p)$ is the electron (hole) diffusion coefficient. In Eqs. (2.3), the first current term represents drift and the second diffusion. Other current mechanisms, e.g., tunneling, hopping conductivity, etc., may also be included by means of additional expressions.

In equilibrium, the electron and hole densities in a non-degenerate semiconductor may be expressed as:

$$n = n_\mathrm{i} \exp\left(\frac{E_\mathrm{F} - E_\mathrm{Fi}}{kT}\right); \qquad p = n_\mathrm{i} \exp\left(\frac{E_\mathrm{Fi} - E_\mathrm{F}}{kT}\right), \tag{2.4}$$

where E_F is the Fermi level, n_i is the intrinsic electron (and hole) carrier density, and E_Fi is the *intrinsic* Fermi level, which is situated close to midgap. The intrinsic Fermi level follows changes in the electric potential since it retains its relative position with respect to the band edges. Therefore:

$$\frac{\mathrm{d}E_\mathrm{Fi}}{\mathrm{d}x} = -\frac{e\mathrm{d}V}{\mathrm{d}x}. \tag{2.5}$$

Since in equilibrium $J_n = J_p = 0$, using Eqs. (2.4) and (2.5) in Eqs. (2.3) yields the well-known Einstein relation:

$$\frac{D_{n,p}}{\mu_{n,p}} = \frac{kT}{e}, \tag{2.6}$$

as well as the Boltzmann relations:

$$n(V_2) = n(V_1) \exp\left[\frac{e(V_2 - V_1)}{kT}\right]; \qquad p(V_2) = p(V_1) \exp\left[\frac{-e(V_2 - V_1)}{kT}\right], \tag{2.7}$$

where the subscripts ‘1’ and ‘2’ correspond to two points in the sample.

Under non-equilibrium conditions, the Fermi level is not defined and therefore Eq. (2.4) is rendered invalid. However, under most circumstances it may be replaced with the approximation [22,26]:

$$n = n_\mathrm{i} \exp\left(\frac{F_n - E_\mathrm{Fi}}{kT}\right); \qquad p = n_\mathrm{i} \exp\left(\frac{E_\mathrm{Fi} - F_p}{kT}\right), \tag{2.8}$$

where F_n and F_p are known as the electron and hole *quasi*-Fermi levels, respectively. While Eq. (2.8) retains the functional form of Eq. (2.4), F_n and F_p are not equal, except at equilibrium where both reduce to E_F. For example, if free electron–hole pairs are generated (e.g., by super-bandgap illumination), F_n moves upwards whereas F_p moves downwards in the bandgap. Hence, the energy difference $F_n - F_p$ is frequently used as a measure of deviation from equilibrium [26]. Moreover, using Eqs. (2.5) and (2.8), Eqs. (2.3) reduce to the compact form:

$$J_n = n\mu_n \frac{\mathrm{d}F_n}{\mathrm{d}x}; \qquad J_p = p\mu_p \frac{\mathrm{d}F_p}{\mathrm{d}x}. \tag{2.9}$$

It should be emphasized that Eqs. (2.3) and (2.9) are absolutely equivalent. The choice of either one depends solely on whether one prefers to work with charge densities or Fermi level positions.

The Poisson equation (Eq. (2.1)) and the two continuity equations (Eq. (2.2)) form a set of three coupled differential equations for three unknown functions of the x coordinate: The electric potential, the electron density, and the hole density. Specifically, Eqs. (2.1)–(2.3) are the starting point for most considerations of photovoltaic phenomena. In special cases, these equations may be solved analytically. For many other cases, a numerical solution is required. The numerical solution of Eqs. (2.1) and (2.2) was discussed in detail by, e.g., Selberherr [27].

2.1.2. Gap states

The periodic structure of an ideal crystalline semiconductor results in the appearance of allowed energy bands separated by forbidden energy gaps. In the allowed bands, the probability of finding an electron in any unit cell is equal because of the perfect three-dimensional translational symmetry. However, even an ideal termination of the semiconductor eliminates this symmetry in the direction perpendicular to the surface. Therefore, the unit cells next to the surface are, in general, not equivalent to those in the bulk and states which are localized in the vicinity of the surface may arise.

The formation of surface-localized states typically involves additional, more complex phenomena which make the surface unit cells not equivalent to the bulk cells. These include: 'Dangling bonds', i.e., the formation of surface atoms with no upper atom to bind to; surface reconstruction or relaxation, i.e., a change in the position and/or chemical bonding configuration of surface atoms, which minimizes the surface energy; steps and kinks at the surface; impurity atoms adsorbed on the surface, etc. Localized states may also arise at semiconductor *interfaces* for ostensibly the same reasons.

A first principles calculation of surface or interface state properties is an extremely difficult task. Consensus has been reached only on a very limited number of special surfaces after intensive investigations and debates. Hence, for practical purposes, the electrical and optical behavior of surface states is typically characterized by a set of phenomenological parameters which may be determined experimentally. For ab initio calculations, the interested reader is referred to, e.g., [28]. In our text, the phenomenological approach is used throughout.

We define three surface-state related parameters: the surface state density, N_t (measured in states per unit area), electron (hole) occupation, $n_t(p_t)$ (measured in charge carriers per unit area), where $n_t + p_t = N_t$, and the surface state energy, E_t. The three quantities defined above are related via standard Fermi–Dirac statistics, namely:

$$n_t = \frac{N_t}{1 + g_t \exp[(E_t - E_F)/kT]}, \tag{2.10}$$

where g_t is the degeneracy factor of the surface state, k the Boltzmann constant, and T the temperature. It is always possible to define an *effective* surface state energy, $E_t' = E_t + kT \ln g_t$, such that Eq. (2.10)

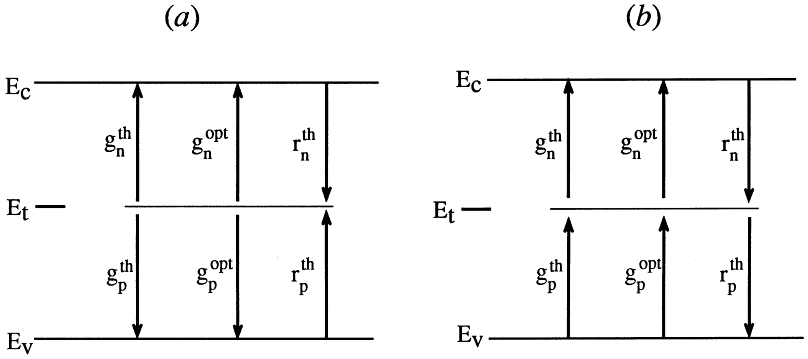

Fig. 1. Schematic representation of surface state-band transitions: (a) Mixed electron/hole representation. (b) Electron representation.

reduces to:

$$n_t = \frac{N_t}{1 + \exp[(E_t' - E_F)/kT]}. \qquad (2.11)$$

Eq. (2.11) is almost always preferred over Eq. (2.10) since it alleviates the need of knowing g_t. To simplify the notation, we shall henceforth use E_t to indicate the *effective* surface state energy level.

The *dynamic* properties of the surface states, i.e., their rates of charge transfer to and from the bulk bands, are usually modeled by means of the well-known Shockley–Read–Hall (SRH) statistics [29]. The possible electron and hole transitions are shown schematically in Fig. 1. Due to thermal excitation, electrons may be excited from the surface state into the conduction band at a rate of g_n^{th}; conduction band electrons may be captured in the surface state at a rate of r_n^{th}. If the semiconductor is illuminated, absorbed photons may excite electrons from the surface state to the conduction band at a rate of g_n^{opt}. All rates are per unit volume. Completely analogous expressions may be written for surface state-valence band transitions, if n is replaced by p, ‘electrons’ by ‘holes’ and ‘conduction’ by ‘valence’. Each hole transition may be described by an equivalent electron transition. For example, thermal generation of a hole from a surface state to the valence band is equivalent to thermal generation of an electron from the valence band to the surface state. Fig. 1(a) features a mixed representation, where the arrows point in the direction of electron transfer to the conduction band and hole transfer to the valence band. In Fig. 1(b) all arrows point in the direction of electron transitions.

All of the above transition rates may be expressed in terms of more fundamental quantities: The electron thermal generation rate must be proportional to the density of electrons in the surface state. If the semiconductor is non-degenerate, most of the electron states in the conduction band are empty, so that the electron concentration in the conduction band does not have to be taken into account. Denoting the proportionality constant as e_n (emission coefficient for electrons), we obtain:

$$g_n^{th} = e_n n_t. \qquad (2.12)$$

Similarly, the optical generation rate must be proportional to n_t, but also to I, the incident photon flux. Denoting the proportionality coefficient as σ_n^{opt}, we obtain:

$$g_n^{opt} = \sigma_n^{opt} I n_t. \qquad (2.13)$$

The electron recombination rate depends on the conduction band electron density (per unit volume) at the semiconductor surface, n_s, but also on the density of available empty sites at the surface state, p_t. Denoting the proportionality constant by c_n (capture coefficient for electrons), we obtain:

$$r_n^{\mathrm{th}} = c_n n_s p_t. \tag{2.14}$$

Again, analogous expressions may be formulated for the hole transition rates.

The two parameters c_n and e_n are not independent: Under thermal equilibrium (indexed by '0'), the relation $g_{n0}^{\mathrm{th}} = r_{n0}^{\mathrm{th}}$ must be valid. Using Eqs. (2.12) and (2.14), and assuming c_n and e_n are independent of surface-state occupation, we obtain:

$$e_n = \frac{c_n n_{s0} p_{t0}}{n_{t0}} \equiv c_n n_1, \tag{2.15}$$

where n_1 is a proportionality constant measured by inverse volume units. The above assumption should be approached with caution. For example, a large change in the electric field may increase the effective emission rate considerably due to Poole–Frenkel emission and/or phonon-assisted tunneling. However, under most typical situations the emission/capture rates change by significantly less than an order of magnitude [30]. Using Boltzmann statistics (appropriate for non-degenerate materials) for the various quantities in Eq. (2.15) and its hole equivalent, one can additionally show that:

$$n_1 = N_c \exp\left[\frac{(E_t - E_c)}{kT}\right], \qquad p_1 = N_v \exp\left[\frac{(E_v - E_t)}{kT}\right], \tag{2.16}$$

where N_c (N_v) is the effective density of states in the conduction (valence band).

It can be further shown [31] that c_n may be expressed in the form:

$$c_n = k_n v_n, \tag{2.17}$$

where k_n is defined as the thermal cross-section for electrons (and has units of area) and v_n is the average electron thermal velocity. Relation (2.17) may be intuitively understood as follows. The capture cross-section should be proportional to the average electron thermal velocity. The larger the latter is, the more volume the electron 'covers' in a given time span and the larger is its probability of getting caught in a surface state-related attractive potential. The thermal cross-section may therefore be interpreted as the 'effective target area' of the surface state. The probability of electron capture is effectively *approximated* as one inside this area and zero outside it. Similarly, the σ_n^{opt} coefficient given in Eq. (2.13) may be defined as an optical cross-section – the effective target area for a photon to induce an electron transition to the conduction band. Both the thermal and optical cross-sections exhibit values which range over many orders of magnitude, depending on the charge of the state involved and its exact potential structure. It is interesting to note that for an uncharged state, the thermal cross-section of a gap state is approximately the same as its physical cross-section – about 10^{-15} cm^{-3} [30].

Under the model presented here, all surface-state properties of practical experimental interest may be expressed in terms of six parameters: the surface-state density, energy level, electron and hole thermal cross-sections, and electron and hole optical cross-sections. Note that the thermal cross-sections may depend on temperature and the optical cross-sections may depend on incident photon energy.

So far, only *surface* gap states have been discussed. However, a local defect in the *bulk* structure (e.g., an impurity atom, a vacancy, an interstitial atom, or an exchange in site between two different atoms) may also induce a localized gap state. If the surface state density and occupation in Eqs. (2.10)–(2.14) are replaced by volume densities, then the obtained relations are valid for a bulk defect gap state as well. In fact, SRH statistics were first developed for bulk defects [29]. An important application of SRH statistics is determining the steady-state *net* recombination rate due to a defect gap state [31]. In steady state, as opposed to equilibrium, the electron (or hole) generation and recombination terms do not have to cancel each other out since a net generation or recombination rate is possible. However, under steady-state conditions n_t must remain constant, so that its net carrier exchange rate with the conduction band must be equal to that of the valence band, and is denoted by R. Using this condition with Eqs. (2.12) and (2.14) and solving for n_t, we obtain:

$$n_\mathrm{t} = \frac{c_n n + c_p p_1}{c_n(n+n_1) + c_p(p+p_1)} N_\mathrm{t}. \tag{2.18}$$

After some additional algebraic manipulation, the well-known SRH recombination expression is obtained:

$$R = \frac{np - n_\mathrm{i}^2}{(1/c_p N_\mathrm{t})(n+n_1) + (1/c_n N_\mathrm{t})(p+p_1)}, \tag{2.19}$$

where in the case of surface recombination n, p should be replaced with $n_\mathrm{s}, p_\mathrm{s}$.

In the case of bulk recombination, the coefficients $1/(c_n N_\mathrm{t})$ and $1/(c_p N_\mathrm{t})$ have units of time and are denoted by τ_n and τ_p, respectively. In the case of surface recombination, the same coefficients have units of (velocity)$^{-1}$ and are denoted by s_n^{-1} and s_p^{-1}, respectively. τ_n and τ_p are known as the minority carrier lifetimes since, e.g., in the case of excess electrons in a p-type material and under the assumption of low injection (i.e., the number of excess carriers is much smaller than the original carrier concentration), Eq. (2.19) reduces to:

$$R = \frac{\Delta n}{\tau_n}. \tag{2.20}$$

A similar expression exists for holes in an n-type material. Thus, $\tau_n(\tau_p)$ may be physically interpreted as the average ‘survival’ time for an excess electron (hole) prior to its recombination. For surface recombination, we similarly obtain:

$$R = s_n \Delta n_\mathrm{s}. \tag{2.21}$$

Here, $s_n \equiv c_n N_\mathrm{t}$ and $s_p \equiv c_p N_\mathrm{t}$ are known as the surface recombination velocities for minority carriers. Physically, if electrons moved towards the surface at a constant velocity, it should be equal to s_n so that their rate of increase at the surface due to that motion would equal to the rate of their decrease at the surface due to recombination. It is important to note that τ_n, τ_p or s_n, s_p only pertain to the case of low level injection of minority carriers. For other cases, notably a high injection level and/or an intrinsic semiconductor, different definitions of lifetimes or surface recombination velocities need to be used in Eqs. (2.20) or (2.21). Therefore, one must exercise extreme caution when using a constant parameter, such as ‘lifetime’ or ‘surface recombination velocity’ as indicative of the properties of the bulk or surface recombination rates under any conditions.

Finally, we note that the charge within any gap state is given by:

$$Q_\mathrm{t} = e(N_\mathrm{t} - n_\mathrm{t}), \quad \text{for donor states}, \qquad Q_\mathrm{t} = -e n_\mathrm{t}, \quad \text{for acceptor states}. \tag{2.22}$$

For an energy distribution of gap states, Eq. (2.22) may be generalized to the form:

$$Q_t = e\left[\sum_d (N_t^d - n_t^d) - \sum_a n_t^a\right], \quad \text{for discrete states} \tag{2.23a}$$

$$Q_t = e\left[\int_d \left(N_t^d(E) - n_t^d(E)\right) dE - \int_a n_t^a(E)\, dE\right], \quad \text{for continuous states,} \tag{2.23b}$$

where the indices 'd' and 'a' denote donor and acceptor states, respectively. The effective optical and thermal cross-sections of a continuously distributed state may also be obtained by appropriate integrals.

2.1.3. Surface space charge region

The charge found in surface states is clearly supplied by the underlying bulk. We therefore expect the carrier density in the vicinity of the surface to deviate from its equilibrium value and result in a surface space charge region (SCR). The surface may be found in three different regimes: (a) accumulation, where the majority carrier concentration at the surface is larger than its bulk value, (b) depletion, where the majority carrier concentration at the surface is smaller than its equilibrium value, but larger than the minority carrier concentration at the surface, and (c) inversion, where the majority carrier concentration at the surface is smaller than the minority carrier concentration at the surface.

According to the Poisson equation (Eq. (2.1)), a non-equilibrium carrier density implies a non-zero electric field and potential. Therefore, even under equilibrium conditions the surface potential, denoted as V_s, is different from the electric potential far away in the bulk. This means that the semiconductor bands are bent in the vicinity of the surface. By definition, the energy band is lower the higher the electrical potential is, so that *a positive* V_s *corresponds to downward-bent bands.*

Within the scope of this review, we are interested primarily in V_s and not in the exact '*shape*' of the surface SCR, i.e., the dependence of the electric potential on the coordinate [22–24]. The reason is that only V_s, and not the entire potential profile, is measured in a surface photovoltage experiment, as described in detail in the next section and chapter. For a given set of semiconductor bulk and surface properties, the value of V_s is dictated by the charge conservation rule:

$$Q_{ss} = -Q_{sc}, \tag{2.24}$$

where Q_{ss} is the net surface charge and Q_{sc} is the net charge in the SCR (both per unit area). This is because the underlying crystal is the sole supplier of the surface charge. For calculating V_s, we must know how Q_{ss} and Q_{sc} depend on it.

We start with the dependence of Q_{ss} on V_s as it is quite simply derived from Fermi–Dirac statistics: Since the surface states have a fixed energy distance from the band edges, their energy distance from the Fermi level changes in the presence of band bending. We denote the Fermi-level to state-energy interval in the absence of band bending by $(E_t - E_F)_0$. Then:

$$Q_{ss} = eN_t\left\{1 - \frac{1}{1+\exp\left[\left((E_t - E_F)_0 - eV_s\right)/kT\right]}\right\}, \quad \text{for a donor state.} \tag{2.25a}$$

$$Q_{ss} = -eN_t\frac{1}{1+\exp\left[\left((E_t - E_F)_0 - eV_s\right)/kT\right]}, \quad \text{for an acceptor state.} \tag{2.25b}$$

If multiple states are present, the total charge may be found by summation and integration as in Eq. (2.23). Note that Q_{ss} may also have a fixed (and hence V_{s} independent) component which is the result of adsorbed ionized species.

We now consider the dependence of Q_{sc} on V_{s}, based on the treatment by Sze [25]. We focus our attention on a p-type semiconductor because the results for an n-type semiconductor may be easily completed by analogy. In the presence of both donors and acceptors, the total (static and dynamic) charge density may be expressed as:

$$\rho(x) = e(N_{\mathrm{d}} - N_{\mathrm{a}} + p - n), \tag{2.26}$$

where N_{d} (N_{a}) is the donor (acceptor) density, assumed to be uniform. If the semiconductor is non-degenerate, we obtain the relation of the electron and hole densities in the SCR to their densities in the quasi-neutral bulk from the Boltzmann relations (Eq. (2.7)):

$$n(x) = n_{\mathrm{b}} \exp\left(\frac{eV(x)}{kT}\right), \qquad p(x) = p_{\mathrm{b}} \exp\left(\frac{-eV(x)}{kT}\right). \tag{2.27}$$

Moreover, in the quasi-neutral region the net charge density is zero so that:

$$N_{\mathrm{d}} - N_{\mathrm{a}} = n_{\mathrm{b}} - p_{\mathrm{b}}, \tag{2.28}$$

where the index 'b' denotes the bulk. Placing expressions (2.26)–(2.28) in the Poisson equation (Eq. (2.1)) we obtain:

$$\frac{\mathrm{d}^2V}{\mathrm{d}x^2} = -\frac{e}{\epsilon}[p_{\mathrm{b}}(\mathrm{e}^{-eV/kT} - 1) - n_{\mathrm{b}}(\mathrm{e}^{eV/kT} - 1)]. \tag{2.29}$$

We denote the position of the surface by $x = 0$, with the semiconductor extending towards the positive x axis. We choose the potential at infinity as zero. Because at infinity the semiconductor is quasi-neutral, the electric field, E, which by definition equals $-\mathrm{d}V/\mathrm{d}x$, must also be zero there.

For obtaining an explicit expression for Q_{sc}, Eq. (2.29) is integrated from the bulk toward the surface using the above boundary conditions, yielding an expression for the surface electric field, E_{s}. Once E_{s} is known, Q_{sc} is obtained by using the relation $Q_{\mathrm{sc}} = -\epsilon_{\mathrm{s}}E_{\mathrm{s}}$. The latter relation is a direct result of the Gauss theorem, where one side of the Gauss surface is located at the quasi-neutral region and the other at $x = 0^+$, i.e., just outside the semiconductor surface. The final result of this procedure is:

$$Q_{\mathrm{sc}} = \mp\frac{\sqrt{2}\epsilon_{\mathrm{s}}kT}{eL_{\mathrm{D}}}F\left(\frac{eV}{kT},\frac{n_{\mathrm{b}}}{p_{\mathrm{b}}}\right), \tag{2.30}$$

where $L_{\mathrm{D}} \equiv \sqrt{kT\epsilon_{\mathrm{s}}/(e^2p_{\mathrm{b}})}$ is the Debye screening length (for holes, in this case) and:

$$F\left(\frac{eV}{kT},\frac{n_{\mathrm{b}}}{p_{\mathrm{b}}}\right) \equiv \left[\left(\mathrm{e}^{-eV/kT} + \frac{eV}{kT} - 1\right) + \frac{n_{\mathrm{b}}}{p_{\mathrm{b}}}\left(\mathrm{e}^{eV/kT} - \frac{eV}{kT} - 1\right)\right]^{1/2}, \tag{2.31}$$

where the positive (negative) sign corresponds to $V_{\mathrm{s}} > 0$ $(V_{\mathrm{s}} < 0)$.

V_{s} may be found by solving Eq. (2.24), where the left hand side is replaced by Eq. (2.25) and the right hand side is replaced by Eq. (2.30). Much physical intuition is obtained if this solution is performed graphically by plotting both Q_{ss} and Q_{sc} versus V_{s} on the same graph [23,32,33]. An example is shown in Fig. 2, which features such a graphical solution for a hypothetical 10^{16} cm^{-3} p-type InP sample with surface donor states of varying density and energy position. All three regimes discussed above – accumulation, depletion, and inversion – are clearly manifested in the Q_{sc} versus V_{s} curve. The

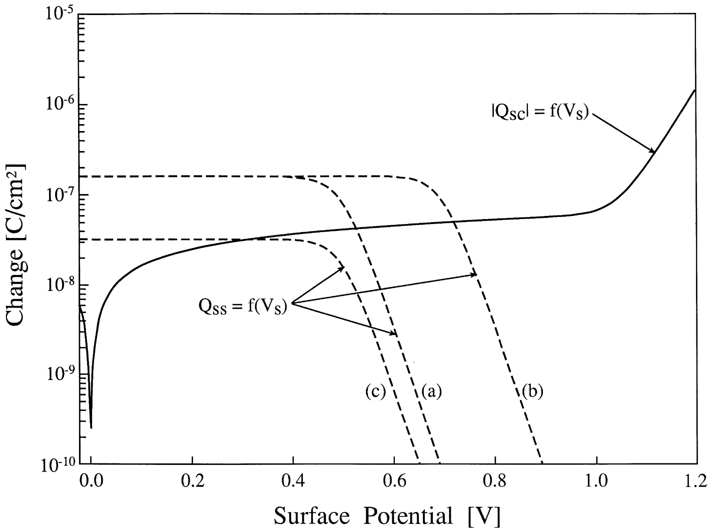

Fig. 2. Graphical determination of V_s for a hypothetical 10^{16} cm^{-3} p-type InP sample with surface denor states. Solid curve: Dependence of $|Q_{sc}|$ on V_s. Dashed curves: Dependence of Q_{ss} on V_s with (a) $N_t = 10^{12}$ cm^{-2}, $(E_t - E_F)_0 = 0.5$ eV. (b) $N_t = 10^{12}$ cm^{-2}, $(E_t - E_F)_0 = 0.7$ eV. (c) $N_t = 2 \cdot 10^{11}$ cm^{-2}, $(E_t - E_F)_0 = 0.5$ eV.

three regimes are easily distinguished because they are dominated by different terms in Eq. (2.31). In the accumulation and inversion regimes, the first and fourth terms in Eq. (2.31) dominate, respectively. Hence, $|Q_{sc}| \simeq \exp(e|V_s|/2kT)$ in both cases. In the depletion regime, however, the second term dominates and thus $|Q_{sc}| \simeq \sqrt{|V_s|}$.

The graphical solution also demonstrates that the higher surface state density is, the larger the band bending is. This is because more charge transfer from surface to bulk is necessary for achieving equilibrium. In addition, the higher the donor state is within the bandgap, the larger the band bending is because a larger change in the surface Fermi level position is required for the surface state population to change appreciably.

Several additional comments are in order. First, in the depletion regime the same square root dependence obtained from Eq. (2.31) would have been obtained had mobile charges been neglected a priori. An often used approximation, known as the *depletion approximation*, assumes that the region in which the mobile carriers are negligible ends abruptly at a distance w from the surface. Hence:

$$|Q_{sc}| \simeq e|N_a - N_d|w, \tag{2.32}$$

Combining Eq. (2.32) with the form of Eq. (2.30) appropriate for the depletion regime one obtains:

$$w = \sqrt{\frac{2\epsilon_s V_s}{e|N_a - N_d|}}. \tag{2.33}$$

For reasonable values, e.g., $V_s = 0.4$ V, $\epsilon_s = 11.8\epsilon_0$ (silicon), and $|N_a - N_d| = 5 \times 10^{15}$ cm^{-3}, we obtain $w = 0.3\,\mu$m. This result reveals the striking influence of surface states on the semiconductor bulk: states localized over no more than several monolayers affect the semiconductor electrically even several *thousand* monolayers away from the surface.

Second, Eq. (2.30) is recast in several equivalent mathematical forms in the literature. A common one is the one given by Kingston and Neustadter [34], who have solved the Poisson equation (Eq. (2.1)), where the mobile charge densities are expressed in terms of the energy distance between the Fermi level and the intrinsic Fermi level, normalized to kT/e, namely:

$$n = n_{\mathrm{i}} e^{-u}, \quad p = n_{\mathrm{i}} e^{u}, \text{ where } u \equiv \frac{e(E_{\mathrm{F}} - E_{\mathrm{Fi}})}{kT}. \tag{2.34}$$

Using the same approach outlined above, they obtained:

$$Q_{\mathrm{sc}} = \pm \frac{\sqrt{2}\epsilon_{\mathrm{s}} kT}{eL_{\mathrm{D}}} F(u_{\mathrm{s}}, u_{\mathrm{b}}), \tag{2.35}$$

where $L_{\mathrm{D}} \equiv \sqrt{kT\epsilon_{\mathrm{s}}/(e^2 n_{\mathrm{i}})}$ is the *intrinsic* Debye screening length and $F(u_{\mathrm{s}}, u_{\mathrm{b}}) \equiv [\sinh u_{\mathrm{b}}(u_{\mathrm{b}} - u_{\mathrm{s}}) - (\cosh u_{\mathrm{b}} - \cosh u_{\mathrm{s}})]^{1/2}$. The subscripts ‘s’ and ‘b’ have their usual meaning of surface and bulk, respectively, and $V_{\mathrm{s}} \equiv (kT/e) \cdot (u_{\mathrm{s}} - u_{\mathrm{b}})$. It should be emphasized that Eqs. (2.30) and (2.35) are absolutely equivalent. Like Eqs. (2.3) and (2.9), they are the charge densities and Fermi level position representations, respectively. Other hybrid forms of Eqs. (2.30) and (2.35) are also commonly used in the literature.

Third, the detailed analysis presented above may be readily extended to cover more general cases at the expense of more complicated mathematics. For example, if the semiconductor is degenerate the expressions in Eq. (2.27) must be replaced by the appropriate Fermi–Dirac expressions [23,24]. When a very strong accumulation or inversion is obtained, majority or minority carriers, respectively, are confined in a very narrow layer. Under such conditions they are typically considered in terms of a two-dimensional carrier gas. The semi-classical approach presented here then fails and one must resort to a simultaneous solution of the Poisson and Schrödinger equations [23,24].

Fourth, another generalization of particular importance arises when the semiconductor bulk contains a non-negligible amount of deep acceptors or donors (or when the temperature is sufficiently low so that not all of the shallow donors/acceptors are completely ionized). In this case, the appropriate donor and acceptor terms in Eq. (2.26) should not be taken as constant but rather should be represented by charge terms similar to Eq. (2.25) (for volume densities, of course) [22]. The effect of deep states is usually negligible in the accumulation and inversion regimes, where Eq. (2.26) is dominated by mobile, rather than static, charges. However, it may be very significant in the depletion regime [35].

2.1.4. Surface dipoles

In addition to surface states, another important phenomenon associated with a semiconductor surface is the surface dipole. Despite its importance, this phenomenon has received considerably less attention than surface state phenomena. Since surface dipole considerations play an important role in some analyses of SPV experiments, it is the purpose of this sub-section to introduce the relevant concepts in an orderly manner.

At a free surface, a ‘tail’ of the surface-localized electron wave functions ‘spills out’ into the vacuum. Therefore, the region just outside the surface has a net negative charge, whereas the region just inside the surface is left with a net positive charge [36]. The separation of positive and negative charges over atomic distances is, by definition, a microscopic dipole. This dipole creates a field which opposes further electron transfer into the vacuum. Electrons reaching the surface are repelled by the negative charge outside the material and attracted by the positive charge inside the material. Thus, an abrupt potential barrier for electrons attempting to leave the semiconductor is formed. This barrier is usually characterized by means of the electron affinity, χ, defined as the energy needed to release an electron from the conduction band into vacuum.

At a real semiconductor surface, the effective surface barrier is not determined solely by the 'spill-out effect'. Many additional microscopic dipole contributions are possible due to different surface effects. As noted in Section 2.1.2, the surface may be relaxed or reconstructed. The exact arrangement of the atomic positions may affect the 'center of gravity' of the charge in the chemical bond between the atoms and hence create a surface dipole. Moreover, a change in atomic positions may create an 'electron smoothing-out effect' in which for a more open surface, electron wave function tails tend to 'fill in' the gaps between atoms, another cause for a surface dipole [36]. Ranke and co-workers have shown that the effective electron affinity undergoes notable changes with surface orientation for Si, Ge, and GaAs [37]. They concluded that in these cases the atomic contribution dominates over the electronic contribution to the surface dipole. Local stoichiometry changes at the semiconductor surface may also create a surface dipole. An adsorbate layer may also result in a surface dipole, the magnitude of which depends on the ionicity of the adsorbate–substrate bond. The ionicity is related to the difference in electronegativity between the adsorbate species and the semiconductor substrate [11]. Partial charge transfer between the adsorbate and a gap state may likewise cause a surface dipole and is also governed by the degree of ionicity of the bond [11].

As in the case of gap states, a dipole layer is not limited to semiconductor surfaces, but also appears at semiconductor interfaces. Any change in the structure and/or chemistry of interface atoms with respect to bulk ones may result in an interface dipole. For example, Nicolini et al. have shown, both theoretically and experimentally, that the local Zn/Se relative concentration at the heterovalent ZnSe/GaAs(0 0 1) interface has a direct influence on the dipole at that interface [38]. Partial charge transfer at a metal/semiconductor or a semiconductor/semiconductor interface (e.g., due to 'tails' of interface state wave functions) may also result in an interface dipole [39–41].

Lambrecht et al. [41] have correctly pointed out that the term 'interface dipole' has been used rather liberally in the literature with different and ambiguous definitions by different authors. In order to unequivocally define the terminology used in this article, we invoke the concept of a local vacuum level, E_l, defined (following Marshak [42]) as the energy of an electron at a given point if it were at rest and free from the influence of the crystal potential (which determines the band structure). It is important to understand the difference between the local and the absolute vacuum level: The absolute vacuum level is defined as the reference energy of an electron at rest which is situated very far from the semiconductor so that it is 'unaware' of the existence of the semiconductor. At the local vacuum level, the electron at rest is free from the crystal *microscopic* potentials caused by the atomic forces, but not from macroscopic potentials, e.g., those due to the electric field at a SCR.

The local vacuum level concept may also be understood by the following '*gedanken*' experiment: Suppose electrons are liberated from the conduction band of a hypothetical semiconductor sample, which consists of a *p–n* homojunction buried deep within the sample. Furthermore, suppose that the surfaces are ideal so that the only SCR is due to the *p–n* junction, as in Fig. 3 and that the two surfaces are exactly equivalent, so they have the same effective electron affinity. Consequently, the two electrons, liberated into vacuum from the conduction band at both sides of the junction, must have energies differing by the amount of energy necessary to overcome the potential barrier so as to bring the electron from one surface to the other. Hence, it is clear that the local vacuum level must follow any

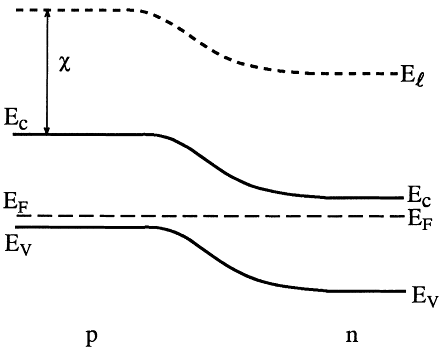

Fig. 3. Schematic diagram of the local vacuum level in a hypothetical *p*–*n* junction.

changes in the electric potential along the sample. This reasoning naturally leads to the definition of the electron affinity as $\chi = E_l - E_C$. According to this definition, χ is really a *bulk* quantity in the sense that it is the amount of energy necessary to remove an electron from the conduction band at a point inside the crystal into vacuum. However, in reality it is, of course, impossible to remove an electron into vacuum without first bringing it to the surface. At the surface, the *effective* electron affinity, χ^* , may differ from that of the bulk due to the various surface dipole effects discussed above. A complete schematic band diagram of a semiconductor surface SCR is shown in Fig. 4. Using the figure, we observe that the surface dipole, $\Delta\phi_s$, manifests itself as a step in the local vacuum level, i.e., in the electric potential at the surface because the potential changes abruptly over several monolayers. This is in contrast to the *macroscopic* dipole created by the surface states and surface SCR, also shown in Fig. 4. In the latter case, the average separation between the positive (Q_{ss}) and the negative (Q_{sc}) charges is *not* on an atomic scale, and the electric potential changes gradually. For consistency with the sign convention of the surface voltage, we define the surface dipole as positive if the local vacuum level drops when passing from the semiconductor into vacuum. Thus, the dipole is positive if its positive side points outwards. Using Fig. 4, we also define the work function at the semiconductor surface in

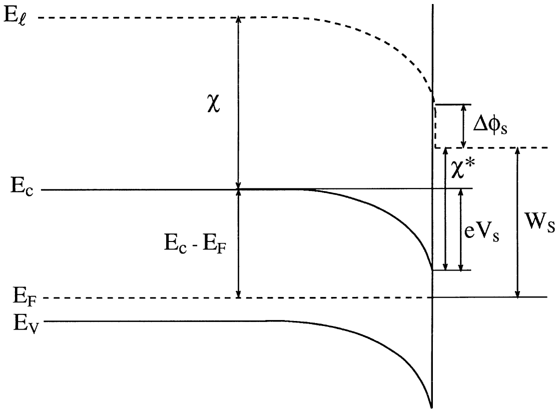

Fig. 4. Schematic diagram of the electronic band structure at a semiconductor surface.

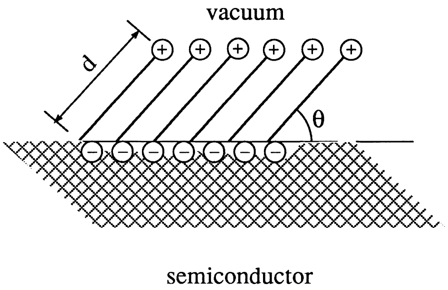

Fig. 5. Schematic diagram of a surface dipole layer.

equilibrium, W_s, as the energy separation between the Fermi level and the local vacuum level at the surface. W_s may be expressed in the form:

$$W_s = (E_c - E_F)_b - eV_s + \chi - \Delta\phi_s \equiv (E_c - E_F)_b - eV_s + \chi^*. \tag{2.36}$$

An estimate of the relation between the dipole moment and the magnitude of the potential step at the surface is easily established with the aid of Fig. 5 [24]. Consider an ordered dipole layer, oriented at an angle θ with respect to the surface, with a dipole moment $\bar{p} \equiv ed$, where d is the length of the dipole. The electric field inside the double layer is the same as in a parallel-plate capacitor, i.e.,

$$E = \frac{eN}{\epsilon}, \tag{2.37}$$

where N is the dipole density. The voltage is given by:

$$|\Delta\phi_s| = \int E \cdot dx = Ed\cos\theta. \tag{2.38}$$

Combining Eqs. (2.37) and (2.38) yields:

$$\Delta\phi_s = \frac{Ned\cos\theta}{\epsilon} \equiv \frac{N\bar{p}\cos\theta}{\epsilon}. \tag{2.39}$$

Eq. (2.39) is only an estimate because the dielectric coefficient of the dipole layer, ϵ, is an ill-defined property since the dipole layer is not a bulk entity. Moreover, if the dipole layer is not perfectly ordered, the angle θ should be considered as an average angle.

Finally, we note that the same physical mechanism (e.g., surface reconstruction) may lead to *both* surface states and surface dipole. Nevertheless, the impact of these two effects on the electrical band diagram is profoundly different. Hence, from an electrical point of view they should be analyzed separately, as given here.

2.1.5. *Interface space charge regions*

In this section, we look into the SCR of several important structures, namely metal–insulator–semiconductor (MIS) structures, metal–semiconductor junctions and semiconductor–semiconductor junctions.

As discussed in the following chapters, MIS structures are of much importance in SPV measurements. Hence, the differences and similarities between the SCR of a MIS structure and that of a free surface merit some elaboration. A MIS structure consists of an insulating layer sandwiched between a metallic layer and a semiconducting material. The insulating layer may be solid but may also be simply air or vacuum. The metallic layer is connected to the back side of the semiconducting material via an external voltage source.

Even if surface states are not present anywhere in the structure and the external voltage source is set at null, a SCR is still expected in the semiconducting material, extending from the semiconductor-insulator interface into the bulk of the semiconductor. The reason is that due to the different work functions of the semiconductor and the metal, charge must be transferred between them in order for their Fermi levels to equilibrate. A schematic band diagram of such a structure ‘before’ and ‘after’ the establishment of a contact between metal and semiconductor in this ideal case is given in Figs. 6(a),(b), respectively. The surface SCR is further affected if surface states do exist, as discussed in Section 2.1.3 above, as well as by an external bias between the metal and semiconductor. Thus, it is necessary to find out how to calculate the surface voltage in the general case, a schematic band diagram of which (neglecting interface dipoles) is given in Fig. 6(c).

In the MIS case, Eq. (2.24), the charge neutrality condition of the free surface, is replaced by the more general charge neutrality condition:

$$Q_{\mathrm{m}} + Q_{\mathrm{sc}} + Q_{\mathrm{ss}} = 0, \tag{2.40}$$

where Q_{m} is the charge density on the metal–insulator surface. However, Eqs. (2.25) and (2.30), describing the dependence of Q_{ss} and Q_{sc}, respectively, on V_{s} are still valid. Using the Gauss theorem it

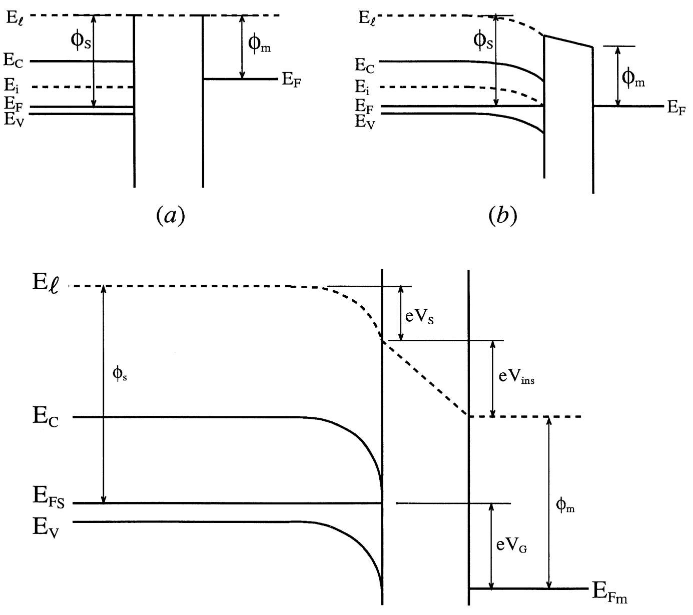

(*a*) (*b*)

(*c*)

Fig. 6. Schematic band diagram of a MIS structure: (a) No surface states, before metal–semiconductor contact. (b) No surface states, after contact, with zero external bias, (c) general case, with non-zero external bias.

is easy to find that:

$$Q_{\rm m} = \epsilon_{\rm ins} E_{\rm ins} = \frac{\epsilon_{\rm ins} V_{\rm ins}}{d_{\rm ins}} = Q_{\rm m} = C_{\rm ins} V_{\rm ins}, \tag{2.41}$$

where $\epsilon_{\rm ins}, E_{\rm ins}, V_{\rm ins}, d_{\rm ins}$, and $C_{\rm ins}$ are the dielectric permittivity, electric field, voltage, thickness, and capacitance per unit area of the insulating layer, respectively. Furthermore, using Fig. 2.6(c), we find the relation:

$$-eV_{\rm ins} = eV_{\rm s} + \phi_{\rm m} - \phi_{\rm s} - eV_{\rm G}, \tag{2.42}$$

where $\phi_{\rm m}$ is the metal work function, $\phi_{\rm s}$ the work function of the semiconductor in the absence of band bending, and $V_{\rm G}$ the external bias. Note that dipoles present at any interface induce steps in the local vacuum level in the band diagram of Fig. 6(c). However, those are usually overlooked in the MIS literature because they are typically absorbed in $\phi_{\rm m} - \phi_{\rm s}$. Expressing $Q_{\rm m}$ as an explicit function of $V_{\rm s}$ via Eqs. (2.41) and (2.42), Eq. (2.40) may be reduced to an equation for $V_{\rm s}$ alone.

Note that Eq. (2.41) shows that the charge on the metal decreases with decreasing insulator capacitance. This means that in the case of a vacuum or air gap, $V_{\rm s}$ of the free surface and $V_{\rm s}$ of the MIS structure are practically identical if the metal is sufficiently removed from the surface because $Q_{\rm m}$ is negligible, so that Eq. (2.40) reduces to Eq. (2.24).

We next discuss rectifying metal–semiconductor junctions [25]. (Ohmic metal–semiconductor junctions are not considered here since usually no significant space charge effects are associated with them). Such junctions may be thought of as a limiting case of the MIS structure, with the thickness of the insulating layer approaching zero. The limiting case in the absence of interface states (known as the Schottky limit) is shown in Fig. 7(a). A potential barrier, $\phi_{\rm b}$, known as the Schottky barrier, is formed between the metal and the semiconductor and is responsible for the rectifying properties of the junction. Using Fig. 7(a), it is clear that in this limit, for the *n*-type semiconductor depicted in the diagram, $\phi_{\rm b} = \phi_{\rm m} - \chi$.

The extreme opposite case, where there is a very high density of interface states (known as the Bardeen limit), is depicted in Fig. 7(b). Here, the interface state density is large enough so that the change in surface voltage when moving from the free semiconductor surface to the metal–semiconductor interface is practically negligible since $Q_{\rm m} \ll Q_{\rm ss}$ (assuming, of course, that the nature of the surface and interface states is the same). In such a case, the Fermi level at the interface is referred

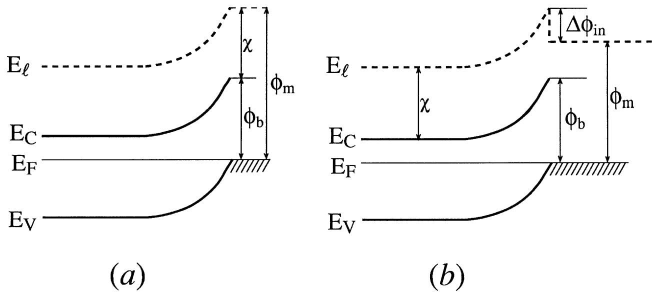

Fig. 7. Schematic band diagram of a rectifying metal–semiconductor junction: (a) No interface states (Schottky limit), (b) High interface state density (Bardeen limit).

to as ‘pinned’ by the interface states since it has approximately the same value, regardless of the metal type. Similarly, the surface Fermi level is independent of metal type and spacing in a MIS structure if ‘pinned’ by a high density of interface states. Fig. 7(b) shows that the Schottky barrier is given by the energy interval between the pinned Fermi level position and the conduction band at the surface and not by the ideal relation. Hence, an interface dipole, $\Delta\phi_{\rm in}$, must be present. This dipole is physically brought about because $Q_{\rm ss}$ and $Q_{\rm m}$ are separated by an atomic distance. Note that in this case the same charge, $Q_{\rm ss}$, is responsible for the interface charge (and hence the SCR), as well as the interface dipole (together with $Q_{\rm m}$). Cowley and Sze [43] have forwarded a more general model, where the Schottky barrier height is determined as a linear combination of the Schottky and Bardeen limits. In practice, the value of the Schottky barrier may be further complicated by various physical and chemical phenomena, such as metal and semiconductor interdiffusion, chemical reactions, lateral junction non-uniformities, etc. Thus, metal–semiconductor junctions still attract a considerable amount of theoretical and experimental research, the results of which are described in detail elsewhere (see, e.g., [7,44]). In practice, $\phi_{\rm b}$ is determined experimentally.

We now move to the band diagram of semiconductor heterojunctions. In these structures, the parameters most pertinent to the electrical behavior of the heterojunction are the conduction and valence band offsets, $\Delta E_{\rm c}$ and $\Delta E_{\rm v}$, respectively. These parameters control the height of the potential barrier (or drop) encountered by electrons or holes trying to traverse the heterojunction interface. As an example, we consider a heterojunction where the larger bandgap material is *p*-type and the smaller bandgap material is *n*-type, with no loss of generality. Such a band lineup, with and without an interface dipole, is shown in Figs. 8(a) and (b), respectively. We adopt the following sign convention for the band offsets. In accordance with the sign conventions for the built-in voltage and the interface dipole, $\Delta E_{\rm c}$ is also defined as positive if the bottom of the conduction band drops on passing from Material 1 to 2. However, $\Delta E_{\rm v}$ is negative if the top of the valence band drops on passing from Material 1 to 2. The latter sign convention implies the relation:

$$\Delta E_{\rm c} + \Delta E_{\rm v} = \Delta E_{\rm g} \equiv E_{\rm g1} - E_{\rm g2}, \tag{2.43}$$

where $E_{\rm g}$ is the semiconductor bandgap. Note that using this sign convention $\Delta E_{\rm c}$ may be assigned

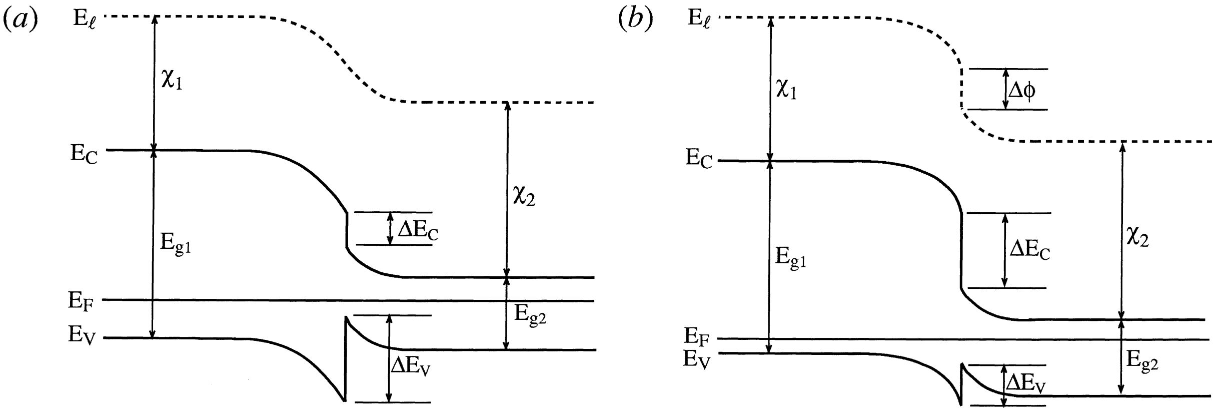

Fig. 8. Schematic energy band lineup at a type I semiconductor heterojunction: (a) without an interface dipole, (b) with a non-zero interface dipole.

either a negative or a positive value, depending on whether the larger bandgap material is referred to as 'Material 1' or '2'. Thus, it can be made equivalent to any sign convention used in the literature. Eq. (2.43) implies that if ΔE_c and the bandgap energies are known, so is ΔE_v. Hence, we focus our attention on ΔE_c.

In the absence of an interface dipole (Fig. 8(a)) and for uniform bulk materials, ΔE_c is equal to $\chi_2 - \chi_1$. This equality is known as the Anderson rule [45]. In many cases this rule is not followed experimentally. One reason for this is the presence of an interface dipole (Fig. 8(b)), which modifies the Anderson rule to $\Delta E_c = \chi_2 - \chi_1 + \Delta\phi_{in}$. Interestingly, a heterojunction band diagram which includes an interface dipole and a local vacuum level as defined in the present text, was proposed by Van Ruyven as early as 1964 [46]. Moreover, in a real experiment one measures the *effective* electron affinity, χ^*, and not the electron affinity as defined using the local vacuum level concept. Thus, the electron affinity values used in the Anderson rule may lead to results which are in disagreement with experiment, even in the absence of an interface dipole. This may explain why 35 years after Anderson's original paper, the accurate and direct determination of the band offsets in a heterojunction under study is still a challenge [47].

Using Fig. 8, ΔE_c may also be expressed as:

$$\Delta E_c = \left[(E_c - E_F)_{b1} - eV_{b1}\right] - \left[(E_c - E_F)_{b2} + eV_{b2}\right], \tag{2.44}$$

where V_b is the potential drop on one side of the heterojunction and all other indices have their usual meaning. The built-in voltage, V_{bi}, is by definition the total voltage drop across the interface SCR:

$$V_{bi} = V_{b1} + V_{b2} + \Delta\phi_{in}. \tag{2.45}$$

Hence, Eqs. (2.44) and (2.45) may be combined to yield:

$$\Delta E_c = E_{c1} - E_{c2} - eV_{bi} + \Delta\phi_{in}. \tag{2.46}$$

An interface SCR also obeys the charge neutrality law, given by:

$$Q_1 + Q_2 + Q_{ss} = 0, \tag{2.47}$$

where Q_1 and Q_2 are the charge densities (per unit area) on both sides of the interface.

Even in the absence of interface states, an interface dipole induces a SCR (in marked contrast to a *surface* dipole). Consider another *gedanken* experiment, shown in Fig. 9, in which an interface dipole is 'inserted' at a *p–n* homojunction. The abrupt discontinuity in the local vacuum level dictated by the dipole layer, combined with the necessarily identical electron affinities far away from the interface, imply that the local vacuum level must be bent. Thus, an electrostatic potential develops and an interface SCR is formed. Physically, insertion of an interface dipole in a uniform semiconductor sample forces the electrons on one side of the dipole to have an average energy which is higher than those on the other side. This induces electron transfer from the high energy to the low energy side, setting up an internal electric field to counteract the flow. In the case of a surface dipole, there are no electrons on the vacuum side and hence this phenomenon is absent.

The insertion of an 'artificial dipole layer' is by no means only a thought experiment. The band offsets of many heterojunctions have been modified by means of inserting thin intralayers of a different material at the interface, which create a net interface dipole [48]. Similarly, an artificial band discontinuity was induced at a GaAs *homojunction* by means of inserting a very thin Si intralayer [49]. An interesting different approach, which modifies the dipole by means of a chemical bond with organic

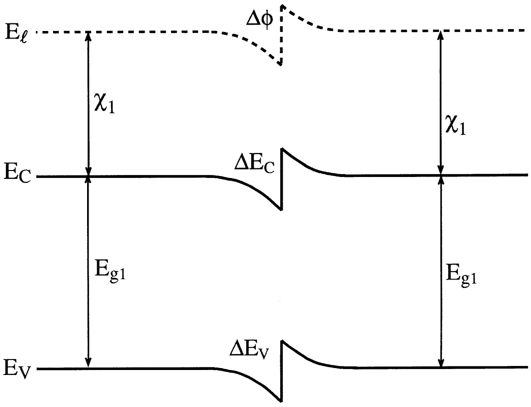

Fig. 9. Schematic energy band diagram of a homogeneous semiconductor into which a dipole layer has been inserted.

molecules, has been demonstrated for both surface [50–57] and interface [58] dipoles. Thus, the band offsets are experimentally found to change due to both natural interface dipoles (mentioned in Section 2.1.4 [38,39]) and 'artificial' ones, in agreement with the theoretical prediction.

2.2. *Surface photovoltage (SPV)*

2.2.1. *Basic concepts*

The photovoltaic effect consists, in general, of an illumination-induced change in the potential distribution in a given structure. It was discovered experimentally by Becquerel as early as 1839 [59]. The photovoltaic effect is typically the result of some charge transfer and/or redistribution within the device due to the incident illumination. A specific variant of the photovoltaic effect is the *surface* photovoltaic effect, which is at the center of the present text. The surface photovoltage (SPV) is defined as the illumination-induced change in the surface potential. This effect, observed at Si and Ge surfaces, was first reported in a short note by Brattain in 1947 [1], followed by a detailed account some years later [2].

The photovoltaic effect at metal–semiconductor and semiconductor–semiconductor junctions is at the heart of semiconductor devices which convert light to electricity. These include photodetectors and imagers, as well as solar and photoelectrochemical cells [25,59,60]. Due to its physical and technological importance, the theory of device-related photovoltaic effects is extremely well developed (see, e.g., [25,59], and references therein). Here, we shall naturally focus on the less familiar surface photovoltaic effect.

We concentrate on the SPV induced at the free surface of a semiconductor sample with a grounded Ohmic back contact. In many SPV theories it is (explicitly or implicitly) assumed that no appreciable voltage drop develops on the quasi-neutral bulk even under illumination, as depicted schematically in Fig. 10 for the case of depletion. In the absence of an external field, the charge neutrality rule, $Q_{ss} + Q_{sc} = 0$ [Eq. (2.24)], must remain valid regardless of illumination. However, both Q_{ss} and Q_{sc} may change, possibly very significantly, upon illumination. The absorbed photons induce the formation of free carriers by creating electron–hole pairs via band-to-band transitions (typically dominant for super-bandgap photons) and/or release captured carriers via trap-to-band transitions (typically dominant for sub-bandgap photons). Thus, a significant amount of charge may be transferred from the surface to the bulk (or vice versa) and/or redistributed within the surface or the bulk. Since the electric potential and the charge distribution are inter-dependent through the Poisson and continuity equations, the potential drop across the surface SCR, and hence the surface potential, changes. It is important to note that the formation of a SPV occurs only if carrier generation per se is followed by net charge *redistribution*. The detailed analysis of the SPV depends strongly on whether the incident photon energy is super-bandgap or sub-bandgap, i.e., on the dominant carrier excitation mechanism. Hence, these two analyses are pursued separately in Sections 2.2.2 and 2.2.3 respectively.

So far, we have attributed the formation of a SPV *only* to changes in the potential drop across the SCR. However, non-uniform generation or recombination may also cause a potential drop across the quasi-neutral region of the sample. This is known as the Dember potential [61] and is discussed in detail in Section 2.2.4. While Sections 2.2.1–2.2.4 all deal with case of a uniform bulk sample, Section 2.2.5 is concerned with the effect of interfaces *within* the sample on the obtained SPV signal. We note that a SPV may also result from a photochemical reaction, in which the incident illumination changes the surface or the bulk chemically [62]. In particular, it may change the various trap densities and hence alter the SPV other than by directly exciting charge carries. This effect is not treated any further in this chapter but is mentioned subsequently where appropriate.

2.2.2. Super-bandgap SPV

Under super-bandgap illumination in reasonable quality material, the probability of band-to-band absorption is typically orders of magnitude larger than the probability of trap-to-band absorption, while the effect of trap-to-band absorption on the SRH recombination statistics is negligible [63]. Therefore, throughout this sub-section we neglect the effect of trap-to-band absorption on the obtained SPV. (For a discussion of experimental examples where this assumption is not valid, see Section 4.2 below). Mathematically, this assumption is equivalent to nullifying the trap-related optical cross-sections, σ_n and σ_p (defined in Eq. (2.13)), for all gap states within the sample. Hence, the illumination may change the surface potential in this case only by the formation of electron–hole pairs.

As shown below, finding the functional relationship between the formed SPV and the illumination intensity and wavelength is not generally amenable to an analytical solution. Therefore, many studies have analyzed the relatively easier problem of finding the relation between the formed SPV and the *excess carrier densities*. Besides facilitating mathematical ease, this analysis results in much physical insight. Since analytical time-resolved analyses are limited to a very narrow range of cases [64], we focus on steady-state analyses.

Based on Section 2.1.3, we now obtain expressions for Q_{sc} and Q_{ss} under illumination, starting with Q_{sc}. Again, one has to solve the Poisson equation (2.1). However, under non-equilibrium conditions the Boltzmann relations (2.7) are not necessarily valid. Thus, the free carrier density in the surface SCR cannot be related to that of the bulk by Eq. (2.27). Instead, one may use Eq. (2.8) which describes the charge densities in terms of the quasi-Fermi levels. In the case of steady-state illumination through the free surface, shown in Fig. 10, the electron and hole quasi-Fermi levels generally depart from the equilibrium Fermi level value, but deep within the sample bulk the illumination is practically negligible and the quasi-Fermi levels converge to the equilibrium value. In addition, recombination in the surface SCR in general, and at the surface itself in particular, may be significantly larger than in the bulk,

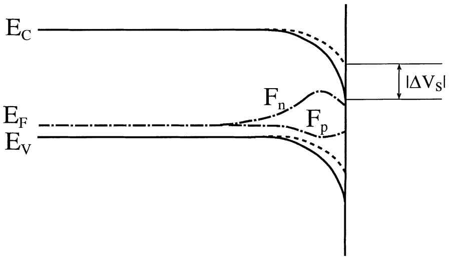

Fig. 10. Schematic band diagram of a surface space charge region under depletion: Solid lines – equilibrium. Dashed lines – under illumination. Dash-dotted lines – quasi-Fermi levels under illumination.

thereby reducing the effective excess carrier density. This may cause the quasi-Fermi levels to deviate less from equilibrium towards the surface than at the edge of the SCR, as in Fig. 10. According to Eq. (2.9), changes in the quasi-Fermi levels indicate a non-zero electron and hole current, even under steady-state conditions. Indeed, under open circuit conditions only the total current, J, must be zero, whereas J_n and J_p may be non-zero. This does not contradict the principle of detailed balance [31], which only demands that J_n and J_p provide carriers at a rate which maintains a steady state surface recombination rate, i.e., $J_n(0) = -J_p(0) = eR_s$, where $R_s = R_n = R_p$ is the steady-state surface recombination rate.

In 1955, Garrett and Brattain have published a classic paper [3], where a first serious attempt was made at a comprehensive theory of semiconductor surfaces, including surface photovoltaic effects. They suggested that under certain conditions, the quasi-Fermi levels may be *approximated* as position-independent (i.e., 'flat') throughout the surface SCR. They identified two conditions for this approximation to hold. First, the SCR width must be considerably smaller than the (electron and hole) diffusion length, L, so that the effect of non-uniform carrier excitation is negligible over the SCR. This condition is quite easily satisfied in many materials of reasonable quality. Second, the defect-related recombination current must not be 'too large' nor the depletion of carriers 'too extreme' [3]. The latter conditions assure that even if J_n , J_p are not zero, the variation in the quasi-Fermi levels, F_n and F_p, given by [see Eq. (2.9)]:

$$\left|\frac{\mathrm{d}F_n}{\mathrm{d}x}\right| = \frac{J_n}{n\mu_n}; \qquad \left|\frac{\mathrm{d}F_p}{\mathrm{d}x}\right| = \frac{J_p}{p\mu_p}, \tag{2.48}$$

may be neglected. For understanding this point further, consider the order of magnitude calculation given by Many et al. [22]. Neglecting recombination in the SCR, the recombination current is constant throughout the SCR and is equal to eR_s, where R_s is given by Eq. (2.19). In the case of a depleted p-type semiconductor, it can be shown that R_s is always smaller than $c_pN_\mathrm{t}p_\mathrm{s}$ and p always larger than p_s. Thus, using Eq. (2.48) we obtain:

$$\left|\frac{\mathrm{d}F_p}{\mathrm{d}x}\right| \leq \frac{c_pN_\mathrm{t}}{\mu_p} \quad \Rightarrow \quad \Delta F_p \leq \frac{c_pN_\mathrm{t}w}{\mu_p}, \tag{2.49}$$

where ΔF_p is the variation of the hole quasi-Fermi level across the entire SCR For, e.g., a Si sample with $w = 0.4$ μm , $c_p = 10^{-8}$ cm^3/s, and $N_t = 10^{12}$ cm^{-2}, we get $\Delta F_p < 1$ meV, which, except at very low temperatures, is much smaller than kT and therefore negligible. Similar considerations apply to the electron quasi-Fermi level.

Frankl [65] has performed more detailed estimates of the validity of the flat quasi-Fermi levels (FQL) approximation. By making various approximations and assumptions regarding on the space charge function F (Eq. (2.31)), he has shown that for a depleted semiconductor with a reasonable SRV, the FQL approximation is typically acceptable as long as the illumination intensities are not too high (since this may result in a too large recombination current). Furthermore, Frankl has shown that the approximation may fail for minority carriers in an accumulation layer and for majority carriers in an inversion layer [65]. Note that in both cases the change in carrier concentration with respect to the bulk value is 'too extreme', as noted above. Following the results of the first-order calculations of Many et al., as well as the more detailed quantitative work of Frankl, we adopt the Garrett–Brattain approximation for further considerations.

Assuming that F_n and F_p are position independent, the dependence of Q_{sc} on the minority carrier density *at the edge of the SCR* is relatively easily found. This is because under this assumption the Boltzmann relations (2.7), and hence Eq. (2.26) hold even for non-equilibrium densities, i.e.,

$$n^*(x) = n_{\mathrm{b}}^* \exp\left(\frac{eV(x)}{kT}\right), \qquad p^*(x) = p_{\mathrm{b}}^* \exp\left(\frac{-eV(x)}{kT}\right), \tag{2.50}$$

where here and in the following the superscript '*' denotes non-equilibrium densities and n_{b}^* and p_{b}^*, refer to the charge density at the SCR edge. We further define the electron and hole excess carrier density, $\delta n \equiv n_{\mathrm{b}}^* - n_{\mathrm{b}}$ and $\delta p \equiv p_{\mathrm{b}}^* - p_{\mathrm{b}}$, where quasi-neutrality in the bulk requires that $\delta n = \delta p$. The use of the 'quasi-Boltzmann' relations [Eqs. (2.50)] makes it possible to separate the solutions of the Poisson equation and the continuity equations, thereby considerably simplifying the problem. As in Section 2.1.3, we consider, without loss of generality, the case of a p-type sample. Since Eqs. (2.26) and (2.28) are valid regardless of illumination, the equivalent of Eq. (2.29) under non-equilibrium conditions is:

$$\frac{\mathrm{d}^2 V}{\mathrm{d}x^2} = -\frac{e}{\epsilon}\left(p_{\mathrm{b}} - n_{\mathrm{b}} + p_{\mathrm{b}}^* \mathrm{e}^{-eV/kT} - n_{\mathrm{b}}^* \mathrm{e}^{eV/kT}\right). \tag{2.51}$$

Following Johnson [66], we define the fractional carrier increase, also known as the injection ratio, as $\Delta_n = \delta_n / n_{\mathrm{b}}$ and $\Delta_p = \delta_p / p_{\mathrm{b}}$. Integrating Eq. (2.51) from the bulk toward the surface, using semi-infinite boundary conditions and proceeding as in Section 2.1.3, we obtain:

$$Q_{\mathrm{sc}} = \mp \frac{\sqrt{2}\epsilon_{\mathrm{s}} kT}{eL_{\mathrm{d}}} F^*\left(\frac{eV_{\mathrm{s}}^*}{kT}, \frac{n_{\mathrm{b}}}{p_{\mathrm{b}}}, \Delta_n\right), \tag{2.52}$$

where:

$$\begin{aligned} F^*\left(\frac{eV_{\mathrm{s}}^*}{kT}, \frac{n_{\mathrm{b}}}{p_{\mathrm{b}}}, \Delta_n\right) &= \left[\left(\mathrm{e}^{-eV^*/kT} + \frac{eV^*}{kT} - 1\right) + \frac{n_{\mathrm{b}}}{p_{\mathrm{b}}}\left(\mathrm{e}^{eV^*/kT} - \frac{eV^*}{kT} - 1\right)\right. \\ &\qquad \left. + \frac{n_{\mathrm{b}}}{p_{\mathrm{b}}}\Delta_n\left(\mathrm{e}^{-eV^*/kT} + \mathrm{e}^{eV^*/kT} - 2\right)\right]^{1/2} \\ &= \left[F^2\left(\frac{eV^*}{kT}, \frac{n_b}{p_b}\right) + \frac{n_b}{p_b}\Delta_n\left(\mathrm{e}^{-eV^*/kT} + \mathrm{e}^{eV^*/kT} - 2\right)\right]^{1/2}. \end{aligned} \tag{2.53}$$

For $\Delta_n = 0, F^*(eV^*/kT, n_{\mathrm{b}}/p_{\mathrm{b}}, \Delta_n)$ reduces to $F(eV^*/kT, n_{\mathrm{b}}/p_{\mathrm{b}})$, as expected. The Kingston–

Neustadter representation for Q_{sc} [Eq. (2.35)] has been extended to non-equilibrium in a similar manner by Frankl and Ulmer [67].

The dependence of Q_{sc} on Δ_n suffices to study the SPV in the case where Q_{ss} (and hence Q_{sc}) does not change upon illumination (such a SPV is sometimes known as a 'barrier SPV' [22]). A fixed surface space charge implies that $F^*(eV_{\mathrm{s}}^*/kT, n_{\mathrm{b}}/p_{\mathrm{b}}, \Delta_n) = F(eV_{\mathrm{s}}/kT, n_{\mathrm{b}}/p_{\mathrm{b}})$, which provides an implicit equation for the difference $V_{\mathrm{s}}^* - V_{\mathrm{s}}$, i.e., for the SPV. According to Eq. (2.53), $F^*(eV_{\mathrm{s}}^*/kT, n_{\mathrm{b}}/p_{\mathrm{b}}, \Delta_n)$ must always be larger than $F(eV_{\mathrm{s}}^*/kT, n_{\mathrm{b}}/p_{\mathrm{b}})$. Furthermore, since both $F(eV_{\mathrm{s}}^*/kT, n_{\mathrm{b}}/p_{\mathrm{b}})$ and the term $(n_{\mathrm{b}}/p_{\mathrm{b}})\Delta_n(e^{-eV^*/kT} + e^{eV^*/kT} - 2)$ increase monotonously with $|V_{\mathrm{s}}|$, so does $F^*(eV_{\mathrm{s}}^*/kT, n_{\mathrm{b}}/p_{\mathrm{b}}, \Delta_n)$. Therefore, $|V_{\mathrm{s}}|$ must decrease upon illumination so as to decrease $F^*(eV_{\mathrm{s}}^*/kT, n_{\mathrm{b}}/p_{\mathrm{b}}, \Delta_n)$ back to its equilibrium value. The resulting conclusion is that *in the absence of change in the surface charge*, illumination always tends to decrease the band bending [66]. Moreover, the band bending should approach zero as the excess carrier density increases. Physically, the photo-induced carriers partially screen the fixed surface state charge, thereby reducing the surface band bending. For a large enough excess density, the screening should be complete. Note that here if the bands are flat (i.e., $V_{\mathrm{s}} = 0$) in equilibrium, they remain flat under illumination.

Based on Eqs. (2.52) and (2.53), one can show that the SPV increases with decreasing n_{i}^2. This is expected physically: the effect of optically-induced band-to-band transitions on the SPV should become more pronounced as thermally-induced transitions are suppressed, i.e., as n_{i} is reduced. It is well known that n_{i}^2 decreases exponentially with both increasing bandgap and decreasing temperature. Thus, for uniform samples the SPV method is significantly more sensitive to large bandgap semiconductors and at lower temperatures.

In the earliest studies [2,3] it was assumed that the surface states were in equilibrium with the semiconductor bands, i.e., that Fermi–Dirac statistics [Eq. (2.11)] adequately described the surface state population even under non-equilibrium conditions. This is clearly a rough approximation and Brattain and Garrett have presented a more complete theory, based on a detailed SRH approach, not long after their preliminary studies [68]. In this approach, the steady-state surface charge is given by Eq. (2.23). For each surface state, we obtain using Eq. (2.18):

$$n_{\mathrm{t}} = \frac{c_n n_{\mathrm{s}}^* + c_{\mathrm{p}} p_1}{c_n\left(n_{\mathrm{s}}^* + n_1\right) + c_{\mathrm{p}}\left(p_{\mathrm{s}}^* + p_1\right)} N_t. \tag{2.54}$$

Eq. (2.54) is valid regardless of the FQL approximation. However, with the latter approximation it may be rewritten as:

$$n_{\mathrm{t}} = \frac{c_n n_{\mathrm{b}}^* e^{eV^*/kT} + c_{\mathrm{p}} p_1}{c_n\left(n_{\mathrm{b}}^* e^{eV^*/kT} + n_1\right) + c_p\left(p_{\mathrm{b}}^* e^{-eV^*/kT} + p_1\right)} N_{\mathrm{t}}, \tag{2.55}$$

which provides an explicit relation between the surface charge, the excess carriers at the edge of the SCR, and the surface voltage. According to Eqs. (2.54) and (2.55), the surface charge changes under illumination due to the change in the surface free carrier densities. The time necessary to reach the steady state distribution depends on the thermal cross-sections, which vary over many orders of magnitude. Thus, Bardeen and Brattain [2] (and consequently many others) distinguished between 'fast states' and 'slow states', according to whether the charge in the surface states follows the illumination (at a given modulation frequency or allowed response time) or not, respectively. Though clearly arbitrary, we adopt this division for the present considerations due to its simplicity. Its practical implication is that while the charge in 'fast states' changes under illumination according to Eqs. (2.23) and (2.55), the charge in ‘slow states’ is assumed to be constant. Thus, the charge neutrality condition implies that the sum of the space charge, the fast state charge, and the slow state charge is zero both in equilibrium and under illumination. The space charge is given by Eq. (2.52), the fast state charge by Eqs. (2.23) and (2.55) with proper surface carrier densities, and the slow state charge is constant. Interestingly, Bardeen and Brattain [2] interpreted their pioneering data by assuming that *all* charge redistribution is among surface states only, i.e., that Q_{sc} is negligible. This is clearly not a good assumption in most cases.

A small-signal analysis of the SPV was performed by Brattain and Garrett [68] and later by Frankl and Ulmer [67] for the case of continuous and discrete surface state distributions, respectively. Within this analysis, it is possible to find an explicit (albeit cumbersome) expression for $\mathrm{d}V_{\mathrm{s}}/\mathrm{d}\Delta_p$, i.e., for the SPV obtained due to a small variation in the carrier injection factor at the edge of the SCR. Upon illumination, Q_{sc} and Q_{ss} change due to both carrier injection and change in surface potential. Therefore, the differential of the charge neutrality condition (2.24) may be written as:

$$\left(\frac{\partial Q_{\mathrm{sc}}}{\partial \Delta_p}\right)_{\substack{V_{\mathrm{s}}^* \to V_{\mathrm{s}}^0 \\ \Delta_p \to 0}} \mathrm{d}\Delta_p + \left(\frac{\partial Q_{\mathrm{sc}}}{\partial V_{\mathrm{s}}}\right)_{\substack{V_{\mathrm{s}}^* \to V_{\mathrm{s}}^0 \\ \Delta_p \to 0}} \mathrm{d}V_s + \left(\frac{\partial Q_{\mathrm{ss}}}{\partial \Delta_p}\right)_{\substack{V_{\mathrm{s}}^* \to V_{\mathrm{s}}^0 \\ \Delta_p \to 0}} \mathrm{d}\Delta_p + \left(\frac{\partial Q_{\mathrm{ss}}}{\partial \Delta_p}\right)_{\substack{V_{\mathrm{s}}^* \to V_{\mathrm{s}}^0 \\ \Delta_p \to 0}} \mathrm{d}V_{\mathrm{s}} = 0, \tag{2.56}$$

yielding:

$$\frac{\mathrm{d}V_{\mathrm{s}}}{\mathrm{d}\Delta_p} = -\left[\frac{(\partial Q_{\mathrm{sc}})/(\partial \Delta_p) + (\partial Q_{\mathrm{ss}})/(\partial \Delta_p)}{(\partial Q_{\mathrm{sc}})/(\partial V_s) + (\partial Q_{\mathrm{ss}})/(\partial V_{\mathrm{s}})}\right]_{\substack{V_{\mathrm{s}}^* \to V_{\mathrm{s}}^0 \\ \Delta_p \to 0}}, \tag{2.57}$$

where V_{s}^0 is the equilibrium value of V_{s}. The terms on the right hand side of Eq. (2.57) are easily obtained from partial derivatives of Eqs. (2.52) and (2.53) for the expressions involving Q_{sc}, and of Eqs. (2.23) and (2.55) for the expressions involving Q_{ss}. An example of such a calculation is given in Fig. 11, which features the dependence of $\left|\mathrm{d}V_{\mathrm{s}}/\mathrm{d}\Delta_p\right|$ on V_{s}^0 for a 10^{15} cm^{-3} *p*-InP sample with surface states of varying density. Here, the equilibrium value of V_{s} is arbitrarily scanned, assuming it is set by a proper density of ‘slow states’.

Much physical insight may be obtained from Fig. 11. As a general trend, the SPV tends to increase with increasing initial band bending. For small V_{s}^0, the obtained SPV is linear in V_{s}^0. For larger V_{s}^0 the slope of the SPV versus V_s^0 gradually decreases. Deep into inversion or accumulation, $\left|\mathrm{d}V_{\mathrm{s}}/\mathrm{d}\Delta_{\mathrm{p}}\right|$ obtains a limiting value, which is independent of the surface states. This independence is obtained because for a given energy position, the states are almost ‘completely full’ or ‘completely empty’ if the band bending is large enough. Hence, the terms describing the variation of Q_{ss} in Eq. (2.57) are negligible with respect to the terms describing the variation of Q_{sc}. The limiting values of $\left|\mathrm{d}V_{\mathrm{s}}/\mathrm{d}\Delta_p\right|$ are easily shown to be (kT/e) and $(kT/e)(n_{\mathrm{b}}/p_{\mathrm{b}})$ (for a *p*-type sample) for the inversion and accumulation regimes, respectively. For reasonably doped samples, the second value is orders of magnitude smaller than the first. Thus, the SPV measurement is, inherently, significantly less sensitive to accumulated surfaces than to depleted or inverted surfaces. Physically, in the case of accumulation, minority photocarriers are swept towards the bulk, where they may easily recombine due to the abundance of majority carriers. However, in the case of depletion or inversion, minority photocarriers are swept towards the surface, where the majority carrier density is lower and chances for recombination are reduced. Thus, in accumulation the sample is inherently more ‘resistant’ to illumination-induced changes in its charge distribution and only a relatively small SPV is necessary to reinstate charge neutrality.

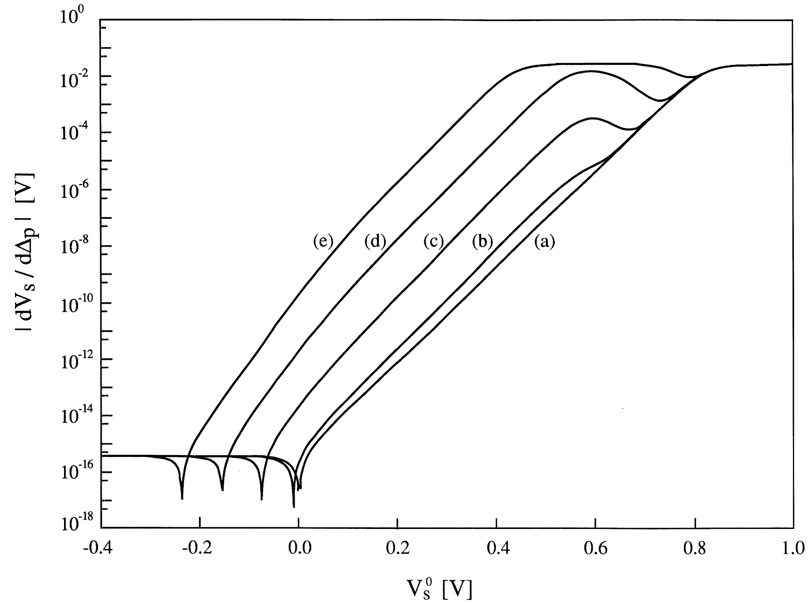

Fig. 11. Dependence of $|dV_s/d\Delta_p|$ on V_s^0 for a 10^{15} cm^{-3} InP sample with surface states situated 180 meV above the intrinsic Fermi level, thermal capture coefficients of $C_n = 10^{-9}$ cm^3 s^{-1}, $C_p = 0$, and a surface density (in cm^{-2}) of: (a) 0, (b) 10^6, (c) 10^8, (d) 10^{10}, (e) 10^{12}.

In the depletion regime, a 'bulge' in the $|dV_s/d\Delta_p|$ versus V_s^0 curves is observed for quite low surface state densities (as low as 10^6 cm^{-3} in Fig. 11). For larger densities, a perceptible maximum is noted. This structure is clearly the result of surface charge dynamics. Additionally, the SPV curves 'shift' towards negative values of V_s^0 upon increasing surface state density, which is explained as follows. The specific surface states assumed capture only electrons because their thermal cross-section for holes is assumed to be zero. Upon illumination, some of the excess electrons, but no excess holes, are captured in surface states. Thus, Q_{ss} must become more negative and hence Q_{sc} must become more positive, i.e., the entire $|dV_s/d\Delta_p|$ curve is pushed in the direction of accumulation. In particular, the selective capture of electrons may induce a non-zero SPV response even if the bands are initially flat. The latter case has been treated in detail by Buimistrov et al. [69] as a 'new form' of SPV, but has been shown to be only a special case soon thereafter [67].

The effects of surface charge trapping on the SPV may be further understood by considering Johnson's graphical method for the calculation of large-signal SPV [66]. Johnson's approach is a natural extension of the method used for generating Fig. 2. In this method, Q_{sc} and Q_{ss} curves are plotted for each excess carrier density of interest, allowing for a calculation of the SPV as a function of arbitrary Δ_n. Johnson performed a comprehensive set of such calculations for Ge and found that the dependence of the SPV on the injection factor was monotonous and that surface states usually did not change the qualitative shape of this dependence. Extensive graphical calculations were also performed by Brouwer [70].

The construction of 'space-charge path' curves is a useful tool for gaining more insight into surface and bulk trapping effects. Consider, for example, the SPV in a CdS sample with bulk acceptor and donor states, as well as surface states situated at varying energies within the bandgap, studied by Maltby et al. [35] Fig. 12(a) features the SPV as a function of the fractional excess carrier density, Δ_n,

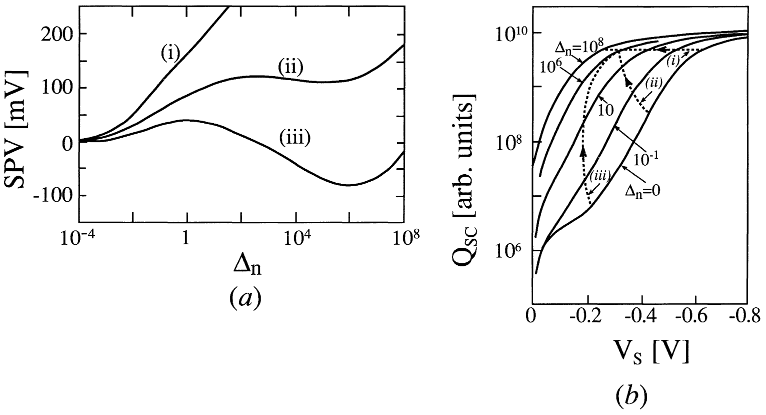

Fig. 12. (a) SPV vs. minority carrier injection ratio, and (b) space charge curves, for a CdS sample with $10^{16}\,\mathrm{cm}^{-3}$ bulk acceptor states, $10^{12}\,\mathrm{cm}^{-3}$ bulk donor states, and $10^{11}\,\mathrm{cm}^{-2}$ surface states situated at: (i) 0.4, (ii) –0.1, (iii) –0.4 eV above the intrinsic Fermi level (after Maltby et al. [35]).

for three different surface state positions, whereas Fig. 12(b) features the space charge curves for the same surface state positions (the calculation is based on extending Eq. (2.96) to include deep levels). In Curve (i) the SPV versus Δ_n curve (Fig. 12(a)) is monotonous. In this case the surface state population (and hence Q_{sc}) remains practically constant so that the corresponding space-charge path (Fig. 12(b)) is horizontal. In the two other curves, Q_{ss} changes considerably with increasing illumination. Interestingly, when Q_{ss} changes significantly the SPV response is *not* a monotonous function of Δ_n. The surface barrier may actually *increase*, rather than decrease, upon illumination, as in Curve (iii), causing an SPV of the opposite sign. However, it should be taken into account that the data of Fig. 12 pertain to unusual experimental conditions, i.e., the density of bulk states is very large and the injection ratio is high. These two factors also limit the validity of the FQL approximation as they increase the magnitude of the recombination current. Therefore, while Fig. 12 adequately presents the qualitative trends involved in these extreme experimental conditions, its quantitative aspects should be examined with caution. We note in passing that the above-given theory may also be extended in other directions. For example, De et al. [71] have extended it to highly-doped semicondcutors.

The dependence of the SPV on the excess carrier density at the edge of the SCR does not allow a comparison with experiments unless the excess carrier density is measured along with the SPV, which is not trivial. Obviously, it is preferable to directly correlate the SPV with the properties of the incident illumination. A very useful approximate solution of the continuity equations for obtaining the dependence of the excess minority carrier density on the illumination has been forwarded by Moss [72]. However, it is frequently referred to in the literature as the ‘Goodman equation’ since Goodman has popularized Moss’s results by using them in a new algorithm for measuring bulk diffusion legnths using SPV [5]. This approximation is discussed here, based on the later perspective of Chiang and Wagner [73]. For front-surface illumination, the optical generation, G, may be expressed as [24]:

$$G(x) = \alpha I \exp(-\alpha x), \tag{2.58}$$

where I is the effective photon flux (which is equal to the real photon flux multiplied by the surface optical transmission and the sample quantum efficiency) and α the absorption coefficient. Under the depletion approximation, the drift current is negligible with respect to the diffusion current in the quasi-neutral region, and vice versa in the depletion region. Let us consider a specific case where the minority carriers are electrons. Based on the above approximation, using Eqs. (2.2), (2.3) and (2.58), and assuming the excitation is sufficiently low-level so that Eq. (2.20) may be used, the continuity equation for electrons becomes:

$$D\frac{\mathrm{d}^2\delta n(x)}{\mathrm{d}x}-\frac{\delta n(x)}{\tau}+\alpha I\exp\left(-\alpha x\right)=0, \tag{2.59}$$

where the subscript 'n' has been omitted from D and τ for brevity.

For a thick sample, the back surface boundary condition is clearly $\delta n(\infty)=0$. At the space charge edge, the following 'surface recombination type' boundary condition is used:

$$D\left.\frac{\mathrm{d}\delta n(x)}{\mathrm{d}x}\right|_{x=w}=S\delta n(w), \tag{2.60}$$

where S is assumed constant. If one further assumes that the SCR width is much smaller than both the absorption length and the diffusion length, i.e., $w\ll 1/\alpha$ and $w\ll L$, the excess minority carrier at the SCR edge may be expressed by the compact form:

$$\delta n(w)=\frac{\alpha L}{1+\alpha L}\cdot\frac{1}{S+D/L}I. \tag{2.61}$$

S should be interpreted as an *effective* drift velocity for electrons reaching the SCR edge, rather than as a true SRV. However, under the above assumptions, the effect of the SCR is negligible. Indeed, Eq. (2.61) would have the same form had w been neglected in advance and S interpreted as a 'real' SRV. Under the above restrictions, $\delta n(w)$, which is proportional to I, may be inserted into Eqs. (2.53) and (2.55). Thus, the obtained SPV is explicitly expressed in terms of the incident photon flux. Interestingly, no use of the majority carrier continuity equation is made in this approach. The reason is that under the assumptions of quasi-neutrality and FQL, the distribution of the majority carriers is completely specified by that of the minority carriers. Such an approach has been used by Frankl and Ulmer [67] for obtaining explicit expressions of the small signal SPV. These expressions were further simplified by Lile [74] for obtaining expressions which may be compared to experiment with relative ease. A generally similar approach has been followed by Zuev and Litovchenko [75]. Note that under the FQL approximation the SRV did not appear in the Poisson equation in any way. At a superficial glance, it may seem as if, e.g., for a constant Q_{ss}, the SRV does not affect the magnitude of the SPV. This is incorrect, because the SRV enters the equations even under this approximation through the dependence of $\delta n(w)$ on the illumination intensity. Indeed, one would physically expect a reduced SPV the larger the SRV is since the illumination-induced deviation from equilibrium is smaller, as also verified numerically [76].

We emphasize that the boundary condition of Eq. (2.60) at the edge of the SCR is only an ad hoc approximation, which stems from neither the continuity equations nor the SRH statistics. Chiang and Wagner [73] suggested that a rigorous analytical approach would involve replacing the boundary condition of Eq. (2.60) with a detailed current balance in the SCR. Such a balance would properly account for generation and recombination processes inside the SCR, as well as use proper SRH statistics instead of SRV-based approximations. This paper has fostered several generalization attempts by other authors, discussed below.

Choo et al. [77] presented a current balance calculation which is simpler than Chiang and Wagner's. By integrating the steady-state continuity equation across the SCR, the relation:

$$J_n(0) - J_n(w) = J_G - J_R, \tag{2.62}$$

is obtained, where:

$$J_G = e\int_0^w G_n(x)\,\mathrm{d}x; \qquad J_R = e\int_0^w R_n(x)\,\mathrm{d}x. \tag{2.63}$$

Here, $J_n(0)$ is the surface recombination current, eR_S, and $J_n(w)$ is the diffusion current at the edge of the SCR, which may be expressed by $\delta n(w)$ from the solution of Eq. (2.59). In principle, the charge balance condition, Eq. (2.24), and the current balance condition, Eq. (2.62), provide two non-linear coupled algebraic equations for the SPV and for $\delta n(w)$. Thus, under the FQL approximation, the SPV may be found by numerically solving algebraic equations, but not differential ones. Moreover, in some cases analytical expressions can be obtained [77,78].

Having made the most out of the FQL approximation, we turn to examining the behavior of the quasi-Fermi levels more closely. A point of frequent confusion is the relation between the energy separation of the quasi-Fermi levels at the depletion region edge, $(F_n - F_p)|_{x=w}$ (see Fig. 10) and the SPV. Fig. 13 features a schematic band-diagram of a *p–n* junction under forward bias. It shows that the potential energy drop across the SCR is equal to the energy separation between the positions of the *majority carrier* quasi-Fermi levels in the quasi-neutral regions [24]. If the potential drop across the SCR is not the result of electrical bias but is rather a *photovoltage* this equality is no longer exact. This is because the illumination may affect the position of the majority carrier quasi-Fermi levels in the quasi-neutral regions, due to photo-induced excess carrier generation. However, for low and moderate injection levels, the equality is still a good and useful approximation. Chiang and Wagner [73] assumed a similar equality, SPV $= (F_n - F_p)\big|_{x=w}$. Unfortunately, the latter relation is erroneous for the case of a free surface [77]. As opposed to the case depicted in Fig. 13, the energy separation here is not between two *majority* carrier quasi-Fermi levels on *opposite sides* of the SCR, but rather between *majority and minority* quasi-Fermi levels on the *same side* of the SCR. In order to understand more clearly why the equality is false, consider another *gedanken* experiment: Suppose one performs the SPV experiment on an 'ideal' uniform sample which has no surface states and no bulk states whatsoever. Such a sample has no band bending in equilibrium and no surface barrier would develop in such a case even under significant illumination. Thus, while the difference between F_n and F_p may be considerable, the SPV would remain zero. (For completeness, one should also assume equal electron and hole mobilities so that the Dember voltage is also zero – see Section 2.2.4 below).

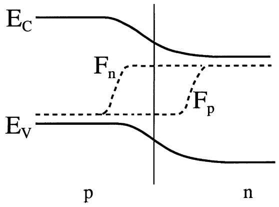

Fig. 13. Schematic diagram of quasi-Fermi levels in an illumination $p-n$ junction.

In many respects, the theory of the open-circuit photovoltage at a metal-semiconductor interface is very similar to the free surface case since in both the SCR is completely contained in the semiconductor part of the junction. A major difference between the two is that the metallic overlayer has a bulk Fermi level, while the surface states do not. Consequently, the identification of the SPV with the difference in majority carrier quasi-Fermi level on the two sides of the metal-semiconductor junction is at least as good an approximation as in the above described *p–n* junction. For, e.g., a *p*-type semiconductor, the relation:

$$\mathrm{SPV} \cong F_n(x=0) - F_p(x=w), \tag{2.64}$$

is a good approximation, as long as there is an intimate contact between the metal and the semiconductor [79]. If the quasi-Fermi levels are flat across the SCR, Eq. (2.64) is equivalent to the ansatz of Chiang and Wagner and the latter is therefore a reasonable approximation for metal–semiconductor interfaces, as also confirmed by numerical simulations [80].

Another difference between the metal–semiconductor junction and the free surface has to do with the current boundary conditions. While the free surface current is of a SRH-type recombination current, the metal–semiconductor interface current is associated with thermionic emission. From thermionic emission considerations, an effective interface recombination rate in the form of $R_n = v_n \delta n$ and $R_p = v_p \delta p$ is deduced [80], where v_n (v_p) is the effective recombination velocity for electrons (holes). This formulation is based on the combined thermionic emission-diffusion approach of Crowell and Sze [81], extended by Green and Shewchun [82] to minority carriers.

The early 1980s have seen a renewed interest in examining the validity of the FQL approximation for metal-semiconductor junctions: By assuming a recombination current which is constant across the SCR and a parabolic SCR potential, Panayotatos and Card [83] have shown that the minority carrier quasi-Fermi level may deviate considerably from the FQL approximation. Heasell [84] has shown that the majority carrier quasi-Fermi level may considerably deviate from flatness near the semiconductor–metal interface, in order to supply the current necessary to support the thermionic emission across the interface. Choo [80] has shown that even if the minority carrier quasi-Fermi level is reasonably flat across most of the SCR, it may undergo significant variations near the SCR edge, to the point of causing order-of-magnitude errors in current calculations.

Physically, the gradients in quasi-Fermi levels (see Fig. 10) imply net electron and hole currents: (a) towards the back part of the surface, driven by a concentration gradient caused by the non-uniform illumination, (b) towards the front surface, driven by the need to supply the surface recombination/emission current. This may also be established mathematically. By using a modified form of the drift-diffusion equation and the integrated continuity equation (Eq. (2.62)), Pauwels et al. expressed the surface current in the form: [85]:

$$J_n(0) = e\nu_{\mathrm{eff}}\left[n(0) - n(w)\exp\left(\frac{-eV_{\mathrm{s}}}{kT}\right)\right] + e\int_0^w [G_n(x) - R_n(x)]\eta_1(x)\,\mathrm{d}x, \tag{2.65}$$

where:

$$\nu_{\mathrm{eff}}(x) = \frac{D_n}{\int_0^w \exp\left(-eV(x)/kT\right)\mathrm{d}x}, \tag{2.66}$$

$$\eta_1(x) = \frac{\int_x^w \exp\left(-eV(x)/kT\right)\mathrm{d}x}{\int_0^w \exp\left(-eV(x)/kT\right)\mathrm{d}x}, \tag{2.67}$$

with a similar expression for holes. The factor in the left square brackets in Eq. (2.65) is the difference between the real surface concentration of electrons and that predicted by the FQL approximation. Thus, v_{eff} is interpreted as an effective transport velocity across the SCR. If generation and recombination in the SCR (and hence the integral term in Eq. (2.65)) are negligible, conservation of the FQL approximation requires that v_{eff} be infinite because a finite current must be sustained. However, from Eq. (2.66) it is clear that v_{eff} is finite. This re-establishes that with non-zero steady-state recombination currents, the FQL assumption is necessarily an approximation. $0 \leq \eta_1(x) \leq 1$ is the fraction of the net generated electron density (at a point x) which is transported to the front surface. A similar equation for the other edge of the SCR, w, results in another similar fraction, $0 \leq \eta_2(x) \leq 1$, such that $\eta_1(x) + \eta_2(x) = 1$ for all x in the SCR. Thus, $\eta_2(x)$ is the fraction of the net generated electron density at a point x which is transported to the back of the SCR, in agreement with the physical picture given above.

Based on the foregoing analysis, De Visschere [86] has formulated a transport validity criterion for the FQL approximation, which states that the transport should not be limited by v_{eff}, i.e., that v_{eff} must be larger than both the effective SRV and the diffusion velocity, v_{d}, in the quasi-neutral region. (This criterion should be added to other FQL validity criteria discussed above). The first transport restriction, $v_{\mathrm{eff}} \gg$ SRV, is, in a sense, a quantitative compact criterion for the allowed magnitude of the surface recombination. The second, $v_{\mathrm{eff}} \gg \nu_{\mathrm{d}}$, is usually satisfied as a result of an earlier condition – the SCR width being smaller than the diffusion length. Similar results have also been obtained by Jang using a somewhat different approach [87]. Finally, Choo has studied numerically both the free surface SPV [77] and the metal–semiconductor interface SPV [80], and concluded that typically the FQL approximation is considerably more satisfactory in the former than in the latter.

In studies of the metal-semiconductor interface, it is evidently meaningless to equate Q_{sc} with Q_{ss}. Instead, one uses current balance considerations. Recent studies have applied the current balance equation (Eq. (2.62)) for both minority and majority carriers [79,80]. In such studies the Poisson equation is circumvented by *assuming* a potential profile in the SCR, usually a parabolic one. The assumption of a parabolic potential lifts the need of using the Poisson equation just as the FQL assumption lifts the need for using the majority carrier continuity equation. As noted in Section 2.1.1, for a comprehensive solution one must determine the distribution of the potential, the electron density and the hole density by solving the Poisson equation with the two continuity equations. Under both assumptions, one makes an educated guess for a reasonably exact solution of one of these three parameters, thereby eliminating one equation. No assumption is free of restrictions. Here, the parabolic potential naturally limits the validity of the treatment to the depletion regime. Worse, under certain conditions a semiconductor in the depletion regime may invert upon illumination [77]. However, when applied with care the approximation may yield very good results. We also note that Dhariwal and Deoraj [79] has expressed the SPV as a function of the photocurrent density. Analogously, we have expressed above the SPV as a function of the injection ratio, but not of the illumination intensity.

Due to the inadequacy of the FQL approximation for some free surface SPV problems, a similar theoretical approach was adapted in the 1990s by some authors not only for metal–semiconductor studies but also for free surface studies [33,88,89]. Konstantinov and Tsarenkov [88] assumed that generation and diffusion currents dominate the minority carrier behavior and thermionic emission dominates the majority carrier behavior. Judging by the full current balance equation (Eq. 2.62), this is clearly not a universal conclusion. Thus, while their analysis leads to very simple mathematical expressions, its validity is limited. Darling [33] performed a complete current balance, but assumed a constant recombination rate throughout the SCR – an assumption which is not always realistic. The recent analysis of Liu et al. [89] is the most advanced one in the sense that it makes a full current analysis with realistic SRH statistics. However, it is limited to the case of a negligible change in Q_{ss}.

So far, we have only discussed the case where $\partial n/\partial t$ and $\partial p/\partial t$ in Eq. (2.2) are both zero, usually known as 'dc SPV'. Use of modulated illumination was mentioned only in the context of the 'fast' and 'slow' surface states. However, if the modulation frequency is high enough ('ac SPV'), a steady-state periodic variation of n, p, and the SPV, must be taken into account. Mathematical analyses of such steady-state solutions usually assume that all pertinent quantities follow a '$\exp(i\omega t)$' dependence, where ω is the modulation frequency. Use of this dependence in Eq. (2.2) yields $\partial n/\partial t = i\omega n \neq 0$, with a similar expression for holes. One particular consequence of this, which is important for some of the advanced analyses reviewed in Section 5, is the modification of the diffusion length [90]. If the steady state diffusion equation (i.e., the continuity equation in the absence of electric field) is solved under steady-state periodic conditions, the effective diffusion length is given by:

$$L(\omega) = \sqrt{\frac{D\tau}{1+i\omega\tau}} = \frac{L(\omega=0)}{\sqrt{1+i\omega\tau}}. \tag{2.68}$$

Analytical expressions for ac SPVs have been developed almost exclusively within the framework of small SPV signals (SPV $\ll kT/e$), where the steady-state periodic SPV can be safely assumed to depend linearly on the steady-state photocurrent. The initial groundwork for such calculations was laid by Nakhmanson [91] with subsequent extensions, refinements, and applications by Nakhmanson himself [92] and by Munakata et al. [93–96]. According to these authors, the photocurrent density, $J_{ph}(\omega)$, is typically extracted from a current-balance calculation. As in the case of the dc SPV, the most simple calculations utilize the Moss approach, i.e., use the concept of an effective, SCR-related, SRV. The photocurrent density, J_{ph}, is then calculated from:

$$J_{ph} = -eD_n \left.\frac{\mathrm{d}\delta n(x)}{\mathrm{d}x}\right|_{x=w} = -eS\delta n(w), \tag{2.69}$$

which results in:

$$J_{ph} = eI\frac{\alpha L(\omega)}{1+\alpha L(\omega)} \cdot \frac{S}{S+D/L(\omega)} \exp(i\omega t), \tag{2.70}$$

where $L(\omega)$ is given by Eq. (2.68).

Eq. (2.70) reduces to particularly simple forms if: (a) the diffusion length is relatively long, so that the effective SRV, S, is much higher than the diffusion velocity, D/L, and (b) the absorption coefficient, α, is much larger or much smaller than $1/L$. Then:

$$J_{ph} = eI\alpha L(\omega)\exp(i\omega t), \quad \text{for}\, \alpha L \ll 1, \tag{2.71a}$$

$$J_{ph} = eI\exp(i\omega t), \quad \text{for}\, \alpha L \gg 1. \tag{2.71b}$$

Once $J_{ph}(\omega)$ is determined, the SPV can be calculated using the relation [91,94]:

$$\mathrm{SPV}(\omega) = J_{ph}(\omega)Z_{eff}(\omega), \tag{2.72}$$

where

$$Z_{eff}(\omega) = \frac{1}{\Sigma(1/R_j + i\omega C_j)} \equiv \frac{1}{1/R_{eq} + i\omega C_{eq}}. \tag{2.73}$$

The effective photovoltage–photocurrent–density impedance, Z_{eff} (with units of Ohm·area), is composed of parallel resistance (R_j) and capacitance (C_j) components, corresponding to the contributions of the various SPV-influencing mechanisms. These may include minority and majority carrier transport, depletion and inversion layers, surface states, etc. [94], and may be lumped into an equivalent resistance, R_{eq}, and capacitance, C_{eq}.

Expressions for the different resistance and capacitance components are obtained by appropriate modifications of the derivations presented above, which take the time-dependence into account. As a simple and illustrative example, which is also used for some quantitative analyses in Section 5, we consider the calculations of Kamieniecki [97], concentrating on an n-type material for simplicity. This author assumed a simple charge balance with negligible SCR generation/recombination, such that the rate of free hole flow to the semiconductor surface is equal to J_{ph}/e. The overall increase rate of free holes (p_{s}) and trapped electrons (n_{t}) at the semiconductor surface is then given by:

$$\frac{\mathrm{d}p_{\mathrm{s}}}{\mathrm{d}t} = \frac{1}{e}J_{\mathrm{ph}} - R_{\mathrm{s}p}; \qquad \frac{\mathrm{d}n_{\mathrm{t}}}{\mathrm{d}t} = R_{\mathrm{s}n} - R_{\mathrm{s}p}, \tag{2.74}$$

where $R_{\mathrm{s}p}$ ($R_{\mathrm{s}n}$) is the surface recombination rate of holes (electrons). Using Eq. (2.74), the overall charge neutrality can be expressed as:

$$-\frac{\mathrm{d}Q_{\mathrm{sc}}}{\mathrm{d}t} = \frac{\mathrm{d}Q_{\mathrm{ss}}}{\mathrm{d}t} = e\frac{\mathrm{d}p_{\mathrm{s}}}{\mathrm{d}t} - e\frac{dn_{\mathrm{t}}}{\mathrm{d}t} = J_{\mathrm{ph}} - eR_{\mathrm{s}n}. \tag{2.75}$$

Assuming a small SPV signal, we obtain:

$$\frac{\mathrm{d}Q_{\mathrm{sc}}}{\mathrm{d}t} = \frac{\mathrm{d}Q_{\mathrm{sc}}}{\mathrm{d(SPV)}} \cdot \frac{\mathrm{d(SPV)}}{\mathrm{d}t} \equiv -C_{\mathrm{sc}}\frac{\mathrm{d(SPV)}}{\mathrm{d}t}, \tag{2.76}$$

where C_{sc} is the SCR capacitance. Assuming the FQL approxination and a small signal SPV approximation and using Eq. (2.21), we obtain:

$$R_{\mathrm{s}n} = s_n \mathrm{d}n_{\mathrm{s}} = s_n \mathrm{d}\left(n_{\mathrm{b}} \exp\left(\frac{eV_{\mathrm{s}}^*}{kT}\right)\right) \simeq s_n\left(\frac{e\mathrm{SPV}}{kT}\right)n_{\mathrm{b}} \exp\left(\frac{eV_{\mathrm{s}}}{kT}\right). \tag{2.77}$$

Combining Eqs. (2.75)–(2.77) yields:

$$C_{\mathrm{sc}}\frac{\mathrm{d(SPV)}}{\mathrm{d}t} = J_{\mathrm{ph}} - C_{\mathrm{sc}}\frac{\mathrm{SPV}}{\tau_s}, \tag{2.78}$$

where

$$\tau_{\mathrm{s}} = \frac{C_{\mathrm{sc}}}{s_n(e^2/kT)n_{\mathrm{b}} \exp\left(eV_{\mathrm{s}}/kT\right)}. \tag{2.79}$$

The steady-state solution of Eq. (2.78) is:

$$\mathrm{SPV}(\omega) = \frac{J_{\mathrm{ph}}}{C_{\mathrm{sc}}/\tau_{\mathrm{s}} + i\omega C_{\mathrm{sc}}}. \tag{2.80}$$

Thus, Eq. (2.80) is indeed a special case of Eq. (2.73), where $C_{\mathrm{eq}} = C_{\mathrm{sc}}$ and $R_{\mathrm{eq}} = \tau_{\mathrm{s}}/C_{\mathrm{sc}}$. Physically, the equivalent capacitance here is due to the space charge region and the equivalent resistance here is related to the *majority carrier* surface recombination.

Obviously, Kamieniecki's model is extremely simple as it neglects many surface- and SCR-related effects. Therefore, it cannot be expected to properly describe the SPV at any SCR. More sophisticated equivalent circuits are not disucssed here. The interested reader is referred to [91–96], and to references therein, for such calculations.

2.2.3. Sub-bandgap SPV

Under sub-bandgap illumination, the probability for band-to-band absorption is essentially zero since the photons do not have sufficient energy for inducing such transitions. The dominant charge generation process here is the exchange of charge carriers between the semiconductor bands and local states via optical excitation. In principle, transitions involving both surface states and bulk states may contribute to the SPV and are discussed separately below. Mathematically, the very low density of local states results in a very small decay of light intensity with sample depth into the sample, i.e., α is negligibly small. It is the non-zero value of the local state optical cross-sections, σ_n^{opt} and σ_p^{opt}, which is responsible for initiating the SPV formation. Hence, the analysis of this section is complementary to the analysis of the previous section in terms of absorption mechanisms. Note that certain mechanisms do allow band-to-band transitions with sub-bandgap photon energies. One notable example is the Franz–Keldysh effect, in which sub-bandgap photons excite band-to-band transitions in a sufficiently large electric field via photon-assisted tunneling [98]. The photon energy under such circumstances is typically close to E_g. Therefore, the Franz–Keldysh mechanism may be considered as a lowering of the effective optical bandgap, where the absorption coefficient α is not negligible but is electric field dependent. The analysis of this case proceeds along lines similar to those of the previous section and is not discussed further here.

The history of the sub-bandgap SPV starts in the early 1970s with the pioneering work of Gatos et al. [99]. In a series of publications, Gatos's group has both observed sub-bandgap SPV experimentally and analyzed it theoretically. We note that Ostrumova [100], Steinrisser and Hetrick [101], and Dinan et al. [102], have also made preliminary attempts at studying sub-bandgap SPV effects at around the same time as Gatos et al., but it was the latter group that did most of the ground-breaking research.

Gatos et al. focused their analysis on direct optical excitation of surface states. We shall also start by considering this case. For simplicity, we concentrate on the case of an n-type semiconductor. The basic phenomenological picture of the physical processes involved is shown in Fig. 14. In a depleted n-type semiconductor, Q_{ss} is negative and Q_{sc} is positive. Illumination by photons with energy $h\nu > E_{\mathrm{c}} - E_{\mathrm{t}}$ may produce electron transitions from a surface state at an energy E_t into the conduction band (Fig. 14(a)), where they are quickly swept to the semiconductor bulk by means of the surface electric field. Hence, Q_{ss} becomes less negative and the space charge region becomes less depleted. Therefore, the surface state depopulation is accompanied by a decrease in the (absolute value of) the band bending, i.e., a SPV. Shortly afterwards, the same group discovered the complementary effect (Fig. 14(b)) [103]. Illumination by photons with energy $h\nu > E_{\mathrm{t}} - E_{\mathrm{v}}$ may produce electron transitions from the valence

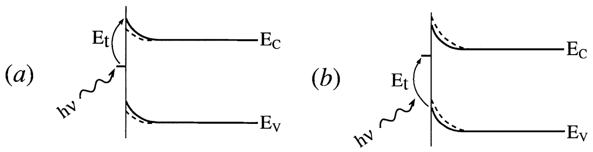

Fig. 14. Surface state depopulation (a) and population (b) in an n-type semiconductor.

band into a surface state situated at an energy E_t above the valence band maximum, E_v (which are equivalent to hole transitions from the surface state to the valence band). Such transitions would make Q_{ss} more negative and hence the surface barrier would increase. Naturally, this requires that the surface state in question be not completely filled prior to excitation. Super-bandgap illumination typically (although not always) tends to decrease the surface barrier. Thus, this effect was first dubbed 'photovoltage inversion' or, when in the presence of other 'regular' transitions, 'photovoltage quenching' [103]. The phenomenology of this type of SPV is more complicated since the photogenerated holes tend to accumulate at the surface rather than be swept away by the electric field. Thus, there is initially no charge separation and hence no SPV. For the SPV to develop it is necessary to have a significant diffusion of the excess holes into the bulk and/or a significant recombination of electrons and holes inside the SCR.

As in the previous section, the key to a quantitative analysis is in finding the surface potential for which charge balance is maintained under illumination. As a first step, let us assume that all transitions involving the minority carriers (holes, in this case) are negligible. This assumption may be valid in practice, for example, if (a) the (filled) state is positioned in the upper half of the bandgap and photons with $h\nu < E_g/2$ are used, and (b) the state's thermal cross-section for holes is very small. With the help of Eqs. (2.12)–(2.15) and Fig. 1, the rate equation for the surface charge density may be written as:

$$\frac{\mathrm{d}n_t}{\mathrm{d}t} = -g_n^{\mathrm{th}} - g_n^{\mathrm{opt}} + r_n^{\mathrm{th}} = -\sigma_n^{\mathrm{opt}} I n_t^* - c_n n_t^* n_1 + c_n (N_t - n_t^*) n_s^*. \tag{2.81}$$

Specifically, under steady-state conditions, we obtain:

$$Q_{ss} = -e n_t^* = -\frac{e c_n n_s^* N_t}{\sigma_n^{\mathrm{opt}} I + c_n (n_1 + n_s^*)}. \tag{2.82}$$

The case of unipolar excitation considered here is particularly simple since the quasi-Fermi level must be rigorously flat. This is because the electron current in itself, and not just the total current as before, must vanish in steady-state. Moreover, if the surface illumination is not too strong, the excess majority carrier density in the bulk is negligible. Physically, this is because the illumination only 'returns to the bulk' electrons caught in the surface state, but does not produce a new excess. Hence:

$$n_s^* = n_b^* \exp\left(-eV_s^*/kT\right) = n_b \exp\left(-eV_s^*/kT\right). \tag{2.83}$$

By combining Eqs. (2.82) and (2.83), Q_{ss} is explicitly expressed in terms of the surface potential. Furthermore, Q_{sc} is expressed by the usual relation (2.52). Therefore, the change in surface potential, i.e., the SPV, may be found. Szaro [104] has studied the theoretical SPV obtained under these assumptions. He has found that the sub-bandgap SPV increases with increasing surface barrier, as in the case of the super-bandgap SPV. However, as opposed to the latter case, the SPV does not change sign at or near the transition from the depletion to the accumulation regime. This is because the nature of the physical process involved always makes the surface more positive regardless of the initial sign of the surface band bending. Szaro has further noted that the SPV signal increases with increasing surface state density, decreasing bulk electron concentration, and decreasing temperature. All these observations are easily explained physically. The larger the surface density is, more electron transitions are induced with the same photon flux, and hence the larger the SPV is. The smaller the bulk charge is, screening of the surface disturbance from equilibrium is more difficult, and hence a larger SPV is needed to change the bulk charge distribution accordingly. Finally, lowering the temperature has the same effect as in the super-SPV case, namely, suppressing thermally-induced transitions. For the latter reason, the sub-bandgap SPV is also expected to decrease with increasing semiconductor bandgap [6,105].

In the particularly simple case of unipolar excitation, a relatively low illumination level may result in a relatively small electron current even during the transient response. As a result, Eq. (2.83) remains a reasonable approximation even under non-steady state conditions. Unlike the super-bandgap SPV case, the transient response may be treated analytically here by combining Eq. (2.81) with Eq. (2.83) and the Poisson equation [110]. Based on these equations, it is readily observed that the change in n_t (and hence the change in surface voltage) is, in general, non-exponential, because n_s^* depends on V_s^* which obviously changes during the transient response. The transient response is approximately exponential, however, if the recombination term is negligible with respect to the generation terms in Eq. (2.81).

The optical cross-section, σ_n^{opt}, is photon energy dependent (just like the band-to-band absorption coefficient). Lucovsky [106] has quantum-mechanically calculated the theoretical dependence of σ_n^{opt} on the photon energy by studying the transition from a *bulk* impurity level to a parabolic band assuming a delta-function potential for the impurity. His work was later generalized by Grimmeiss and Ledebo [107] for non-parabolic, non-spherical bands. These calculations show that in general:

$$\sigma_n^{\mathrm{opt}} \simeq (h\nu)^{-k}(h\nu - E_\mathrm{t})^n, \tag{2.84}$$

where k is either 1 or 3 and n is either 1, 1.5, 2, 2.5, or 3, depending on the nature of the optical transitions and the type of the impurity center. Unfortunately, it is much more difficult to calculate similar expressions for surface states due to the reduced symmetry of the energy levels and potentials involved. Nevertheless, for lack of a better model, a dependence of the type given by Eq. (2.84) is often used for surface states as well, with an adequate fit between theory and experiment [108].

The case of optical interaction of the surface states with minority carriers is less amenable to simple analysis. While the rate equation (Eq. (2.81)) may be easily extended to account for transitions involving the valence band, the quasi-Boltzmann relation (Eq. (2.83)) is not expected to hold for holes. The reason is that excess holes are generated and accumulated locally near the surface, as opposed to the previous case where the electrons were quickly swept out of the space charge region. To the best of our knowledge, this case has not been dealt with analytically in the literature and one must resort to numerical analysis.

Several other complications to the simple picture may arise. If there is more than one type of independent surface states, a rate equation similar to Eq. (2.81) – for interaction with one or both of the bands – must be written for each level separately. Therefore, different surface states may ‘communicate’ via the bands. For example, some electrons excited from a given surface state into the conduction band may be re-trapped by a different state, thereby reducing the deviation from equilibrium and hence the SPV [109]. If the surface state density is very high, or two surface states are derived from the same physical complex, direct optical excitation of carriers from one level to the other may become possible. Mathematically, this would require the addition of appropriate terms to the rate equations. Another possible complication is related to the effectiveness of the ‘communication’ between surface states and the semiconductor bulk. As noted in the previous sub-section, the time necessary for the equilibration of the surface and the bulk may vary over many orders of magnitude and results in the distinction between ‘slow’ and ‘fast’ states. A somewhat similar effect is related to the relaxation time of the sample back to its equilibrium surface voltage value following optical excitation [110,111]. If, for example, the SPV was a result of electron excitation from surface states into the bulk,

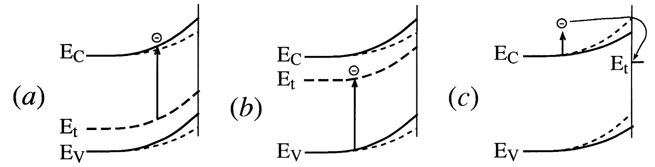

Fig. 15. Schematic representation of various sub-bandgap illumination photovoltaic effects: (a) Bulk state to conduction band electron transitions. (b) Valence band to bulk state electron transitions (c) Intra conduction band electron transitions. Dashed line indicates the position of the conduction band under illumination (after Gatos and Lagowski [6]).

its relaxation would necessarily involve the return of the same amount of electrons to the surface states. If the surface barrier is very high with respect to the thermal voltage, bulk electrons would take a long time to overcome the surface potential barrier, reach the surface, be trapped in surface states and resume the equilibrium distribution. The relaxation process may also be hindered by very small thermal cross-sections (and hence capture coefficients) of the surface states. As a result, very long relaxation times may be obtained, possibly extending over many hours [110].

So far, only sub-bandgap SPV due to carrier transitions involving surface states has been considered. Gatos and Lagowski [6] have considered other mechanisms for the absorption of sub-bandgap illumination, shown in Fig. 15. Figs. 15(a) and (b) feature the impact on the SPV of sub-bandgap absorption in bulk gap states present in the SCR of an *n*-type semiconductor. In Case (a), trapped electrons are excited to the conduction band, where they are swept to the bulk. The final result is a net charge separation where, for each transition, a positively charged impurity is positioned closer to the surface and the electron, previously contained in it, is positioned further from the surface. This creates a *macroscopic* electrical dipole, which is pointed in the opposite direction of the surface barrier and hence screens it. In Case (b), electrons are excited from the valence band to gap states, leaving free holes behind (or alternatively, trapped holes are excited to the valence band). The free holes are swept to the semiconductor surface. The final result is again a net charge separation and a *macroscopic* electrical dipole which is pointed in the opposite direction of the surface barrier and hence reduces it. Alternatively, electrons bound in the surface electron states may recombine with the holes accumulated in the vicinity of the surface. This does not change the net charge balance but provides another physical way of understanding the effect by a reduction of the surface charge and hence the surface barrier. In principle, the situation depicted here is quite similar to that of super-bandgap illumination, except that in the latter case the screening of the surface barrier is achieved via the separation of electron–hole pairs and not by the separation of a charge carrier – charged impurity pair. A clear difference between surface states and bulk states is also apparent from this discussion. Whereas the sign of the SPV due to transitions involving the conduction band and the valence band is opposite in the case of surface states, it is *not* in the case of bulk states. Fig. 15(c) features intra-band absorption, where electrons are promoted to a higher energy within the conduction band and thus can surmount the surface barrier, reach the semiconductor surface and be trapped in surface states. This increases the surface state charge and hence the surface barrier. However, the free carrier absorption coefficient, which is proportional to square of the wavelength [98], is typically negligibly small with respect to surface and/or bulk electron transitions unless extremely long wavelengths are used [6] and is not considered further here.

As noted above, the possible significance of bulk states has been recognized very early in the history of the sub-bandgap SPV. Nevertheless, it has only been seriously studied theoretically in the first half of the 1980s. Germanova et al. [111] and Szaro [112] have theoretically considered the case of unipolar excitation of bulk states for p- and n-type semiconductors, respectively. For ease of comparison with the previous considerations in this section, let us consider the case of an n-type semiconductor which contains both shallow donors and deep donors [112]. The corresponding form of the Poisson equation is then:

$$\frac{\mathrm{d}^2V^*}{\mathrm{d}x^2} = -\frac{e}{\epsilon}\left(N_\mathrm{d} + p_\mathrm{t}^* - n_\mathrm{b}^*\right), \tag{2.85}$$

where p_t^* is the density of trapped holes in the deep donors and N_d is the shallow donor density. Furthermore, the quasi-Boltzmann relation (Eq. (2.83)) is applicable in the unipolar excitation case for the same reasons given above. The analog of Eq. (2.82) in the bulk is:

$$p_\mathrm{t}^* \equiv N_\mathrm{t} - n_\mathrm{t}^* = \frac{\sigma_n^{\mathrm{opt}} I + c_n n_1}{\sigma_n^{\mathrm{opt}} I + c_n\left(n_1 + n_\mathrm{b}^* e^{-V_\mathrm{s}^*/kT}\right)} N_\mathrm{t}. \tag{2.86}$$

Hence, for a given excess electron density (δn), p_t^* is known, and Eq. (2.85) may be integrated to yield the appropriate space charge function F^*, and thus Q_sc. Surface trapping effects may be taken into account by calculating Q_ss using Eq. (2.82). The sub-bandgap SPV may be found by calculating V_s for which the space charge is equal to the surface charge both in the dark and under steady-state illumination. A typical result of such calculations is given in Fig. 16 [112]. Essentially, Fig. 16 is the sub-bandgap analogue of Fig. 11 discussed in the previous section. In both figures, the SPV increases with increasing initial barrier height until finally reaching saturation. ‘Bulges’ are observed in the curves due to the differences in the effectiveness of surface capture processes for different barrier heights. Here, the SPV signal at low barrier heights (and also at accumulation) is quite negligible. This

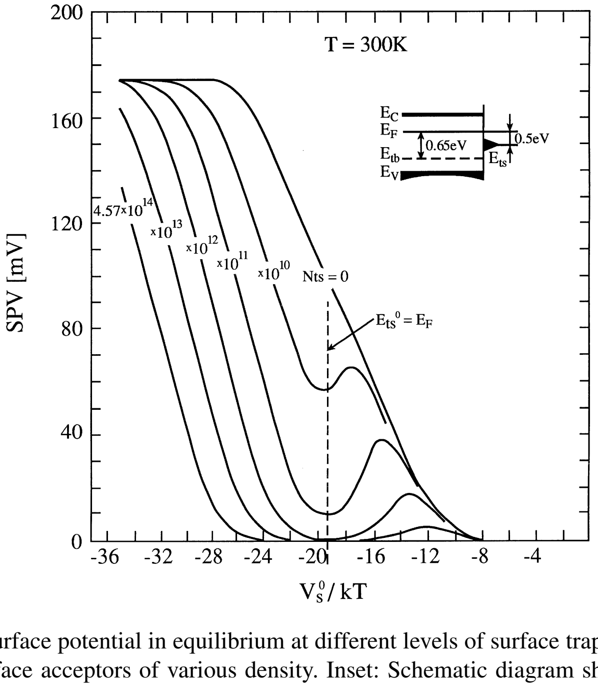

Fig. 16. SPV as a function of surface potential in equilibrium at different levels of surface trapping, for an n-type sample with $10^{16}\ \mathrm{cm}^{-3}$ bulk donors and surface acceptors of various density. Inset: Schematic diagram showing gap state energies (after Szaro [112]).

is because the sub-bandgap SPV response is smaller due to the smaller number of bulk states with respect to the band density of states. The saturation in the SPV with increasing barrier height is due to an additional mechanism. As the barrier height increases, some of the bulk states in the vicinity of the surface may be shifted *above* the Fermi level. Such states are essentially empty and do not contribute to optical absorption. Thus, as the barrier height is increased, there are more bulk states in the surface SCR, but the number of those participating in the SPV generation remains constant beyond a certain barrier height.

Performing a similar analysis, Germanova et al. [111] have noticed that in certain situations a bulk state involving majority carriers may actually increase the surface barrier rather than decrease it. Consider, for example, an *n*-type semiconductor with a depletion-type surface barrier. As explained above, electrons excited from bulk states into the conduction band should decrease the surface potential. However, the increase of the free electron density also enhances the probability for electron capture in surface states and hence increases the surface state occupation. Evidently, making the surface more negative in an *n*-type semiconductor should increase the surface barrier.

In order to consider the specific results of Germanova et al. [111], we note they have been obtained for a *p*-type semiconductor, i.e., holes are excited from deep bulk states to the valence band, whereby some of them are trapped in donor-like surface states. Fig. 17(a) features the dependence of the SPV on the bulk state density obtained by Germanova et al. For relatively large bulk densities, the SPV is negative, i.e., the (*p*-type) surface barrier is decreased, as is the normal case. For decreased bulk state densities the SPV is inverted, i.e., the surface trapping effect is dominant and the surface barrier increases. This behavior may be further understood with the help of Fig. 17(b), which shows the corresponding space-charge curves for high and low bulk state densities. In the high bulk state density case, the surface states are essentially filled with holes even before illumination (which means that all surface donors are ionized). Hence, the capture of holes under illumination is negligible, Q_{ss} does not change appreciably under illumination, and the increase in Q_{sc} decreases the band bending, just like in

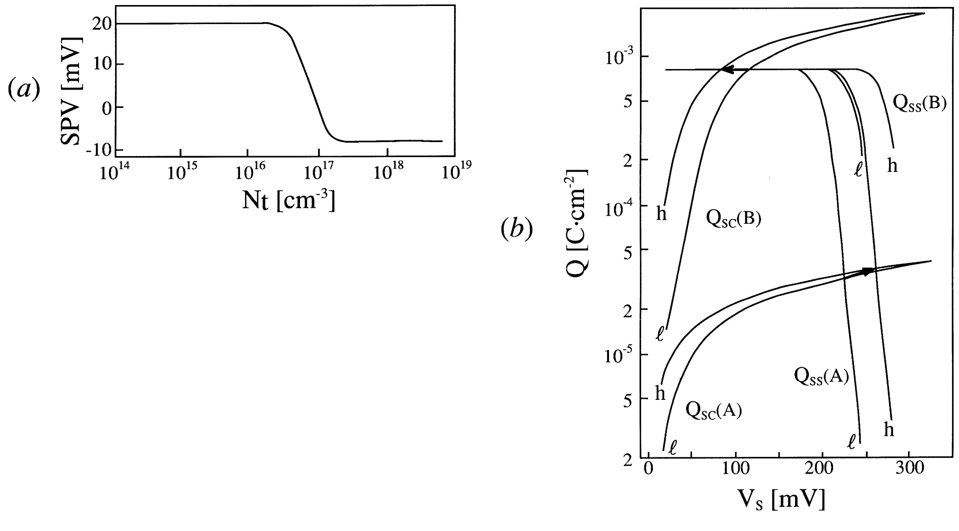

Fig. 17. (a) SPV vs. bulk state density, and (b) space charge curves in the dark (solid lines) and under equilibrium (dashed lines) for a bulk state density of $1.5\cdot10^{14}\,\mathrm{cm}^{-3}$ (A) and $1.1\cdot10^{18}\,\mathrm{cm}^{-3}$ (B), in a *p*-type sample with $5\cdot10^{11}\,\mathrm{cm}^{-2}$ surface states. ℓ – low illumination intensity, h – high illumination intensity (after Germanova et al. [111]).

the super-bandgap SPV case. However, in the low bulk state density case, the surface states are significantly populated by electrons under equilibrium. Hence, a substantial increase in Q_{ss} is observed under illumination. Since the increase of Q_{sc} upon illumination in this case is relatively slight, the net result is an increase in the surface barrier. Such a SPV inversion mechanism has been observed experimentally (see Section 4.2 below) as well as re-confirmed theoretically by Davydov et al. [113].

Szaro [114] has also studied the case of an *n*-type semiconductor with a deep donor-like bulk state under *bipolar* sub-bandgap excitation. There, electrons may overall be excited from the valence band to the conduction band, via the intermediate gap state, and the problem is quite similar to that of super-bandgap SPV. Therefore, the SPV problem may be solved analytically as in Section 2.2.2. Szaro performed such calculations while varying the ratio between surface state electron and hole capture coefficients. He noted that hole trapping in acceptor-like surface states greatly increases the SPV by reducing the surface charge. This is also feasible with super-bandgap illumination, but here surface effects are much more pronounced with respect to free carrier screening effects. Finally, Szaro noted that if the bulk state density were relatively small, its effect on the Poisson equation would be negligible, and the excess free carrier densities in the bulk would become independent of the bulk state density. Thus, it may seem as if for low bulk state densities the SPV is independent of this density. The only difference (analysed in a subsequent publication [115]) is that the lower the bulk state density the longer is the transient response. This conclusion may seem quite strange as one expects that the more bulk states there are, the more efficient the optical generation is and the larger is the deviation from equilibrium (and hence SPV). Szaro's analysis was performed assuming that those bulk states provided the *sole* recombination mechanism and not only the sole generation mechanism. Under such conditions, the excess carrier density is really independent of bulk state density since the reduced generation is compensated by reduced recombination. However, in the presence of a competing recombination mechanism (e.g., via other defect states or via band-to-band recombination), these conclusions are no longer valid.

Several of the studies surveyed above [111,114] suggest that bulk state effects on the SPV are relatively weak with respect to surface state effects. The relative importance of surface and bulk transitions has been examined by Leibovitch et al. [116]. By performing two integrations of the Poisson equation and using integration by parts, one may recast the Poisson equation in the one-dimensional integral form:

$$V_s = -\int_0^w \frac{x\rho(x)}{\epsilon}\,dx, \tag{2.87}$$

which facilitates a direct relation between the charge density in the SCR and the surface potential. Moreover, the charge balance condition may be written in the form:

$$Q_{ss} = -Q_{sc} = -\int_0^w \rho(x)\,dx. \tag{2.88}$$

Let us consider the case of small perturbations, which is more readily amenable to analytical procedures. For small signals, the variation in the surface potential may be related to the variation in the charge density by performing calculus of variations, while taking into account that w is also dependent on the perturbation. This yields:

$$\delta V_s = \frac{w}{\epsilon}\delta Q_{ss} + \int_0^w \frac{(w-x)\delta\rho(x)}{\epsilon}\,dx. \tag{2.89}$$

For an order of magnitude estimate, let us assume that $\delta\rho(x)$ is constant throughout the SCR. Furthermore, we define the *effective* surface density of the variation in bulk state volume density as $\delta Q_{\mathrm{b}} \cong w \cdot \delta\rho$. Assuming that δQ_{b} and δQ_{ss} are equal, integrating Eq. (2.89) directly yields that the SPV due to the surface perturbation is really larger, but only by a factor of two. Thus, SPS is indeed inherently more sensitive to surface states than to bulk states, but not by much. (This is compatible with the linguistic observation that 'surface' pertains to the 'photovoltage' rather than to the 'spectroscopy'). A larger difference between surface and bulk state excitation on the SPV arises in detailed calculations. This is because for, e.g., $w = 0.1\,\mu\mathrm{m}$, a reasonable surface state density of 10^{11} cm^{-2} is equivalent to a bulk volume density of 10^{16} cm^{-3}, which is a relatively high value for samples of reasonable quality.

2.2.4. The Dember potential

In the two preceding sections, we have consistently assumed that the SPV stems only from changes in the surface potential drop across the SCR. In this sub-section, we examine the validity of this assumption by studying the voltage which may form across the region of the sample which is electrically neutral in equilibrium, known as the Dember photovoltage [25,61]. Consider a sample which has no surface states and hence no surface SCR and no SCR-related SPV. The physics of the Dember photovoltage has to do with non-uniform generation or recombination in a sample. For example, under super-bandgap illumination through the top surface of the sample, the generation decays into the sample due to optical absorption [see Eq. (2.58)]. The ensuing gradient in excess carrier concentration results in the diffusion of both electrons and holes further into the semiconductor bulk. The electrons are more mobile than holes and hence diffuse faster into the bulk. This creates a net electric field in the direction of the bulk, which drives the holes deeper into the sample and retards the motion of the electrons into the sample. Even though the sample is entirely neutral in the dark, it is no longer so under illumination. The sign of the Dember photovoltage is determined solely by the sign of the faster diffusing species and hence it is positive for both *n*-type and *p*-type semiconductors.

The steady-state illumination-induced electric field across the sample may be calculated from the requirement of zero total current, $J_n + J_p = 0$. Expressing the currents by the drift-diffusion expressions (Eq. (2.3)) and assuming quasi-neutrality, i.e.,

$$\delta n(x) = \delta\rho(x); \qquad \frac{\mathrm{d}\delta n(x)}{\mathrm{d}x} = \frac{\mathrm{d}\delta p(x)}{\mathrm{d}x}, \tag{2.90}$$

it is easy to show that the electric field is given by [90]:

$$E(x) = \frac{(D_p - D_n)(\mathrm{d}\delta n(x)/\mathrm{d}x)}{\sigma_0 + q(\mu_n + \mu_p)\delta n(x)}, \tag{2.91}$$

where $\sigma_0 = e(n_{\mathrm{b}}\mu_n + p_{\mathrm{b}}\mu_p)$ is the dark conductivity of the sample. It should be noted that the quasi-equilibrium conditions (Eq. (2.90)) are clearly an approximation because a non-zero net charge must exist in the presence of a non-zero electric field. However, the electric field as given by Eq. (2.91) may be used in Poisson's equation to calculate the net difference $\delta p - \delta n$ and thus estimate the error involved [117]. For, e.g., extrinsic silicon, the quasi-neutrality assumption is good for any injection level [90]. Since under the above assumptions the surface voltage is zero in equilibrium, the SPV is immediately calculated by integrating Eq. (2.91). Using the semi-infinity boundary condition (i.e., no excess carriers at the back side) and the Einstein relations (Eq. (2.6)), we obtain [118]:

$$\mathrm{SPV} = -\int_0^{\infty} E(x)\,\mathrm{d}x = \frac{kT}{e}\frac{\mu_n - \mu_p}{\mu_n + \mu_p}\ln\left[1 + \frac{e(\mu_n + \mu_p)\delta n(0)}{\sigma_0}\right]. \tag{2.92}$$

Relation (2.92) describes the dependence of the Dember photovoltage on the excess carrier density at the front end of the nominally quasi-neutral region. The Dember photovoltage vanishes when $\mu_n = \mu_p$ since no net separation of charge and hence no electric field are to be expected when both charge species are equally mobile. In addition, it is clear that the Dember effect is more pronounced in materials where the mobility difference between electrons and holes is fairly large. The Dember effect is typically significant only under high injection conditions where $\delta n(0)$ is of the order of n_b (see Eq. (2.92)). For example, for n-type GaAs at $\delta n/n_b = 10^{-2}$ one obtains that the SPV is only ~ 5 mV. The number is even smaller for, e.g., silicon, where the ratio of electron to hole mobility is smaller. However, since the magnitude of the Dember potential increases logarithmically with excess carrier density, it is not always negligible at higher illumination intensities.

The Dember photovoltage is related to electron and hole diffusion coupled by means of the electric field in the quasi-neutral region. Therefore, in order to determine $\delta n(0)$ the ambipolar transport equation [90] which properly describes such coupled transport should be used. (The ambipolar transport equation is obtained from inserting the drift-diffusion current expressions (Eq. (2.3)) in the continuity equations (Eq. (2.2)). The resulting equations are linearly combined so as to nullify the term containing the derivative of the electric field.) Assuming the electron and hole generation and recombination rates are equal, the result is:

$$\mu_\mathrm{a} E(x)\frac{\mathrm{d}\delta n(x)}{\mathrm{d}x} + D_\mathrm{a}\frac{\mathrm{d}^2\delta n(x)}{\mathrm{d}x^2} + G(x) - R(x) = 0, \tag{2.93}$$

where μ_a and D_a are the ambipolar mobility and diffusion coefficient, respectively, given by:

$$\mu_\mathrm{a} = \frac{(n-p)\mu_n\mu_p}{n\mu_n + p\mu_p};\quad D_\mathrm{a} = \frac{(n+p)D_nD_p}{nD_n + pD_p}. \tag{2.94}$$

Eq. (2.93) implies that in the presence of a coupling electric field, the effective mobility and diffusion coefficient of the charge carriers are modified to account for the coupling effect to the other charge carrier type. Even if a standard SRV type boundary condition (see Eq. (2.60)) is taken at the surface ($x = 0$), Eq. (2.93) cannot usually be analytically solved. This is because of the electric field term which couples it to the Poisson equation. An analytical solution can be obtained if $\mu_\mathrm{a} = 0$, i.e., $n = p$. This is a reasonable approximation only if the sample is close to intrinsic or the injection is extremely high.

A few more comments are in order. So far we have only discussed the case where the bands are flat in the dark and no surface states are present. Then, the Dember effect is the sole cause of the SPV. In the general case, it is usually assumed that the overall SPV is the sum of the SCR-related SPV and the Dember photovoltage, where each is calculated separately. However, the two potentials are interrelated: Under significant Dember effect conditions, the minority carrier transport equation (Eq. (2.59)) has to be replaced by the ambipolar transport equation (Eq. (2.93)). In addition, the boundary condition for the Dember potential should either be taken as an *effective* SRV at the edge of the SCR (Eq. (2.60)), or be replaced with the detailed current balance equation (Eq. (2.62)). This coupling alters the precise value of the SPV due to each mechanism with respect to its value in the absence of the other mechanism. However, it does not modify the physical picture given above.

While the 'classical' Dember photovoltage discussed above is due to non-uniform *generation*, non-uniform *recombination* also results in a photovoltage 'of the same genre as the Dember voltage' [119]. For example, Buimistrov et al. [69] have discussed the presence of a significant bulk state density which causes a significant difference between electron and hole capture as a source of SPV. If the generation is fairly uniform (as in, e.g., sub-bandgap illumination) and there is a significant surface recombination, electrons and holes will diffuse in the direction of the surface and the Dember voltage would be negative, rather than positive. Interestingly, a sub-bandgap photovoltage signal which has been observed as early as 1965(!) by Nadzhakov and Balabanov [120], was intepreted in terms of such a recombination-related Dember effect rather than in terms of defect state transitions, as in Section 2.2.3. While Nadzhakov and Balabanov offered no proof for this mechanism in their specific case, its possible contribution in other cases is almost always overlooked.

2.2.5. Effect of buried interfaces

All of the preceding discussion has been devoted solely to a study of semi-infinite, uniform bulk samples. However, actual semiconductor samples may be thin, i.e., not much larger than the diffusion length and/or the absorption length, so that excess carriers may be present near their back part as well. Samples may also comprise of a multi-layer structure, which has several buried interfaces due to homojunctions and heterojunctions in the structure.

At a first glance, interfaces which are buried deep enough into the sample may seem unable to contribute to the measured SPV signal, due to screening by a thick enough quasi-neutral region. However, this statement is erroneous. To understand why, let us consider a semiconductor sample comprising a semiconducting film grown on a semiconducting bulk substrate, which may have different material parameters. A schematic typical band-lineup of such a structure in the dark (solid curve) and under illumination (dashed curve) is shown in Fig. 18 [20]. There are two SCRs in such a sample (not including the back contact, assumed to be Ohmic): an interface one (between the substrate and the film) and a surface one (between the film and the ambient). Fig. 18 clearly shows that optical absorption in *any* non-neutral region present within the sample (be it band-to-band or defect state to band) may contribute to the measured SPV signal because the potential of the free surface is linked to any other illuminated region, no matter how deep within the sample, as the energy bands are serially connected. Moreover, Dember effects may arise from any illuminated quasi-neutral region of the sample. Thus, the sensitivity of SPV measurements to a certain region in the semiconductor is limited only by the absorption length of the photons, i.e., by the possibility of introducing an excess of free carriers in the region of interest.

The sensitivity of SPV measurements to buried interfaces is underscored by the two different SPV scenarios shown in Fig. 18. In both, the SPV is produced by changes in the band-bending of both the interface and the surface SCRs. However, in one case the surface related SPV dominates, whereas in the other case the interface-related SPV dominates. At a second glance, the sensitivity to buried interfaces should not be too surprising: In a normal photodiode, the potential difference between the two contacts changes even though the photovoltaically active region may be very far from the contacts. The same occurs here, except that one 'contact' is free.

While the above arguments are simple, they have been frequently overlooked in the past. As a result, relatively little experimental or theoretical work has been devoted to studying the influence of buried interfaces on the SPV. The theory of junction-related surface photovoltage is given in detail elsewhere [25,59], as noted in Section 2.2.1. Thus, it is worthwhile to elaborate on it here only to the extent that

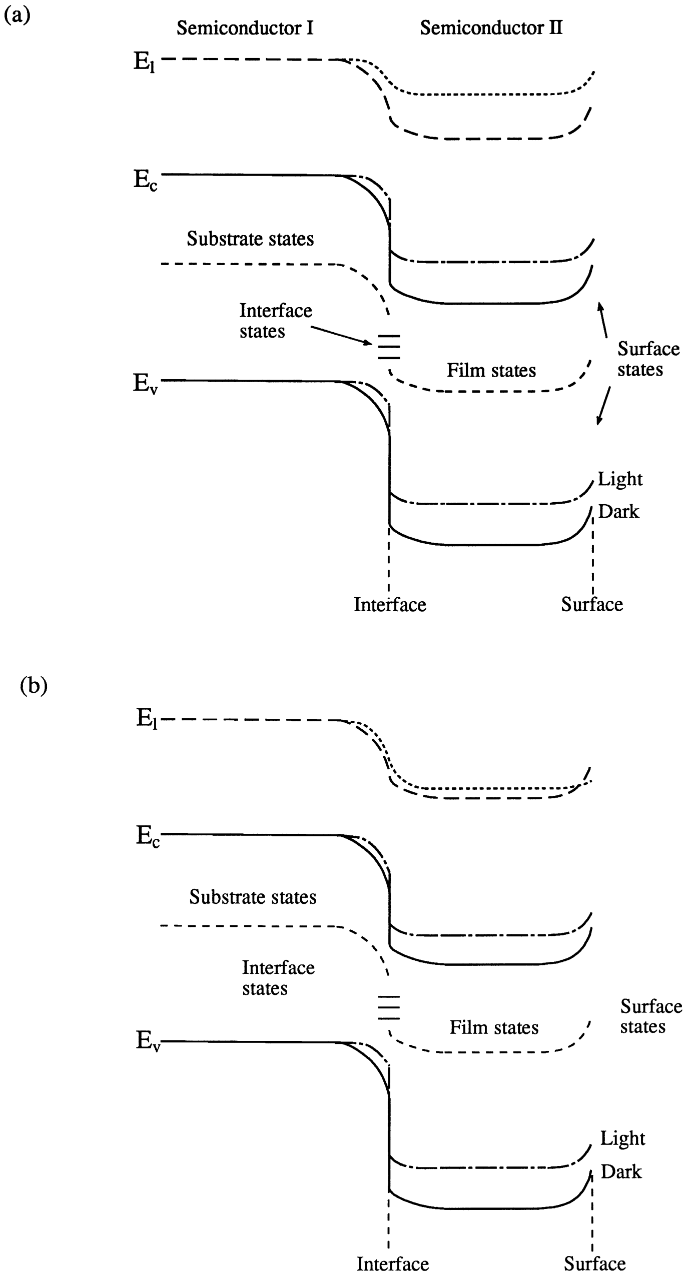
(a)
Semiconductor I
Semiconductor II
E_l
E_c
Substrate states
Interface states
Film states
Surface states
E_v
Light
Dark
Interface
Surface
(b)
E_l
E_c
Substrate states
Interface states
Film states
Surface states
E_v
Light
Dark
Interface
Surface

Fig. 18. Band-lineup of a typical thin film structure in the dark (solid curve) and under illumination (dashed curve), where the dominating contribution to the SPV is from the: (a) surface SCR, (b) interface SCR.

buried interfaces interact with the external surface or in the context of quantitative interpretation of specific SPV experiments. Accordingly, it is discussed further where appropriate in Section 5 below, especially in Section 5.5.

To conclude this section, we note that in SPV the experimentally measured quantity is strictly a surface quantity and as a result the technique is highly surface-sensitive. However, it is by no means sensitive *only* to the surface. Rather, it is sensitive to the entire surface SCR (via super- or sub-bandgap absorption), to the quasi-neutral bulk (via the Dember effect) and even to buried interfaces located anywhere within the sample (as long as they can be reached by photons). Therefore, by proper design and interpretation of experiments the SPV may be effectively used to gain information about various semiconductor interface and bulk properties, in addition to semiconductor surface properties.

3. Experimental methods

SPV measurements are non-trivial because the surface potential is a built-in potential, rather than an external potential. In other words, the surface potential is not equal to the difference in Fermi levels between the front and back surfaces. Therefore, it cannot be measured simply with some form of voltmeter. Moreover, in the case of a free surface, the application of any contact for indirect electrical measurements of the built-in voltage (e.g., current–voltage or capacitance–voltage analyses) will invariably alter the surface properties and hence the quantity under measurement. Consequently, many elaborate techniques for measuring the surface potential (or at least *changes* of it) without applying a direct electrical contact have emerged. This chapter is dedicated to a discussion of these methods.

3.1. The Kelvin probe

3.1.1. Principles of operation

An important key to several SPV measurement techniques may be found by re-examining the electronic band structure at a semiconductor surface. By using Fig. 4, as well as Eq. (2.36), we conclude that any change in the surface potential, eV_s, causes a change of equal magnitude in the surface work function, W_s. Therefore, *in the absence of photochemical activity, the change in surface work function is equal to the* SPV (in absolute value terms).

One of the oldest techniques for determining relative changes in work functions is measuring the work function difference between two materials forming the two sides of a parallel plate capacitor. A schematic band diagram of two metals in such an arrangement (first employed by Kohlrausch [121]) is shown in Fig. 19. Prior to connection (Fig. 19(a)) the metals are electrically neutral, no macroscopic electrical fields arise, and the two metals share the same local vacuum level. Upon short-circuiting the metals (Fig. 19(b)) charge must flow from the metal with smaller work function to the metal with larger work function until equilibration of the Fermi levels is achieved. As in any parallel plate capacitor, this charge transfer results in an electric field in the gap between the two plates and a drop in the local vacuum level across this gap. Using Fig. 19(b) we conclude that this potential energy drop is equal to the difference in the work functions of the two metals. The corresponding potential drop is usually known as the contact potential difference (CPD) [22,24], i.e., $eV_{\mathrm{CPD}} = W_1 - W_2$.

As opposed to a 'textbook' parallel plate capacitor, the potential drop described here is *built-in* and is achieved under zero bias conditions. Theoretically, if both the stored charge, Q, and the overall capacitance, C_0, are known, the CPD may be easily calculated, because $Q = C_0 V_{\mathrm{CPD}}$. However, the precise measurement of the stored charge is non-trivial. This obstacle has been overcome by Lord Kelvin [122], who suggested that the CPD may be measured directly by a null-method. When an

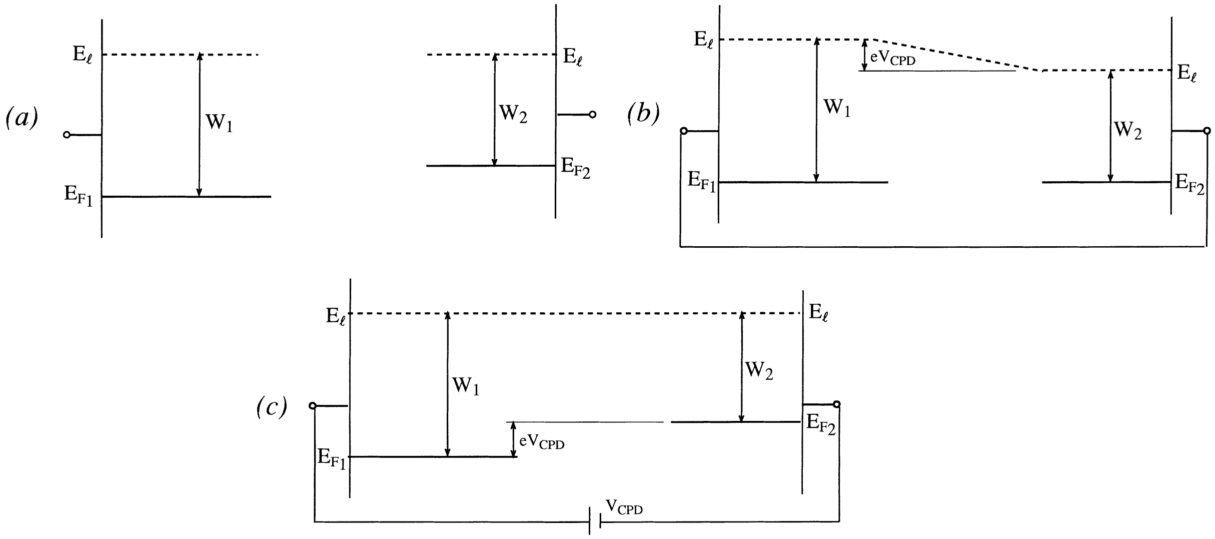

Fig. 19. Schematic band diagram of a parallel plate capacitor formed from two different metals, with the two plates: (a) isolated, (b) short-circuited, (c) connected through a DC bias equal and opposite to the contact potential difference.

external dc bias, equal and opposite to the CPD, is applied to the capacitor (Fig. 19(c)), the Fermi levels on both metals differ by V_{CPD}, just as in the isolated case (Fig. 19(a)). No charge exchange between the metals need take place and the capacitor is discharged. Hence, in order to determine the CPD, it suffices to determine the applied bias which discharges the capacitor, even if neither capacitor charge nor capacitance are known. If the spacing between the two plates is varied while the plates remain connected under bias, the resulting capacitance change should induce a change in the capacitor charge and hence a current in the external circuit. This current can be zero if and only if the capacitor is discharged. Thus, the CPD may be easily found by determining the external bias for which no external currents are observed upon changing the spacing between the plates. This type of arrangement is known as the Kelvin probe arrangement, after its inventor.

The Kelvin probe arrangement has been extensively applied to the measurement of illumination-induced changes in work function starting from the earliest experiments of Bardeen and Brattain [2], and ever since. This has been achieved by Ohmically contacting the back side of the semiconductor sample to a metallic reference electrode. Since the work function of the metallic electrode does not change under illumination the relation:

$$-e\Delta\mathrm{SPV} = \Delta W_{\mathrm{s}} = e\Delta V_{\mathrm{CPD}}, \tag{3.1}$$

is assumed, based on Eq. (2.36). It is worthwhile to closely inspect the validity of relation (3.1) for a metal–semiconductor Kelvin probe arrangement. The main cause for concern is shown in the schematic band diagram of this arrangement, given in Fig. 20. In the isolated semiconductor (Fig. 20(a)) the surface band bending is determined by the free surface charge neutrality condition, $Q_{\mathrm{ss}} + Q_{\mathrm{sc}} = 0$. As the metal is connected to the back side of the semiconductor (Fig. 20(b)) a MIS structure is formed. Thus, the band bending in the semiconductor, and hence its work function, may change. As explained in Section 2.1.5, the appropriate charge neutrality condition becomes $Q_{\mathrm{m}} + Q_{\mathrm{ss}} + Q_{\mathrm{sc}} = 0$, where the effect of Q_{m} may be significant if the width of the capacitor gap is not much larger than the width of the

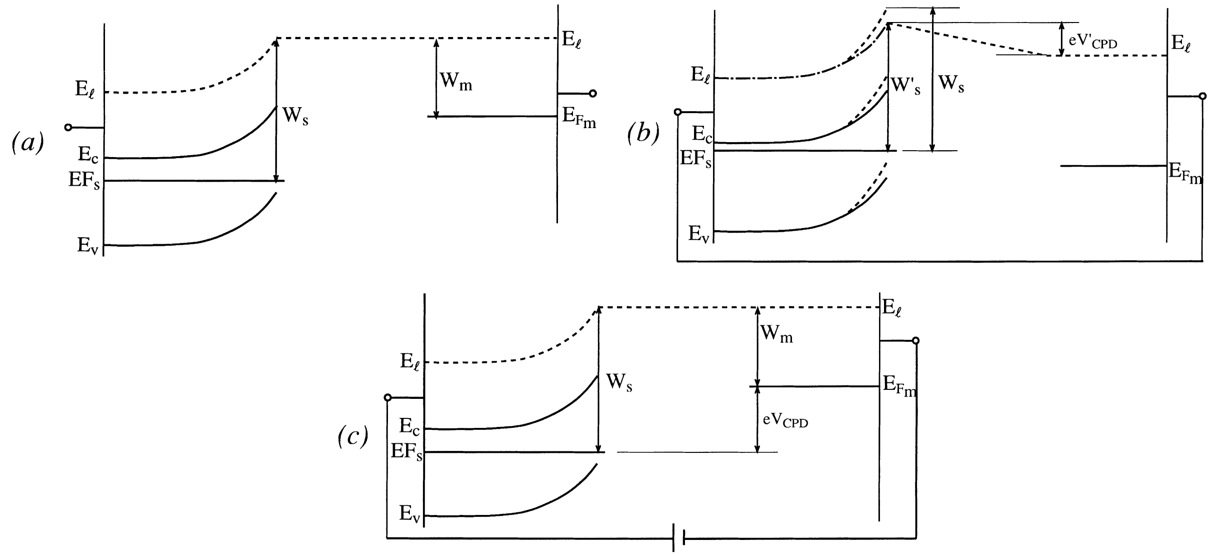

Fig. 20. Schematic band diagram of a parallel plate capacitor formed from a metal and a semiconductor, with the the two plates: (a) isolated, (b) short-circuited, (c) connected through a DC bias such that the capacitor is discharged.

surface depletion region. Therefore, the potential energy drop across the capacitor gap may be modified to $eV'_{\mathrm{CPD}} = W'_1 - W_2$ (where W'_1 is the modified work function of the semiconductor) instead of $eV_{\mathrm{CPD}} = W_1 - W_2$. However, the magnitude of the external DC bias required to discharge the capacitor remains equal and opposite to the real contact potential difference, V_{CPD}, rather than to V'_{CPD}. This is because when the capacitor is discharged Q_{m} is by definition zero, the charge neutrality condition reduces to that of a free surface, and the semiconductor work function returns to its original value, as shown in Fig. 20(c). Hence, the rigorous theoretical validity of the Kelvin probe technique for SPV experiments is established.

In Lord Kelvin's original experiments, the verification of the capacitor discharge was performed by manually moving the capacitor and measuring the resulting charge exchange with an electrometer [121,122]. Consequently, a single CPD determination of limited precision required several minutes. In 1932, Zisman [123] introduced the vibrating capacitor Kelvin probe technique, in which the capacitor is vibrated periodically so that a steady state ac current develops in the capacitor. This current is easily monitored continuously. Thus, the dc bias is adjusted until the ac current is nullified. The Zisman approach increases the measurement sensitivity drastically since the measured ac voltage may be considerably amplified. Moreover, the measurement time is reduced from several minutes to several seconds. As a result, it has become the standard setup.

3.1.2. Practical considerations

Anderson and Alexander [124] and later MacDonald and Edmondson [125] have analyzed the dependence of the ac current on the modulation of the capacitance in terms of a simple equivalent circuit, shown in Fig. 21. In the equivalent circuit, all potentials are *overall* (i.e., sum of external and built-in) potentials since it is the overall voltage drop which controls the current behavior. Specifically, the overall potential difference between the two capacitor plates is the sum of the built-in voltage, V_{CPD},

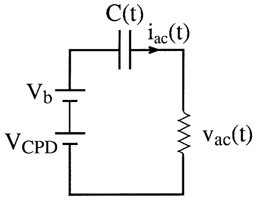

Fig. 21. Equivalent circuit diagram for the vibrating Kelvin probe arrangement.

and the external potential difference (manifested as an energy difference between the position of the Fermi levels on both sides of the capacitor). The latter is the sum of the applied bias, V_b, and the voltage drop across the resistor R. Hence, the equivalent circuit is very similar to the real circuit except that the built-in potential, V_{CPD}, is represented as a battery which is in series with the variable external dc bias, V_b. Using the equivalent circuit, a simple use of Kirchoff's laws yields an equation for the charge on the capacitor, $Q(t)$:

$$\frac{dQ(t)}{dt}+\frac{Q(t)}{RC(t)}=\frac{V_{CPD}+V_b}{R}, \tag{3.2}$$

with the current obviously being the time derivative of the charge:

$$i=\frac{d}{dt}(C(t)V_c(t)), \tag{3.3}$$

where $V_c(t)$ is the overall voltage on the capacitor.

Naturally, the ac current increases with increasing ac capacitance. Therefore, it increases with increasing probe area, increasing amplitude of vibrations, and decreasing probe-to-plate distance. However, increasing the probe area decreases the spatial resolution. Decreasing the sample-to-probe distance introduces mechanical difficulties and increases the risk of landing the sample with the probe. In addition, mechanical instabilities, which change the sample-to-probe distance, become more important since they constitute a larger fraction of the overall distance. Let us consider some typical values for the parameters at hand: For a probe area of 0.5 cm^2 and a probe-plate average distance of 0.5 mm, C_0 is less than 1 pF. With typical CPDs amounting to several volts at most, the ac current is expected to be in the pA range at most. If one wishes to measure CPD changes down to the mV level, for example, the currents may be as small as several fA. The easiest way to read such minute currents is to use a very large value for the resistor R. For example, $R = 1\ G\Omega$ yields voltages of the order of μV to mV. It is usually convenient to construct a circuit such that the large input resistance of a voltage amplifier serves as the resistor R. Since the late 1970s, following Bonnet et al. [126], it has become increasingly popular to use a low input impedance current amplifier (i.e., a current to voltage converter). While theoretically equivalent, current detection has several practical advantages over voltage detection, which are discussed below. If a current amplifier is used, Eq. (3.3) is further simplified to:

$$i=(V_{CPD}+V_b)\frac{dC}{dt}. \tag{3.4}$$

Eq. (3.4) is strictly valid only when the input resistance of the current amplifier, R, is zero, but is a reasonable approximation as long as R is negligible with respect to the impedance of the capacitor at the vibration frequency. Unfortunately, Eq. (3.4) is frequently used in the literature for analyzing the voltage amplifier configuration, for which it is clearly inappropriate.

Eq. (3.2) is a time-varying first order differential equation. As such, its solution is not expected to generally be sinusoidal even if the capacitance modulation is sinusoidal [125], unless R is negligible. Moreover, usually it is the *distance* between the capacitor plates rather than the capacitance itself, which is modulated sinusoidally, i.e., $C(t) = C_0/[1 + m\sin(\omega t)]$, where ω is the vibration frequency and m is the modulation index. A practical criterion for nullifying the current, regardless of its exact mathematical form, is to establish the nullifying of the fundamental harmonic only. Typically, the fundamental harmonic is isolated in two stages, shown in Fig. 22(a). First, the ac voltage (or current) is amplified in a (voltage- or current-sensitive) pre-amplifier with a band pass filter centered at the fundamental frequency. This greatly reduces higher harmonic contributions as well as noise at other frequencies [127]. Next, the fundamental frequency is amplified selectively using a lock-in amplifier. The final output is a dc voltage which may be measured using any simple voltage meter and which is nullified when $V_b = -V_{CPD}$, as appropriate.

Coupling to modern automatic data acquisition systems is done by using well known negative feedback techniques, first applied to CPD measurements by Simon [128] following the work of Palevsky et al. [129]. The desired automatic readout of V_{CPD} may be obtained by applying the obtained dc output (in reverse polarity) back to the vibrating capacitor circuit, as shown in Fig. 22(b). In order to understand why this yields the desired result, consider the formulation of the feedback circuit in terms of an equivalent feedback loop, shown in Fig. 22(c). The charge on the capacitor is determined by the effective potential difference, $V_{CPD} + V_b$. For $V_{CPD} + V_b \neq 0$, an ac voltage develops on the capacitor, and is amplified by means of the pre-amplifier and the lock-in amplifier, resulting in the dc output, V_{dc}. We define the effective gain, G, as the ratio of the dc output to the effective potential difference input, i.e., $G \equiv V_{dc}/(V_{CPD} + V_b)$. In the feedback scheme of Fig. 22(b), $V_{dc} = -V_b$. Therefore, we obtain the relation:

$$G = \frac{V_{dc}}{V_{CPD} - V_{dc}} \Rightarrow \quad V_{dc} = \frac{G}{1+G} V_{CPD}. \tag{3.5}$$

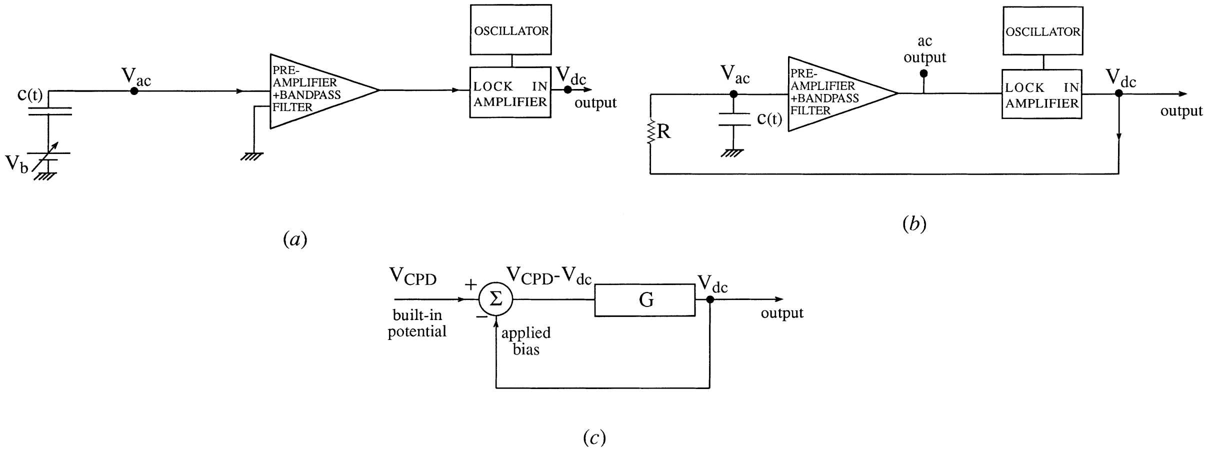

Fig. 22. Schematic block diagram of a Kelvin probe electrical circuit: (a) Manual mode. (b) Automatic mode. (c) Equivalent feedback loop.

If G is made large enough, V_{dc} approaches V_{CPD} and may be monitored continuously, as in Fig. 22(b) (assuming, of course, that the time interval between two consecutive measurement points is larger than the electronic settling time of the circuit).

For successful Kelvin probe measurements of semiconductors, a reasonable back Ohmic contact must be present for proper flow of ac current between the capacitor plates. The resistance of this Ohmic contact can be rather large without disturbing the measurements due to the large impedance typically present anyway between the two capacitor plates. The measurement of semi-insulating samples is problematic both because a good Ohmic contact is difficult to make and because the insulation of the sample mount must be extremely high or the signal is lost through leakage [130]. Furthermore, for a semi-insulating sample the voltage at the free surface of the sample may be different than the voltage applied to the sample electrode due to the potential drop across the sample itself [131]. Finally, high resistance samples are vulnerable to stray charges and to spurious dielectric response to stray electric fields [132]. Thus, while the measurement of high resistance samples is not impossible [130,131], it requires extreme caution.

It is also necessary to consider the means by which a sustained and stable periodic vibration of the probe plate is obtained. Early rudimentary mechanical designs [123,133–135] have not delivered sufficient performance on either count. Therefore, they were gradually replaced by electromechanical methods – typically attaching the probe plate to a moving coil or to the flexible diaphragm of a loudspeaker [136–138], or employing electromagnetic drivers [139–141]. Both the former [142] and the latter [143] approaches are still employed in modern day high performance Kelvin probes. However, it is the piezoelectric drive technique, first suggested by Besocke and Berger [144], which is currently most commonly used. In this approach, the vibrating electrode is mounted on an oscillator reed, which is fastened at the other end to a piezoelectric ceramic. This results in a simple and easy to handle probe, which provides stable vibrations simply by applying an appropriate ac voltage to the piezoelectric element. Furthermore, the probe-to-sample distance may be fine tuned by dc biasing the piezoelectric element. More recently, it has been shown that a bimorphous piezoelectric element may increase the immunity of the probe to mechanical noises and provide an even more stable operation [145].

For completeness, we note that electrode vibration has also been obtained by utilizing the ac electric force present between capacitor plates under ac voltage [146–148]. While the performance of this approach (known as electrostatic excitation) is similar to that obtained using other means, it is more complicated and has not found widespread use, except in the Kelvin probe force microscope, discussed in detail in Section 3.4.1 below.

Being a purely electrical measurement, the Kelvin probe approach should, in principle, provide accurate CPD readings under any ambient. Nevertheless, most surface physics experiments require UHV conditions for obtaining a well defined surface for a reasonable amount of time. For such experiments, the Kelvin probe itself, as well as any auxiliary mechanical and electrical parts introduced into the vacuum chamber, should be vacuum compatible. High-vacuum-compatible Kelvin probes have been demonstrated in the 1950s [141,149], and many UHV compatible probes have been demonstrated since ([142–144, 150–152] are a few examples).

Despite the evident success in constructing and operating Kelvin probes in vacuum, the presence of continuously moving parts in vacuo does present (surmountable) design challenges and is thus not particularly welcome by vacuum engineers. As shall be seen below, it may also introduce problematic mechanical noises. Consequently, two alternative approaches have emerged. Delchar et al. [153] used a static capacitor approach. In this approach, the charge flow which occurs upon CPD changes is detected and a potential which nulls the charge flow is applied within a time which is much smaller than the capacitor discharge time constant. Anderson and Alexander [124] have suggested a double-capacitor approach: A static capacitor which is inside the vacuum chamber is serially connected to a vibrating capacitor which is outside the vacuum chamber. Thus, the equivalent series capacitance is modulated and an ac current is produced without motion in the vacuum chamber. Although both techniques are elegant, they suffer from serious disadvantages. The static capacitor approach does not employ synchronous detection and hence results in a reduced signal to noise ratio (SNR). Furthermore, spurious currents may be misinterpreted as CPD changes. In the double capacitor approach, the equivalent capacitance is smaller than that obtained from a single capacitor unless the static capacitor is much larger than the dynamic one. However, this is hard to achieve since we have already noted that the Kelvin probe capacitance is rather small to begin with. Hence, the resulting ac current is diminished and the SNR is reduced. Bodrova et al. [154] seem to be the only ones to have actually employed such an arrangement and have reported a factor of 6 reduction in the SNR with respect to a single vibrating capacitor arrangement. Both the static capacitor and the double capacitor approach can only detect CPD changes and not absolute CPD values. The former because it is only sensitive to changes in the charging of the capacitor [155] and the latter because it cannot take into account the CPD between the static and the dynamic capacitor plates [156]. However, for SPV measurements this suffices.

An implicit assumption in CPD measurements is that the work function of the reference electrode remains constant during the measurement. However, the work function may be very sensitive to variations in the ambient and thus invalidate the measurement. It is common practice to use an inert reference surface, typically gold or tin oxide [156]. Both materials maintain their work function over a relatively large range of pressures and temperatures. Tungsten is eminently suitable as a reference electrode material in vacuum but is very sensitive to adsorption-related changes in work function [156]. More recently, a probe head made of aluminized mylar with holes allowing the continuous flow of purge gas has been suggested for maintaining a constant reference work function in air and/or under a partial pressure of adsorbates [157]. With proper design, successful CPD measurements have been demonstrated even under extreme conditions. These include a flow reactor with temperatures as high as 750 K and partial pressures of H_2, O_2, and CO [158], or a furnace for redox processes with temperatures up to 1000°C and partial pressures of oxygen [159]. If the constancy of the reference work function is under any doubt, it is always a good practice to examine it by taking a CPD measurement with respect to a well-defined auxiliary surface [156].

Many studies compare the work function of the sample before and after various treatments, e.g., overlayer deposition. To that end, various mechanical arrangements where the probe may be moved away from the sample for the duration of the treatment are usually used [130,141,149,160]. During such sample treatments, the reference electrode must be adequately protected so that its work function does not change. A recent example is a Kelvin probe arrangement, which is compatible with a plasma enhanced chemical vapor deposition process [161]. In this arrangement, the Kelvin probe is repeatedly moved between a vacuum chamber, when the plasma is on, and a deposition chamber, when the plasma is off. Following each measurement, the stability of the Kelvin probe work function is checked against a gold reference present in the vacuum chamber.

If in situ measurements are to be pursued, two conditions must be fulfilled. The first condition, discussed above, is that the work function of the reference electrode does not change due to the process. The second condition is that the Kelvin probe must not interfere with the studied process. An obvious example is that during SPV experiments, the Kelvin probe must be semi-transparent, i.e., made of a metallic grid or a transparent conductor. A less obvious example is that during adsorption studies, the probe may act as a shield hindering the impinging gas molecules from hitting the area below the probe [162]. Consequently, a grid structure is to be preferred for such studies. Another configuration sometimes used for in-situ studies is that of the rotational Kelvin probe [120,163–165]. In this arrangement, the capacitance modulation is achieved by rotating one of the capacitor plates with respect to the other one so that a current pulse is obtained each time the moving electrode passes over the stationary one. Other variations on this idea include moving the Kelvin probe *in parallel* to the sample [166,167] or in a diagonal mode [167], or swinging the moving electrode in a pendulum motion above the sample [168]. The moving probe may be positioned so that it does not obstruct the sample significantly and thus measurements may be performed during, e.g., adsorption [166], particle beam bombardment [168], or evaporation [169,170] experiments. Another advantage of this approach is that if several samples are positioned along the track of the moving electrode they may be measured simultaneously [163,170]. The 'penalty' of simultaneous measurements, however, is that because current pulses have to be detected, a larger bandwidth of frequencies needs to be followed and hence the SNR is reduced.

So far, only CPD measurements of solids has been described. However, CPD measurements of liquids or objects immersed in liquids have also been performed from the earliest days of the Kelvin probe [136–138]. The CPD between two liquids may also be measured by means of rotating a metallic auxiliary electrode above two juxtaposed liquid electrodes [171]. Some pitfalls have to be avoided when attempting such measurements. When (at least) one electrode is liquid, an obvious problem is the necessity to contact the liquid. Moreover, the vibration of the Kelvin probe may disturb the surface of the liquid and disrupt the measurement [171]. The relatively high vapor pressure of liquids makes a contamination of the probe electrode more likely, even in a gas ambient, and thus the stability of its work function needs to be particularly examined [157]. Finally, accidental dunking of the probe head in the solution may ruin it. Therefore, use of a disposable probe head for such measurements has been suggested [157].

An interesting application of measuring the CPD of a liquid is that the liquid provides a clean, reproducible, and easy to obtain reference surface in a gas ambient. This is because a new uncontaminated surface can be exposed simply by pouring out some liquid [157]. Moreover, the work function can be calibrated using absolute half cell potential data [172]. CPD measurements where both electrodes are solid but one or both of them are immersed in a liquid [127,173,174] are also of importance since the humid environment may be crucial for accurately reproducing the required chemical state of the surface. While properly designed and interpreted experiments may produce a wealth of important information, several pitfalls must be recognized and avoided in order to complete such measurements successfully. Viscous damping and wave propagation in the liquid call for a low frequency of vibration [127]. The vibration of the reference electrode may cause a change in the CPD between supposedly stable electrodes due to the disruption of a structure in the liquid, e.g., a film of unsaturated hydrocarbon present at the surface of a metal electrode in the case of unsaturated organic liquids [173]. Severe problems may ensue if the liquid is partially conducting. The current between the electrodes causes the apparent CPD value to approach the value of the bias between the electrodes, the alternating current may be very high even in the null position, and the sensitivity of the electrodes to stray electric fields increases. All three effects have been observed when CPD measurements at a polar liquid ambient were attempted [173]. Moreover, unless proper insulation is provided, the liquid may short circuit the sample surface to the sample holder. Finally, a different difficulty may occur if one electrode is immersed in a thick solution. The work function at the electrolyte/ambient interface may differ from that at the sample surface due to potential drops across the solution [174].

3.1.3. Limitations and solutions

In this section, we describe the general factors which limit the sensitivity and accuracy of Kelvin probe measurements. We also propose practical solutions which make it possible to minimize or circumvent these limitations.

As in any electronic measurement, the ultimate resolution with which the CPD may be resolved is determined by the noise spectrum of the measurement. A comprehensive treatment of this noise spectrum was provided by Baikie et al. [175]. Many of the noise sources may be significantly reduced by judicious use of electrostatic shielding. However, total shielding is extremely difficult, especially in the presence of additional electrical connections [175]. Strong magnets should not be placed in proximity to the Kelvin electrodes either [156]. Much of the noise spectrum is effectively eliminated by using a narrow-band lock-in amplifier, where the lock-in frequency is *not* a multiple of a frequency with significant noise components.

The most problematic noise sources are those with a frequency equal to the vibration frequency since they are not eliminated by the lock-in amplifier. One source for such signals is the residual electrostatic pick-up by the Kelvin capacitor and/or (internal and external) connecting cables. Probe driver designs have been offered, which reduce this noise by removing the driver as much as possible from the vibrating capacitor [157,175]. However, many practical designs are subject to geometrical, ease of handling, or other limitations which preclude such arrangements. A particularly problematic type of driver frequency noise is contributed by microphonics, which is a general name for ac electrical signals produced as a result of the vibration of conductors and insulators [176]. Since a maximal ac current is obtained when the ac capacitance is maximal, the modulation index should be large. However, an increased amplitude of vibrations increases the microphonic effects as well [177]. Thus, a significant effort has been devoted to eliminating any sources of mechanical vibrations [130,133,141,175,178–180]. Noise contributions at the driver frequency may be modeled as parasitic ac current and voltage sources, which are connected in parallel and in series, respectively, to the vibrating capacitor [176]. These prevent the ac current from being perfectly nullified and produce a systematic error in the CPD reading. Worse, the relative magnitude of the error term with respect to the real one, and therefore the CPD reading, may become spacing dependent [176].

A different and major cause for inaccuracy in CPD readings is stray capacitance. The two Kelvin probe plates are also capacitively coupled to, e.g., the electrostatic shield, the walls of the vacuum chamber, and any other metallic or dielectric object [181], including sample areas of different work function which are not situated directly under the probe [182], and supports and connecting wires [177]. If there is an appreciable CPD and/or applied bias between the electrode connected to the amplifier and the stray capacitance sources, the current-nullifying bias may differ from the real CPD.

Fig. 23 features a very simple equivalent circuit for analyzing stray capacitance effects. The Kelvin electrodes are designated as ‘1’ and ‘2’, where ‘1’ is the electrode connected to the amplifier, and all stray capacitance is *lumped* into a single stray electrode ‘s’ with an effective external bias, V_{st}. The nullifying bias V_b may be applied to Electrode ‘2’ or ‘1’, as in Figs. 23(a) and (b), respectively. For simplicity, we assume a current amplifier. Using Eq. (3.4), the total ac current sensed by the amplifier in

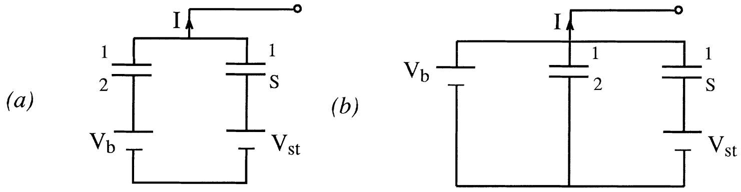

Fig. 23. Equivalent circuit for including stray capacitance effects. The Kelvin electrodes are designated as ‘1’ and ‘2’. Electrode ‘1’ is connected to the amplifier. ‘s’ – stray electrode with an effective external bias. V_{st}. (a) V_{b} applied to electrode ‘2’, (b) V_{b} applied to Electrode ‘1’.

the two cases is [182]:

$$i = C_{12}\left[\frac{1}{e}(W_1 - W_2) + V_{\mathrm{b}}\right] + C_{1\mathrm{s}}\left[\frac{1}{e}(W_1 - W_{\mathrm{s}}) + V_{\mathrm{st}}\right], \quad \text{bias at Electrode 2,} \tag{3.6a}$$

$$i = C_{12}\left[\frac{1}{e}(W_1 - W_2) + V_{\mathrm{b}}\right] + C_{1\mathrm{s}}\left[\frac{1}{e}(W_1 - W_{\mathrm{s}}) + V_{\mathrm{st}} - V_{\mathrm{b}}\right], \quad \text{bias at Electrode 1,} \tag{3.6b}$$

where W is the work function of the different electrodes, C_{12} the ac Kelvin capacitance, and $C_{1\mathrm{s}}$ the in-phase component of the ac stray capacitance. Using Eqs. (3.6), the bias V_{b}^0 required to nullify the ac current is given by:

$$eV_{\mathrm{b}}^0 = W_2 - W_1 + \frac{C_{1\mathrm{s}}}{C_{12}}(W_{\mathrm{s}} - W_1 - eV_{\mathrm{st}}), \quad \text{for bias at Electrode 2,} \tag{3.7a}$$

$$eV_{\mathrm{b}}^0 = W_2 - W_1 + \frac{C_{1\mathrm{s}}}{C_{12} + C_{1\mathrm{s}}}(W_{\mathrm{s}} - W_2 - eV_{\mathrm{st}}), \quad \text{for bias at Electrode 1,} \tag{3.7b}$$

Eqs. (3.7) demonstrate that in both configurations there is a systematic error between V_{b}^0 and the real CPD between the Kelvin electrodes. This error is significant if the stray capacitance is large enough [181]. As the stray to desired capacitance ratio depends on the sample-to-probe distance, V_{b}^0 will become spacing-dependent, as in the case of spurious signals.

In SPV measurements only CPD *changes* need to be measured. Consequently, if the error term in Eqs. (3.7) remains constant upon illumination (i.e., upon changes in the work function of the *sample* electrode), the SPV measurement is precise even if the error in CPD is considerable. Electrode 1 can be either the sample or the probe, i.e., either the static or the vibrating electrode. Inspection of Eqs. (3.7) reveals that in either case for a constant error the bias V_{b} should be applied to the sample, rather than to the probe [182,183]. Interestingly, this extremely simple and effective means of *completely avoiding* stray capacitance errors in SPV measurements is barely noted in the literature. Potter [139] has mentioned already in 1940 that the stray capacitance error is an additive constant but has neither proved his claim nor discussed the conditions for its validity. Thus, his work was largely ignored or criticized [181]. The issue was finally clarified by de Boer et al. [182], but is still frequently a source of confusion, as correctly mentioned by Baikie et al. [183].

As shown in Section 5 below, some advanced SPV analyses combine SPV and CPD experiments for data extraction. Therefore, we briefly discuss stray capacitance effects and means of minimizing them, even though they should not affect SPV experiments. A simple precaution against stray capacitance is keeping the sample-to-probe distance, d, constant. Then, the relative difference between CPD measurements of different samples is minimized [130,184]. This may be impractical at liquid surfaces [157] or in the presence of thermal expansion and/or applied stress effects. Actively controlling d with a feedback loop offers a more reliable solution [142,185]. If this is not possible, it may be better to select a spacing in which the *slope* of the dependence of V_b^0 on d is minimal, so that the error in CPD is close to a constant [179]. Connecting the amplifier to the static electrode [181] (i.e., to the sample rather than to the probe) may reduce the CPD error by an order of magnitude [183]. This is because it minimizes the stray capacities which oscillate at the same frequency as the Kelvin probe and produce stray signals which are picked up by the lock-in amplifier [141]. Unfortunately, this may interfere with other electrical connections [184,186].

Many stray capacities may be eliminated with an electrostatic shield [149]. The stray capacitance of the shield itself is eliminated if the shield and probe are made of the same material [160] or if an auxilliary shield bias is used [139,181]. Many different shield designs have been proposed (see, e.g., [131,150,176,179,184,188,189]).

Further complications arise at samples with a non-uniform work function. In an ideal parallel-plate capacitor, the measured CPD is an area weighted mean work function of the surface underneath the probe, as long as 'patches' of different work function are small with respect to d [187]. In practice, fringing effects cause the probe to sense its surroundings as well [182,183]. The relative weight of the area underneath the probe with respect to the bordering areas depends on d and is another cause for spacing-dependent CPD readings [177].

An excellent tool for assessing stray capacities is studying the dependence of V_b^0 on d. For samples with uniform work function, the real Kelvin signal must dominate for $d \to 0$, so that the CPD error at a given distance can be assessed [128,181,182]. For samples with a non-uniform work function, this is valid only if V_b^0 is 'flat' over a range which extends from a value of d which is much smaller than all other characteristic lengths of the system [177,182]. Studying the dependence of V_b^0 on the amplitude of vibrations allows for a distinction between stray capacitance amd microphonic effects. This is because an increased accuracy with increasing amplitude of vibrations is indicative of a stray capacitance, while the opposite is true for microphonics. Indeed, a decreased accuracy in CPD reading with increased amplitude of vibrations has been misinterpreted for an increase in stray capacitance [181] when in fact it was due to microphonics [177]. Changing bias polarity and/or the phase between reference and signal in the lock-in amplifier may also provide a key for detecting systematic CPD errors [127].

We now turn to considering how the measurement sensitivity and accuracy may be increased using electronic methods. We have noted above that a significant modulation of the capacitance is usually desirable because it increases the overall current and hence the overall sensitivity of the measurement. However, this increases the harmonic distortion [125]. For a large enough modulation index, the second harmonic may be larger than the fundamental one and further increases in the modulation index actually reduce the signal at the fundamental harmonic. At very high frequencies, the harmonic distortion becomes negligible. This is because for $\omega \gg 1/RC_0$, the capacitor cannot change its charge appreciably within a vibration period and therefore the potential on the capacitor varies as $1/C$ and is purely sinusoidal [124,125]. Practically, a high enough frequency is often difficult to obtain because of mechanical limitations and noise problems.

A large value of the resistor R is preferable for both minimizing harmonic distortions and maximizing the measured ac signal. However, a large resistor R is also a source of many difficulties.

Kolm [163] has noted that the probe may effectively 'float' with respect to ground, resulting in electrostatic accumulation which may produce even the *wrong sign* of CPD change following exposure to ozone. A more prevalent problem is the effective short-circuiting of the large resistor by parallel parasitic capacitance [124,179]. Although satisfactory performance was reported in some cases [191], this problem has not been universally overcome. Bonnet et al. [126] were the first to use a low input impedance current-to-voltage amplifier. Using a current amplifier, parasitic capacitance only serves to decrease the input impedance further, making the device even closer to an ideal current meter. This makes it possible to increase the distance between the pre-amplifier and the Kelvin probe, reducing spurious signals [185]. The input impedance does not have to be really low either – an impedance as high as hundreds of kΩ is still much lower than the impedance of the Kelvin capacitor and will produce a negligible voltage drop [143]. Thus, most modern Kelvin probe designs rely on current, rather than voltage, detection.

The electronic design can be used to correct, compensate, or reduce some of the problems associated with synchronous pick-up and/or stray capacitance. Several authors have attempted to reduce synchronous pick-up noises from the driver mechanism by using different frequencies for the mechanical excitation and the electrical current. For example, when using electrostatic excitation [147] or electromagnetic excitation with a non-polarized electromagnet [141], the ensuing ac current is automatically obtained at twice the frequency of the exciting voltage. In an extreme application of this concept, Harris and Fiasson have found that pick-up from the driving coil is acceptably small only at the *sixth* harmonic [131]. Other advantages may be associated with multiple frequency schemes. For example, Blott and Lee [178] excited the probe at two *simultaneous* frequencies and nullified the low-frequency envelope of the ac signal. This provided an accurate CPD reading even in the presence of emission currents between sample and probe. While potentially useful, such excitation/detection schemes invariably complicate circuit design and handling and do not always offer significant performance enhancement. In some cases they may even adversely affect the SNR of the measurement [193]. Thus, they are not of very wide-spread use.

Recently, attempts at correcting spacing-dependent CPD readings have been made. Addition of a deliberate dc offset inside the lock-in amplifier has been shown to compensate for microphonics-induced spacing-dependence [176]. Stray capacitance-induced spacing-dependence has been compensated for analytically by extracting the stray coefficients and adding a correction term [161]. While such corrections may make reading of the absolute CPD impossible, they provide accurate, spacing-independent, monitoring of CPD changes. Just as properly designed electronics may decrease the spacing-dependence, improperly designed electronics may increase them: The lock-in amplifier output may be below noise level (and thus considered zero) in some range of biases around the balance point. Thus, the feedback loop would lock to the end of this range, rather than to its middle [131]. Since the noise level may be spacing-dependent, errors which are spacing-dependent may be produced. In addition, an insufficient feedback loop gain may produce an error between the real and measured CPD. This error has also been shown to be spacing-dependent [176].

As clearly demonstrated above, applying a bias which nullifies the lock-in amplifier output has many advantages. It also has some distinct disadvantages [175]. First, at balance the SNR is minimal since the signal is smallest. Second, any part of the signal not contained in the detected frequency is wasted. Third, the phase inversion around the balance point can cause lock-in complications. Finally, as explained in the preceding paragraph, noise may cause a systematic error in CPD reading. Using a current amplifier, a linear relation between the current and $V_{\mathrm{CPD}} + V_{\mathrm{b}}$ is obtained (see Eq. (3.4)).

Hence, by performing *off-null* measurements, i.e., measuring the current for many biases *around* the bias point, the latter may be found using linear regression with significant gains in the SNR [194]. This may be rather easily performed automatically using appropriate software [142,195]. Moreover, the average of the signal obtained at symmetric biases around the balance points should ideally be null and hence produces the noise contribution only. This contribution may be dynamically subtracted to increase the SNR [175]. A difficulty, related with off-null measurements and not taken into account in the literature, is that if the probe-to-sample distance is of the order of the depletion region width, the influence of the probe on the work function (see Fig. 20) may be considerable. Then, off-null measurements may exhibit a deviation from the linearity of the ac current on $V_{\mathrm{CPD}} + V_{\mathrm{b}}$ and may be rendered invalid. A different approach was used by Baczynski [196], who analyzed the signal in the time domain. While more complicated, his approach makes it possible to eliminate stray signals by means of detecting the phase difference between them and the desired signal.

The voltage resolution with which the balance point is determined is ultimately governed by either the minimal noise level [191,194] or the minimal offset current [179,197] of the electronics. It is almost invariably between $\sim$0.1 and $\sim$10 mV, depending on the probe size and distance from the sample and on the sophistication of the electronics. It is very important to distinguish between the accuracy, with which the balance point (i.e., the apparent CPD) is read, and the accuracy of the real CPD reading [177,183]. The latter is subject to various systematic errors, discussed above. Using sufficient precautions on both measurement and ambient stability, an accuracy which is better than several tens of mV may be achieved. The error with which the SPV may be determined is much closer to the accuracy of V_{b}^0. This is because the SPV is usually not (or almost not) subject to systematic errors, being a difference between two CPD values in a given configuration. Consequently, SPV values may routinely be read with mV precision.

A significant disadvantage of Kelvin probe measurements is that their temporal resolution is poor. The dominant time constant is typically associated with the lock-in amplifier. It is of the order of at least tens of msec to several seconds, with the SNR decreasing the shorter the response time is, due to the gain-bandwidth product rule. For example, decreasing the frequency band allowed into the lock-in amplifier requires a larger settling time and makes the measurement susceptible to instabilities in oscillation frequency [127]. The time constant increases even more if off-null measurements are employed [195]. Using the static capacitor approach [153], a time constant of 120 μs has been achieved [198]. This value is still rather high for some applications but is extremely low for Kelvin probe measurements. Therefore, it is clear that the Kelvin probe is ill-suited for measurements of the ac SPV.

3.1.4. Scanning Kelvin probes

A Kelvin probe may also be employed in a scanning mode: if the probe is scanned across the sample, lateral variation mapping of the CPD (and hence also SPV) may be obtained. This concept was first employed by Parker and Warren [180], who studied lateral variations in work functions of gold and graphite with a resolution of several mm. Since then, many authors have built and successfully used scanning Kelvin probes with lateral resolutions of several tenths of a mm to several mm (see, e.g., [150,181,185,188,191,197,199–201]).

Butz and Wagner [202] used a 6 μm wire as the vibrating probe. Thus, they have sacrificed lateral resolution at one axis and obtained an effective resolution of $\sim$50 μm with a voltage resolution of $\sim$20 mV at the other axis. With more advanced designs, probe resolutions of several tens of μm on both axes has been achieved [174,203,204]. Mäckel et al. constructed a scanning Kelvin probe which features a

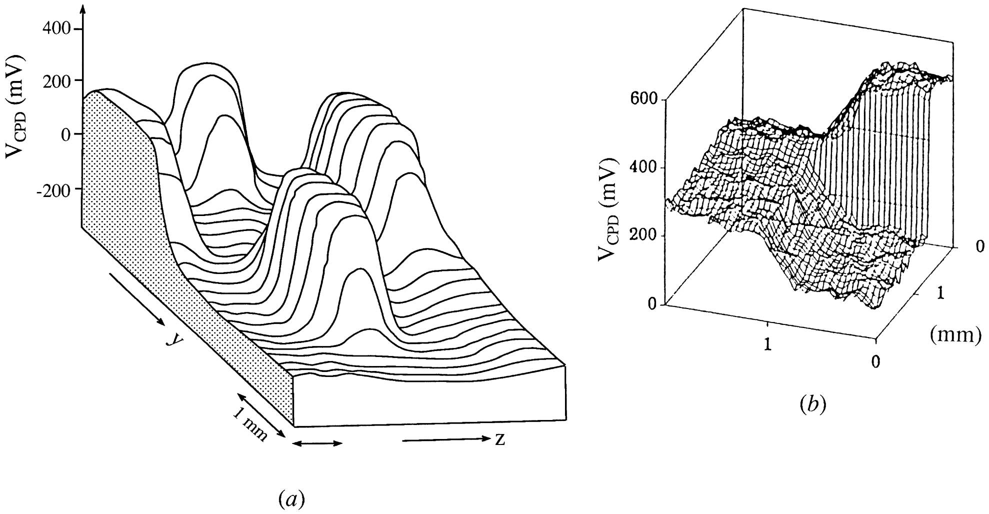

(*a*) (*b*)

Fig. 24. (a) CPD map of a mechano-chemically polished (100) p-GaAs surface on which 1.3 mm silver dots have been evaporated (after Palau and Bonnet [197]). (b) CPD map of a lateral Ti/Si(111) interface in the dark (foreground) and under illumination (background) (after Baikie and Bruggink [201]).

spatial resolution of 5 μm, with a voltage resolution of several tens of mV [205,206]. In their arrangement, the probe tip is prepared using STM-like techniques but is flattened to several μm. The probe is actively maintained at a distance of about 50 nm from the surface. The distance control makes it possible to use the microprobe for topographic mapping as well. A Kelvin probe with a record lateral resolution of ~100 nm and a voltage resolution of several mV was recently reported by Nabhan et al. [208]. It is also based on active distance control, with the improvement obtained primarily through the construction of a carefully shielded probe tip and the use of ultra-low-noise electronics.

Fig. 24 features two examples of semiconductor CPD maps obtained using a scanning Kelvin probe. A CPD map of a (1 0 0) p-GaAs surface, on which 1.3 mm silver dots have been evaporated [197] is shown in Fig. 24(a). The dots are easily detected by the probe because their work function is different from that of the GaAs. A CPD map of a lateral Ti/Si(111) interface [201] is shown in Fig. 24(b), both in the dark and under illumination. The SPV distribution is, by definition, equal to the difference between the two maps. As expected, the metal (left side) shows no change in CPD under illumination, whereas the semiconductor (right side) features a significant change.

The successful use of a scanning Kelvin probe requires very careful attention since it is particularly prone to many of the difficulties of Kelvin probe operation explained above. First, an increased spatial resolution requires the decrease of the probe size. This reduces the obtained ac current and decreases the SNR, unless the probe-to-sample distance is minimized. The reduced size also makes the probe particularly susceptible to stray capacitance effects [180]. Worse, the stray capacitance may significantly vary across the sample due to the changing distance between the probe and sources of stray capacitance [181]. This may warp the obtained CPD map and cause serious artifacts. Furthermore, edge effects, i.e., the probe sensing areas which are not directly underneath it, decrease the spatial resolution of the probe. Such problems can be reduced but not necessarily eliminated by using appropriate shields [150]. Because of stray capacitance problems (and also because of the importance of mechanical stability when the probe is close to the sample), active probe-to-sample distance control, discussed above, is very important for keeping the error in CPD as close to an additive constant as possible [185,204]. In many cases, this is implemented by superimposing a high frequency ac bias on the normal dc bias. This generates an ac current at the high frequency, which is proportional to the instantaneous sample-probe capacitance. Therefore, it is an effective measure of sample-probe distance [185,204,206,208]. Baumgärtner [207] has shown that the ratio of the second and first harmonics of the ac current depends on the modulation index alone. For a fixed amplitude of vibrations, this ratio is a measure of the sample-to-probe distance and may also be used to close a distance-control loop, eliminating the need for additional biases [205]. The 'penalty' for this bias elimination, however, is difficulties in obtaining a reasonable SNR when, with an appropriate compensation bias, the current approaches zero [206]. We note that in addition to spacing variations, deviation from plate parallelism has also been shown to be detrimental to Kelvin probe operation and should be avoided [185,205].

Another problem is associated with the finite size of the probe head, even if fringing effects and non-uniformities in probe work function are completely negligible [203]. Since the probe averages the work functions underneath it, a rectangular change in the sample work function as a function of distance (Fig. 25(a)) will appear as a trapezoidal change if the feature is larger than the probe head (Fig. 25(b)) or a triangular one if the two are equal (Fig. 25(c)). Particularly bothersome is that if the feature is smaller than the probe, it will also appear to be trapezoidal, but with the largest *measured* change in work function smaller than the real change (Fig. 25(d)). Fig. 26 features an experimental verification of these considerations [185]. A variation of 500 mV in CPD may be warped in both spatial shape and magnitude, depending on the feature size. One must always take this effect into account when analyzing spatially resolved CPD data. Indeed, several authors have used test structures of known CPDs and various feature sizes in order to determine the minimal feature size for which no distortion of the CPD magnitude is obtained [174,185,191,203].

To conclude our description of the Kelvin probe, we note that although the physical principles of the Kelvin probe are simple, many technical questions need to be addressed for its successful operation. However, once these questions are adequately answered, the Kelvin probe may be safely and reproducibly used for contactless, non-destructive CPD and SPV measurements in an extremely a wide range of samples, environments, temperatures, lateral resolutions, and more. The maturity of Kelvin probe technology is perhaps best demonstrated by the several types of state-of-the-art Kelvin probes which can be obtained commercially [209–211].

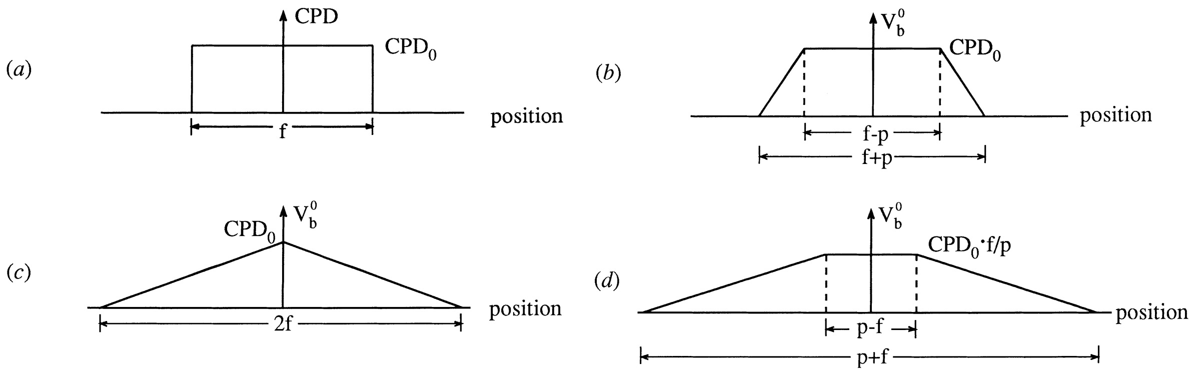

Fig. 25. Lateral distribution of sample work function (a) and measured CPD for a feature larger than (b), equal to (c), and smaller than (d) the Kelvin probe size. p – probe diameter, f – feature size (after Baumgärtner and Liess [203]).

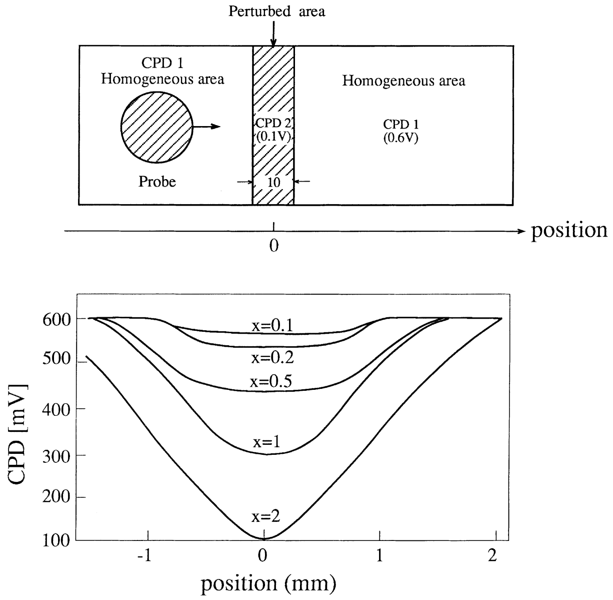

Fig. 26. CPD variations across a perturbed area of variable width, *x*. Probe diameter: 2 mm (after Bonnet et al. [185]).

3.2. MIS structures

Let us reconsider the energy band diagram of a MIS structure, shown in Fig. 6(c). Assume that after equilibrium is established, the capacitor is brought into open-circuit mode by disconnecting its two terminals. If illumination is now applied to the capacitor, V_s may change due to the photovoltaic effect. However, V_{ins}, which is determined by Eq. (2.41), may *not* change because Q_m cannot change in open-circuit. Using Eq. (2.42), we conclude that the change in V_s must produce an equal change in V_G, which in this case is the voltage measurable between the two capacitor terminals. Thus, the SPV at the semiconductor/insulator interface in a MIS structure can be found by measuring the photo-induced (*external*) voltage changes between the MIS capacitor terminals. Morrison [212] seems to have been the first to apply the above explained approach for studying the SPV at a free semiconductor surface. This has been achieved by placing a static platinum grid in front of the sample. Thus, an 'artificial' MIS structure where the insulator was simply air or vacuum was produced and contactless, non-destructive SPV measurements were taken. Subsequently, his approach has been used by many other scientists. An insulating spacer (e.g., mylar) may replace the air/vacuum gap (see, e.g., [213]), as long as the placement of the spacer does not alter the surface properties of the semiconductor.

As in the case of the Kelvin probe, the simple physical principles of the measurement are complicated by technical problems. In practice, every Voltmeter has a finite resistance. This means that the MIS capacitor gradually discharges and the measurement is distorted. Hence, for steady-state measurements the light source must be chopped at a sufficient rate so that this discharge is negligible. (Moreover, chopping the light is desirable since it makes a replacement of the simple voltmeter with a lock-in amplifier possible). This argument may be more readily understood using the simple equivalent circuit of Fig. 27(a), where C_{ins} is the capacitance of the MIS insulator and R_i the input resistance of the

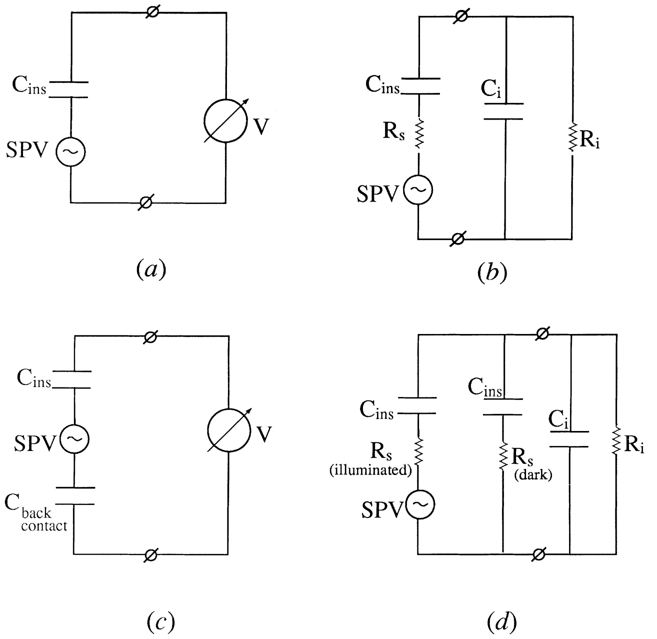

Fig. 27. Equivalent circuits for MIS capacitor SPV measurements: (a) Simple equivalent circuit. (b) Equivalent circuit including sample resistance and voltmeter resistance and capacitance. (c) Equivalent circuit for a capacitive back contact. (d) Equivalent circuit for a 'flying spot' SPV apparatus.

voltmeter. Using the circuit, we conclude that in steady-state V_{meas} is related to the real SPV by the relation:

$$V_{\text{meas}} = \frac{1}{1 + (i\omega C_{\text{ins}} R_{\text{i}})^{-1}} \cdot \text{SPV}. \tag{3.8}$$

Thus, $V_{\text{meas}} \rightarrow$ SPV if and only if $\omega \gg (R_{\text{i}} C_{\text{ins}})^{-1}$, where ω is the modulation frequency. On the other hand, as noted in Section 2.2.2, ω must not be too high or the ac SPV will differ appreciably from the dc SPV. Thus, the measurement is precise if and only ω is inside a limited range [213]. The minimal ω necessary may be lowered if R_{i} and/or C_{ins} are increased. However, increasing the former may increase the noise and also lengthen the time-constant of the lock-in amplifier [213]. An increase of C_{ins} may be achieved by decreasing the sample-to-metal distance. The problems associated with this decrease are discussed below. Johnson [66] suggested that for calibration purposes, an ac voltage source may be placed in series with the MIS capacitor so as to simulate the effect of illumination. This makes it possible to experimentally obtain the dependence of V_{meas} on the SPV, thereby making a precise determination of the latter possible. If the relation between V_{meas} and the SPV has not been examined, theoretically or experimentally, one must settle for measuring the SPV in arbitrary units. Such data representation is indeed frequently encountered in the literature.

SPV measurement using an MIS structure is clearly an off-null technique. Therefore, its application to semiconductors may be subject to some serious difficulties. First, since the free surface structure has been replaced with a MIS structure, the MIS charge conservation rule, $Q_{\text{sc}} + Q_{\text{ss}} + Q_{\text{m}} = 0$, rather than the free surface rule, $Q_{sc} + Q_{ss} = 0$, should be used. If Q_m is negligible with respect to Q_{sc}, this is insignificant. However, the metal is frequently placed within several microns from the semiconductor surface for increasing C_{ins}. Then, Q_m is not negligible, as explained in Section 2.1.5. Mathematically, adding a constant charge density, Q_m, to the free surface charge conservation rule is equivalent to the addition of slow surface states (see Section 2.2.2). Thus, V_s^0, the equilibrium value of V_s, may be altered and a different SPV obtained. The importance of this is application dependent and is discussed where appropriate in Sections 4 and 5.

For some applications, controlling V_s^0 via an external bias may prove beneficial. Here, this is easily performed by applying a dc-bias to the metal electrode. This bias must be supplied through a large resistor or the ensuing ac signal will be effectively short-circuited. As noted in Section 2.1.5, the effect of the applied bias on V_s^0 may be very small if the surface state density is large, due to screening. This requires an increased electric field which is typically limited by the breakdown voltage of the dielectric. Schulz et al. [214] suggested that in such cases some control of V_s^0 may be achieved by using a ferroelectric crystal instead of a dielectric. This results in a very large electric field between metal and semiconductor due to the spontaneous polarization of the ferroelectric.

A severe problem may occur if Q_m is significant and ω is too low to meet the condition $\omega \gg (R_i C_{ins})^{-1}$. If the capacitor has enough time to change its charge during illumination, Q_m may change appreciably and the SPV may be different than that obtained with constant Q_m. Here the problem is *not* that V_{meas} will differ from the SPV, as in Eq. (3.8). Rather, the SPV *itself* will be different. Consequently, it cannot be corrected by a calibration signal. Worse, the extent of the change in the SPV may depend on the intensity and the photon energy of the illumination. Thus, the measured SPV spectrum may be very different from the real SPV spectrum. While spectra taken under such conditions may still be (cautiously) used for qualitative purposes, any quantitative analysis of them is dubious unless the time-dependence of Q_m is explicitly taken into account.

The direct reading of the SPV via off-null measurements in the MIS capacitor approach also has some distinct advantages over the null measurements performed in the Kelvin probe approach. First, its noise level (and hence minimum attainable signal) is much better than that of the Kelvin probe and can be rather easily reduced to the μV or sub-μV level [215]. Note that a μV noise level is also attained at the output of the lock-in amplifier used in Kelvin probe measurements. However, since there it is not this voltage directly, but rather the dc bias used to nullify it, which is measured, the voltage resolution is decreased. For example, detecting a 1 μV voltage across a 1 GΩ resistor is tantamount to a current resolution of 1 fA. For a probe capacitance of 1 pF, this implies a dc bias resolution of fA/pF ~1 mV. Second, the temporal resolution of MIS structures is considerably superior to that of the Kelvin probe. Indeed, Johnson has used MIS structures as early as 1957 for measuring transient SPV responses in the μs range [4].

Time-resolved measurements require that V_{meas} reflect the real SPV over the entire time scale involved. This calls for the relation between V_{meas} and the SPV to be frequency independent at the entire frequency range extending between the inverses of the longest and shortest times measured. Recently, Hlávka and Švehla [216] have reexamined the frequency response of a MIS structure for SPV measurements, using the more general equivalent circuit shown in Fig. 27(b) [215,216], where R_s is the (often negligible) sample resistance, R_i is the Voltmeter resistance, and C_i is the Voltmeter capacitance (including lead capacitance). They have noted that $V_{meas} \to$ SPV as long as $Z_i \gg Z_s$, where $1/Z_i = \sqrt{(1/R_i)^2 + (\omega C_i)^2}$ is the total input impedance of the voltmeter and $Z_s = \sqrt{R_s^2 + (1/\omega C_{ins})^2}$.

By analyzing the circuit of Fig. 27(b), it may be shown that $V_{\mathrm{meas}} \rightarrow$ SPV if [216]:

$$R_{\mathrm{i}} \gg R_{\mathrm{s}}; \qquad C_{\mathrm{ins}} \gg C_{\mathrm{i}}, \tag{3.9a}$$

$$(R_{\mathrm{i}}C_{\mathrm{ins}})^{-1} \ll \omega \ll (R_{\mathrm{s}}C_{\mathrm{i}})^{-1}. \tag{3.9b}$$

Inspection of Eqs. (3.9) reveals that if the prerequisite condition, (3.9a), on voltmeter resistance and capacitance is fulfilled, the frequency response is constant in a range in which the lower bound has already been discussed above and the upper bound is dictated by sample resistance and voltmeter capacitance. The minimal time which can be safely measured is of the order of $R_{\mathrm{s}}C_{\mathrm{i}}$. Since R_{s} is typically small, a very good temporal resolution can be obtained even if C_{i} is non-negligible. Using this approach, a temporal resolution of 0.1 μs has been demonstrated [216]. Such a resolution is clearly many orders of magnitude better than that afforded by a Kelvin probe. However, the MIS capacitor approach is not suitable for following long transients. From Eq. (3.9b), the maximal time for which a transient signal can be adequately followed is bounded by $R_{\mathrm{i}}C_{\mathrm{ins}}$, which is typically of the order of msec. Longer transients must therefore be followed with a Kelvin probe. Meshkov and Akimov [217] have constructed an apparatus where both the metallic electrode and the photon beam can be either fixed or modulated. This device may be operated as either a Kelvin probe or an SPV-sensing MIS structure and allows the user to enjoy the best of both worlds, depending on the application. Subsequent authors devised other apparata which combine a Kelvin probe and a MIS structure. A recent example may be found in [218], where the fixed and vibrating plates are located adjacent to each other.

Another important advantage of the MIS approach is that the Ohmic back contact, crucial for Kelvin probe measurements, may be replaced by contactless capacitive coupling (e.g., by means of a spacer) [12]. An appropriate equivalent circuit is shown in Fig. 27(c). The capacitive coupling creates a parasitic MIS capacitor in the back of the sample. However, as long as the capacitance of the back capacitor is much larger than that of the front capacitor, the impedance of the former will be much smaller that of the latter. Hence, the ac voltage on the back capacitor will be negligible and the measurement will not lose in accuracy. This condition may be met either by decreasing the thickness of the back insulator (which may be difficult), or simply by making the back capacitor area much larger than that of front capacitor [12].

The MIS measuring technique is amenable to scanning applications and is also used for obtaining spatially-resolved SPV maps. Kozhevin [219] provided an early demonstration of a line-scan of the SPV at a 'real' MIS capacitor, by scanning the surface with a narrow, modulated, light beam. More recently, Munakata et al. [215] have designed a 'flying spot' scanning SPV apparatus. The device is based on an 'artificial' MIS structure involving the sample under study. An illumination spot is scanned across the surface via (one or more) cathode ray tubes. The ensuing SPV map is acquired using a computer and displayed on a TV screen. They have extensively used this device for non-destructive monitoring of defects and inhomogeneities (see, e.g., [213,215,220–231]). As an illustrative simple example, an SPV image of a Si wafer after various treatments is shown in Fig. 28 [222]. Various degrees of surface damage are easily exposed since they affect the magnitude of the obtained SPV signal.

In the 'flying spot' approach, the metallic electrode covers the entire sample, whereas only a small portion of the sample is illuminated at a given time. From an equivalent circuit point of view (Fig. 27(d)), the unilluminated area introduces a shunting path in parallel with the illuminated area and the SPV signal is effectively attenuated by the ratio of the illuminated area to the overall area. Therefore, the magnitude of the signal is limited by the size of the illumination spot and *not* by the size

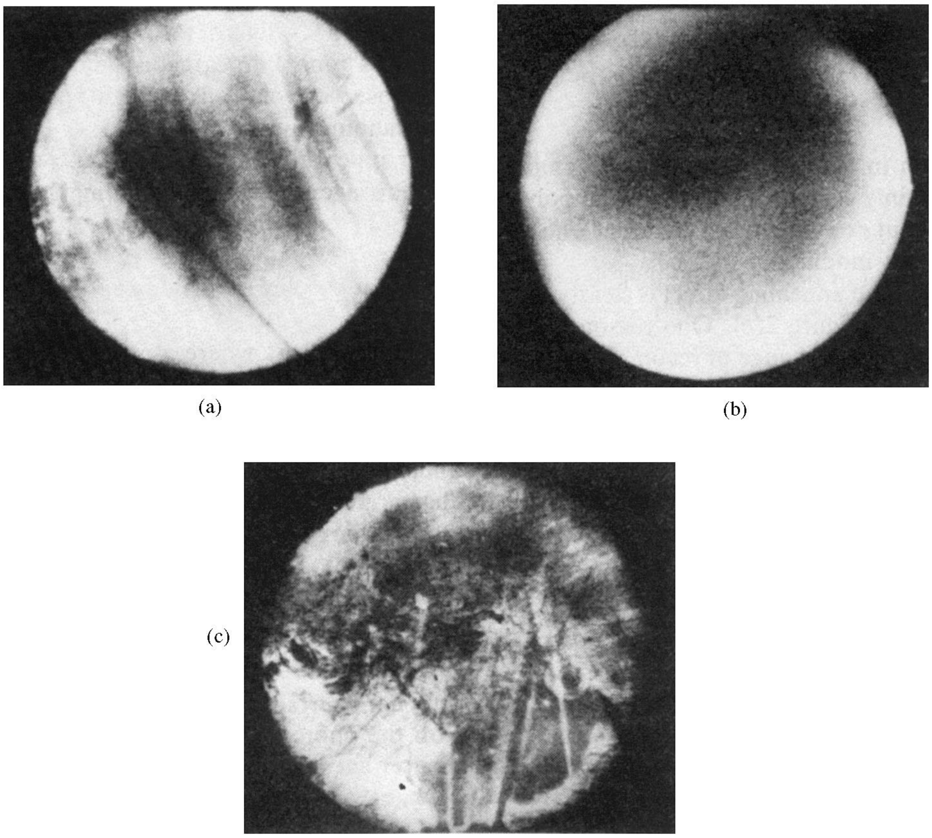

Fig. 28. SPV images of a Si wafer: (a) Rough surface. (b) Polished surface. (c) Annealed surface (after Munakata and Matsubara [222]).

of the capacitor. More recently, Lagowski et al. have suggested the arrangement shown in Fig. 2.29 [12]. In their device, the illumination point is fixed in space and applied to the sample via a fiber optic cable inserted in the small metal electrode. Lateral resolution is obtained by placing the sample on a moving stage.

To conclude this section, we note that 'Artificial' MIS capacitor arrangements for SPV measurements are commercially available [232–235] and are applied to many interesting and technologically important quantitative analyses which are discussed in Section 5.

3.3. Other methods

3.3.1. E-beam analysis

In Section 3.1, we noted that the SPV causes a change of equal magnitude in the surface work function, W_{S}. Therefore, *any* method for work function measurements (and not just the Kelvin probe approach) can be used for SPV measurements simply by detecting illumination-induced changes in W_{S} (a detailed discussion of such methods may be found in, e.g., [121,155,236]). Since the Kelvin probe is one of the most sensitive and accurate methods for detecting changes in W_s, most other work function

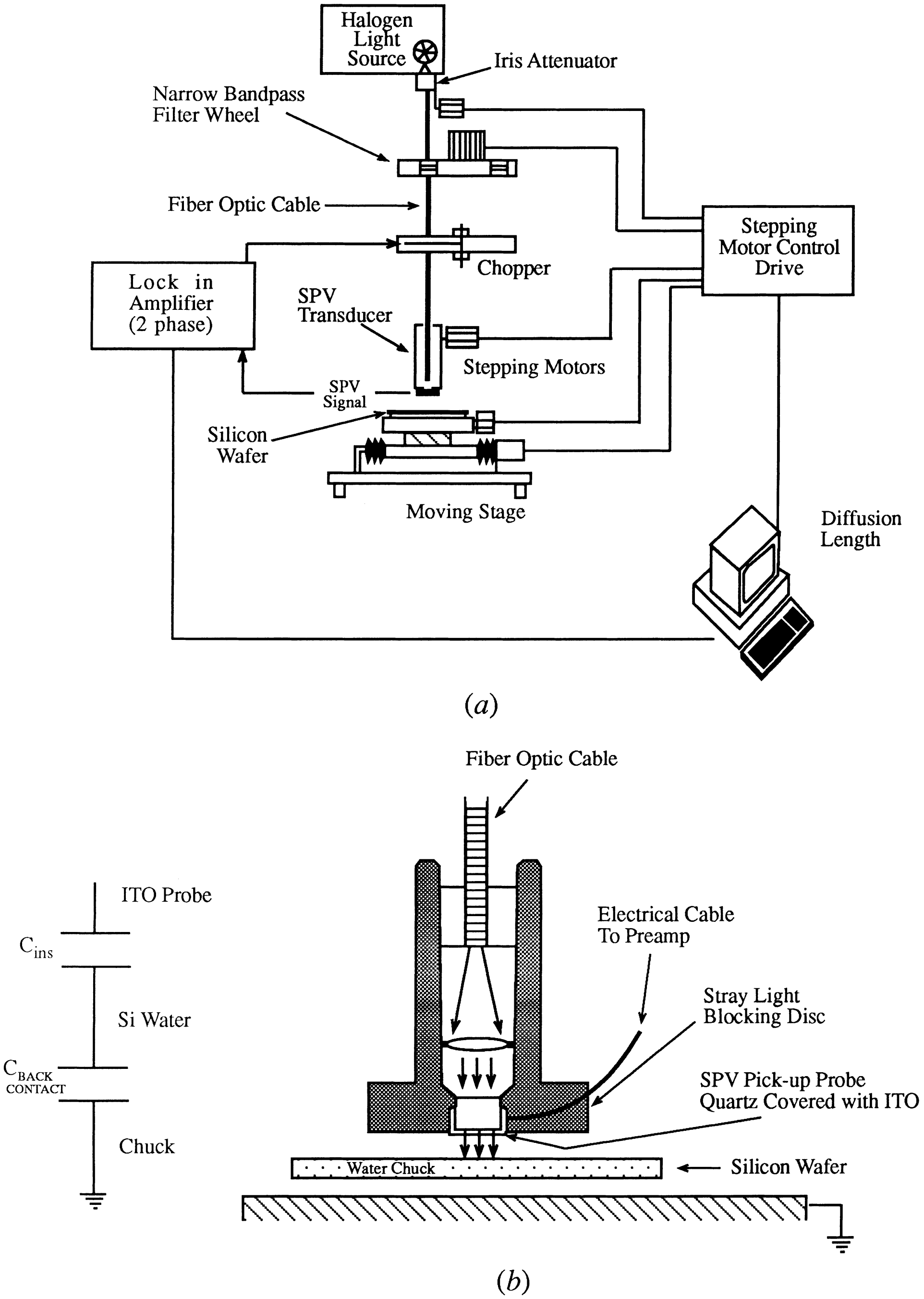
Halogen Light Source
Iris Attenuator
Narrow Bandpass Filter Wheel
Fiber Optic Cable
Stepping Motor Control Drive
Chopper
Lock in Amplifier (2 phase)
SPV Transducer
Stepping Motors
SPV Signal
Silicon Wafer
Moving Stage
Diffusion Length
(a)
Fiber Optic Cable
ITO Probe
C_{ins}
Si Water
$C_{BACK\ CONTACT}$
Chuck
Electrical Cable To Preamp
Stray Light Blocking Disc
SPV Pick-up Probe Quartz Covered with ITO
Water Chuck
Silicon Wafer
(b)

Fig. 29. (a) General schematic drawing of a SPV mapping apparatus. (b) Detailed schematic drawing of the probe head (after Lagowski et al. [12]).

techniques have not been used for SPV purposes. The only notable exception is the electron-beam method [155].

This method uses an electron gun and the sample as the cathode and anode of a vacuum diode, respectively. If an electron beam impinges on the sample, the external current, I, is a monotonous function of $W_s - V$, where V is the diode bias. Assuming no change in the functional form of this dependence, a change in W_s produces a rigid horizontal shift in the I–V curve. The difference between V values needed to sustain a certain current (in the retarding field regime of the diode) in two different samples is thus equal to the difference in W_s between the samples. This yields an (indirect) measurement of the CPD between two samples [160].

A similar rigid horizontal shift in the I–V curve should be obtained due to illumination-induced changes in W_s, where the shift is equal to the SPV. This effect has been used for SPV measurements as early as the 1950s (e.g., by Wlerick [237] and Zyrianov [238]). As an example, the I–V curves obtained from an electron gun – CdS sample diode in the dark and under super-bandgap illumination are given in curves (I) and (II), respectively, of Fig. 30, indicating an SPV of ~200 meV [239]. The current is most sensitive to variations in W_s where the slope of the I–V curve is maximal. This is demonstrated in curve (III) of Fig. 30, which shows the difference between curves (I) and (II). Steinrisser and Hetrick [239] have used chopped illumination in conjunction with a lock-in amplifier at a diode bias corresponding to the maximum sensitivity. This produced an ac diode current with an amplitude of:

$$I = I(V + \mathrm{SPV}) - I(V) \overset{\mathrm{SPV} \ll V}{=} \mathrm{SPV}\frac{\mathrm{d}I(V)}{\mathrm{d}V}. \tag{3.10}$$

Since at maximum sensitivity $\mathrm{d}I(V)/\mathrm{d}V$ may be as high as several $\mu\Omega^{-1}$, SPVs as low as 1 μV can be detected.

Despite its elegance, use of the electron-beam method has been limited. On the one hand, use of an electron-beam requires adequate vacuum, which restricts the applications of the technique. On the other hand, the 1 μV sensitivity can be matched by a well-designed MIS structure. On the positive side, the inherently small lateral dimensions of the electron-beam provide for a relatively simple solution for measuring very small samples or for performing scanning measurements. An example of the latter is

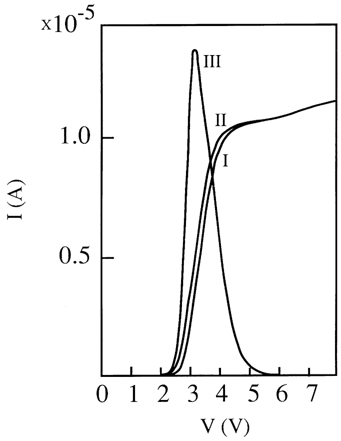

Fig. 30. Current-voltage characterics of an electron gun – CdS sample vacuum diode: (I) in the dark, (II) under super-bandgap illumination, (III) difference between the former two curves, in arbitrary units (after Steinrisser and Hetrick [239]).

the distinct correlation between the SPV distribution and the angle of inclination towards the (111) plane, found by Henzler and Clabes at cleaved Si(111) crystals. This correlation was obtained by comparing electron-beam-based scanning SPV measurements and scanning optical reflection measurements [240].

3.3.2. Photoelectron spectroscopy

Photoelectron spectroscopy (PES) is an extremely useful tool for surface chemical analysis and for elucidation of the band-structure [155,236,241]. Briefly, in PES the electrons emitted into the vacuum due to ultraviolet or X-ray radiation are studied using an electron energy analyzer. The obtained energy distribution curve (EDC) typically exhibits peaks at relatively low kinetic energies due to emission from core levels and a broad distribution at relatively high kinetic energies due to emission from the valence band. If there is no significant photoemission from surface states, the most energetic electrons are emitted from the valence band edge. This edge may be identified experimentally as a clear emission onset at the high energy end of the electron distribution. SPV-induced shifts in the position of the valence band edge are therefore manifested as changes of equal magnitude in that onset [242–246].

An example of a SPV measurement, which is based on this effect, is shown in Fig. 31 [243]. In this figure, the photoemission current from GaAs samples is recorded as a function of external bias. The electron emission high energy edge is found by locating the bias necessary to nullify the emission current. Shifts in the current–voltage curves due to additional super-bandgap illumination are clearly observed. Note that these shifts are of opposite sign for the *n*- and *p*-type samples, as appropriate.

Throughout the above discussion, we have tacitly assumed that the ultraviolet (or X-ray) radiation causes no changes in band bending by itself. This assumption is further discussed in Section 5.2.2. A further source of potential error in PES-based SPV measurements has been noted by Maragaritondo et al. [247]. Upon illumination, the EDC may change not only because of the surface photovoltaic effect but also due to a reduction in radiation-induced charging effects and/or free-carrier induced changes in the intrinsic lineshapes. These authors suggested that the presence or absence of these extraneous effects may be ascertained by monitoring photo-induced shifts in the core level peaks. These peaks shift in energy upon illumination just like the valence band edge, but their shape remains unchanged only in the case of a 'pure' SPV effect. Comparing the SPV shifts of *different* core level

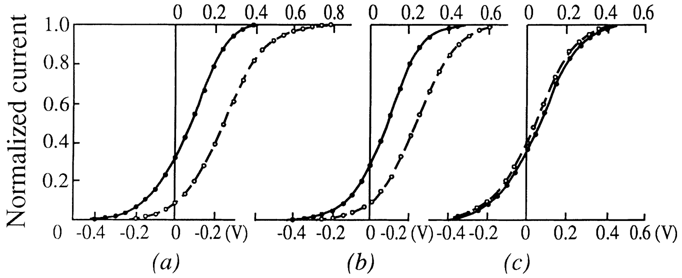

Fig. 31. Photoemission current-voltage characteristics of GaAs samples with (dashed lines) and without (solid lines) additional super-bandgap illumination: (a) $n = 4 \cdot 10^{15}\,\mathrm{cm}^{-3}$, (b) $n = 354 \cdot 10^{17}\,\mathrm{cm}^{-3}$, (c) $p = 5 \cdot 10^{16}\,\mathrm{cm}^{-3}$ (after Pao-k'un and Arsen'eva-Geil [243]).

peaks can also yield additional information. For example, Schlaf et al. studied the In adsorption on the $WSe_2(0001)$ surface and found that the SPV shift of the In 4d and W 4f features are not equal [248]. This was interpreted as indicating a laterally inhomogeneous interface, where the band bending below the In clusters was larger than that deduced from bare-area-related substrate emission.

The voltage resolution, with which the emission edge (or other spectral features in the EDC) can be determined, varies with the radiation source, the analyzer type used, and the detailed band structure of the studied sample. It is several tens of mV at best and typically 100–150 meV. This resolution is considerably inferior to that of either the Kelvin probe or the MIS structure. Moreover, if a surface of non-uniform work function is studied, the resulting SPV is *not* a weighted mean of the SPVs involved, as in the previous methods, but rather is biased towards regions in which electron emission is more significant [155].

The chief advantage of PES-based SPV determination is that it is *insensitive to changes in the surface dipole* [24]. At a first glance, it may seem odd that changes in the surface dipole, which modify the position of the vacuum level, do not change the EDC at all. However, all electrons reaching the analyzer are subject to the built-in voltage between sample and electron analyzer due to the CPD between the two, which changes their kinetic energy. Therefore, the kinetic energy of any feature in the EDC is determined by the energy difference between the level associated with that feature and the *fixed* vacuum level of the *analyzer.* Another significant advantage of PES-based SPV measurements is that its temporal resolution is in the nsec range [249]. Such values are far superior to those of MIS-based measurements, and certainly to those of Kelvin probe measurements.

The insensitivity of PES to the surface dipole (or, equivalently, to the effective surface affinity) makes it possible to directly determine the absolute value of the band bending in the dark, V_s^0: Since the back of the sample is electrically connected to the analyzer, the sample and analyzer share a common Fermi level. The electron kinetic energy corresponding to this energy may be determined by placing a metal instead of the sample since the emission edge in a metal (which has no bandgap) signifies its Fermi level. Thus, the band bending is found as the difference in kinetic energy between the emission edge of the metal and the semiconductor. An example of such a determination is given in Fig. 32 [24,250], which features the EDCs obtained at an *n*-type GaAs(1 1 0) surface with various thicknesses of Sn. The position of the Fermi level is found by observing the emission edge from the sample covered with a thick Sn film, whose EDC is governed exclusively by the Sn. The evolution of the band-bending with Sn-coverage may be monitored by observing the position of the valence band edge with respect to the Fermi level. In practice, it is advisable to follow the position of a spectral feature, whose shape does not alter with metal deposition since the edge emission may be influenced by adsorption-induced changes in surface states.

We note in passing that absolute values of band bending at III–V semiconductor surfaces have also been determined by other techniques, notably modulation spectroscopy [251] and electric field induced Raman spectroscopy [252]. To the best of our knowledge, the latter technique has not been used for SPV (as opposed to equilibrium band bending) determination. The use of the former for SPV measurements has been extremely limited. Kanata et al. have shown that if the SPV is much smaller than the equilibrium band-bending, the modulation of the dielectric function of the semiconductor, and hence the amplitude of the (normalized) modulation of its reflectance, is proportional to the SPV [253]. This has been used to assess surface-treatment-induced SPV changes, *in arbitrary units* [254]. Due to their very limited SPV usage to date, these techniques are not discussed further here. The interested reader is referred to previous review articles [251,252] for a more detailed discussion.

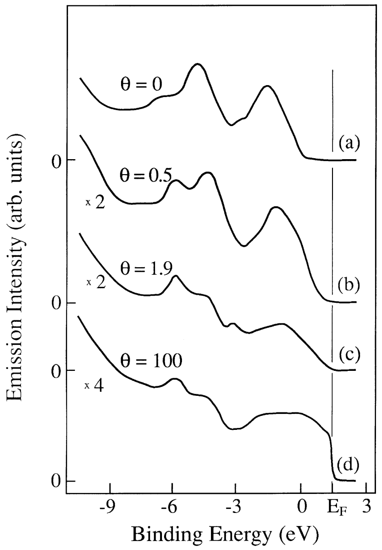

Fig. 32. Ultra-violet photoemission spectroscopy EDCs of a clean (a) and Sn-covered (b–d) n-GaAs(1 1 0) surface. The binding energy is defined relative to the valence band edge at the clean surface (after Mattern-Klosson and Lüth [250]).

3.4. *High resolution scanning techniques*

As noted above, both the scanning Kelvin probe and the scanning MIS capacitor are typically limited to a lateral resolution of $\sim 1\,\mu m$ at best, which is insufficient for many applications. Two high-resolution techniques for topographic mapping of surfaces have emerged in the 1980s [255]. Scanning tunneling microscopy (STM) is based on sensing the tunneling current between a tip and the sample. Atomic force microscopy (AFM) is based on sensing the deflection of the tip due to tip-sample forces. Both techniques have rapidly evolved and are used today for a wide range of applications [255]. In the early 1990s both have been shown to be useful for SPV measurements as well [13–15], opening new horizons for SPV mapping with a resolution previously unknown. The operation principles and capabilities of these techniques are described in this section.

3.4.1. *Kelvin probe force microscopy*

The Kelvin force microscope is a modified version of the atomic force microscope (AFM). The (contactless mode) AFM measures the deflection of a cantilever-mounted tip due to local forces exerted on the tip by the surface of the sample (e.g., van der Waals forces) [256]. This deflection is typically monitored by studying the optical deflection of a laser off the cantilever using a position sensitive detector or by a laser interferometer. Many other schemes have also been devised [256]. For topographic mapping, the tip is usually vibrated at a given frequency, ω_1. The amplitude of the forced vibration is influenced by the tip-sample forces. Using a feedback circuit which modifies the tip–sample distance so as to keep the vibration amplitude constant, the tip follows the surface topography of the sample (assuming the nature of the forces has no lateral variations).

If the AFM tip is *conducting* (e.g., an etched gold wire, an aluminum-coated silicon nitride tip, etc. [257]) and the tip and sample are electrically connected, the electric potential and field between them are well defined. Then, a vertical electric force, F, given by minus the derivative of the electrostatic energy, acts on the tip:

$$F = -\frac{\mathrm{d}}{\mathrm{d}z}\left(\frac{1}{2}CV^2\right) = -\frac{V^2}{2}\frac{\mathrm{d}C}{\mathrm{d}z}, \tag{3.11}$$

where V is the voltage between the tip and the portion of sample beneath it, C, the tip–sample capacitance, and z, the tip-to-sample distance. Martin et al. [258] used an ac voltage for V and detected the induced oscillation of the tip as a measure of F. However, mapping of F has proved difficult to translate into a mapping of V because $\mathrm{d}C/\mathrm{d}z$ is neither well known nor well-controllable. For example, $\mathrm{d}C/\mathrm{d}z$ may change due to variations in the gap dielectric constant, variations in z due to inadequate feedback control, variation in the nature of the non-electrostatic forces acting on the tip, etc. [15,259].

In 1990, Weaver et al. [15,259] have shown that Eq. (3.11) can be used for accurate surface potential mapping if V is given by:

$$V = V_{\mathrm{dc}} + V_{\mathrm{ac}}\sin(\omega_2 t). \tag{3.12}$$

Inserting Eq. (3.12) in Eq. (3.11), we obtain:

$$F = -\frac{1}{2}\frac{\mathrm{d}C}{\mathrm{d}z}\left[V_{\mathrm{dc}}^2 + \tfrac{1}{2}V_{\mathrm{ac}}^2 + 2V_{\mathrm{dc}}V_{\mathrm{ac}}\sin(\omega_2 t) - \tfrac{1}{2}V_{\mathrm{ac}}^2\cos(2\omega_2 t)\right], \tag{3.13}$$

i.e., the force acting on the tip has a dc component as well as ac components at ω_2 and $2\omega_2$. In particular, the vibration amplitude at ω_2 is proportional to the product $V_{\mathrm{dc}}V_{\mathrm{ac}}$. A mixed dc and ac bias is therefore applied to the tip in order to measure the dc surface potential of a sample. A feedback loop adjusts the dc bias between tip and sample until the ac vibration of the tip at ω_2 is nullified [15,259]. At this point V_{dc} is zero and the dc potentials of the tip and sample surface are necessarily equal. Thus, any calibration involving $\mathrm{d}C/\mathrm{d}z$ is avoided.

From a practical point of view, the voltage feedback loop can be performed simultaneously with a topographic feedback loop as they operate at different frequencies. Such a dual topography/voltage mapping arrangement is shown in Fig. 33. The topography feedback loop maintains a constant oscillation at the forced oscillation frequency, ω_1, by changing the tip–sample distance. The potentiometry loop maintains a null oscillation at the ac voltage-induced oscillation frequency, ω_2, by varying the dc bias on the tip. This simple approach has been adopted by most scientists, with several improvements and modifications suggested. Kikukawa et al. [261] have used a dual resonance cantilever so that separate optimization of the two feedback loops is made possible. Yasutake [262] noted that the dc component of the electrostatic force (see Eq. (3.13)) is inherently less local than, e.g., van der Waals forces used for topography measurements. Consequently, at each measurement point he has deactivated the probe bias during the topography measurements and increased the lateral resolution of the latter. For overcoming the same difficulty, Jacobs et al. performed a surface topography scan immediately followed by an electrical scan which retraced the same topography for each line scan [263]. In a different approach, Yokoyama and Inoue [260] have discarded the ω_1 feedback loop altogether. Instead, they based the topography measurement on a second electrical feedback loop, which maintained a constant current (and hence tip-sample capacitance) at $2\omega_2$. While simple to construct, the resulting topography map has two disadvantages: first, its resolution is reduced due to the above mentioned less local character of the electrostatic force; second, since the feedback follows

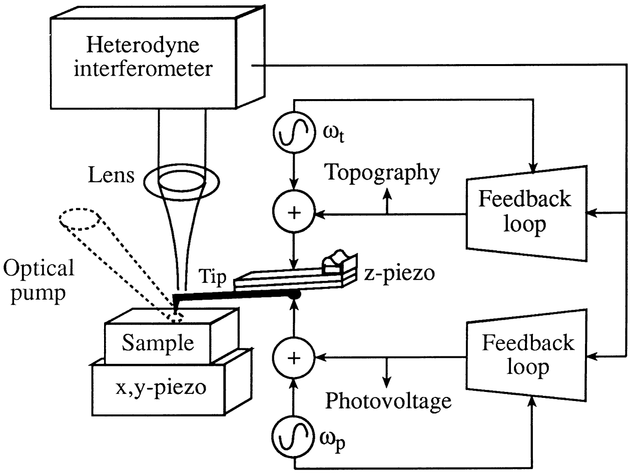

Fig. 33. Block diagram of a dual topography/potential mapping AFM-based apparatus (after Weaver and Abraham [259]).

capacitance, rather than distance changes, the topographic map would be warped, should changes in the effective dielectric constant occur (e.g., due to variations in a surface passivation layer).

We note in passing that *any* local probe, which is sensitive to both atomic and electrical forces, can be converted into a KFM. For example, Steinke et al. have recently converted an acoustic near field microscope into a surface-potential measuring device, using the same principles described here [264].

Nonnenmacher et al. [265] have shown that the above approach can be used for performing high resolution CPD measurements. This is because:

$$V_{dc} = V_{CPD} + V_b, \tag{3.14}$$

as in Eq. (3.4) above. Therefore, tip vibration at ω_2 is nullified when the applied bias is equal and opposite to the CPD. Since finding a condition at which $V_b = -V_{CPD}$ is also at the heart of the Kelvin probe, Nonnenmacher et al. [265] have coined the name ‘Kelvin force microscope’ (KFM) for their apparatus. Indeed, in many respects the Kelvin probe and the KFM are very similar devices. Both are based on finding an external bias which nullifies the CPD-induced electric field between an external probe and a sample, placed in a capacitor configuration (see Fig. 19). However, the former is based on nullifying the ac *current* in the capacitor, whereas the latter is based on nullifying the ac *force* between the capacitor electrodes. Indeed, macroscopic Kelvin-probe-like devices based on force measurements, mentioned briefly in Section 3.1 [146,148], are based on the operation principles outlined in Eqs. (3.13) and (3.14), albeit using a different force-measuring device. The similar operation principle dictates many other similarities. Both devices require adequate electrostatic shielding [257], both place similar limits on the minimum sample conductivity which can be measured, both are useful even when there is a thin dielectric layer on top of the sample [260], and both may be operated in any ambient if constructed accordingly [260,261]. For example, in vacuum measurements, the damping of the forced vibrations is reduced, resulting in long amplitude-settling times. Determination of the *frequency*, rather than the *amplitude*, of cantilever vibration, has been shown to be preferable for vacuum measurements both in terms of response time and in terms of the noise level [261].

The fundamental advantage of force measurements over current measurements is that (to first order) the latter is proportional to the probe size whereas the former is independent of it. Thus, as the size of the capacitor plates is shrunk (with all other experimental parameters being nominally the same), the sensitivity of the classic Kelvin probe is diminished and finally lost. Force measurements are not subject to the same physical limitation. Another advantage of the KFM is that deflection, rather then current, is being measured. Therefore, parasitic capacities in the external electronics which are a major problem in Kelvin probe measurements, as explained in Section 3.1, are meaningless in KFM measurements.

The major noise mechanism limiting the voltage resolution of KFM measurements is thermally induced random fluctuations in tip position [261,265]. The minimum measurable voltage corresponding to the noise level depends on many factors, e.g., tip radius and height, magnitude and frequency of the modulating voltage, and finally the quality factor of cantilever resonance and the detection bandwidth. Typically, it is in the sub-mV to 10 mV range [261,265], i.e., the KFM voltage resolution is comparable to or even better than that of a macroscopic Kelvin probe, despite its significantly smaller dimensions. For good voltage resolution, it is important to avoid the trapping of stray charges on the AFM tip. Such charges considerably modify the electric field due to the small dimensions of the tip and may alter the potential distribution significantly [259,260,265].

The spatial resolution limit of the KFM is typically several tens of nm [259,265,266]. This value is about two to five orders of magnitude better than that of most scanning Kelvin probes and one order of magnitude better than the record-resolution Kelvin probe mentioned in Section 3.1 [208]. As in the classic Kelvin probe, if the work function in the area sensed by the tip is non-uniform, the measured CPD is a weighted average of the differences CPDs present. The only difference is that in the KFM the weighting coefficients are not the capacities between the tip and areas of different work function. Rather, they are the derivatives of these capacities, as evident from Eq. (3.13) [260,263].

Due to its promise of high-spatial-resolution surface potential measurements, the KFM has found many diverse applications in just a few years. These applications include work function mapping [263,265], dopant profiling [266–268], heterojunction imaging (in both surface [269] and cross-section [263,270] modes), circuit potentiometry [259,263,271,272], characterization of Langmuir–Blodgett films [273,274], and of course SPV measurements (which are based on measuring photo-induced CPD changes). All applications but the latter are outside the scope of this review. SPV mapping using a KFM was first demonstrated by Weaver and Wickramasinghe [15], who performed SPV mapping of silicon and GaAs wafers. An illustrative example is shown in Fig. 34, which shows a photovoltage map of the (1 0 0) surface near the edge of a GaAs wafer in a (1 1 0) direction. The SPV features in the figure have been interpreted as arising from dislocations lying just below the sample surface. Thus, using the KFM information similar to that in Fig. 28 can be obtained, with a much higher spatial resolution.

Having discussed KFM principles and applications, we now describe several phenomena which are potential sources of artifacts in KFM readings and must be taken into account when interpreting experimental data: Just as the Kelvin probe, the KFM is also susceptible to systematic errors in CPD reading due to stray capacitance [263,266,268,271], as described in detail in Section 3.1. In the ideal treatment presented above, we have assumed that all capacitance is due to the tip apex only. In practice, contribution from the tip side-walls and from the cantilever can be very significant. Accordingly, spacing-dependent CPD readings have been obtained [271]. Fortunately, KFM readings are usually performed with topography-mapping, i.e., active spacing-control which reduces the variation in the CPD error is built-in [266]. CPD changes which were ‘smeared-out’ spatially and whose magnitude was smaller than the true changes by a multiplicative factor were also attributed to stray capacitance [266]. Hochwitz et al. [268] studied a model in which the main parasitic capacitance was due to cantilever-

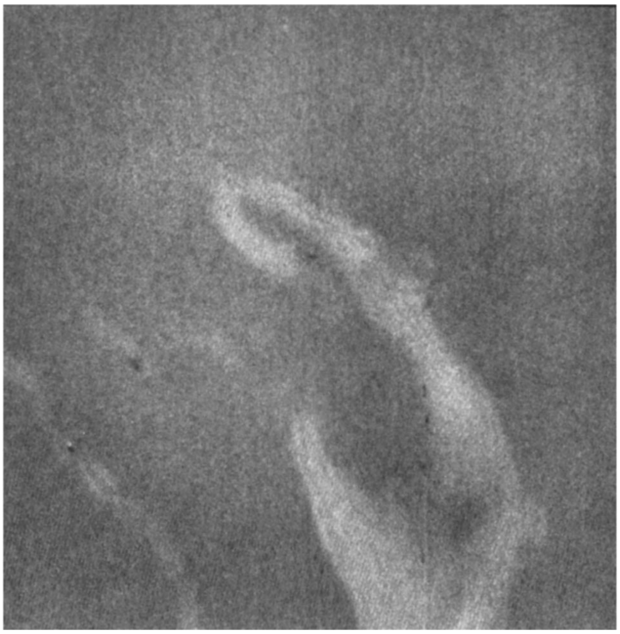

Fig. 34. SPV map of an unprocessed GaAs wafer showing dislocations. Map size: $\sim 30\,\mu m^2$; Voltage range: 55 mV (after Weaver and Wickramasinghe [15]).

sample capacitance. The ratio of desired to stray capacitance as a function of the tip to cantilever spacing and area ratios calculated by them is shown in Fig. 35. For meaningful CPD readings, the KFM must be operated on the bottom left side of the two-dimensional surface shown in the figure. As expected (and as in the Kelvin probe) a meaningful reading is harder to obtain as finer tips are used. Similar conclusions were reached by Jacobs et al [263]. In addition, if there is a significant relief in surface topography, a portion of the sample may be closer to the cantilever than expected, thereby increasing its stray effect and causing an erroneous reading [268].

Due to the close proximity of the KFM tip to the sample, a very significant field (in the order of $MV\,cm^{-1}$) can exist between the tip and sample even for tip biases of several volts [257,270]. Depending on the sample studied, such an intense field may induce Fowler–Nordheim emission from the sample. The emission may change the surface properties of the sample (possibly irreversibly). It is therefore recommended to study the $I-V$ characteristics of the tip–sample system in order to estimate the voltages at which this effect is insignificant and to restrict KFM measurement to that range.

Another source of potential trouble is unique to CPD measurements of *semiconductors*. As in all methods in which a metal is in proximity to the sample surface, it is related to the possible effect of the tip on the surface band-bending of the semiconductor, due to a MIS-like effect (see Fig. 20 above). In that figure, we have shown that for a classic Kelvin probe this effect is ‘automatically’ canceled by a dc bias which is equal and opposite to the CPD. However, there is a fundamental difference between the Kelvin probe and the KFM. In the latter, an overall ac bias between tip and sample is present even when the overall dc bias is zero. Indeed, it is this ac bias which makes the verification of a null overall dc bias possible. If the influence of this additional bias on the CPD is significant, the latter becomes time-

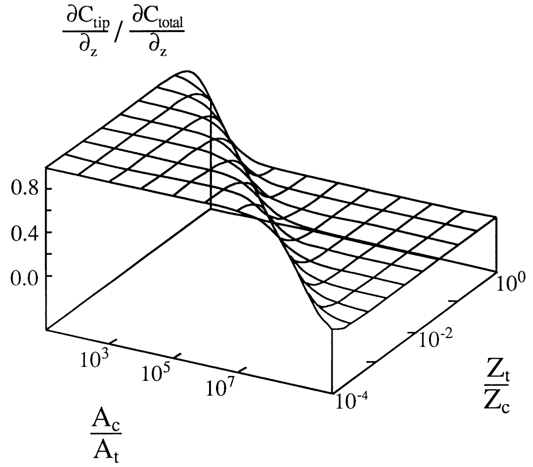

Fig. 35. Relative contribution of tip-sample capacitance to the total probe-sample capacitance as a function of cantilever/tip area and spacing ratios (A_c/A_t and Z_c/Z_t, respectively) at a topographically flat surface and a fixed tip-sample spacing (after Hochwitz et al. [268]).

dependent, i.e., Eq. (3.13) should be generalized to the form:

$$F = -\frac{1}{2}\frac{dC}{dz}\left[V_b + V_{CPD}^{Ideal} + \Delta V_{CPD}(t) + V_{ac}\sin(\omega_2 t)\right]^2, \tag{3.15}$$

where V_{CPD}^{Ideal} is the CPD in the absence of tip-induced band-bending, and $\Delta V_{CPD}(t)$ is the time-dependent tip-induced change in CPD.

If $\Delta V_{CPD}(t)$ has no dc component (i.e., if changing the polarity of V_b changes the sign of $\Delta V_{CPD}(t)$ without changing its magnitude), the force component at ω_2 remains unaffected and the CPD measurement is valid (although using the $2\omega_2$ component for topography would fail). Unfortunately, this does not have to be the case. It is well known that the bias dependence of the band bending at an MIS structure is highly non-symmetric [25]. Essentially, this is because biases of opposite polarities push the surface band bending in the opposite directions of inversion and accumulation (see Section 2.1.3). Under such conditions, the measured value of the CPD *does not* reflect its true value.

The possible effects of ac-bias-dependent CPD readings have been elegantly demonstrated by Leng et al. [270]. These authors have studied CPD variations across a cleaved cross-section of a GaAs/GaInP(disordered)/GaInP(ordered) structure. The dependence of the CPD on the ac-bias for each of the three regions is shown in Fig. 36. While the apparent CPDs at the GaAs and the ordered GaInP regions were bias-independent, the apparent CPD at the disordered GaInP region was highly bias-dependent. Leng et al. have concluded that, in the former two regions, the band-bending is pinned by surface states which screen out the tip-induced field, whereas the disordered GaInP surface is unpinned and is therefore very sensitive to the tip bias. (For completeness, we note that they have not ruled out Fowler–Nordheim effects as the cause of the bias-dependent CPD reading since they have not studied tip–sample *I*–*V* curves). More recently, ac bias-dependent KFM readings have also been obtained by Arakawa et al. [272].

It is usually convenient to work with sizable ac biases since this increases the amplitude of the measured ac force (see Eq. (3.13)) and hence the SNR. However, the results shown in Fig. 36 should

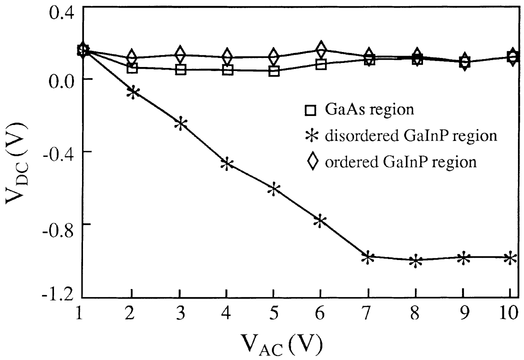

Fig. 36. Dependence of V_b^0 on V_{ac} in the three regions of a GaAs/GaInP(disordered)/GaInP(ordered) sample (after Leng et al. [270]).

caution against doing so without explicitly studying the dependence of V_b^0 on V_{ac}. On the other hand, influencing the CPD via tip-induced band-bending is not necessarily bad if one is aware of the effect. For example, the apparent CPDs of the ordered and disordered GaInP regions are practically identical for low ac bias whereas they are very different for high ac bias. Thus, in this case the tip was used for obtaining significant contrast-enhancement in the 'CPD' (or more accurately, the V_b^0) map [270].

Having discussed the KFM in some detail, we conclude this section by briefly describing a different, interesting SPV-based application of the AFM. Mertz et al. demonstrated that if the AFM *tip* material is a semiconductor, then illumination of the *tip* may change the electrical forces acting on it due to a change in its band-bending, just as in the case of illuminating a semiconductor *sample* discussed so far [275]. Thus, force measurement may be used as a local probe of illumination intensity incident on the tip and optical near field imaging may be performed. Mertz et al. used this principle to obtain imaging of an evanescent standing wave, with a lateral resolution of 170 nm. Similar measurements were recently performed by Abe et al. [276]. The latter confirmed that detection is really facilitated by a surface photovoltaic effect (rather than a photothermal effect) by studying the optical intensity and electrical bias dependence of the force modulation.

3.4.2. Scanning tunneling microscopy

Using STM, it is possible to further improve the spatial resolution of SPV measurements, theoretically down to the atomic level. This is because STM-based SPV measurements rely on some kind or another of monitoring of the tip-sample tunneling current which is highly localized. As in any STM measurement, this high-resolution mapping is feasible as long as the sample is reasonably conducting and has a well-defined surface.

The application of STM to SPV measurements was first demonstrated by Hamers and Markert [13]. Studying the Si(1 1 1)-(7 × 7) surface, they have measured the tunneling current through the tip-sample vacuum junction as a function of sample bias, with and without laser illumination. The resulting *I–V* curves are shown in Fig. 37(a). Under illumination, the *I–V* curve shifts because of the photo-induced bias, which results in a non-zero tunneling current even under zero external bias. The tunneling current is zero only when the tip and surface are at the same potential. Therefore, the external voltage applied to nullify the tunneling current must be equal and opposite to the SPV. This measurement principle is very similar to the measurement of the SPV at a semiconductor–metal junction by measuring its open-

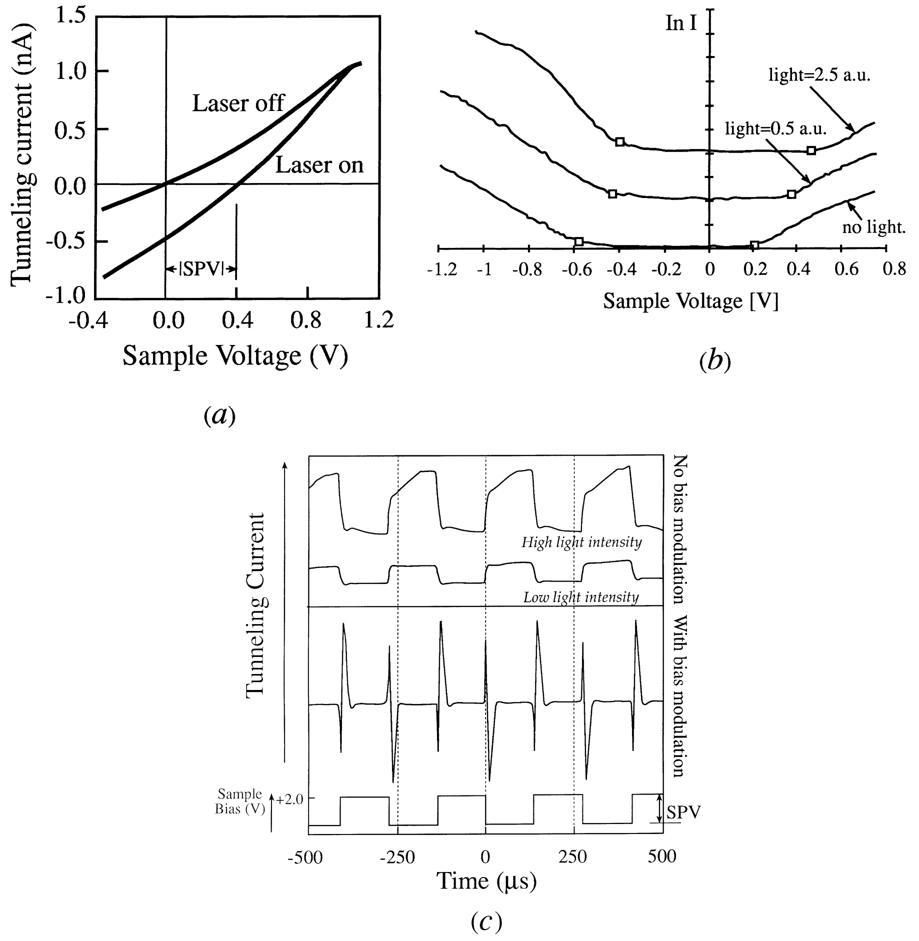

Fig. 37. Methods for STM-based SPV measurements: (a) Tunneling current vs. voltage at a p-type Si(1 1 1)-(7 × 7) surface, with and without laser illumination (after Hamers and Markert [13]). (b) I–V curves at a $WSe_2(0001)$ surface at different illumination intensities (after Möller et al. [279]). (c) Double modulation at a n-Si(1 0 0)-(2 × 1) surface (after Haase and Hamers [287]).

circuit voltage. However, here the measurement is made in a *contactless and highly localized* mode. For obtaining SPV images, the STM electronics is gated into two cycles per point of measurement. First, a feedback system adjusts the tip height to maintain a constant tunneling current. This feedback is then switched off and a voltage feedback which nullifies the tunneling current is switched on. The accuracy of the measurement is limited by illumination-induced thermal expansion of the sample and by electronic noises. Normally, the overall noise level is several mV [13].

Although elegant, this null technique suffers from several drawbacks: In the earliest measurements [13], an atomic-scale periodic variation of ~10–40 mV in the SPV was observed. Shortly thereafter, Kuk et al. [14] reasoned that this observation contradicts band-structure concepts in which variations in the photo-induced bias should have a characteristic screening length extending over many atomic sites. Therefore, it must be an experimental artifact. They have further shown that the observed SPV map bears a striking resemblance to the photocurrent map obtained at the same surface. The latter map is well-known to reflect the spatial symmetry and energy of surface states [277]. Thus, if a significant steady-state error in current nullifying occurs in the feedback circuitry, the remaining traces of the current will cause a bogus 'atomic variation' in the SPV. Indeed, use of more sophisticated feedback loops has greatly diminished the effect [14]. Geometry-dependent rectification of the optical field by the antenna-like configuration of the sample and tip has also been suggested as a parasitic source of error. This atomically periodic error in SPV maps may be responsible for the small residual variation [14]. Another demonstration of the extreme sensitivity of the null method to even the slightest variations in the null point has been given by Kochanski and Bell [278]. They have shown that if the feedback is designed so that the current is not nullified but is rather reduced to $\sim$400 fA an 'artificial' photovoltage map is produced even in complete darkness at a Si(1 1 1) : Ge surface. This map is really the potential map obtained from solving the relation $I(V) = 400$ fA.

A major limitation of the current null technique is that it assumes that the slope $\mathrm{d}I/\mathrm{d}V$ near the null point is significant so that the feedback loop can lock on to the proper value of V. However, this requires a non-negligible density of surface states through which current can tunnel close to the energy of the relevant quasi-Fermi level. The Si(1 1 1)-(7$\times$7) surface, on which the method has been demonstrated, is well known to have a sizable density of surface states throughout the bandgap [13]. However, most semiconductor surfaces do not exhibit this property. Thus, a *region* in the *I–V* curve, rather than a *point*, at which the current is negligible, is obtained, as shown in Fig. 37(b) for the case of $\mathrm{WSe_2}$(0 0 0 1) [279]. Use of the null technique in such a case typically produces a weak streaking pattern in the direction of the scan, which simply indicates accumulation of noise by the integrating feedback rather than a real SPV map [278].

If tunneling via surface states is negligible, the width of 'negligible current region' in the *I–V* curve should be equal to the bandgap of the material. Möller et al. [279] have suggested that in such a situation the shift of either 'knee' at the *I–V* curve, rather than its null point, is equal to the SPV (see Fig. 37(b)). While valid for the specific surface studied, this method also suffers from significant drawbacks. The 'flat region' in such *I–V* curves is frequently larger than the material bandgap because of additional band-bending induced by the tip bias [280]. This effect tends to decrease with increasing illumination intensity due to increased free carrier screening of the bias-induced field. Consequently, photovoltaic shifts in the *I–V* curves may become difficult or impossible to separate from screening-induced shifts [281].

Cahill and Hamers have proposed and used a double modulation technique for measuring surfaces exhibiting a 'dead region' in their *I–V* curves [282–286]. In their approach, the tunneling current is alternatively modulated by periodic illumination and by an electrical ac modulation bias. The SPV measurement is based on assuming that the change in current is the same as would be obtained if an equal electrical bias were used. If, additionally, the *I–V* dependence is linear, then the SPV can be calculated from the ratio of the photo-induced tunneling current and the electrically induced tunneling current. In practice, a small signal electrical bias is used and the SPV is calculated using the relation:

$$\mathrm{SPV} = CI_{\mathrm{ph}}(\mathrm{d}I/\mathrm{d}V)^{-1}, \tag{3.16}$$

where I_{ph} is the photo-induced tunneling current, $\mathrm{d}I/\mathrm{d}V$ is the differential conductance, and C is a constant which compensates for the different wave-forms of the optical and electrical signals. This technique can be applied at any dc electrical bias between the tip and sample and may therefore always be operated outside the 'dead region' of the *I–V* curve. The real *I–V* response is clearly non-linear and may render Eq. (3.16) invalid in the general case. For the specific cases studied, it has been estimated to introduce an error of only several percent [285,286]. The major disadvantage of this technique is that all measurements are conducted in the presence of a finite photo-induced tunneling current. This current can charge the surface and is discussed in more detail below.

McEllistrem et al. [280] have suggested a synchronized null method. At a fixed dc bias, chopped illumination which results in a modulated photocurrent is applied. Then, an ac bias which is synchronized with the illumination is applied so as to nullify the modulation in the photocurrent. The synchronized null enjoys the advantages of the regular null technique but circumvents the difficulties associated with the 'dead region' in the *I–V* curve, due to the added ac bias. An example of the application of this technique to a *n*-Si(1 0 0)-(2 × 1) surface is shown in Fig. 37(c) [287]. With no ac bias and low illumination intensities, a clear modulation of the photocurrent is observed. With the proper ac bias, the ac current is nullified, except for current 'spikes' which result from capacitive coupling of the ac bias and are irrelevant. At high illumination intensities, the tunneling current features two time constants – a short one, associated with the electronic response, and a long one, associated with sample heating. Clearly, nullifying the current *after the short time constant only* should be used in such a case.

It is very important to realize that *all four* STM-based SPV measurement techniques are prone to influence from the measurement tip. In both the simple and the synchronized null schemes, an electric field exists between sample and tip due to the CPD between them and/or the applied bias. This field may affect the surface potential of the sample. Due to the feedback loop, the overall (internal and external) voltage drop between tip and sample remains constant upon illumination. Using Eq. (2.41), this implies that Q_m, the metal charge, is constant, and hence the interference of the tip is limited to a change in V_s^0, as in the case of the MIS structure. The situation is quite different for the other two techniques. We have already discussed how tip-induced biases can hamper the analysis of shifts in the *I–V* curves. In the double modulation technique, in addition to the possible surface charging mentioned above, the tip-to-sample voltage drop (and hence Q_m) does not remain constant upon illumination. This may further change the acquired SPV with respect to that present in the absence of the tip. Therefore, any discussion of obtained SPV features cannot be separated from an evaluation of possible interference of the measurement technique.

Having fully examined the principles, advantages, and disadvantages of STM-based SPV measurement techniques, we turn to examin the spatially-resolved information which can be extracted using these tools. Hamers and Markert [13] and Kuk et al. [14] have observed atomic-scale spatial changes (i.e., with a diameter of several tens of Å) in the SPV at the Si(1 1 1)-(7 × 7) surface using the simple null technique. An example is shown in Fig. 38. Both groups have argued that such a well-resolved feature should be produced by a trap-related local variation in band bending and/or recombination rate. This is because the surface Debye screening length at the surface-state rich surface is expected to be significantly shorter than that of the bulk. This is a result of the high density of surface states, of surface segregation of the dopant, and of enhanced screening due to the photocarriers. However, subsequent measurements of clean, Ge-adsorbed [278], Ag-adsorbed [283], and K-adsorbed [284] Si(1 1 1)-(7 × 7), Si(0 0 1) [282,285], and Si(1 1 1)-(2 × 1) [286] surfaces produced microscopically uniform SPVs unless charging effects, due to finite tunneling currents, were present. The latter point is well-demonstrated in Fig. 39 [282] which clearly shows how all spatially-resolved SPV features obtained at an *n*-Si(0 0 1) surface using the double modulation technique are strongly reduced as the tunneling current is decreased. This is not necessarily a disadvantage of the double modulation technique. While originally a 'parasitic effect', the finite current enhances local-defect-induced SPVs and thus provides much new information.

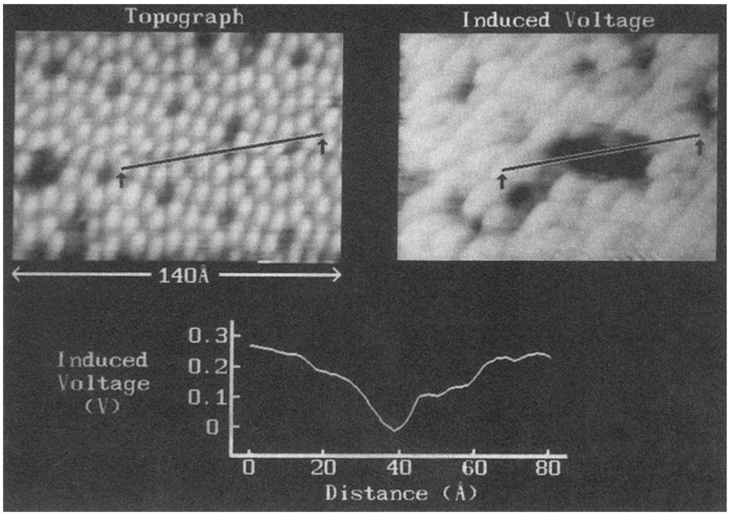

Fig. 38. An STM topograph of a Si(1 1 1)-(7 × 7) surface and a simultaneously obtained photovoltage image of 120 × 90 Å^2, along with a cross-sectional view of the photovoltage distribution along the solid line (after Kuk et al. [14]).

McEllistrem et al. [280] have shown that spatially-resolved SPV features may also stem from a spatially-resolved tip-induced bias. To that end, they have studied three prototypical Si surfaces, which are strongly pinned [(1 1 1)-(7 × 7)], moderately pinned [(1 0 0)-(2 × 1)] and unpinned [(1 1 1) : H] using

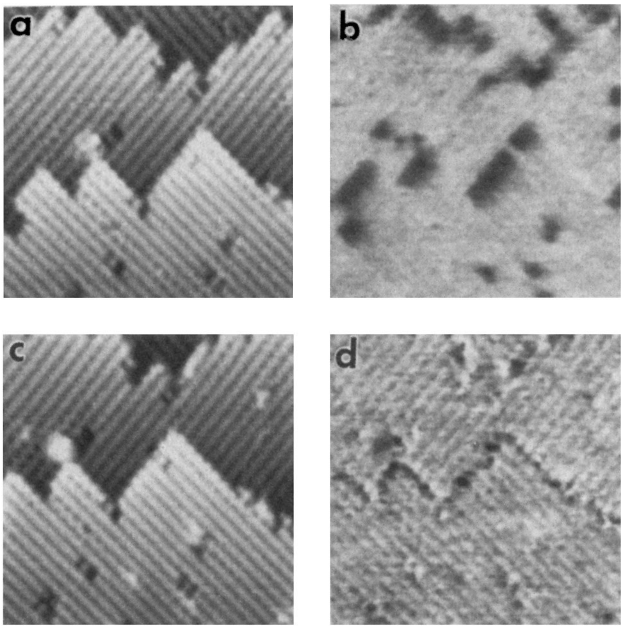

Fig. 39. Topography (left) and SPV (right) maps obtained at an n-Si(0 0 1) surface using the double modulation technique at a current of 0.4 nA (top) and 0.15 nA (bottom). Map size: 200×200 Å^2 (after Cahill and Hamers [282]).

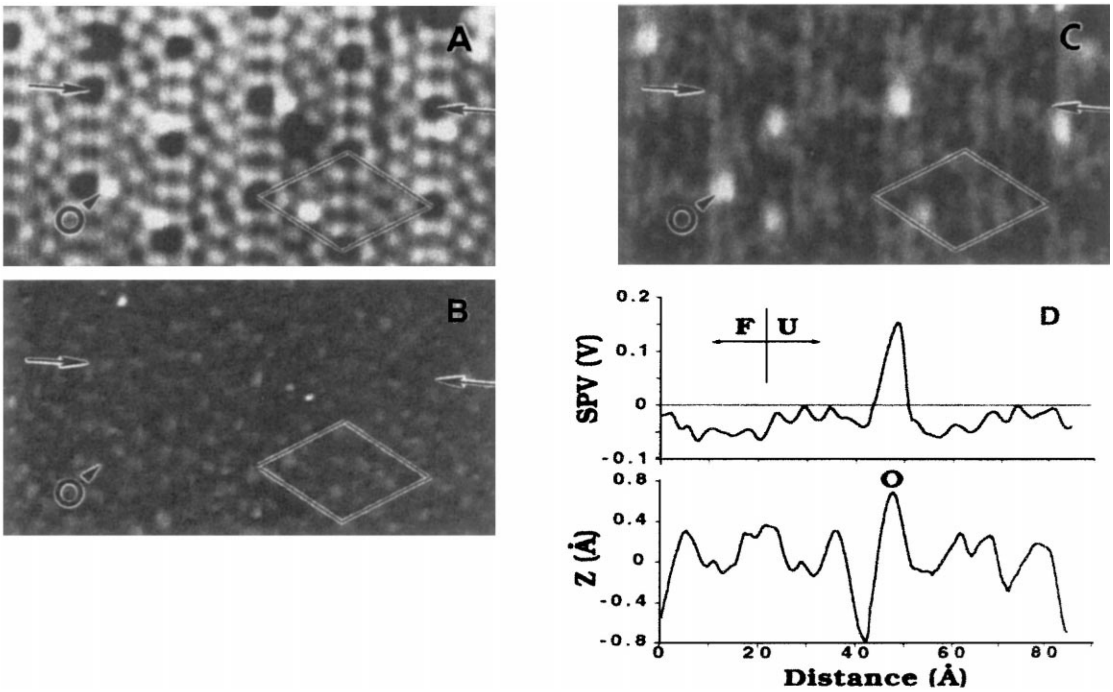

Fig. 40. Topography and SPV maps obtained at a *p*-Si(1 1 1)-(7 × 7) surface after exposure to ~0.1 L of O_2. "O" indicates an oxygen atom. (A) Topography at a sample bias of +2.0 V. (B) SPV at a sample bias of +0.5 V. (C) SPV at a sample bias of +2.0 V. (D) Line scan of SPV and topography measured between the arrows indicated in (A) and (C). 'F' and 'U' correspond to the the faulted and unfaulted parts of the unit cell (after McEllistrem et al. [280]).

the synchronized null approach. First, they have shown that, as expected, the influence of (dc) sample bias was negligible, moderate, and high, for the above mentioned three surfaces, respectively. Consequently, they have taken an SPV map of the (1 1 1)-(7 × 7) surface exposed to ~0.1 L of O_2, as shown in Fig. 40. While at a low sample bias the SPV is quite uniform, at a high enough sample bias a well-resolved increase in SPV is clearly correlated with adsorbed oxygen atoms. These authors have argued that oxygen adsorption locally removes the pinning surface states and thus makes it easier for the tip-induced electric field to alter the local band bending.

Currently, while there is no conclusive evidence of a 'pure' highly localized SPV feature, there is also no fundamental reason why such features could not be present at some surfaces. However, as in the KFM, tip-induced SPV features, such as those apparent in Figs. 39 and 40, are not necessarily worthless, if they are properly analyzed. Specifically, they are an excellent source for direct and spatially-resolved information on the electronic properties of surface defects.

4. Basic surface photovoltage spectroscopy

In elementary surface photovoltage spectroscopy (SPS), one studies the SPV as a function of incident photon energy. Useful information about important semiconductor properties may be extracted using a simple and qualitative analysis of the ensuing spectra. These properties include, but are not limited to, the semiconductor bandgap energy and type and its (surface and bulk) defect states. Since its introduction in the early 1970s, such simply analyzed SPS has been applied to practically all of the important semiconductor materials. These include: Group IV semiconductors – Si [100,288–301], Ge [302], a-Si:H [303–307], and recently porous-Si [308–316] and C_{60} [317,318] semiconducting films; III–V semiconductors – GaAs and related materials [102,290,319–346], InP and related materials [20,21,108,324,341,347–357], InSb [358], GaP [290], and recently GaN and related materials [359,360]; II–VI semiconductors – CdS [6,99,101,361–375], CdSe and related materials [370,373,375–380], CdTe and related alloys [381–396], ZnS [397], ZnSe [113,398], and ZnO [6,374,399–401]); other, more exotic semiconductors – $Cu(In,Ga)Se_2$ [402–404], TiO_2 [405,406], Zn_3P_2 [349,407], t-Se [408] and various organic semiconductors [409–414] and overlayers [299–301,307,357,369,374,401,406]. (Note: the references also include SPS studies of films and heterostructures, the discussion of which is deferred to Section 5.5.)

SPS has found significant uses in the fields of surface electronic structure and surface reactions, metal-semiconductor interfaces, bulk defects, process control, and more. In this section, the methodology of elementary SPS is presented in detail and is illustrated by numerous selected applications.

4.1. Bandgap energy and semiconductor type

The first application of elementary SPS we discuss is the approximate determination of the semiconductor bandgap. In most semiconductors, there is a large increase in the absorption coefficient near the bandgap energy, E_g. Therefore, a significant SPV increase is to be expected at approximately this energy. Such a simple E_g extraction is nothing more than an emulation of absorption spectroscopy. However, as opposed to transmission measurements, in SPS analyses the sample can be arbitrarily thick and it does not have to be removed from the substrate or grown on a transparent one.

As an example where these principles have been applied towards process control, consider the polycrystalline CdTe, CdZnTe, and CdMnTe thin films, intended for photovoltaic applications, studied by Rohatgi et al. [381]. In Fig. 41(a), a clear onset of the SPV signal at a sufficiently short wavelength is found in all samples studied. This onset is in very good agreement with the bandgaps of the different alloys used. Note that the cutoff edge of CdMnTe is much less sharp than that of the other samples. In this case, it is due to a non-uniform distribution of the Mn atoms within the film (as confirmed by Auger depth profiling), resulting in a distribution of alloy composition, and hence bandgap energy, in different grains. Fig. 41(b) shows the SPV spectra of CdZnTe films annealed at different temperatures: the SPV response increases without any change in the bandgap energy up to an annealing temperature of 385°C. As discussed in more detail below, this increase indicates an improvement in film quality. At 410°C, however, the SPV response is significantly reduced and a red-shift in the bandgap energy is observed. This suggests the loss of Zn from the film. Thus, SPS is successfully used for determining the optimal annealing temperature.

In a different application of this simple approach, Lagowski et al. [295] have studied the SPV response of silicon-on-sapphire films. They have discovered that aside from the fundamental Si bandgap at $\sim$1.1 eV, a second, distinct, knee in the SPV spectrum is found at $\sim$1.4 eV, which is typically the onset of significant absorption at amorphous silicon films. The second knee therefore indicates the partial amorphization of the studied films. More recently, Tong et al. [368] and Kronik et al. [380] have used SPS to monitor the well-known quantum size effect (i.e., the increase of the

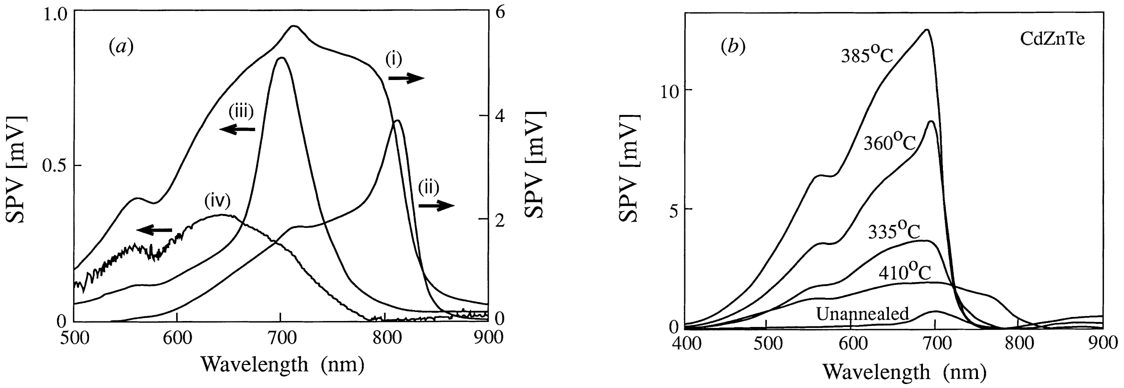

Fig. 41. SPV spectra of: (a) (i) MBE-grown CdTe (E_g=1.45 eV), (ii) MOCVD-grown CdTe (E_g=1.45 eV), (iii) MBE-grown CdZnTe (E_g=1.7 eV), and (iv) MOCVD-grown CdMnTe (E_g=1.7 eV) polycrystalline films grown on glass/SnO_2/CdS substrates. (b) CdZnTe films annealed at different temperatures in air for 30 minutes (after Rohatgi et al. [381]).

bandgap with decreasing crystallite size) at nanocrystalline CdS and CdSe quantum dot films, respectively.

While the simple analysis described above is quite useful, one must bear in mind that it is only *approximate*. In Fig. 41, the nominal bandgap is indeed within the onset of the largest SPV signal. However, this onset is relatively broad, the exact position of E_g within it is by no means obvious, and

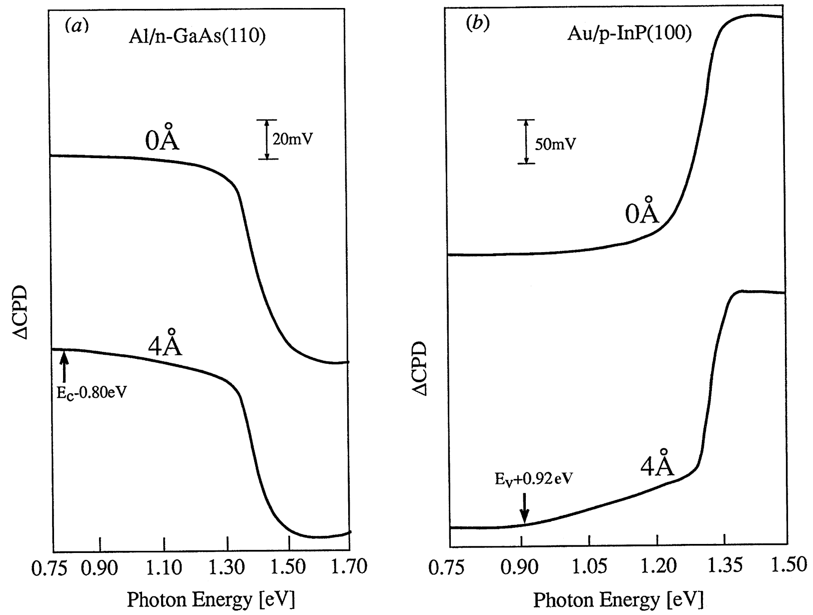

Fig. 42. SPV spectra of: (a) An n-type GaAs(1 1 0) surface, UHV cleaved (top curve) and with a 4 Å Al overlayer (bottom curve). (b) A p-type InP(1 1 0) surface, UHV cleaved (top curve) and with a 4 Å Au overlayer (bottom curve) (after Burstein et al. [324]).

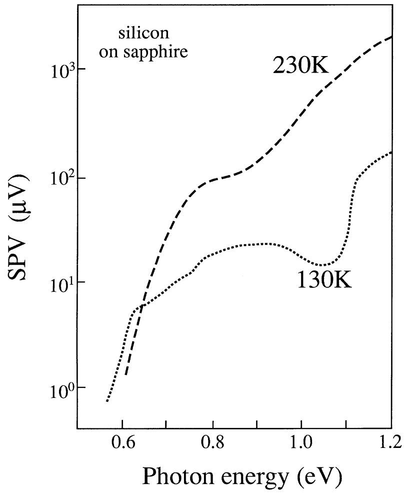

Fig. 43. SPV spectra of a silicon-on-sapphire sample at two temperatures (after Lagowski et al. [295]).

the error associated with determining E_g may be as large as 0.2 eV in some cases. This observation is true even for clean surfaces of high quality single crystals, as clearly shown in Fig. 42 [324], which features the SPV spectra of *n*-type GaAs and *p*-type InP (other aspects of this figure are discussed below).

The broad onset of the super-bandgap SPV is due to two distinct absorption mechanism for photons with an energy slightly below E_g: first, a non-negligible electric field is always associated with a significant SCR. Therefore, sub-bandgap absorption which is electric-field-assisted (i.e., the Franz–Keldysh effect, already mentioned in Section 2.2.3) is expected to blur the sharp onset of the absorption [415]. Second, photo-assisted charge transfer may take place between shallow states extending from the bandgap (also known as 'tail states') and one of the bands [295,303,316]. This induces a gap-state related SPV, as explained in Section 2.2.3, which may also blur the onset of the super-bandgap SPV. A case in point is the SPV spectra of silicon-on-sapphire samples taken by Lagowski et al. [295], shown in Fig. 43. In this case, ion implantation is known to produce both valence and conduction band tail states. At 230 K, charge transfer between the tail states, complemented by thermal emission of carriers into the bands, masks the super-bandgap SPV so effectively that the position of E_g cannot be determined at all. At 130 K, however, the thermal step, and therefore the crucial step of charge separation, are suppressed, and the E_g related onset is clearly visible. Note that the effects of sub-bandgap absorption tails are usually considerably more noticeable in SPS than in absorption spectroscopy. This is because, as explained in Section 2.2.3, SPS is inherently much more sensitive to sub-bandgap effects in the surface and SCR than absorption spectroscopy. While this inherent sensitivity is in many cases a distinct advantage, it is a disadvantage when trying to determine E_g.

Due to the near-E_g parasitic mechanisms, it is very seldom the case that a relatively accurate value of E_g can be obtained from the figure simply by inspection [327]. In fact, we are aware of only one such case [328]. Lassabatere et al. [329] suggested to use the maximum of the derivative of the SPV signal with respect to the photon wavelength as indicative of the bandgap, and obtained results of the temperature dependence of the GaAs bandgap which were in very good agreement with the literature. This approach has also been used by Kuzminski and Szaynok [387].

A mathematical analysis shows that this procedure is justified if sub-bandgap absorption decays exponentially below the bandgap energy [416] (and the SPV spectrum closely follows the absorption spectrum [417] – see below). However, the position of the derivative maximum may considerably deviate from E_g in the presence of a significant Franz–Keldysh effect [98] or an arbitrary distribution of tail states. For example, Lagowski et al. determined that a structure in the *second* derivative of the SPV spectrum, near the bandgap energy of GaAs, was actually due to residual impurities [333]. This was accomplished by observing that this structure is independent of an applied magnetic field. It has been our experience that the error associated with E_g determination is frequently (but not always) improved to a several tens of meV at most when using the derivative approach on single crystals. Usually, we have found no improvement in accuracy when applying the same procedure to polycrystalline samples.

With the non-ideal mechanisms cited, E_g should no longer be treated as an outstanding numerical threshold. Rather, it should be treated as a fitting parameter (albeit a very important one), as usually done when interpreting absorption spectra. In order to apply such an approach to SPS data, it is important to consider how well SPV spectra are expected to resemble absorption spectra. Detailed experimental comparisons between SPV and absorption spectra reveal that the two are often similar, but never identical [102,409,410]. Let us consider the sources of this discrepancy: first, the SPV is proportional to the excess carrier density only for a low enough injection of excess carriers, δn (see Eq. (2.57)). For higher injection levels, a sub-linear dependence of SPV on δn is expected (see Section 5.2 below). The increase of the absorption coefficient, α, with increasing photon energy, increases the injection level and may therefore decrease the SPV/δn ratio. Consequently, the rise of the SPV with increasing photon energy may be slower than that of α. We note that δn is typically proportional to the illumination intensity, I (see Eq. (2.61)). Thus, the attainment of an injection level which is low enough to assure a constant SPV/δn ratio, may be ascertained experimentally by means of examining the linearity between the SPV and I.

While a low I is a necessary condition for a meaningful comparison between SPV and absorption spectra, it is *not* a sufficient one. Using Eq. (2.61), it is easy to see that the SPV is proportional to the absorption coefficient, α, only if the condition $\alpha L \ll 1$ is satisfied [290,333]. In many cases, the absorption coefficient increases with increasing photon energy, so that this condition is ultimately violated. Thus, the SPV/I ratio decreases with increasing photon energy. This is another reason why, while α typically increases with increasing photon energy, the SPV may (following its super-bandgap onset) increase at a much slower rate or even reach a plateau (as in Fig. 42), depending on the ratio between α and L.

Yet another reason for the difference between SPV and absorption spectra has to do with the relation between δn and I. Eq. (2.61) predicts a monotonous dependence of the SPV on the absorption coefficient. However, this equation is only an approximation which assumes an effective SRV rather than considering SCR effects in detail. A more rigorous analysis [325] shows that if, e.g., the surface barrier is not too high and a significant recombination flow is directed toward the surface, increasing α may actually *decrease* the SPV signal. This is because as the free carriers are generated closer to the surface, surface recombination becomes more dominant, the net excess carrier density is diminished, and the resulting SPV signal is decreased. Accordingly, SPV versus photon energy spectra have been observed to change from monotonically increasing to displaying a maximum upon, e.g., hydrostatic pressure which increased the SRV [327], or background white light which reduced the barrier height [325]. A very pronounced peak is found in the SPV spectrum corresponding to the MOCVD-grown

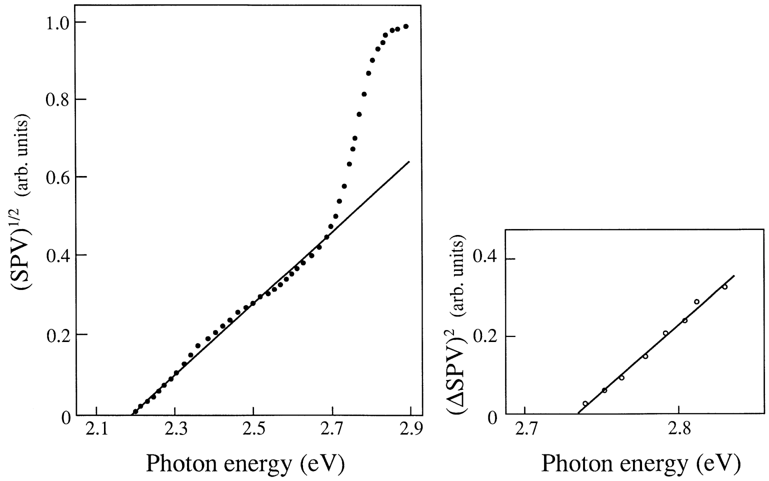

Fig. 44. SPV spectra of a GaP(1 0 0) surface: (a) Extrapolation of the indirect bandgap. (b) Extrapolation of the direct bandgap following the subtraction of the indirect bandgap contribution (after Adamowicz and Szuber [290]).

CdTe sample in Fig. 41(a). The drastic difference between the SPV spectra of the MOCVD- and MBE-grown CdTe films in this figure can therefore be assigned to major differences in sample parameters, such as the surface barrier, the SRV, and the diffusion length (a detailed study of these differences would require quantitative analysis). We note that while a peak in the spectral response is ubiquitous in photoconductivity spectra [418], it is much less frequent in SPS curves. This is because the photocurrent directly reflects the overall excess carrier density whereas the SPV is a much weaker function of it.

If experimental conditions are such that the super-bandgap SPV is indicative of absorption, E_g may be reliably extrapolated [290,304,328] using the simple relations:

$$\text{SPV} \sim \alpha \sim (h\nu - E_g)^2 \quad \text{for indirect gap semiconductors,} \tag{4.1a}$$

$$\text{SPV} \sim \alpha \sim \sqrt{h\nu - E_g} \quad \text{for direct gap semiconductors.} \tag{4.1b}$$

An application of this procedure to GaP is shown in Fig. 44 [290]. First, the indirect energy gap is determined by fitting Eq. (4.1a) (Fig. 44(a)). The indirect-absorption contribution to the SPV is then subtracted out and the remaining SPV is attributed to direct-gap transitions. Finally, the direct bandgap is determined by fitting Eq. (4.1b) to the remaining SPV (see Fig. 44(b)).

We now turn our attention to determining the type (*p* or *n*) of the semiconductor. This may be achieved with the help of the *sign* of the knee associated with the SPV onset. Most semiconductor surfaces are either depleted or inverted, which means that the bands of *p*-type semiconductors are bent downwards towards the surface, whereas the bands of *n*-type semiconductors are bent upwards. As explained in the Section 2.2.2, super-bandgap illumination typically tends to decrease the surface band-bending. Due to the different signs of the equilibrium surface potential, this would result in a positive SPV in *n*-type semiconductors and a negative SPV in *p*-type semiconductors. For example, the SPV spectra of *n*-type GaAs and *p*-type InP, shown in Fig. 42, clearly feature opposite onset signs. Note that in this figure, as well as in some of the following ones, changes in the CPD, rather the SPV, are plotted,

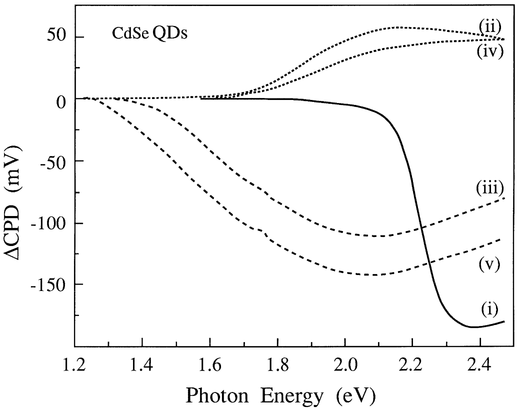

Fig. 45. SPV spectra of a 4.5 nm crystallite size, CdSe quantum dot film after the following sequence of treatments: (i) as-deposited, (ii) after etching, (iii) in a dry ambient, (iv) in a humid ambient, and (v) in a dry ambient – second cycle (after Kronik et al. [380]).

for the purpose of adhering to the original data. According to Eq. (3.1), changes in the CPD are of opposite sign than those of the SPV.

While in many cases the type of the semiconductor is known a priori, this is not always the case and SPS can become very useful in determining the semiconductor type. This is highlighted by several recent examples: first, SPS studies on free-standing porous-Si films made from p-type Si revealed that the films may be of either conduction type, depending on the resistivity of the Si substrate used [316]. Second, etched CdSe quantum dot films were found to exhibit a p-type response in a humid ambient and an n-type response in a dry ambient, as shown in Fig. 45 [380]. We note that the SPV onset in Fig. 45 is relatively broad, indicating an inhomogeneous layer, as in Curve (iv) of Fig. 41(a). Here, it is attributed to a distribution in crystallite sizes which results in different magnitudes of the quantum size effect. Third, SPS was used for fast and non-destructive verification of the semiconductor type in GaN films [359]. This is very important because the p-doping of GaN is known to be non-trivial and subject to compensation by the native n-type doping.

The distinction between n- and p-type samples is not without limitations either: if the SCR is not in significant depletion or inversion, but rather in significant accumulation, the sign of the SPV is expected to reverse (see Fig. 2). For example, Musser and Dahlberg studied an organic semiconductor known to be n-type [410]. However, judging by the SPV sign rules given above the sample would have been branded as p-type. These authors therefore concluded that the surface is in accumulation, as previously found for other, p-type organic semiconductors.

If the band-bending is small, such that the SCR is neither in significant depletion nor in significant accumulation, the Dember contribution may dominate over the band-bending-related contribution. For charge separation due to different carrier mobilities (see Section 2.2.4), the sign of the SPV would always be n-type-like. For a Dember contribution due to preferential trapping, the sign would depend on the type of carrier trapped. In either case, this would have nothing to do with the sample type. Such phenomena have been frequently observed when studying surfaces with a small band-bending [302,348,352,419]. For example, the etched CdSe quantum dot films mentioned above were found, using PES, to remain n-type at all times in terms of the position of the Fermi level. The ambient sensitivity of the 'type conversion' shown in Fig. 45 (as well as other evidence) suggest that the SPV

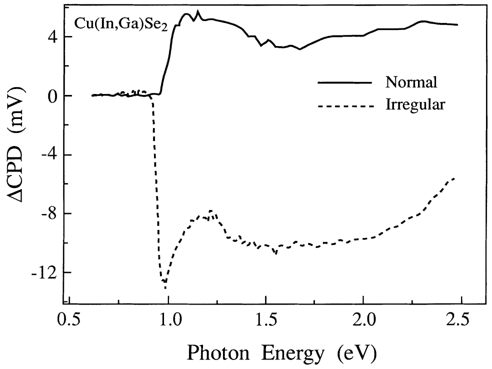

Fig. 46. SPV spectra of Cu(In,Ga)Se_2 polycrystalline films: a typical response and an irregular response (after Kronik et al. [404]).

signal is primarily due to the Dember effect caused by preferential trapping of holes or electrons in a dry or humid ambient, respectively.

Very significant sub-bandgap absorption may also make determination of the true type of the sample more difficult. The upper curve in Fig. 46 [404] features the usual SPV response obtained from *p*-Cu(In,Ga)Se_2 polycrystalline films. It shows a positive CPD change near the Cu(In,Ga)Se_2 bandgap energy, as expected. In an irregular sample, a considerable negative CPD sub-bandgap signal (probably associated with surface states), is obtained. This signal is larger than the bandgap response, causing a change in the sign of the *overall* super-bandgap response. Therefore, assessing the sample type based on the SPV at a single super-bandgap photon energy would lead to erroneous conclusions. However. the sign of the bandgap-related *knee* has not altered, so that by using the entire spectrum it is clear that the irregular sample is also *p*-type.

It has already been noted in Section 2.2.1 that an SPV signal depends on both photon absorption and charge separation. So far we have shown how to use the former for determining E_g and the latter for determining the sample type. More information on both absorption and transport properties can be extracted from the near-bandgap region of SPS data. Let us review some notable examples. Based on absorption considerations, excitonic effects can be observed at low enough temperatures [239,367]. If the samples are very thin, an interference pattern emerging in the super-bandgap region may be used for determining the thickness of the sample [295]. Based on transport considerations, Lagowski et al. [327] studied Γ–X valley scattering via the dependence of the SPV spectrum on hydrostatic pressure. Morawski and Lagowski [326] measured the SPV spectra of GaAs samples at liquid helium temperatures, as shown in Fig. 47. The resulting spectra feature an oscillating behavior with two series of distinct minima. These minima were related to resonant emission of phonons by electrons photo-excited from the heavy-hole band, with the two bands corresponding to surface and bulk phonons.

We conclude this section with another example in which both absorption and transport considerations are used. Liu et al. [299] have studied the SPV spectra of a Si(1 1 1) substrate, on which a CuTsPc Langmuir–Blodgett film with a varying number of layers was deposited. Their results are shown in Fig. 48. Two absorption peaks (at energies above the Si bandgap), characteristic of the Langmuir–Blodgett film, are clearly visible. These peaks are not present in the SPV spectrum of the bare Si surface (not shown). Transport information is revealed by considering that the magnitude of the SPV response *decreases* with an increasing number of film layers. Liu et al. argued that this indicates that the

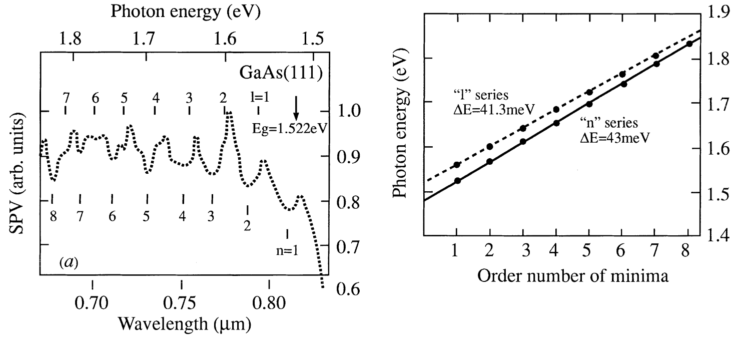

Fig. 47. (a) SPV spectrum of a GaAs(1 1 1) surface at liquid helium temperature. (b) Energies of SPV minima vs. their order number (after Morawski and Lagowski [326]).

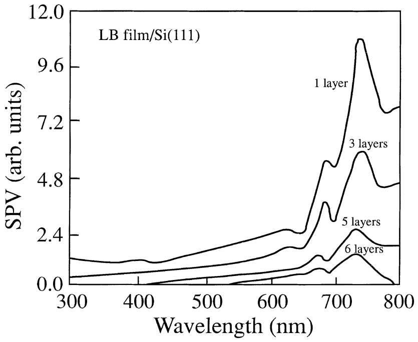

Fig. 48. SPV spectra of a Si(1 1 1) substrate covered with a CuTsPc Langmuir-Blodgett film of varying thickness (after Liu et al. [299]).

observed SPV is mainly due to charge transfer between the first layer and the Si substrate, which changes the band bending in the latter. Although electron–hole pairs are also created in the other film layers, their transport is apparently ineffective. The additional layers therefore produce a very small photovoltaic contribution, but their non-negligible absorption acts as a filter which reduces the overall signal. We note that a reduction of the surface band-bending must also be examined as a possible cause of some of the signal reduction.

4.2. Gap state spectroscopy

In Section 2.2.3, we have shown how photons may excite charge carriers from a surface state to a band, if the photon energy is greater than the surface-state to band energy separation. Therefore, we expect a knee in the SPV spectrum whenever the photon energy exceeds the threshold energy of a certain transition. If the latter involves excitation of electrons from the surface state to the conduction band (Fig. 14(a)), a positive change in the surface charge is induced, and hence a positive SPV (or, equivalently, a negative change in CPD) is expected. Conversely, excitation of holes to the valence band (Fig. 14(b)) makes the surface charge more negative and a negative SPV is expected. Thus, the combination of surface state threshold energy and sign make the determination of the approximate

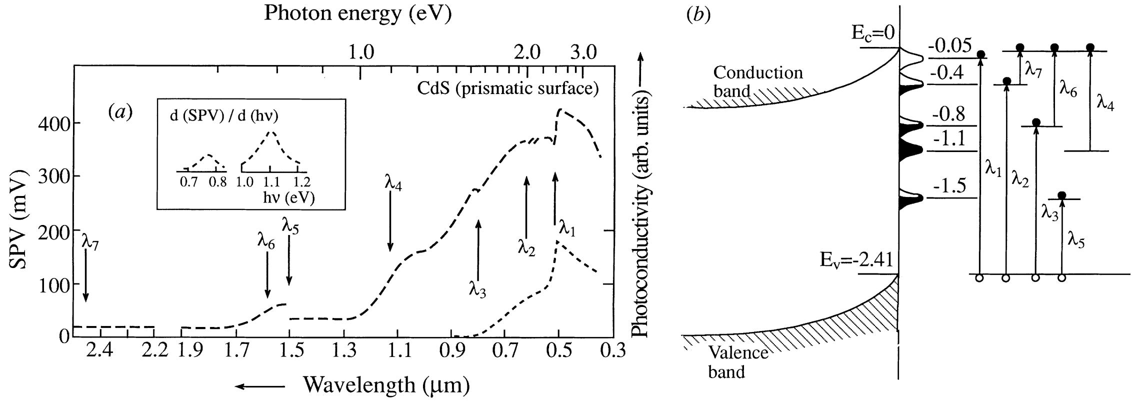

Fig. 49. (a) SPV (solid line) and photoconductivity (dashed line) spectra of a prismatic CdS surface in air. Inset: derivative of the SPV spectrum with respect to the photon energy. (b) Schematic representation of surface states and electron transitions associated with the SPV spectrum (after Lagowski et al. [361]).

position of the surface state within the bandgap possible. As a first illustrative example, let us consider how SPS can be used to monitor metal-induced surface states, as shown in Fig. 42 [324]. After cleaving in UHV, neither the GaAs(1 1 0) nor the InP(1 1 0) surfaces display any knees associated with deep surface states, as expected for these surfaces. However, upon deposition of a very thin metallic overlayer, distinct sub-bandgap knees emerge. These knees, associated with a negative and positive CPD change at the Al/GaAs(1 1 0) and Au/InP(1 1 0) interfaces, respectively, indicate the formation of a surface states situated approximately 0.8 eV below the conduction band edge and 0.9 eV above the valence band edge, respectively.

In Fig. 42, both surface state transitions found are associated with the emission of majority carriers from the surface state into the SCR. As explained in Section 2.2.3, transitions associated with emission of minority carriers are less frequently observed due to the unfavorable direction of the electric field in the SCR. Nevertheless, they are not uncommon. This is readily observed in one of the earliest SPV spectra (of a prismatic CdS surface in air), shown in Fig. 49(a) [361], which features many knees, of both signs. The surface states and associated electron transitions found using SPS are shown schematically in Fig. 49(b). The ability to identify the band with which charges communicate and therefore correctly position the surface state in the gap is a unique feature of SPS. Indeed, SPS has been used to reinterpret the results of other techniques, e.g., photoluminescence [360,363] or surface conductivity [292] measurements, which resolve the threshold energy of different transitions, but not the band involved.

Since SPS is contactless and non-destructive, it can be applied not only to clean surfaces, but also to real ones, in practically any ambient. Therefore, since its earliest days SPS has been used for determining ambient effects on surface state properties. Changes in SPV spectra with the degree of vacuum [99,361] or following a prolonged storage period [100] were detected. SPS was also immediately put to use in discerning differences in electronic structure between different real surfaces of the same material. For example, the SPV spectra of prismatic CdS surfaces were found to be very different than those of basal surfaces [361]. More recently, Burstein et al. suggested that the very different SPV spectra of the CdTe(1 1 1)A and (1 1 1)B surfaces may be used as a means of *contactless* distinction between the two, as opposed to the usual etch-based distinction schemes [385].

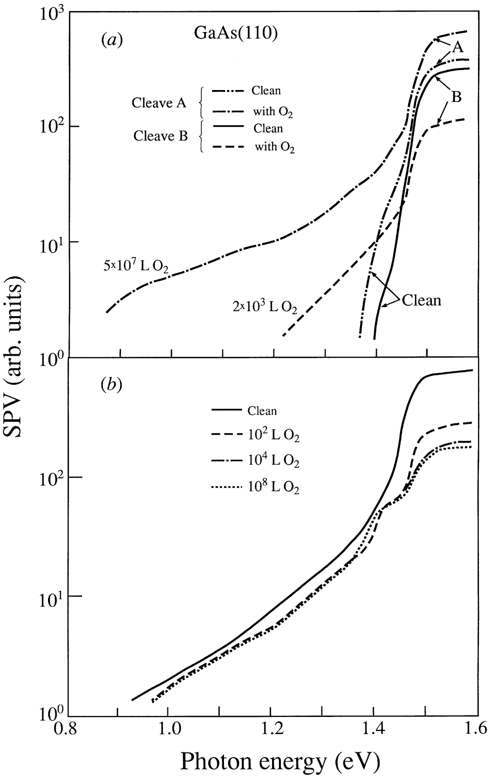

Fig. 50. SPV spectra at 100 K of the clean and oxygen-exposed GaAs(1 1 0) surface after exposure to different oxygen doses. (a) 'Good' cleave. (b) 'Bad' cleave (after Lüth et al. [336]).

SPS has found much use in studying the impact of adsorption processes in a gaseous ambient and the effects of chemical reactions between semiconductor and gas. The most favorite topic of such investigations was the oxidation of, or oxygen adsorption on, Ge [302], Si [292,297], a-Si:H [303], GaAs [322,336], InP [350,352], CdS [101,363,364], CdSe [375,376], ZnO [400], and more. Effects of hydrogen [303,335] and water vapor [335,361] were also studied. Here, we bring an example of the oxidation of the p-GaAs(110) surface, studied by Lüth et al. [336] SPV spectra of the clean surface, and after exposure to different oxygen doses, are shown in Fig. 50 for 'good' and 'bad' cleaves of the GaAs surface. For a 'good' cleave, the clean surface only features some tail states (in agreement with Fig. 42). Introduction of oxygen produces additional structure within the bandgap, that becomes more prominent with increasing oxygen exposure. At high oxygen doses the onset of this additional structure is between 0.8 and 0.9 eV. Thus, oxygen exposure introduces deep states at the 'well cleaved' GaAs(1 1 0) surface in a manner similar to that found with metal deposition (Fig. 42). For a 'badly cleaved' surface, deep states are found even in the clean surface. These must be related to a cleavage-induced high step density and remain unchanged upon oxygen exposure, which only introduces a knee at ~1.35 eV.

Another venue in which SPS is frequently used is the evaluation of the effect of various treatments, such as electron [101] or ion [349,352] bombardment, etching [352,354], annealing [383,384], light-soaking [304,306], etc., on semiconductor surfaces.

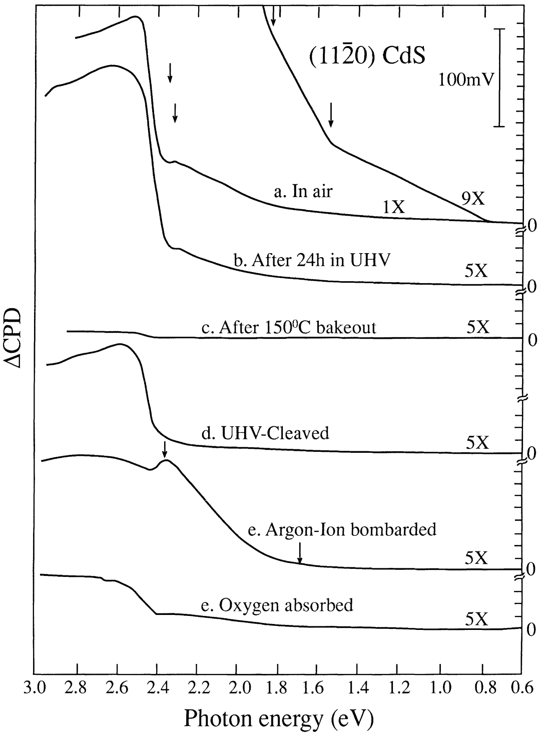

Fig. 51. SPV spectra of the CdS(1 1 $\bar{2}$ 0) surface under various conditions: (a) In air. (b) After 24 h in UHV. (c) UHV-cleaved. (d) Same as (b) after a 6 h, 150°C bakeout. (e) Ar$^+$-bobarded. (f) O-adsorbed (after Brillson [363]).

Brillson [363,364,372,373,375,376] has pioneered the use of SPS in tandem with chemical analytical tools in order to assess the impact of surface chemistry on surface electronic properties. An early study of Brillson, which merits some discussion here, has been the SPS analysis of the CdS(1 1 $\bar{2}$ 0) surface under various conditions and treatments, shown in Fig. 51 [363]. In this case, the accompanying chemical tool was Auger electron spectroscopy (AES) analysis (results not shown for brevity). The SPV spectrum in air is characterized by several surface-state related onsets, all of which diminish in magnitude following 24 h in UHV, and are absent on the cleaved surface. This is in agreement with the considerable surface contamination (by O, C, and Cl) in air, detected by AES, which diminishes after 24 h in UHV due to contaminant species desorption and is absent from the cleaved surface. Thus, the spectral features in air are clearly due to extrinsic surface states induced by contaminants.

After bakeout, the overall SPV signal is greatly reduced. Usually, one is tempted to assign this to a reduction in band bending (see Fig. 11), brought about by the lack of contamination and hence of surface states. However, it may actually be due to an *increase* in contamination, which increases the surface recombination velocity and decreases the excess carrier density (see Eq. (2.61)). Using AES, the baked-out surface was found to be highly carbon-contaminated, supporting the second interpretation.

Other authors have also encountered the difficulty of distinguishing between band-bending changes and recombination rate changes without quantitative analysis, and have solved them in different manners. Szuber [322] observed an increase of the SPV signal upon oxygen-exposure of polar GaAs surfaces. Here, this increase was assigned to an increase in band-bending since it is very unlikely that the additional O-induced states would actually decrease recombination rates. Wang et al. [307] have observed an increase in the SPV signal from a-Si:H films after depositing a monolayer of a Langmuir–Blodgett film. Here, the increase was attributed to a decrease in recombination rates because of an increased relaxation time. Several authors used complementary SPV and PL spectra [344–346,420]. If the increase in SPV was accompanied by an increase in PL, they concluded that this was due to a reduction in SRV. This is because the latter increases the SPV and decreases the non-radiative recombination which competes with the PL. Finally, Kinrot et al. [357] employed complementary *time-resolved* PL measurements for direct assessment of SRV changes.

Going back to Brillson's experiment, argon bombardment and oxygen adsorption both induce new surface states, at different energies. The naive interpretation is that these are again extrinsic states brought about by the presence of argon or oxygen. However, for argon-ions it was known that no significant gap states are induced, and the effect of oxygen depended on surface preparation prior to oxidation. AES revealed that for argon bombardment, and at least partially for oxygen adsorption, the extrinsic features were *not* a direct result of the contaminants. Rather, they were due to a treatment-induced change in surface stoichiometry.

The ability to directly correlate surface electronic structure with chemical treatments may also be used beneficially in surface passivation studies [348,357]. Such a study on the effect of organic polymer overlayers on the *p*-InP(1 0 0) surface, is shown in Fig. 52 [357]. The bare, etched surface displays two knees, associated with both electron and hole transitions, involving states situated ~1.2 eV below the conduction band ('A') and ~1.05 eV above the valence band edge ('D'), respectively. These states were assigned, based on previous SPS studies [352], to excess P and adsorbed O at the surface, respectively. The 'A' state is suppressed only in the presence of N-containing polymers, whereas the 'D' state is suppressed only by S- or F-containing polymers. This suggests that the surface states are passivated by P–N and (S or F)–O ion exchange processes, respectively.

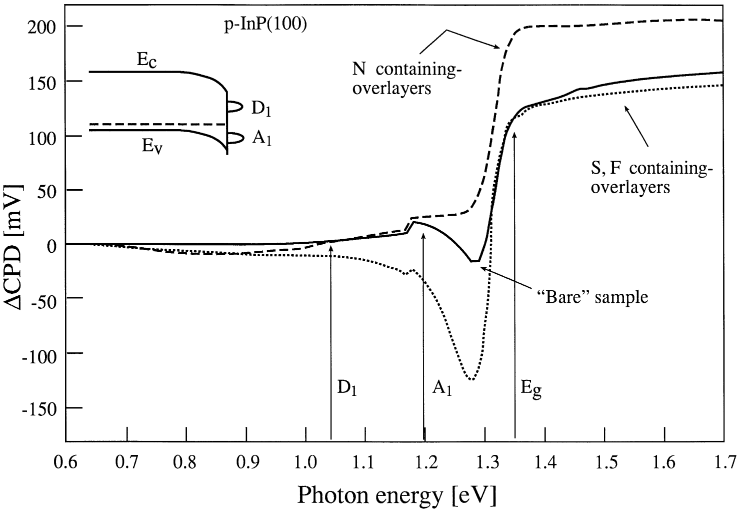

Fig. 52. SPV spectra of *p*-InP(1 0 0) surfaces: (a) Etched. (b) Coated with N-containing polymers. (c) Coated with S- or F-containing polymers (after Kinrot et al. [357]).

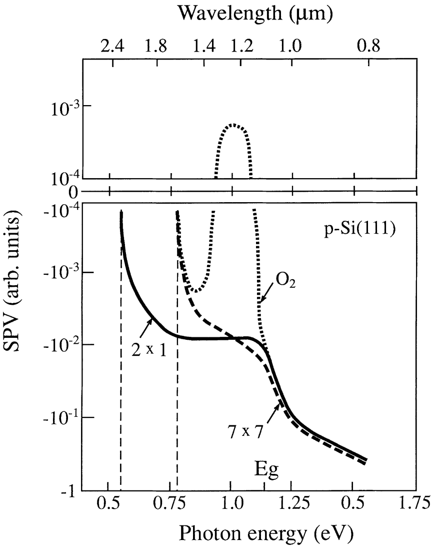

Fig. 53. SPV spectra of the p-type Si(1 1 1) surface for different surface configurations (after Clabes and Henzler [292]).

SPS has also been employed for basic studies of surface electronic structure at well-defined, clean surfaces. Several authors have found a correlation between the observed surface states and the surface structure. For example, Büchel and Lüth have found that an additional surface state arises when annealing the Ge(1 1 1)-(2 × 1) surface to the (8 × 8) configuration [302]. Mönch et al. have found good agreement between measured and calculated surface states at the Si(0 0 1)-(2×1) surface, supporting the asymmetric dimer reconstruction model used in the calculations [289]. Clabes and Henzler have performed similar studies on the Si(1 1 1) surface [292]. Fig. 53 shows their results for a p-type sample. A distinct difference between surface state energies at the (2 × 1) and (7 × 7) surface configurations is apparent. Oxygen adsorption at the (7 × 7) surface greatly changes the SPV spectrum, such that positive-SPV-producing transitions to the conduction band are apparent.

Studies of the evolution of metal–semiconductor interfaces using SPS were pioneered by Mönch et al. [330] and by Brillson [323,372,373], with later studies being conducted mostly by Shapira et al. [324,352,370] and Musatov et al. [108,338,339,347]. An example is found in Fig. 54, [372] which features the evolution of SPV spectra of the CdS($1 0 \bar{1} 0$) surface with increasing Au overlayer thickness. While some surface states are already present at the cleaved surface, Au deposition introduces new surface states. These states vary somewhat with overlayer thickness, before approaching a saturation regime at ~7 Å. Note that at relatively large Au thickness the signal is lost due to absorption in the Au layer. An example of a similar SPS study of metals on III–V semiconductors has already been given in Fig. 42. These studies, as well as others cited above, provide clear-cut experimental evidence for the induction of gap states at metal–semiconductor interface by metal deposition.

In addition to confirming the existence of interface states, SPS has also been used to understand *how* they are formed. A case in point is shown in Fig. 55 [347]. It shows the SPV spectra of the p-InP(1 0 0) surface, thermally cleaned at temperatures below and close to the decomposition temperature of InP, as well as Pd- and Ag-adsorbed. The striking similarity between the surface states induced by metal

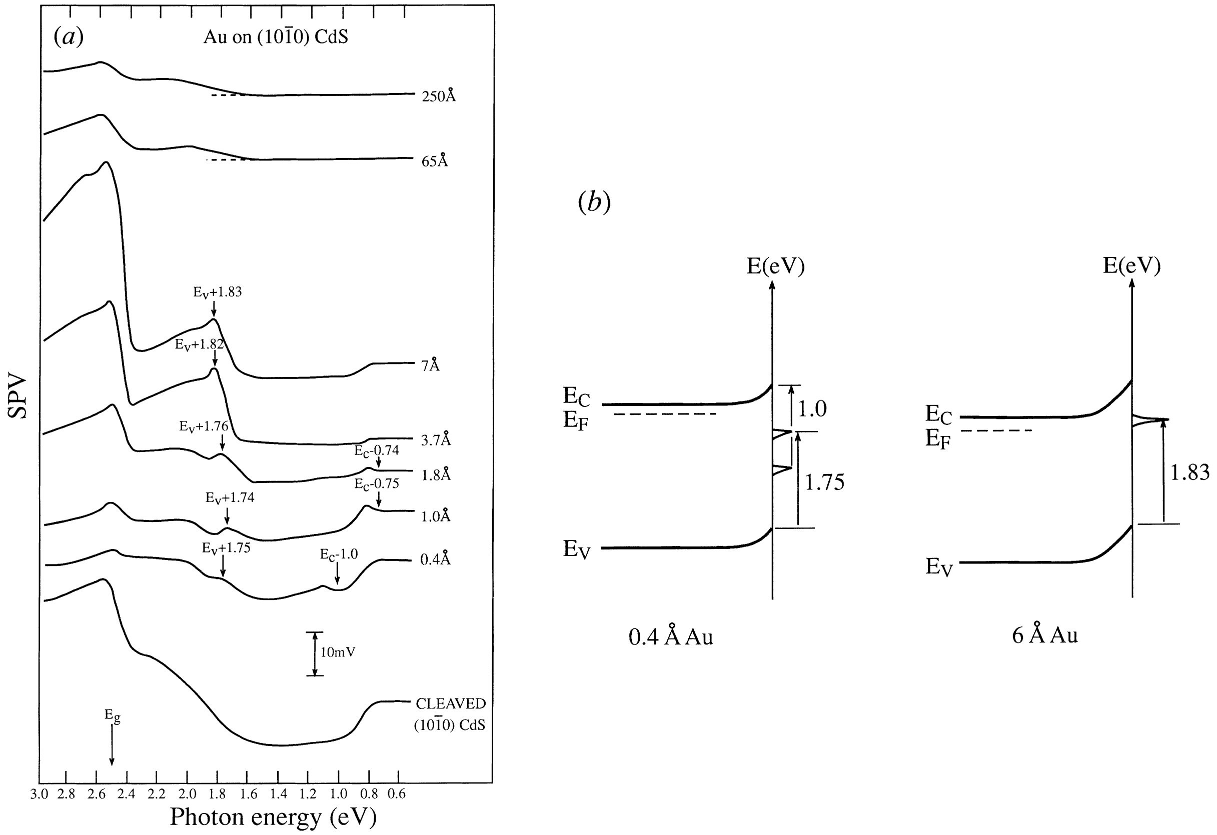

Fig. 54. (a) SPV spectra of Au on cleaved $(10\bar{1}0)$ CdS as a function of equivalent metal overlayer thickness. (b) Schematic energy-level diagram of optical transitions corresponding to the SPV spectra (after Brillson [372]).

(especially Ag) deposition and by InP decomposition suggest that they are of the same chemical origin, i.e., metal deposition induced disruption of the In–P bonds at the interface.

SPS also provides insight into the relation between surface states and surface or interface electronic properties. For example, the Schottky barrier height in metal/semiconductor junctions is almost always found to agree, usually to better than 0.1 eV, with the position of the dominant surface states found by SPS [323,324,347,352,372,373]. This constitutes a direct experimental verification of Bardeen's model of Fermi level pinning by surface states, discussed in Section 2.1.5 (see Fig. 7(b)). In another interesting application, Rosenwaks et al. [370] found a correlation between surface states and SRV at etched CdS$(11\bar{2}0)$ surfaces, treated in metal containing solutions. The more 'rich' with surface states the SPV spectrum was, and the closer the surface states were to midgap, the higher the (independently measured) SRV was. This is clearly due to the additional recombination paths afforded by the presence of more surface states and the high recombination efficiency of midgap states.

So far, our SPS analysis has been limited to *surface* states. However, SPS is also sensitive to *bulk* states. Accordingly, SPS has been used for studying, e.g., Cr-related defects in GaAs [334,340], Fe-related defects in InP [351], and Mn-related defects in CdMnTe [395]. The possibility of bulk contributions should always be taken into account when analyzing SPV spectra. For example, Mönch et al. [334]

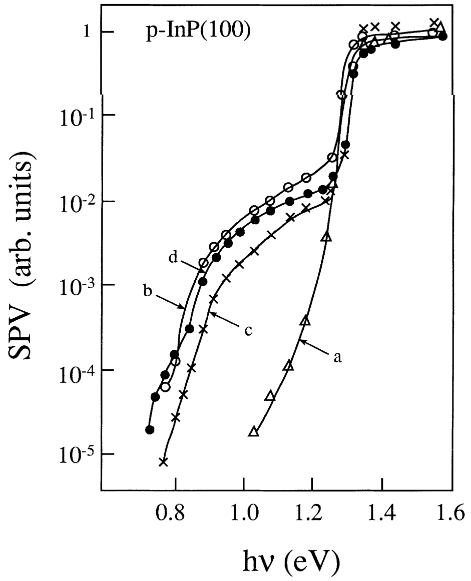

Fig. 55. SPV spectra of the *p*-InP(100) surface: (a) Thermally cleaned below the InP decomposition temprature. (b) Thermally cleaned close to the InP decomposition temprature. (c) After deposition of 0.5 monolayers of Pd. (d) After deposition of 0.3 monolayers of Ag (after Musatov et al. [347]).

have warned against misinterpreting bulk-defects in GaAs as evidence of surface states at the cleaved GaAs(110) surface. Unfortunately, as already discussed in Section 2.2.3, the simple distinction between transitions involving the valence or conduction band based on the sign of the SPV is *not* valid for bulk states. Briefly, transitions involving bulk states usually decrease the band-bending regardless of the band involved (see Fig. 15) [6]. Under special circumstances, the same bulk transition may contribute an either negative or positive knee to the SPV spectrum, depending on the state of the surface charge (see Fig. 17 and the corresponding discussion) [111,113]. The restriction of SPS sign analysis for bulk transitions is not always recognized in the literature and may have led to mis-assignment of state positions. For example, Simov et al. [362] studied the SPV spectra of polycrystalline CdS thin films. They have observed (among other transitions) the 'λ_1' and 'λ_2' transitions found by Lagowski et al. [361] on single-crystalline CdS, shown in Fig. 49(a), but with the opposite knee sign. They therefore assumed that the surface states had interacted with the conduction band, rather than with the valence band. While this may be true, the agreement in observed SPS threshold energies seems striking. Thus, it is also possible that the states observed by Simov et al. were actually located at grain boundaries. From the SPS point of view, these would be 'bulk' states as they are not located at the front (free) surface. Thus, the sign of their contribution would be reversed.

The distinction between surface and bulk states is not always an easy task and has attracted some attention in SPS-related research. We defer the discussion of quantitative approaches to such distinction to Section 5.4.3 and describe some qualitative means here: the most obvious means for distinguishing between surface and bulk states is by checking on the sensitivity of the relevant SPV feature to surface treatments or to the crystal face studied. SPV features found to 'persist' under various conditions [375,377] are attributed to bulk states. Conversely, a marked change upon surface treatment, as in, e.g., Figs. 42, 51 or 53, is attributed to surface states. A comparison between contact and contactless SPS measurements has also been suggested [294,295] and may be considered as a special case of surface modification. In the case of the QD films shown in Fig. 45, the sensitivity of the sub-bandgap spectrum to the ambient suggests a surface state contribution. However, here these states are probably at grain surfaces and not necessarily at the front surface, as the film is porous. Two pitfalls should be avoided when performing such a distinction: (a) even a bulk transition may be 'lost' in the SPV spectra if the surface is passivated and the band-bending is too low to obtain a meaningful signal. Therefore it is important to assess the impact of the surface treatment on the super-bandgap signal as well. (b) as mentioned above, in rare cases, an SPV feature corresponding to a bulk level may 'flip signs' due to surface treatment [113]. Sign reversals of the *same* feature should therefore be treated with caution. Distinction between surface and bulk states has also been performed by means of treating the *bulk*, e.g., by changing the bulk dopant [296,340,351,395], or sample fabrication procedures [305,333,393,409].

In the absence of surface or bulk treatments, one of the most popular methods of distinguishing between surface and bulk states is comparing SPV and photoconductivity spectra. The latter spectra are inherently insensitive to surface transitions because the photocurrent is collected from the entire bulk of the sample, so that the contribution of the SCR is typically negligible. Therefore, transitions appearing in both types of spectra are usually attributed to bulk transitions, whereas transitions appearing in the SPV spectra alone are assigned to surface states. In fact, the lack of correlation between photoconductivity and SPV spectra was used as proof of observing 'true' surface phenomena in the earliest days of SPS, as shown in Fig. 49. A more comprehensive example, measured at Si-doped GaAs epitaxial thin films, where three bulk states ('E_1'–'E_3') and two surface states ('E_{t4}', 'E_{t5}') are found, is shown in Fig. 56 [337]. The '*l* series' and '*n* series' phonons in Fig. 47 were identified as bulk and surface phonons, respectively, using a similar comparison with photoconductivity. More examples of use of this procedure may be found in, e.g., [319,334,360,365,366,371,375,386,407].

While very useful, photoconductivity is not fail-safe: Vyvenko et al. [371] have used SPS to point out a misinterpretation of photoconductivity data of CdS:Te crystals. They noted that the bandgap-related feature found in SPS is completely absent in the photoconductivity spectrum, due to the unusually large absorption coefficient which reduces the photoconducting layer. Therefore, the energy previously assigned to the bandgap was actually related to a bulk defect. Szaro [377] has found an SPS feature which behaved as a bulk state in the sense that it persisted through various surface treatments and orientations, but was not apparent in photoconductivity nevertheless. The reason for the discrepancy is not clear. Another case worth mentioning is the studies of a-Si:H, with and without H_2 dilution, performed by Fefer et al. [305], which is shown in Fig. 57. Based on the agreement between the SPS results and the constant photocurrent method, on the sensitivity of the spectra to bulk treatment evident in the figure, and on the agreement with theoretical models, the transitions observed have been assigned to bulk states. Nevertheless, agreement with theoretical models is only established when using sign conventions appropriate for *surface* states. Therefore, it was assumed that the surface has a defect structure similar to the bulk in this case, which is reasonable for an amorphous material.

In Fig. 57, an increase of both the bandgap-related SPV (at ~1.7 eV) and the gap-state-related SPV (at ~1.1–1.2 eV) upon H_2 dilution is observed. This is not coincidental, as gap states associated with the band with which they communicate typically feature the same dependence as the bandgap energy on the bandgap-modulating parameter. Using this idea in a systematic manner, a correlation between gap states and bands was found in CdTe [387] and CdMnTe [388] via temperature-induced bandgap changes, and in InAlAs thin films [355] via alloy-composition-induced bandgap changes. In the latter

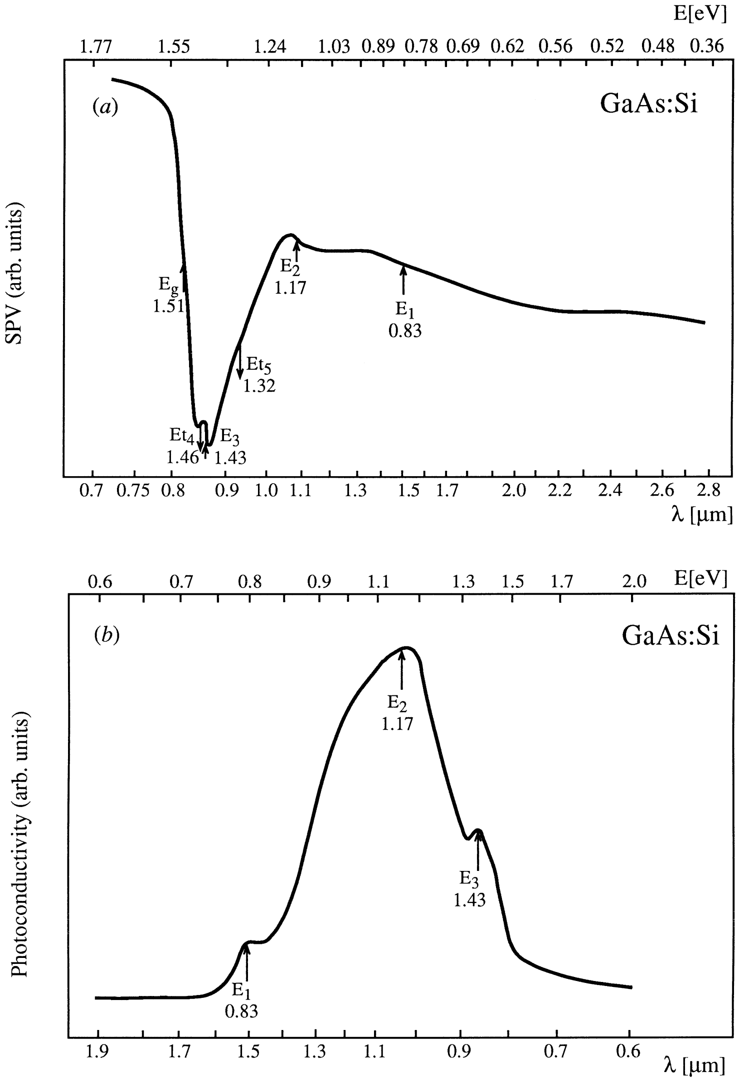

Fig. 56. (a) SPV and (b) photoconductivity spectra of Si-doped GaAs epitaxial thin films. 'E_1'–'E_3' – bulk state transitions, 'E_{t4}', 'E_{t5}' – surface state transitions (after Czekala-Mukalled et al. [337]).

case, other groups of gap states whose energy position was clearly not associated with any band were also found.

Having reviewed many SPS applications, we now consider some limitations of the analysis and means of overcoming them. First, the measured transition energy may not reflect the real position of the surface state if the transition involves a phonon [289,361] or any other thermal step [295,303]. A thermal contribution can usually be assessed from the temperature dependence of the SPV spectra, as in, e.g., Fig. 43. Second, shallow states may be difficult to observe due to the uncertainty in pointing out the exact E_g threshold. For example, the SPV spectra of UHV-cleaved surfaces in some cases (see the top curves of Fig. 42 and Curve (d) of Fig. 51) frequently feature a sizable super-bandgap SPV. This

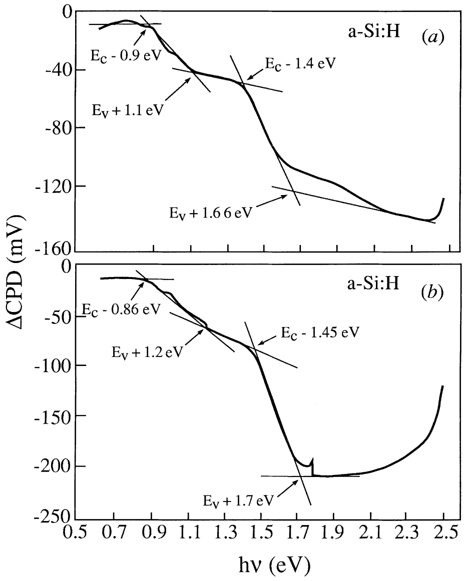

Fig. 57. SPV spectra of device quality a-Si:H, deposited (a) without and (b) with H_2 dilution on tin oxide coated glass (after Fefer et al. [305]).

SPV is *not* due to Dember interference as its sign changes with sample type. It therefore reflects a non-negligible equilibrium band-bending, even though no surface state features are observed. This is because the band-bending is probably formed by shallow states which ‘hide’ in the onset tail of the super-bandgap SPV. These band-tails may be as large as several tenths of an eV in amorphous or otherwise non-ideal materials, such as a-Si:H [305], porous Si [316], or semiconducting C-60 films [317]. We note that it is customary to explain all near-bandgap features in terms of tail states [328,350]. While in both papers cited here, and in others, tail states are probably indeed present, a full analysis must also take the Franz–Keldysh contribution into account.

Some authors have interpreted *super-bandgap* structure in terms of surface states found in the energy range of an allowed band [297,298,303,384]. As demonstrated in Fig. 48, additional absorption in a thin surface layer may indeed greatly influence the super-bandgap SPV. However, this absorption must be very strong in order to successfully compete with the response relying on the bulk density of states. Therefore, other interpretations, such as features related to, e.g., critical points in the band structure [290,327,333,358] or electron–photon interactions [326,332] must be ruled out first. Finally, throughout our discussion we assume that the *only* effect of illumination is to induce carrier transitions. However, photochemical processes are also possible. These are not very common when using the relatively low-intensity illumination afforded by a standard monochromator. However, they are not impossible. For example, Lagowski et al. have used SPS to ascertain that even modest illumination induces photodesorption of oxygen from a ZnO surface in vacuum [400], as shown earlier using other tools [421].

Some technological limitations to SPS interpretation must also be considered: the ability to observe a transition involving a gap state depends on generating a signal which is larger than the noise level. Therefore, states with a too small optical cross-section may be missed. Indeed, it has been our experience that when the output intensity of the monochromator is decreased (in order to improve its energy resolution) some of the weaker features may disappear (a recent example may be found in [318]). As shown in Section 2.2.3, the SPV signal decreases with decreasing semiconductor bandgap and surface band-bending. Thus, sub-bandgap features are more likely to be missed in relatively small bandgap materials and/or reasonably passivated surfaces. For example, Tong and Lam [105] failed to observe any sub-bandgap signals related to the Si–SiO_2 interface, even though the existence of gap states at that interface is well-known from, e.g., electrical measurements. They then confirmed theoretically that for reasonable interface state parameters, the SPV signal is indeed expected to be smaller than the noise level.

An associated problem is that the energy at which the onset of a certain transition is identified may actually be larger than the real threshold, reflecting only the energy at which the SPV change induced by this transition exceeds the noise level. The identification of the lowest-energy threshold may be particularly difficult when using a logarithmic representation. As long as the SPV curve approaches a vertical asymptote, as in, e.g., Fig. 53, this asymptote obviously reflects the energy threshold. However, if the asymptote is not vertical, as in, e.g., Fig. 50, the energy threshold is not obvious.

As demonstrated in Fig. 16, the sub-bandgap SPV increases with increasing equilibrium band bending in a manner similar (though not identical) to that of super-bandgap SPV. Therefore, small decreases in surface-state position upon increasing metal coverage (e.g., the change between 1.75 and 1.74 eV in Fig. 54) may actually reflect the improving SNR due to an increasing band-bending, rather than a true shift in energy position. Similar, but larger (as much as 0.1 eV) pseudo-shifts have been identified by Burstein et al. [324]. A shift of threshold energies has also been observed when performing SPS as a function of external bias in a MIS arrangement [291]. Note that *increases* in threshold energies for larger Au coverages in Fig. 54 *do* reflect physical changes as the equilibrium band-bending, which increases with increasing Au coverage, can only decrease the threshold energy.

The problems associated with determining state transition energies by inspection may be circumvented by an extrapolation which is very similar to that suggested for determining E_g. As in super-bandgap illumination, sub-bandgap illumination is also expected to reasonably reflect the absorption spectrum for sufficiently low illumination [289,293,374]. Accordingly, assuming a discrete surface state the SPV intensity should reflect the photon-energy dependence of the optical cross-section. The above-threshold SPV may therefore be fitted with an exponential dependence, or other functional forms deemed relevant (see Eq. (2.84)), and extrapolated to zero to find the threshold energy [101,108,289]. Using this approach, Musatov et al. [108,338,339] have studied the coverage dependence of metal-induced surface states. They have found that in many cases the energy position of the induced states is fixed, but in some cases it varies with coverage. Such a change probably reflects a change in the physical/chemical origin of the state at some thickness.

One obvious possibility of improving the SNR is increasing the illumination intensity. While optimizing the illumination source has been shown to have some success in resolving extra features [390], the improvement obtained is limited. Increasing the band-bending via an external dc bias in a MIS arrangement also improves the SNR. A different approach relies on lowering the measurement temperature [298,386], which suppresses thermally-induced transitions and hence increases both the super- and sub-bandgap SPV (see Section 2). An example is shown in Fig. 58(a) [395], which shows SPV spectra of unintentionally doped CdMnTe at various temperatures. At room temperature, the onset of the sub-bandgap SPV seems to be at ~0.9 μm, whereas at lower temperatures it is clear that the onset is much deeper (at ~1.5 μm), and was obscured by the noise level at room temperature. This feature was found to be correlated to Mn-induced bulk states. Unfortunately, the SPV spectra do not always

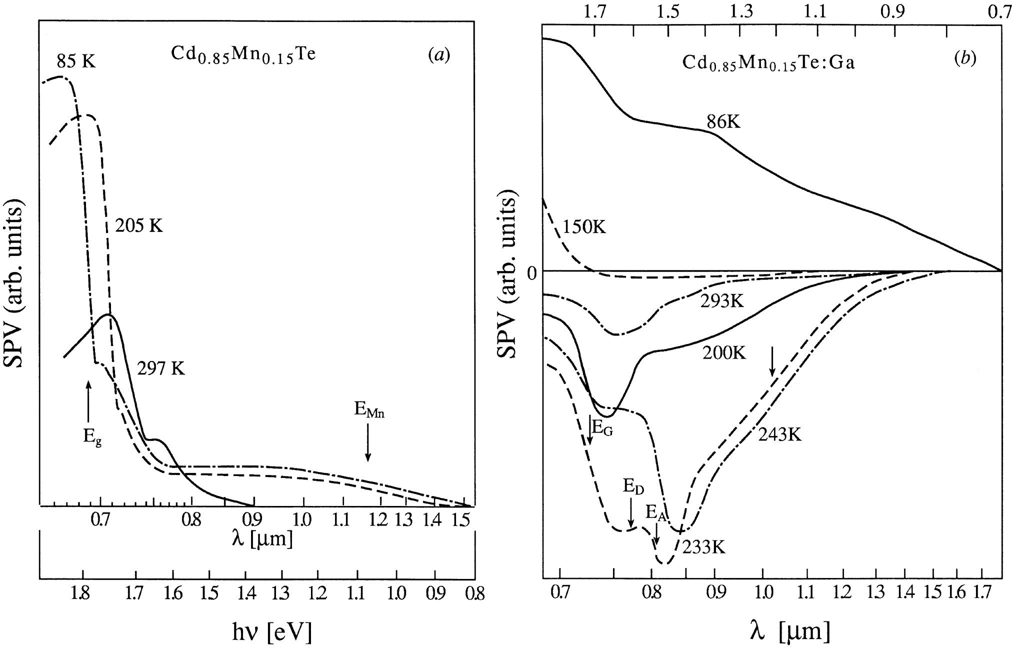

Fig. 58. SPV spectra of (a) unintentionally-doped and (b) Ga-doped $Cd_{0.85}Mn_{0.15}Te$ at various temperatures (after Kuzminski et al. [395]).

display a monotonous increase in magnitude with decreasing temperature. Other factors, such as impurity adsorption [393], state filling and emptying [303], and even lifetime variation effects in ac SPV [295], may complicate the SPV spectrum. For example, Fig. 58(b) which features SPV spectra of Ga-doped CdMnTe at various temperatures, shows a complicated temperature-dependence, with both *n*-type and *p*-type behavior, and with various defect states. While not amenable to simple interpretations, such a behavior may provide insight into sample characteristics if accompanied by a suitable quantitative analysis.

So far, only discrete gap states were considered. However, it is intuitively clear that in many cases a continuous distribution of gap states may be expected. In some cases, a rough distinction between discrete and distributed states was made on the basis of the ‘sharpness’ or ‘smoothness’ of the associated SPS features [288,291,375]. While of some value, such distinctions are clearly too subjective to be generalized. For example, a fairly sharp threshold is associated with the Si(111)-(7×7) spectrum in Fig. 53, although today this particular surface is well-known to have a distributed density of states [280]. By considering distributed states, the band-bending-induced shifts in energy thresholds discussed above may also be explained by a physical, rather than a measurement-dependent, mechanism. A change in band bending changes the position of the surface Fermi-level. Since electron (hole) transitions to the conduction (valence) band must involve filled (empty) states, a change in filling may shift the observed SPV threshold [291,322].

When a continuous distribution is expected, e.g., in a-Si:H, the smoothness of the SPV features may hinder assignment of threshold energies [303]. One approach to determining thresholds is finding the intersection of the asymptotic parts of the SPV curve. This approach has been applied in, e.g., Fig. 57.

Essentially, it attempts to locate photon energies at which slope changes in the SPV signal are maximal. Extrema in the *second* derivative of the SPV spectrum may be used as an equivalent of asymptotic intersection. This is because, by definition, these extrema indicate the positions of the sharpest slope changes.

An alternative approach which found some use relies on determining the maximum in the first derivative of the SPV spectrum. This approach has been used in, e.g., determining the 'λ_4' and 'λ_6' transitions in Fig. 49(a) and the various states in Fig. 58. The rationale of this approach is that the increase in the SPV signal is due to an increase in the density of states whose carriers may be excited into one of the bands. Therefore, the photon energy at which the SPV change is maximal should coincide with the peak of the density of states, i.e., with the state center, as shown in the inset of Fig. 49(a). The approach assumes that the state in question is completely filled or completely emptied. If this is not the case, the position of the obtained peak will vary with illumination intensity [319].

An implicit assumption in the first derivative technique is that *all* changes in SPV intensity are due to changes in the density of states [422], whereas we have seen above that these changes may also be governed by the photon-energy dependence of the optical cross-section. This may explain the considerable discrepancy between state positions found using this technique and those found by inspection in, e.g., Fig. 58. The distinction between density-of-states and optical cross-section contributions requires quantitative analysis and is deferred to Section 5. Since by using the extrapolation technique or the derivative approach one must assume a priori the dominance of optical cross-section or energy-distribution effects, respectively, we usually use the simple, if less accurate, asymptotic-slope-intersection approach for performing qualitative analyses. Interestingly, Lagowski et al. have suggested derivative SPS as a general tool for easier identification and analysis of gap states [294,333]. However, they have based their argumentation on the erroneous assumption that the SPV derivative indicates the derivative of the optical cross-section, σ^{opt}, rather than the density-of-states. A simple derivation of the dependence of σ^{opt} on $h\nu$ for a discrete gap state (Eq. (2.84)), shows that the derivative is *not* maximal at the gap state energy, E_{t}.

We now consider the possible influence of transitions between two localized states on the SPV spectrum. Promoting an electron from a lower-energy to a higher energy local state does not induce any SPV per se. This is because, by itself, the electron transition does not induce any charge separation. For the latter to occur, either the electron promoted to the higher-energy state or the hole left in the lower-energy state must be excited to the conduction or valence band, respectively (with the sign of the SPV depending on the type of free carrier). This usually means that at least one of the states must be shallow enough for effective thermal excitation to take place [293,321,335]. Other mechanisms, such as excitation involving two photons [371], or an excited state in resonance with the conduction band [334] (for Cr in GaAs), have also been suggested. Since absorption between two localized levels typically peaks at photon eneregies corresponding to their energy difference, localized-state-related transitions are identified by observing *peaks*, rather than *knees*, in the SPV spectrum.

An elegant example of SPS features due to transitions between local states at the Si(111)-(2×1) surface was given by Assmann and Mönch and is shown in Fig. 59 [293]. After cleavage (Fig. 59(a)), a double-peaked structure is observed. This structure is washed out following oxygen adsorption or annealing at 600 K, both of which destroy the (2×1) configuration. After annealing at 500 K, which enhances the (2×1) configuration, a well-defined single peak emerges (Fig. 59(b)). Since the (2×1) configuration exhibits a two-fold symmetry, transitions between filled and empty surface states must be polarization-dependent. Indeed, the SPV signal was found to be minimal for light polarized along

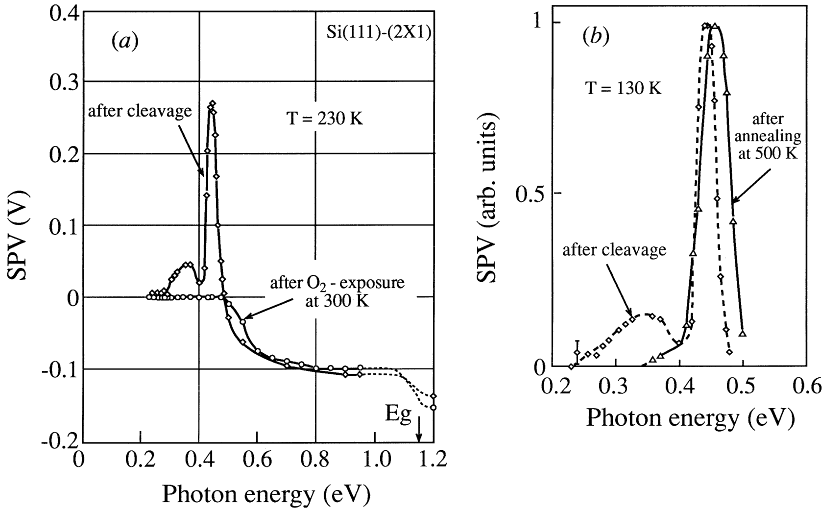

Fig. 59. SPV spectra of a Si(1 1 1)-(2×1) surface: (a) After cleavage and following exposure to O_2 at 300 K. (b) After cleavage and following 10 min annealing at 500 K (after Assmann and Mönch [293]).

$(1\bar{1}0)$ directions and maximal for light polarized along $(11\bar{2})$ directions. The observed peak was therefore interpreted as arising from transitions between filled and empty bond states, localized at alternate rows of raised and depressed atoms, respectively, running along a $(1\bar{1}0)$ direction.

4.3. Points of importance

In this section, we point out a number of important elements, related to the measurement conditions, that must be taken into account in order to obtain meaningful SPS data.

We have assumed so far that thermal equilibrium is always established between the surface and bulk in the dark. However, this is not necessarily true since the relaxation times of excited samples may be as long as several *days* if the surface barrier is much larger than the thermal energy. At room temperature, this phenomena has been observed primarily for high bandgap samples [6,360,361]. At low temperature, it has been observed in a-Si:H [303], in plastically deformed Si and Ge [419], and even in crystalline Si [298]. Evidence of SPS performed in the absence of thermal equilibrium prior to illumination may be found in, e.g., Fig. 49, where transitions with both bands involving the *same* surface state were obtained. States which are well removed from the surface Fermi level (as is the case here) are expected to be completely filled or completely empty in equilibrium. Therefore, only electron or hole transitions, respectively, are expected. The observation of both transitions indicates a partial filling of the state involved, and hence non-equilibrium conditions. Similar effects have also been encountered by other groups [386,393,397]. Goldstein and Szostak measured a-Si:H samples at low temperatures [303]. They reported a lack of relaxation so severe that the sample had to be re-heated and than cooled down again after each data point on the spectrum to allow thermal equilibrium conditions to develop.

Due to different initial surface conditions, SPV spectra taken after equilibrium and non-equilibrium conditions in the dark may differ drastically. Moreover, many quantitative analyses, which assume thermal equilibrium in the dark, would yield erroneous information when applied to measurements in which this assumption is not valid. For obtaining unequivocal measurements, it is thus very important

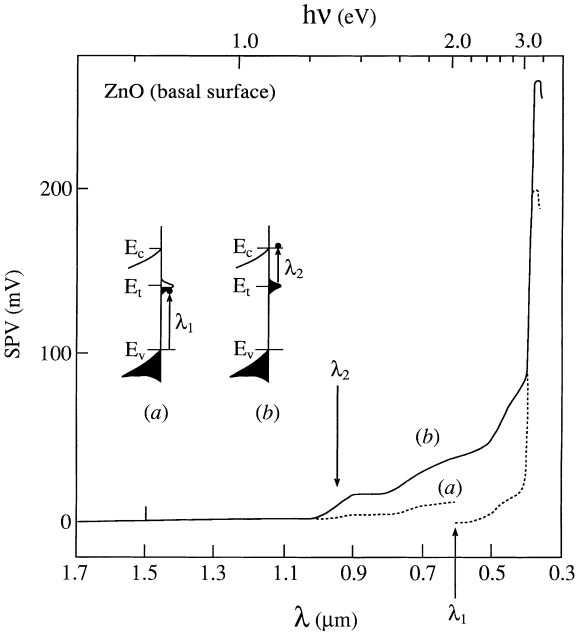

Fig. 60. SPV spectra of the basal ZnO surface in room temperature and ambient, (a) 1 h and (b) 24 h after illumination with white light. Insets represent the dominant transitions involved (after Gatos and Lagowski [6]).

to let the sample relax for a sufficient time in complete darkness. When working with a Kelvin probe, it is possible to ascertain that the sample has relaxed by monitoring the CPD in the dark as a function of time. We caution that a casual reading of a seemingly stable CPD does not suffice, as the relaxation times involved may be extremely long.

Varying the initial surface conditions by *deliberately* avoiding thermal equilibrium in the dark may be advantageous if proper adjustments to any interpretations are made. For example, Gatos and Lagowski [6] have compared between the SPV spectra of ZnO basal surfaces measured 1 h and 24 h after illumination with white light, as shown in Fig. 60. The completely different spectra may be interpreted as follows: after 24 h, thermal equilibrium is approximately established, the observed surface state is filled with electrons, and electron transitions from the state to the conduction band are observed. However, 1 h after illumination thermal equilibrium has not been established yet, the same surface state is empty, and hole transitions to the valence band are observed. This is supported by noting that the sum of the two corresponding transition energies is very nearly equal to the ZnO bandgap. In a different example, Yang et al. [301] have compared SPV spectra taken after different initial conditions (illumination and bias) in order to confirm photo-memory effects in Langmuir–Blodgett films capping a Si sample.

When using dc SPV, it is equally important to ascertain that steady-state conditions have indeed been reached following illumination since response times may also be very long if, e.g., ‘slow’ surface states are involved. It is therefore strongly recommended to make sure that sufficient time is allowed at each photon energy for steady-state to be obtained, which can be examined by checking for an influence of variations in the monochromator dwell time at each wavelength on the obtained spectrum. This has recently been demonstrated by Shalish et al. [360], who used SPS to study GaN films, as shown in

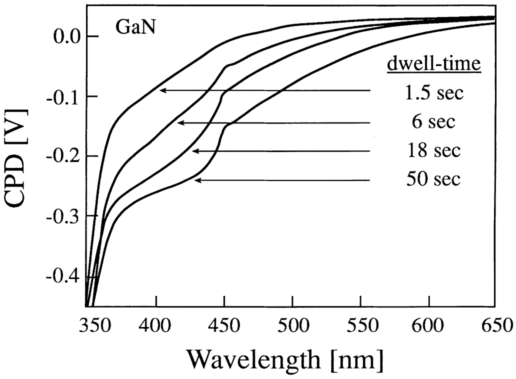

Fig. 61. SPV spectra of a GaN film at different monochromator dwell times (after Shalish et al. [360]).

Fig. 61. As the dwell time at each measurement point increases, the sub-bandgap SPV signal increases and more gap-state related features are exposed. Many of these features would have been overlooked had the SPV spectrum at the shorter dwell time been mistaken for a steady-state one. We note that appropriate dwell times should be sought with particular caution at wavelengths in which filters or gratings are exchanged because the disruption from the previous steady-state conditions may be more significant at such points. In addition, light may reach the sample during these changes and cause an additional undesirable excitation which must be allowed to relax before resuming the measurement.

When long response-time transitions are involved, their corresponding SPV features are likely to go undetected when using ac SPV because the illumination chopping rate may be too fast to allow any non-negligible population changes in the 'slow' states involved [100,110,321,386]. In fact, Gatos et al. [6] have been able to advance SPS much more than other early researchers [100,239] partly because they used dc, rather than ac, spectroscopy, thereby revealing a set of surface states not previously exposed. The lack of sensitivity of ac SPV to slow states has also been used beneficially. The presence of some spectral features in dc, but not ac, SPV, has been used to conclude that the observed features are related to surface, rather than bulk, states [6,386,393,394]. While this method has been used with some success, it is in fact quite limited because it assumes that bulk states are invariably fast and surface states are invariably slow, which is not always true.

Even if steady-state conditions have been ascertained, it is always a good idea to examine the details of the transient SPV response as well. This point has been elegantly demonstrated by Morawski et al. [321], who studied etched GaAs surfaces. A comparison between ac and dc SPS (Fig. 62(a)) reveals that the two spectroscopies converge for super-bandgap illumination, but the SPV signal is much greater in dc SPS. The difference in magnitudes confirms that steady-state conditions have not been obtained in ac SPV. While the shape of the spectra is also somewhat different, no immediately evident major difference in spectral features is noted. The transient response (Fig. 62(b)) reveals that the SPV signal is composed of a slow and a fast component. Whereas ac SPV only shows the latter, steady-state dc SPV shows the sum of both components, so that the slow state is never explicitly presented. If the magnitude of the two processes is *independently* plotted versus photon energy (Fig. 62(c)), it becomes clear that two physical mechanisms, and not one, have been monitored: The fast state, which has a 'knee' shape, is related to a state-band transition, whereas the slow component, which has a 'peak' shape, is related to transitions between two localized levels.

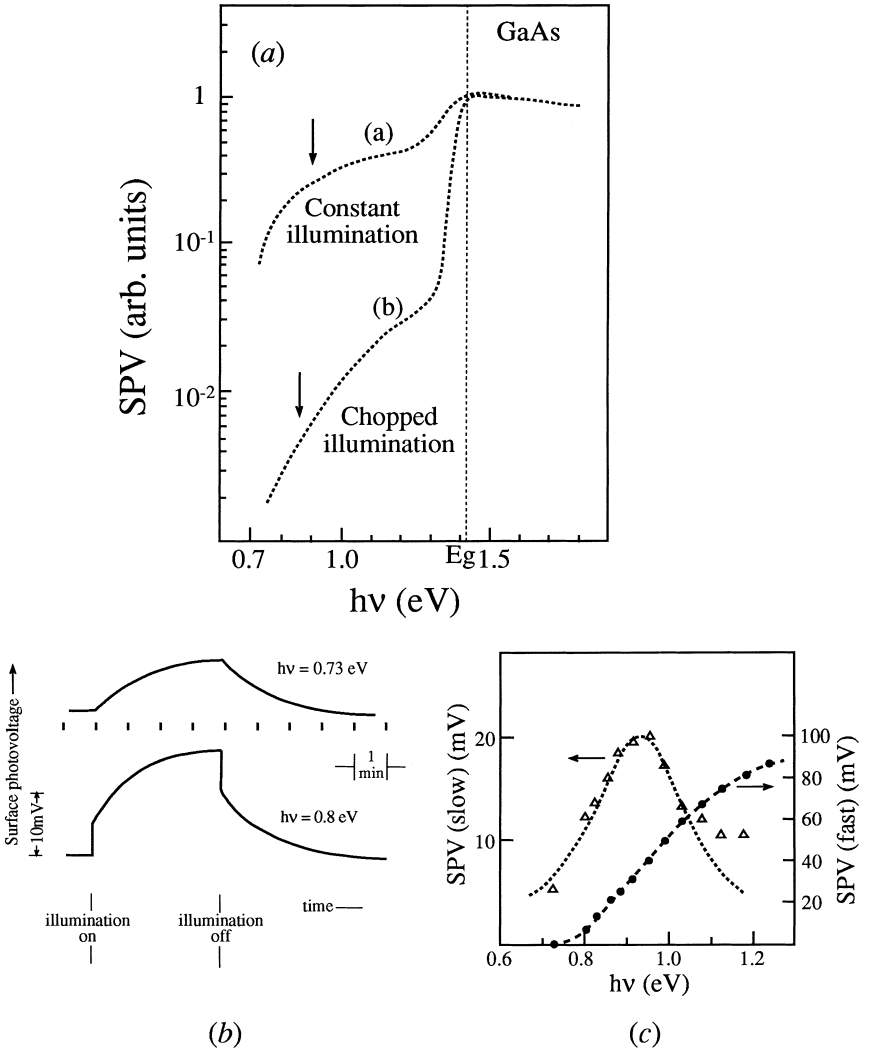

Fig. 62. SPS analysis of etched GaAs surfaces: (a) comparison between dc and ac SPS (b) SPV transients at 0.73 and 0.8 eV (c) Spectral dependence of the fast and slow SPV components found in (b) (after Morawski et al. [321]).

When using a Kelvin probe, an adequate back Ohmic contact is very important. While the resistance of this contact may be fairly high without obstructing the measurement (see Section 3.1), it is imperative that the back contact will not be of a Schottky type. The latter impedes current flow in the external circuit. This may result in extremely long response times unrelated to sample physics [380], or, even worse, to a complete failure in stabilizing the CPD reading. In this respect, ac SPS based on a MIS structure, is preferable. This is because the back contact may be replaced by capacitive coupling (see Section 3.2). As noted in Section 3, a major difference between Kelvin-probe- and MIS-structure-based SPS is that the latter may influence the surface band bending. This influence is undesirable if the true surface conditions are sought. However, in many cases influencing the intrinsic surface condition is desired since the band-bending can be increased, thereby increasing SPS sensitivity. Moreover, using a MIS structure, the surface band-bending may be systematically changed by means of an external dc bias. This additional degree of freedom may assist in uncovering and characterizing further gap states [291,405]. We note that several groups have employed SPS principles with *contact* measurements – via an electrolyte [354], a metallic contact [294,295,313,407], or a transparent conductor [307,314, 315,369]. Obviously, the effect of the contact on surface properties must be particularly considered in such cases.

An issue of great importance is the possible variation of photon flux with photon energy. In a conventional monochromator, the photon flux exhibits a rather significant spectral dependence (at times over several orders of magnitude) and only recently has a systematic SPS setup with a constant photon flux been demonstrated [423]. The variations in photon flux may introduce bogus features in SPV spectra, which reflect nothing but changes in the excitation level [417]. It is therefore a standard and widely used procedure to normalize all spectra by dividing the SPV signal by the photon flux at each photon energy. Unfortunately, this procedure is clearly unjustified since the dependence of the SPV on the photon flux may be highly non-linear! Such normalization is *strictly forbidden*, unless a linearity between the SPV and photon flux has been deomnstrated in the *entire* spectral range studied.

If the SPV is not linear in the photon flux, it seems natural to normalize the SPV based on its exact intensity-dependence. However, this procedure is cumbersome since the intensity-dependence in some spectral regions may differ. Büchel and Lüth [302] have therefore studied the intensity-dependence of two representative photon energies – one at a sub-bandgap energy and the other at a super-bandgap energy – and normalized the two portions of the spectrum independently. While this approach was a major step in the right direction, it has not been in much use, because it requires many extra measurements. Moreover, the intensity dependence may vary in different regions *inside* the sub- or super-bandgap regimes, so that normalization by two photon energies is not necessarily sufficient. Another mistake sometimes made is confusing time- and intensity-saturation [350], i.e., assuming that at steady-state the dependence on illumination intensity is negligible. In light of the analysis in Section 2 and in this section, this is clearly wrong, unless recombination rates are negligible.

If a constant photon flux or a proper SPV normalization procedure are not attainable, it is best not to perform any manipulation on the as-measured spectrum as this may corrupt the data. Instead, the SPV spectrum should be compared with the spectral features of the light source to check for suspected artifacts. For example, the feature at ~1.18 eV in Fig. 52 is simply due to a change of filter at that energy. When in doubt, comparing between spectra obtained using different gratings or different filter-exchange energies usually provides a clear-cut distinction between photon-flux-induced artifacts and real features.

Finally, as in any spectroscopy, removal of stray light is crucial for increasing the energy resolution and avoiding artifacts due to second-order reflections of monochromator gratings. In SPS, it is particularly important to consider stray-light effects in the vicinity of the bandgap energy. Since the absorption coefficient drastically increases around this energy, even a small number of stray photons with higher energies may produce a significant stray signal. This is an additional, measurement-dependent reason, for the broad onset of the super-bandgap signal discussed in Section 4.1. Therefore, it is *extremely important* to rule out stray light effects (or at least to assess their magnitude) before interpreting the near-bandgap signal in terms of physical effects, e.g., tail-states and/or the Franz–Keldysh effect.

5. Advanced analyses

5.1. Carrier diffusion length

The determination of the minority carrier diffusion length, L, is one of the most important applications of the surface photovoltaic effect. It is certainly the branch of SPV measurements which has had the most significant impact on the semiconductor manufacturing industry. Perhaps the best proof of how commonplace such measurements have become is the American Society for Testing and Materials (ASTM) protocol devoted to describing their proper use [424]. The methodology of the technique and its numerous applications are discussed in this section. Special attention is paid to practical considerations, as well as to the limitations of the analysis and the means of alleviating them.

5.1.1. Analysis principles

The extraction of L relies on the 'Goodman' (Moss) equation, introduced in Section 2.2.2 (Eq. (2.61)). The fairly simple dependence of $\delta n(w)$ on L_n given in that equation has been envisioned by Moss as a possible key for the extraction of the L_n [72]. Moss suggested using the SPV in the linear regime, i.e., for a signal level low enough such that SPV $\propto \delta n(w)$. He suggested that the left hand side of Eq. (2.61) is maximal where α is very large, i.e., for very short wavelengths. The SPV signal would be half the maximal value at a wavelength such that $\alpha L_n = 1$. Therefore, L_n may be found by measuring α at that wavelength. While seemingly simple to apply, this approach has rarely been used in practice. As already discussed in Section 4.1, the SPV does not necessarily increase monotonously until reaching a plateau with increasing photon energy, as predicted by Eq. (2.61). Therefore, identification of the maximal SPV may be very problematic. In addition, a wavelength corresponding to a SPV value which is half of the maximal one is not necessarily found within the relevant wavelength range.

Goodman used Moss's equation to form a much more general and rigorous algorithm for extracting the diffusion length [5]. He showed that as long as the SPV dependence on $\delta n(w)$ was monotonous (an assumption shown to be very reasonable in Section 2.2.2), its exact form did not have to be known. Goodman suggested that the photon flux necessary to maintain a fixed, pre-selected, value of SPV should be measured for several super-bandgap wavelengths. Since a constant SPV implies a constant $\delta n(w)$ (upon assuming a monotonous dependence between the two quantities), the right hand side of Eq. (2.61) must also be constant for all wavelengths studied. Therefore,

$$\frac{\alpha(\lambda)L_n}{1+\alpha(\lambda)L_n}\cdot\frac{1}{S+D_n/L_n}I(\lambda)=\text{const}, \tag{5.1}$$

which can be re-written in the form:

$$I(\lambda)=\text{const}\cdot(\alpha^{-1}(\lambda)+L_n). \tag{5.2}$$

Eq. (5.2) implies that if $I(\lambda)$ is plotted as a function of $1/\alpha(\lambda)$, the x-axis intercept is equal to $-L_n$, so that the latter is easily extracted. Goodman's method is usually referred to as the 'constant SPV' approach, or as 'method A' (in the ASTM protocol). An experimental example of this approach is shown in Fig. 63 [425], which shows the extraction of the minority carrier diffusion length in InP samples. The extracted diffusion length is seen to be independent of the pre-selected SPV value and of the surface conditions, as appropriate.

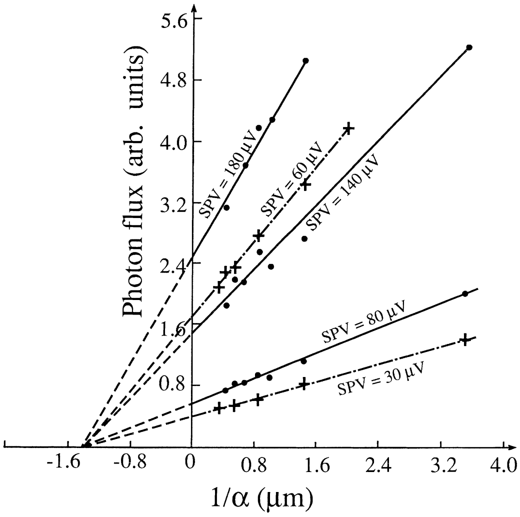

Fig. 63. Photon flux vs. the inverse absorption coefficient, α^{-1}, of (100) InP samples, for several SPV values. circles – sample with a relatively low SRV, crosses – sample with a relatively high SRV (after Li [425]).

A modification of Goodman's approach, usually referred to as the 'linear SPV' approach or as 'Method B', relies on measuring the SPV in the linear regime. Using this linearity in Eq. (2.61) yields:

$$\frac{I(\lambda)}{\mathrm{SPV}(\lambda)} = \mathrm{const} \cdot \frac{1+\alpha L_n}{\alpha L_n} = \mathrm{const} \cdot (\alpha^{-1}(\lambda) + L_n). \tag{5.3}$$

Eq. (5.3) suggests that in the linear SPV regime, L_n may be extracted using a linear plot very similar to that shown in Fig. 63, except that the y-axis is $I(\lambda)/\mathrm{SPV}(\lambda)$, rather than $I(\lambda)$ which maintains a constant SPV. This method is usually attributed to Quilliet and Gosar [426]. However, while these authors did suggest using the SPV in the linear regime, they did not suggest using an extrapolation scheme based on Eq. (5.3). Rather, they extracted L_n from the slope of a SPV/α versus α curve.

Using SPV to extract the minority carrier diffusion length has two distinct advantages over other techniques: First, the method presented here is a *steady-state* method. As a result, it is immune to time constants which combine bulk and surface processes – a major limitation of methods such as photoconductive decay (PCD) [427]. Surface recombination processes affect the SPV method only via S, the surface recombination velocity. As can be judged by either Eq. (5.1) or Fig. 63, changes in S can change the SPV magnitude as well as the slope of the linear curve used to extract L_n, but not the intercept (and hence extracted L_n) value. The second advantage of the SPV technique is that it may be used in a contactless manner and that it is cheaper and more simple in both operation and interpretation than other contactless methods, e.g., microwave PCD (μPCD) [428,429]. The SPV technique is also easy to use due to the availability of an ASTM protocol. In addition, it is readily amenable to operation in a scanning mode, as first demonstrated by Lile [427] and followed by many others in various applications [431–438].

Despite its numerous advantages, the acceptance of the SPV technique as a main-stream diffusion length measurement tool did not happen at once. While used successfully by other groups shortly after its initial introduction [439,440], the technique has largely lay dormant. In fact, in the 15 years after the pioneering work performed in the early 1960s [5,426], only a handful of additional articles which used the technique and/or developed it further have been published [425,427,441–443]. The first community, which seriously embraced the SPV approach, starting in the mid-1970s, was the solar cell community [433,434,443–451]. This is because the minority carrier diffusion length is one of the most important parameters which control the conversion efficiency of solar cell devices [452]. Following the success of these early SPV measurements in the evaluation of solar energy materials, the technique has become a standard tool of solar-cell research. Some relatively recent applications may be found in [435,436,453–463]. Specifically, throughout the 1980s and early 1990s, much attention has been devoted to a-Si:H. These studies were pioneered by Dresner, Goldstein, and Szostak [464], and were followed by many other research groups [304,465–485]. Measurements of a-Si:H are presented in Section 5.1.3 as part of the discussion of the limitations of the SPV approach.

The second area where SPV-based diffusion length measurements have become very popular, especially in recent years, is the monitoring of Si wafers for the semiconductor industry. Here, the minority carrier diffusion length is used as a sensitive tool for observing contamination and/or defects which serve as charge recombination centers. As in the case of solar cells, the technique did not become wide-spread for many years. Despite early successful applications of the approach to single-crystal Si [426,427,439] and the emergence of the first ASTM protocol in 1978, no sustained effort of using SPV for Si wafers has been undertaken. In 1983, it was up to Goodman himself to show that SPV-monitoring can successfully detect various contamination sources, such as loading stations in ion implanters, boron-doping sources, and inadequate wafer cleaning and handling [486]. Goodman et al. have specifically lamented the under-utilization of SPV tools in the Si industry in general and in contamination monitoring in particular [486]. Nevertheless, use of such tools remained sporadic at best throughout most of the 1980s (see [486,487], and references therein).

The situation changed dramatically towards the end of the 1980s. Within a few years, the importance of SPV tools had risen dramatically, mostly due to a fortunate coincidence of two major developments, designed to answer the increasing needs of the Si industry.

In the first development, Lagowski et al. have designed and commercialized [232] a computerized, scanning, contactless SPV machine (already shown in Fig. 29) [12]. By specifically targeting the Si industry, both in terms of developing tools suitable for an industrial environment and in terms of aggressively exposing the new tools to the relevant community, these scientists have contributed to the promotion of SPV methods considerably. Today, their SPV equipment, as well as that of others [233] is extensively used for both industrial monitoring and research applications.

The second development is related to the increasing importance of metal impurities. Specifically, Fe is known to be a problematic metallic impurity since it is a main constituent of many important materials and a common impurity in chemicals [488]. Moreover, due to its high solubility and fast diffusivity at elevated temperatures, Fe is easily introduced in the IC fabrication environment [489]. Fe contamination has been found to increase leakage currents [487,490] and decrease the breakdown voltage [12,491,492] and the radiation hardness [490] in MOS-based integrated circuits. It has also been found to degrade bipolar transistor performance [12,493] and decrease the breakdown voltage of power devices [494]. The more advanced the Si manufacturing technology is, the more severe contamination effects become. Ultra-large-scale integrated Si circuits are particularly vulnerable to detrimental effects of contamination on their performance, due to smaller device geometries, shallower junctions, decreased gate oxide thickness, and larger chip areas [12,488,491].

An elegant solution for the increasing need of an accurate, non-destructive, monitoring of the Fe concentration in B-doped Si wafers, based on SPV diffusion length measurements, has been forwarded by Zoth and Bergholz [488]. Their approach is based on the fact that Fe may appear in B-doped Si either as a (positively charged) interstitial defect, Fe_i, or as a FeB pair, according to the point defect reaction:

$$\mathrm{Fe}_i^+ + \mathrm{B}^- \leftrightarrow \mathrm{FeB}. \tag{5.4}$$

At room temperature equilibrium with $[\mathrm{B}] > 10^{14}$ cm^{-3}, All Fe is bound in FeB pairs, whereas at temperatures above 200 °C with $[\mathrm{B}] < 10^{16}$ cm^{-3}, most of the Fe is at interstitial sites. Since Fe_i introduces a deeper level than FeB into the Si bandgap, it is a more effective recombination center. Hence, the diffusion length in the sample is supposed to decrease upon annealing to above 200 °C, which is followed by rapid thermal quenching to room temperature. This process converts most FeB pairs into Fe_i defects. Let us assume that Fe is the only contaminant to undergo a point-defect reaction due to the annealing. Then since $1/\tau = \Sigma_i(1/\tau_i)$ (where τ_i is the electron lifetime due to specific contaminants) and since $L \equiv \sqrt{D\tau}$, we obtain the relation:

$$[\mathrm{Fe}] = \mathrm{const} \cdot (1/L_1^2 - 1/L_0^2), \tag{5.5}$$

where L_0 and L_1 are the electron diffusion lengths before and after the thermal treatment, respectively. Zoth and Bergholz have calibrated the multiplicative constant using DLTS, allowing a complete quantification of the Fe concentration.

A recent example of the combination of wafer-size SPV scanning and Fe-detection capabilities, clearly showing the strength of combining the achievements of Lagowski et al. with the method of Zoth and Bergholz, is shown in Fig. 64 [495]. First, diffusion length maps before and after the FeB pair-dissociation step are taken ((a) and (b)). Eq. (5.5) is than used to form a Fe contamination map (c). Finally, the contribution of Fe-related recombination centers is subtracted out using the known capture coefficients of these centers, resulting in a map of other recombination centers (d). (The exact calibration of this extraneous contamination requires assumptions regarding its effective capture coefficient, but the corresponding map contains useful information even if it is taken in arbitrary units). Fig. 64 is just one example of many studies devoted to investigating and eliminating Fe contamination sources using SPV mapping (see, e.g., [12,428,487,496–499]). All correlation mentioned above between Fe-contamination and faulty device properties has also been obtained using SPV investigations. In addition, surface contamination of Fe has been investigated using SPV (albeit in a destructive manner) by performing a rapid thermal annealing Fe drive-in step prior to SPV measurements [12,428,488,498–500]. Fe and Fe-silicide precipitation in Si wafers has also been examined recently [501,502].

The thermal-annealing-based SPV method for Fe concentration is usually sensitive down to $\sim 10^{10}$–10^{11} cm^{-3} [12,488,503] because below this limit other annealing-induced defect reactions can also change L_n by a similar amount. Such 'parasitic' reactions typically include the dissociation of other metal–B pairs (most notably Cr–B pairs) and oxygen-related effects in wafers with a large oxygen concentration [495,499]. One approach to improving this sensitivity further relies on monitoring the time response of the pairing process (left to right direction in Reaction 5.4) after the annealing in order to check for consistency with the known kinetics of the Fe-related response [488,503]. However, this process is time-consuming and is not desirable in an industrial environment. Lagowski et al. [504] have discovered that Fe–B pairs may be dissociated with intense super-bandgap illumination with the same efficiency as with thermal annealing. (For example, Fig. 64 has been obtained using photo-dissociation). The chief advantage of using photo-dissociation is that it selectively excites the Fe–B pairs. This has been shown to increase the sensitivity of the method down to a Fe concentration of

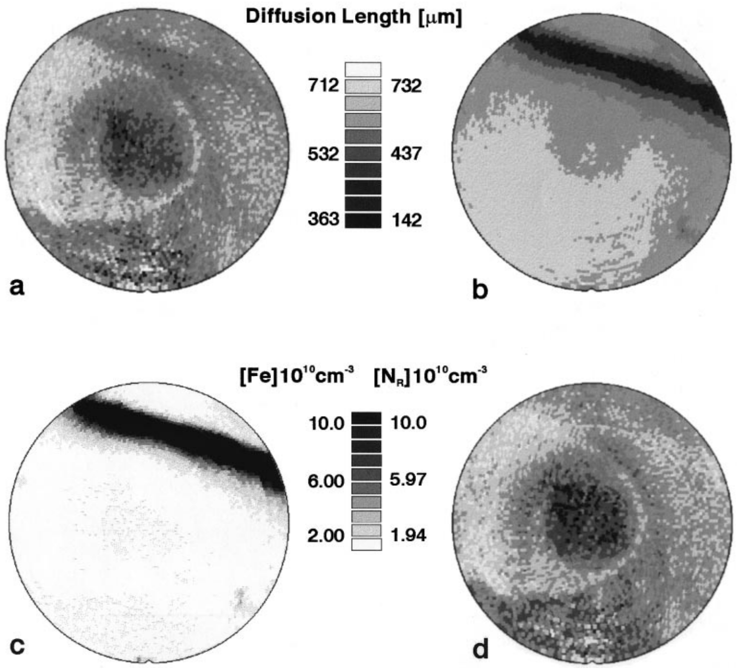

Fig. 64. Mapping and identification of recombination centers in a Si wafer: (a) Diffusion length before FeB pair dissociation. (b) Diffusion length after FeB pair dissociation. (c) Fe contamination. (d) Other recombination centers (after Lagowski et al. [530]).

$\sim 7 \cdot 10^7$ cm^{-3}, which is close to one part per quadrillion (!). Moreover, if the Fe-mapping photo-dissociation step is *followed* by a thermal dissociation step, the Cr concentration can be quantitatively mapped in a similar manner (assuming Cr–B pairs dominate the change in L_n due to the thermal step) [505]. Fe and Cr mapping has also been successfully applied to poly-Si films [435,457,459].

In light of the clear advantages of SPV-based Fe-monitoring tools, it is no wonder that recent literature suggests that such tools are actively used or evaluated for in-line monitoring at many leading Si-technology centers, including, e.g., Hewlett-Packard [506], Hitachi [493], IMEC [429] SGS-Thomson [498], Advanced Micro Devices [507–511], Nortel [499], Philips Semiconductors [500], and more. SPV-based diffusion length monitoring and mapping in Si wafers has been used not only to assess Fe and Cr contamination, but also to assess the impact of a host of other technological steps, e.g., rapid thermal processing [512,513] and other annealing steps [514,515], gettering procedures [513,515,516], and plasma processes [496,506]. Structural defects have also been studied [517]. Recently, SPV measurements have been used to quantify the precipitation of interstitial Cu in Si wafers [518].

While the vast majority of SPV-based diffusion length measurements were conducted on Si, we emphasize that the method is general and has been shown to yield useful information about most important semiconductor materials. These include GaAs [5,118,431,432,440,449], AlGaAs [454], InGaAs [437], InP [425,433,451,455,519,520], CdS [521], CdSe [455,521–523], ZnSe [524], CdMnTe [525], and even WSe$_2$ [526], Cu(In,Ga)Se$_2$ [463], and CdP$_2$ [485].

5.1.2. Practical considerations

Contactless diffusion length measurements are almost invariably performed using the MIS approach and not the Kelvin probe approach, for two reasons. On the one hand, since we are interested in extracting a *bulk* quantity, a possible influence of the measurement on surface band bending and/or surface state filling is of no consequence. Thus, one of the main advantages of the Kelvin probe is lost. On the other hand, MIS measurements are considerably faster and may be performed with better SNRs. This is particularly important for linear SPV measurements which are usually taken at very low signal levels.

The SPV measurement relies on having a sizable surface band bending. If the latter is too small, the signal will be very small and ultimately 'drown' in the noise. Use of etching reagents to produce a surface depletion layer and hence increase the signal is commonplace [434,527] and also recommended by the ASTM protocol [424]. Prolonged exposure to intense light for Fe–B photo-dissociation purposes is known to reduce the SPV [498,504] and may require subsequent exposure to water vapor or another etching reagent. In Section 3.2 we have pointed out that the surface band bending can also be controlled with an external dc bias in the MIS approach. To the best of our knowledge, use of this feature in diffusion length measurements has not been attempted.

Slow changes (taking, e.g., several minutes) in surface state properties may change the surface band bending between different measurement points taken to construct curves as in Fig. 63. This may result in serious errors because, as shown in Section 2.2.2, the relation between the SPV and the illumination intensity is highly dependent on V_s^0 [434,448,528]. In many cases, a higher chopping rate reduces such phenomena to a tolerable level because it makes more surface states 'slow' with respect to the chopping frequency [12]. However, the situation is usually very severe immediately after etching, where V_s^0 is not yet established, so that the sample must be allowed to relax prior to L measurements [434]. In addition, long surface-state-related transients following illumination may cause similar effects. For example, in the first a-Si:H diffusion length SPV studies, slow surface trapping effects precluded chopped light measurements and a Kelvin probe was used [464,471,473].

For applications where contactless, non-destructive testing is not very significant, diffusion length measurements can also be performed using a contact. This contact can be removable (electrolyte) or fixed (Schottky) as well, as first shown by Lile [427]. In many cases, such contacts have been found to alleviate the surface state relaxation phenomena mentioned above (see, e.g., [465,528]). They have also been used to circumvent problems associated with surface topographies which precluded the attainment of a stable capacitive surface [456,458].

Contact SPV measurements have found much use in solar cell characterization. This is because such measurements potentially enable the extraction of L in the absorber material *inside a complete cell structure*. Diffusion length values were successfully extracted from open circuit voltage measurements on solar cell junctions [433,443,444,446,449,451,455]. As long as the top region in a homojunction, or the window layer in a heterojunction, are considerably more heavily doped than the absorber (which is usually the case), the depletion region is contained almost entirely within the absorber layer, just like in the case of a free surface or a Schottky contact. Thus, diffusion length measurements may be performed using the same setup normally used for spectral response measurements in many solar cell configurations. The diffusion length can even be extracted from short-circuit current measurements in a similar manner [444], with an improved linear dependence of the signal on the illumination intensity.

We now address the relative advantages and disadvantages of the constant and linear SPV approaches. The chief advantage of the linear SPV approach is the speed with which the data points on the Goodman plot can be acquired. This is because the feedback scheme required to maintain a constant

SPV value, which slows the measurement down considerably, is absent in the linear SPV technique. The linear SPV approach has therefore become the method of choice in Si-wafer monitoring applications [12,529]. A speed advantage is always very important in an industrial environment as it increases the throughput of the measurement. It is of particular importance when SPV measurements are used for Fe concentration monitoring. This is because after Fe–B photo-dissociation the measurement must be completed within a few minutes, or a non-negligible Fe–B re-pairing will affect the measurement.

Due to its shorter measurement time, the linear SPV method can be employed with a higher chopping rate. Originally, very low chopping rates (tens of Hz) were employed. Lagowski et al. [12] suggested increasing the frequency to several hundred of Hz for reducing surface-state-related errors, as explained above. In this configuration, the measurements are limited primarily by the low level of the signal [495]. At a typical signal level of 1 mV, the measurement time required to maintain a reasonable SNR allowed a Fe concentration map of only 177 points, even when using the absolute minimum of two SPV points per extrapolation of a single L 'pixel'. More recently, Lagowski et al. implemented a new approach, where a signal level of about 10 mV is used. At this level, the SPV signal is no longer proportional to the photon flux, with the dependence being slightly sub-linear. By pre-calibrating this dependence, Lagowski et al. managed to decrease the measurement time significantly, so that Fe maps now contain over 6000 points. This is very important as experience has shown that Fe-contamination patterns are sometimes highly localized and can be 'missed' by low-resolution maps [495]. This newer, high resolution, mapping was used to generate the data shown in Fig. 64.

Working with very short-time-constant measurements requires increasing the chopping rate even further. At very high chopping rates, however, the measured L will no longer be the steady-state diffusion length, but rather will be decreased according to Eq. (2.68). Lagowski et al. [530] have shown that this error may be corrected, based on Eq. (2.68). Moreover, they have shown that the frequency-dependence of L can be used beneficially. At frequencies such that $\omega\tau \gg 1$:

$$|L(\omega)| \overset{\omega\tau\gg 1}{\rightarrow} \frac{L(\omega=0)}{\sqrt{\omega\tau}} = \frac{\sqrt{D\tau}}{\sqrt{\omega\tau}} = \sqrt{D/\omega}. \tag{5.6}$$

Therefore, at high frequencies L may be used as an alternative tool for measuring D, and hence μ (see Eq. (2.6)). Furthermore, since the value of D is much less sensitive than L to contamination, high-frequency measurements of relatively high-purity thick samples can be used for calibration of L-measuring equipment.

The linear SPV method also has a significant disadvantage, which makes it the less-preferred technique when speed is not a important issue. Aside from the obvious need of insuring linearity (or calibrating non-linearities), some other difficulties remain. First, an implicit condition for the validity of Eq. (2.61) is that the SRV is the same for all wavelengths used in constructing the Goodman plot. In the constant SPV method, where the excitation level is fixed, this is a highly reasonable assumption. However, in the linear SPV method changes in the barrier height for different wavelengths may lead to differing SRVs and hence an error in the measurements [73,441,531]. The maximal SPV signal used is therefore not limited solely by the linearity range of the SPV signal at each measurement wavelength. Using numerical simulations, Choo et al. [77] have shown that the linear SPV method can yield very significant errors in L even if the linearity of the SPV signal is maintained and the obtained Goodman plot is highly linear as well. Therefore, they concluded that the linear SPV approach is not to be used at all. In light of the success of Lagowski et al., this conclusion seems exaggerated.

A key to the large difference between theory and experiment in this case may be found in the work of Howland and Fonash [532]. These authors have compared between the two SPV methods for the case of a Schottky contact. They concluded that if very low signal levels are used, the two methods are in complete agreement. However, the linear SPV method begins to have problems at an SPV which is as low as 0.61% of kT/e (!). We therefore conclude that while the linear SPV method can indeed be used, its validity should be examined very closely, preferably by a comparison to the results of the constant SPV method. For the case of a Schottky contact, Howland and Fonash recommended using a new technique, which they dubbed 'Method C': We have already noted that the linearity of the short-circuit current dependence on the illumination intensity is much better than that of the open-circuit voltage. It is therefore advisable to use $[\exp(e\mathrm{SPV}/kT) - 1]$, which is a measure of the short-circuit current, rather than the SPV itself, in the Goodman plot. An extension of this idea to MIS-based measurements has not been attempted yet.

Successful L measurements rely not only on reliable SPV measurements, but also on reliable absorption data. Theoretically, one would wish to complement SPV measurements with absorption measurements *on the same sample*. However, this is frequently not possible, and in many cases not desirable either (e.g., for industrial monitoring). This is particularly true for Si, where the spectral dependence of the absorption coefficient is supposedly very well known. Nevertheless, many scientists have observed that significantly different values of L are obtained when using different absorption data given in the literature [448,527,533]. In addition, it is very important to properly account for other effects which are not taken into account in literature absorption data, but may be present in samples under study. These include free carrier absorption in heavily-doped samples [527] or photon recycling effects [519].

A specific problem in Si is the difference in absorption between stressed and stress-relieved layers, causing a relatively large scatter of absorption spectrum data. Nartowitz and Goodman [534] have compared between diffusion lengths gathered using different absorption data, including that recommended by the ASTM protocol. They discovered that an uncertainty of many tens of percent may ensue, especially for short diffusion lengths. Accordingly, they constructed a set of 'compromise' absorption data which, when used over a narrower wavelength region where different absorption data are in better agreement, reduces the uncertainty in L. However, the reduced wavelength range used increases the weight of errors in the illumination intensity.

Hwang and Schroder [456] have compared the Goodman plots obtained for Czochralski-grown mono-crystalline Si and cast poly-crystalline Si, shown in Fig. 65. While the mono-crystalline Si exhibits a conventional linear dependence of the photon flux on the absorption length, as in, e.g., Fig. 63, the poly-Si sample exhibits two linear regions with distinctly different slopes. From SPV information alone, it is impossible to determine which of the two, if any, should be extrapolated to obtain the true L. Using additional spectral response and short-circuit measurements, Hwang and Schroder have concluded that extrapolation of the short $1/\alpha$ region represents the true L, whereas the extrapolation of the long $1/\alpha$ region gives unrealistically high values of L. They have thus concluded that stress in the poly-Si affects the absorption coefficient mostly at longer wavelengths (corresponding to long $1/\alpha$), which are closer to the bandgap energy. By extrapolating the short $1/\alpha$ of the Goodman plot, they have been able to extract the correct dependence of α on wavelength at longer wavelengths.

Interestingly, Chiang et al. [520] used a similar concept for extrapolating the 'absorption tail' of InP : Mn samples at long wavelengths some ten years earlier. They based their extrapolation on the known absorption coefficient of InP at short wavelengths, assuming that the Mn-doping does not affect α significantly for sufficiently high photon energies.

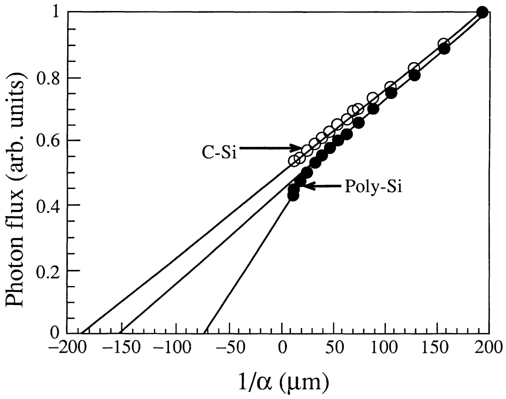

Fig. 65. Goodman plots of Czochralski-grown mono-crystalline Si and of cast poly-crystalline Si. Solid lines are linear-regressions fits to different parts of the data (after Hwang and Schroder [456]).

5.1.3. Limitations and solutions

This sub-section is devoted to examining the validity of the assumptions on which Eq. (2.61) is based and the possiblity of extracting L even when these assumptions are not valid. We start with several implicit approximations which are sometimes ignored or underestimated. First, the validity of Eq. (2.61) is entirely dependent on the validity of the boundary condition (2.60). The latter is merely an approximation, which assumes that all SCR generation/recombination processes may be effectively lumped in a single SRV-like parameter. This assumption has been examined by increasingly elaborate numerical simulations as well as analytical developments [77,78,80,89,441,532,535,536]. It was usually found to be satisfactory (i.e., introducing an error of several percent at most) for free surfaces as well as Schottky contacts, including cases with minority carrier trapping. The one clear exception is cases where the SPV is a significant portion of V_s^0 [535] or that V_s^0 is very small to begin with [89]. In these cases, SCR-related current components may be of the same order of magnitude as the minority carrier diffusion current, resulting in very significant errors in the determination of L.

Another sometimes overlooked assumption in Eq. (2.61) is the one-dimensional nature of the problem. Naturally, this assumption has to be examined with particular caution in scanning applications. Sopori et al. [537] noted relatively early on that the spot size must be large enough to avoid lateral diffusion effects. They predicted that lateral diffusion would be negligible and the true value of L obtained only if the spot size is at least 30 times as wide as L. In view of the results of, e.g., Lile [427] and Lagowski et al. [12,529], this quantitative criterion seems to be much too harsh. Nevertheless, the qualitative conclusion is correct. Indeed, other scientists have also observed errors in measuring L with a too small spot size [517,525]. A calibration scheme for correcting these effects, based on comparing measurements with ‘local’ and ‘global’ illumination has been suggested by Mariani et al. [517]. More recently, Faifer et al. [538] have examined the relation between the spot and electrode size in scanning systems and concluded that the latter should be bigger than the former by at least one diffusion length on either side in order to reduce errors due to lateral diffusion effects. This point was further investigated by Lagowski et al. [530]. They concluded that when the electrode and spot size are essentially the same, as in Fig. 29, the measurement error increases significantly with increasing L. They have therefore redesigned the pick-up electrode so as to increase the spot size with respect to the electrode size.

Another possible pitfall is that, as noted in Section 2.2.2, I in Eq. (2.61) is not the incident photon flux, but is rather the latter multiplied by the surface optical transmission and the sample quantum efficiency. While most authors have found reflectivity variations to have a negligible effect on the results in the narrow wavelength range usually probed, some have noted an influence of reflectivity on the results [446,469], especially for low values of L [527].

Eq. (2.61) also assumes a homogenous sample. Phillips [442] was the first to theoretically investigate the possible effects of an epitaxial layer with a different diffusion length on the apparent (extracted) diffusion length, L_{app}. He has shown that the Goodman plot remains linear for any epitaxial layer thickness. However, L_{app} reflects the true substrate diffusion length only if the epitaxial layer is thinner than half this diffusion length. Similarly, L_{app} reflects the diffusion length of the epitaxial layer if the latter is thicker than four times its diffusion length. For intermediate cases, L_{app} is an effective value which is not trivially related to any diffusion length.

The predictions of Phillips have been confirmed experimentally by Gouskov et al. [451]. These authors have extracted widely differing L values from electron beam induced current (EBIC) measurements, quantum efficiency curves, and SPV measurements (the latter in both contactless and short-circuit current modes) at ITO/InP heterojunctions. These differences were attributed to a defective surface layer of $\sim 3\ \mu\mathrm{m}$ in the ITO/InP junction which has a much smaller diffusion length than the InP bulk. Damaged surface layers have also been observed to result in various non-linearities of the Goodman plot by Goodman et al. [486,534,539]. Specifically, Goodman has shown that a reduced quantum efficiency in a defective surface layer may distort the Goodman plot at short $1/\alpha$ values [539].

More recently, Lowell et al. used wavelengths with low penetration depths for extracting the Fe content in Si epitaxial layers using the SPV approach [540]. They showed that better correlation to DLTS and SIMS results is obtained with decreasing $1/\alpha$ values. This is because more selective probing of the epitaxial layer is achieved. It should be noted that in their measurements the extracted L is still larger than the epitaxial layer thickness. Therefore, some contribution from the substrate cannot be avoided. Nevertheless, the weight of the epitaxial layer contribution is certainly enhanced, which explains the improved correlation with other techniques.

If the recombination centers which limit the diffusion length are inhomogeneously spread in the vertical direction, the resulting L would obviously be some average of the local L values. Some information about the vertical distribution of L may be obtained in a destructive manner by repeated etch and measurement sequences [458,512]. Specifically, when used for Fe-monitoring purposes, it should be remembered that the Fe contamination may vary as a function of sample depth, with the Fe most detrimental to device performance found in the vicinity of the surface. This explains why the Fe contents measured by SPV and by techniques which only probe the SCR (e.g., those based on capacitance transients) may differ [541,542]. The latter techniques are more directly relevant to device performance. Nevertheless, SPV has been found to yield very good predictions to device performance, as discussed above.

While diffusion length measurements in non-homogenous samples should be treated with the utmost caution, they are not necessarily erroneous. Contactless measurement of Si wafers has been shown to be possible even when the wafer has an n^{+} overlayer, is oxidized [12,491], or is even patterned with circuits [12]. According to Phillips's theory, this is because the thickness of the overlayer(s) is negligible with respect to the bulk diffusion length. It should be noted, however, that when measuring oxidized samples, special care should be taken to correct reflectivity changes due to interference, and also a possible loss of signal due to oxide-passivation of the SCR [529]. Commercial SPV equipment has recently been installed with corona-induced oxide charging capabilities to overcome the latter obstacle.

Oxygen impurities are sometimes deliberately introduced into Si wafers, away from its surface, in order to serve as internal gettering sources. This process yields a near-surface region, known as the denuded zone, which is relatively free of metallic impurities even if the wafer quality is not very high. Chappell et al. [543] suggested that such wafers may be modelled as a bulk region with low L and an epitaxial layer with high L (i.e., opposite to the ITO/InP case studied by Gouskov et al. [451]). Using numerical simulations, they concluded that if the denuded zone width is between the L values of the denuded zone and the substrate, L_{app} is proportional to the denuded zone width and may serve as an indicator of it. Although their analysis has later been shown to be too simplistic [531], it has been successfully used in practice for at least qualitative determination of trends in denuded zone widths [487,544].

Except for the general underlying assumptions described above, Eq. (2.61) also relies on five quantitative limitations [5,531,545]. They are:

$$1/\alpha \gg w, \tag{5.7a}$$

$$L \gg w, \tag{5.7b}$$

$$1/\alpha \ll l, \tag{5.7c}$$

$$L \ll l, \tag{5.7d}$$

$$\delta n(w) \ll p \quad \text{or} \quad \delta p(w) \ll n, \tag{5.7e}$$

where l is the sample thickness. All five mathematical conditions have an immediate physical meaning. The first two conditions state that the absorption depth, $1/\alpha$, and the diffusion length, L, must be much larger than the SCR width, w. This facilitates the neglect of SCR-related processes, mentioned above. The two following conditions state that both the absorption depth and diffusion length must be much smaller than the sample thickness. This means that neither photons nor excess carriers may reach the back sample surface, so that back-contact effects can be neglected. Finally, the fifth condition implies weak injection conditions. Unfortunately, in many cases the Goodman plots remain linear even if one or more of the five conditions is grossly violated [531]. However, in such cases L_{app} may deviate from the true L very significantly. This may be very misleading because the experimentalist cannot tell by inspection whether any of assumptions (5.7) have been violated or not. Therefore, a rigorous examination of the validity of the five conditions must be performed. Much theoretical and experimental work has been devoted to extracting L even if some of the conditions (5.7) are not satisfied. The rest of this section is devoted to a detailed examination of such approaches.

In some cases, Goodman plots manifest a clear deviation from linearity in the short $1/\alpha$ part of the curve. Usually, the curves exhibit a minimum and a 'curve up' part [464–466,523], as shown in Fig. 66 [466]. This behavior is typical of a violation of condition (5.7a), $1/\alpha \gg w$. It is due to the flow of excess carriers, formed in the SCR, towards the surface, in order to supply the surface recombination current [466]. This decreases the SPV and therefore a larger photon flux is necessary to maintain the same excess carrier density. The same effect is also responsible for the near-bandgap peak in SPS data (Fig. 41(a)), discussed in Section 4.1. If $1/\alpha \gg w$ *is* valid at longer $1/\alpha$, than L can still be successfully extracted, as long as the short $1/\alpha$ region is not used in the extrapolation. Since this is almost always the case, little effort has been devoted to extracting L if $1/\alpha \gg w$ is violated throughout the Goodman plot.

The limitations from condition (5.7b), $L \gg w$, were mostly investigated in the context of a-Si:H. The reason is that for other materials, L is at least a fraction of a micron, so that $L \gg w$ is satisfied even at fairly low doping levels. a-Si:H films, however, usually combine a large w, due to a low effective carrier density, with a small L, due to the great density of trapping centers. Numerical simulations of Goodman plots [469] showed that as w is increased with respect to L, L_{app} is increased such that $L_{\mathrm{app}} \sim L + w$. This indicates that if $L \gg w$ is violated, L_{app} should be treated as a field-enhanced *collection length* [471], which is roughly equal to the sum of the diffusion (L) and field (w) collection lengths. This interpretation was later confirmed experimentally by combining SPV and C-V measurements [476].

Early steps towards extraction of the true L from L_{app}, where condition (5.7b) is violated, involved the use of intense bias illumination. The purpose of the latter was to shrink w to the range where $L \gg w$ is valid [465,469,471]. Except in the very first SPV-based L measurement of a-Si:H [464], L_{app} was indeed found to decrease with increasing photo-bias, as shown in Fig. 66, typically saturating at ~1 sun illumination. The saturation value was interpreted as the true L. Similar results were obtained by Storr and Haneman, who measured CdSe thin films [522]. They showed that L_{app} strongly depended on bias illumination. Moreover, L_{app} found using two different electrolytic contacts was approximately the same *only* for intense bias illumination. This was because the very different redox potentials of the two electrolytes dictated very different SCR widths and the latter did not contribute to L_{app} only for intense bias illumination.

Based on a more detailed charge balance theory, Moore [466] proposed a more general Goodman-like equation which did not make any assumptions about the SCR width. Using his generalized equation, Moore showed that if $1/\alpha \gg w$ was valid, L_{app} was given by:

$$L_{\mathrm{app}} = L[1 + (w/L)^2/2(1 + w/L)]. \tag{5.8}$$

Eq. (5.8) made it possible to construct the dependence of w on the photo-bias intensity. By studying this dependence, Moore noticed that the reduction of w with increasing I was very significant and could not be explained by the usual SPV theory. He assigned the difference to an increase of the space charge density, ρ, with increasing I, due to carrier trapping. This dependence could therefore be quantitatively studied.

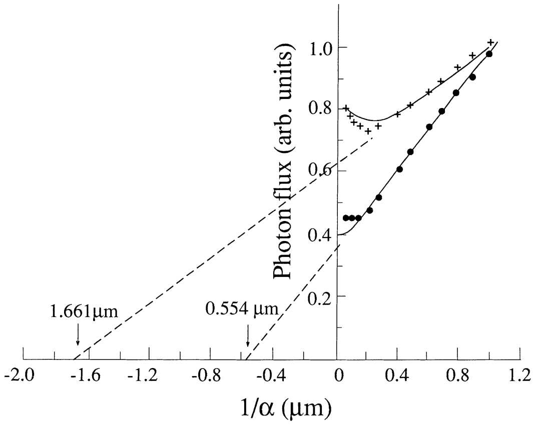

Fig. 66. Goodman plots of a-Si:H with (circles) and without (pluses) 1 sun bias illumination. Solid lines are theoretical fits (after Moore [466]).

Complicating the situation further, Hack et al. [470] showed that L should also be intensity-dependent because the same excess charge trapping that modifies ρ may also change the recombination statistics. Shortly thereafter, Moore has incorporated this effect into his analysis [467]. By combining contact-SPV measurements in both electrical and optical bias modes he showed that the detailed dependence of L on I can be extracted. The only remaining problem with this algorithm was the assumption that at 1 sun the SCR was sufficiently collapsed, so that L could be identified with the saturation value of L_{app}. As the quality of a-Si:H films gradually improved, excess-carrier trapping became less severe and consequently the reduction of w with increasing I became less significant. This, in turn, made the assumption that w is sufficiently reduced more and more dubious. Moore and Lin therefore developed a more sophisticated data extraction algorithm, which relied on taking Goodman plots at three different photo-bias points [468]. Moore's developments popularized the use of SPV for a-Si:H in the 1980s since they provided much needed information not easily extracted by other techniques. Specifically, it was found to be a very good predictor of solar cell performance [476]. Moreover, SPV measurements made it possible to ascertain whether the well-known illumination-induced performance degradation was primarily due to a decrease in L or in w. The different conclusions reached by different groups suggest that the answer is not universal but rather depends on sample preparation [477].

Violation of condition (5.7c), $1/\alpha \ll l$, has several repercussions. First, photon absorption may be incomplete due to the finite sample thickness [546]. In addition, reflection from the back (and possibly multiple reflections as well) must be taken into account [483]. Thus, the generation term in Eq. (2.59) is no longer well-described by the simple relation (2.58) and must be replaced with a more general expression. This makes $\delta n(w)$ dependent on $1/\alpha$. Moreover, reflections result in (usually highly) non-linear Goodman plots. Van den Heuvel et al. [483] have shown that under such conditions, L may still be extracted, but the simple, intercept-based, extraction must be replaced with a more sophisticated mathematical analysis.

Another reprecussion of violating condition (5.7c) is a possible SPV contribution from the SCR at the back side of the sample (brought about by a non-Ohmic back contact) [468,479,480,525]. According to the discussion in Section 2.2.5 and to Fig. 18, if the two SCRs are separated by a quasi-neutral region, the measured SPV is a superposition of front- and back-surface SPVs (where the sign of front and back SPVs is inverted because the band bending in the two SCRs is in opposite directions). Goodman plots are then highly non-linear and L cannot be extracted.

While no algorithms for the extraction of L in the presence of SPV due to absorption in both SCRs have evolved, several approaches for the *suppression* of the back SCR contribution were suggested. Studying a-Si:H films, Schwartz et al. [479] suggested a differential SPV method, according to which the band bending at both front and back SCRs is reduced via relatively intense near-bandgap light (which is necessary anyway to obtain $L \ll w$). A less intense higher-photon-energy beam (which has a shorter absorption length and does not reach the back contact) is added to the near-bandgap beam. The Goodman analysis is then performed on the difference signal, which only contains information of the front SCR. Naturally, the $1/\alpha$ values used must still be long enough so that condition (5.7a), $1/\alpha \gg w$, is not violated [480]. This approach, although elegant, is complicated and cannot be performed in the absence of significant photo-bias [468]. A more simple approach is to shine short $1/\alpha$ illumination directly via the back contact (assuming the latter is at least semi-transparent) so that the back band bending (and hence SPV) is greatly diminished [468,480]. The back SPV contribution can be eliminated destructively in the case of a free back surface by applying procedures which greatly increase the SRV, e.g., sand-blasting [533].

Violation of condition (5.7d), $L \ll l$, implies that carriers which are photo-excited in the vicinity of the front surface may reach the back one. It is therefore clear that even if there is no *direct* excitation of the back part of the sample (i.e., condition (5.7c), $1/\alpha \ll l$, is maintained), the sample cannot be treated as semi-infinite and the effects of the back surface must be taken into account. While Goodman plots made when condition (5.7c) is not valid frequently remain highly linear, it is clear that use of the simple equations (2.61) or (5.3) should yield an erroneous value of L. Indeed, comparisons between SPV and PCD [445,547], μPCD [429,430], or electrolytic metal tracing (ELYMAT) [430,548] measurements on Si indicated a very good agreement for large sample thicknesses and a poor one for sample thicknesses approaching the diffusion length. In recent years, this has become a more and more pressing problem, especially in industrially-oriented monitoring of Si wafers, due to the improvement in Si wafer quality. In the 1960s, diffusion lengths in Si wafers were of the order of tens of microns and the condition $L \ll l$ was easily satisfied. In the 1990s, high-purity Si wafers typically feature diffusion lengths of at least many hundreds of microns and in some cases over a mm [529,549]. These values are of the order of, or exceed, typical wafer thicknesses. Thus, ironically, where the SPV method for Fe detection is supposed to be at its best because the diffusion lengths are very long, determining the Fe concentration using the simple analyses described above becomes erroneous [498].

The effect of the back contact on the measured SPV, where the former is not directly illuminated, depends on whether the back *contact* and the back *surface* are one and the same. If this is indeed the case (as in, e.g., the non-scanning SPV of films deposited on a metallic substrate), some of the photo-excited carriers generated outside the back SCR will reach it nevertheless because the diffusion length is of the order of the sample thickness [550]. Thus, both SCRs would contribute to the measured SPV. Just as in the case of violating condition (5.7c), this means that L cannot be extracted, unless S_b is very high and the back-SCR-related SPV is negligible.

In many cases, the back-contact is *not* the same as the back surface. For example, in scanning applications the back-contact (which can also be capacitive) may be placed on a small portion of the sample. If this contact is sufficiently well-removed from the illumination spot, photo-excited carriers cannot reach its vicinity even by diffusion. In such cases, the back surface affects the front SPV by modifying the excess carrier density, but does not contribute directly to the measured SPV. Back-surface effects are usually expressed quantitatively by replacing the semi-infinite sample boundary conditions with a SRV-type condition:

$$D \left. \frac{\mathrm{d}\delta n(x)}{\mathrm{d}x} \right|_{x=l} = -S_b \delta n(l), \tag{5.9}$$

where S_b is the back-surface SRV, and solving the continuity equation (2.59).

Anttila and Hahn [531] examined the relation between L_{app}, extracted from a simple Goodman plot, and the real L, by performing extensive simulations, based on including the back surface boundary condition (5.9). A typical result is shown in Fig. 67 [531]. As long as $L \leq l$, $L_{app} = L$. For larger L/l ratios, L_{app} is highly dependent on S_b. For high (low) values of S_b, L is highly underestimated (overestimated) by L_{app}. Unrealistically large and small apparent diffusion lengths correlated with low and high S_b, respectively, have indeed been observed by several groups [429,513,547,548]. The demarcation line between the two phenomena lies at $S_b = D/L$, for which $L_{app} = L$, regardless of sample thickness. These results may be readily explained in physical terms: $S_b = D/L$ implies that the back SRV is equal to the diffusion velocity. In this case, the recombination current at $x = l$ is equal to the diffusion current which would have existed at $x = l$ had there not been a back contact there.

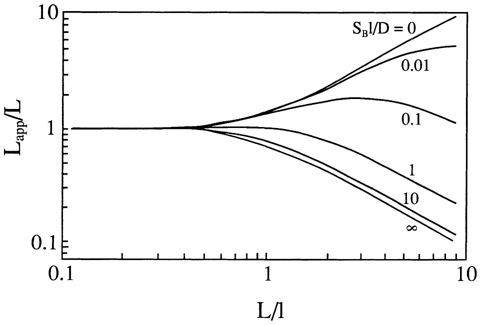

Fig. 67. Dependence of simulated L_{app}/L on L/l in p-type Si as a function of $S_b l/D$ (after Anttila and Hahn [531]).

Therefore, the excess carrier distribution in the sample remains the same irrespective of sample thickness and no error in L is introduced. For $S_b > D/L$ ($S_b < D/L$), the recombination current is larger than (smaller than) the expected diffusion current and the excess carrier density is smaller than (larger than) that expected in the absence of a contact. Accordingly, the apparent diffusion length, as 'viewed' from the surface ($x = 0$), is decreased (increased). If S_b could be precisely controlled, it would be best to set it to D/L, but this impractical. Instead, Anttila and Hahn suggested measuring L_{app} for both very high and very low S_b since their theory shows that the true L will be given by the geometric mean of the two L_{app} values, regardless of sample thickness. To the best of our knowledge, this has not been attempted experimentally yet.

Some significant attempts at extracting the true L by considering the detailed dependence of $\delta n(w)$ on S_b have been made in recent years [453,533,547]. Of these, the most general and useful approach was given by Lagowski et al. [549]. By solving the continuity equation (2.59) with the back boundary condition (5.9), they showed that the SPV can be expressed as:

$$\mathrm{SPV/I} = \mathrm{const} \cdot \frac{1}{1 - 1/\alpha^2 L^2} \cdot \left(1 - \frac{B}{\alpha L}\right), \tag{5.10}$$

where

$$B = \frac{(D/LS_b)\sinh(l/L) + \cosh(l/L)}{\sinh(l/L) + (D/LS_b)\cosh(l/L)}. \tag{5.11}$$

It can be readily ascertained that Eq. (5.10) reduces to Eq. (5.3) if $L \ll l$, as appropriate.

At relatively large α, condition (5.7), i.e., $1/\alpha \ll L$, is valid. Therefore, the non-linear term in Eq. (5.10) is negligible. Thus, by plotting SPV/I (rather than ϕ/SPV versus $1/\alpha$), a linear curve with an x-axis intercept of L/B (rather than L), is obtained. If S_b is known (which generally requires auxiliary measurements), L can be calculated from this intercept value. A particularly useful case, which frequently arises in practice, is the case where $S_b \gg D/L$. Then, Eq. (5.11) reduces to:

$$B = \coth(l/L), \tag{5.12}$$

so that L can be calculated regardless of the exact value of S_b.

An experimental example of the latter procedure is shown in Fig. 68 [549]. When using the usual Goodman plot (Fig. 68(a)), thinning of a high-purity Si wafer from 2 mm to 490 μm reduced L_{app} from 743 to 332 μm, clearly due to the violation of condition (5.7d) after thinning. When using the SPV

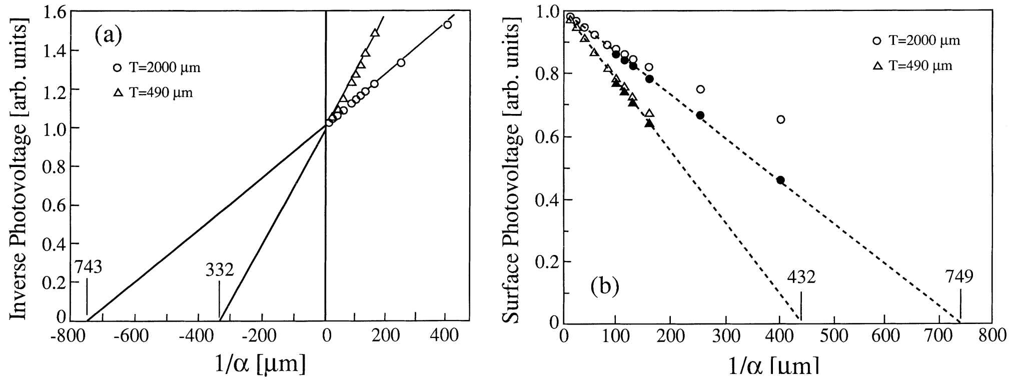

Fig. 68. (a) Normal 'linear SPV' Goodman plot of a high purity 2 mm thick Si wafer, before and after thinning to 490 μm. (b) SPV vs. $1/\alpha$ plot of the same sample. Open and filled symbols correspond to the as-measured values and the values corrected for the non-linear term in Eq. (5.10), respectively. All curves were measured using a constant photon flux (after Lagowski et al. [549]).

versus $1/\alpha$ plot (Fig. 68(b)), the initial part of the curve, where $1/\alpha \ll L$, was indeed linear. Using the intercept values of the plot with Eq. (5.12), L values of 749 and 760 μm were obtained before and after thinning, respectively. These values are in excellent agreement with the L obtained from the Goodman plot prior to thinning. A further check on the correctness of the result is that after correcting the measured data for the non-linear term in Eq. (5.10), based on the now-known value of L, an excellent fit with the extrapolation of the straight line is obtained.

We note in passing that a calibration chart for obtaining the true L from L_{app} based on wafer thickness and assuming an infinite S_{b} is now included in the ASTM standard [424]. In light of the above discussion, it is clear that the calibration should be different if S_{b} is finite.

The fifth and final condition (5.7e), states that for measuring the *minority carrier* diffusion length the injection level must be low. As explained in Section 2.2.4, if the injection level is not low enough, the electric field across the quasi-neutral region, i.e., the Dember field, is not necessarily negligible. Then, the ambipolar transport equation (2.93) must be used instead of the more simple equation (2.59). Thus, the assignment of an experimentally obtained diffusion length to the *minority carrier* diffusion length is equivalent to assuming that the illumination intensity was low enough to ensure a negligible Dember effect. The qualitative considerations given here have been fully confirmed by numerical simulations. Early numerical simulations by Choo and Anderson [441] showed that at low illumination intensities, SPV measurements can be applied successfully even to samples with minority carrier trapping centers. This is because the Dember field is usually negligible even in the presence of minority carrier trapping, unless the latter is very significant. More recent numerical simulations performed by Zhang et al. [536] showed that at high illumination intensities, the apparent L departs from its real value (in a manner that is SRV-dependent).

The fact that SPV can (and should) be used under low-injection conditions is a significant advantage of the technique with respect to other methods which rely on high-level excitation, such as μPCD or ELYMAT [428,430,551]. In the latter techniques, the obtained lifetime cannot be directly related to the minority carriers without further information. Similarly, a possible influence of excess charge carriers on the 'true' minority carrier diffusion length must be taken into account when performing SPV measurements with a photo-bias or with an increased illumination intensity. For example, the apparent L in ribbon Si solar cells has been shown (using SPV [450] as well as other techniques [552]) to *increase* with increasing illumination intensity due to trap filling.

If the injection level is fairly high, i.e., the Dember effect contribution is very significant, the ambipolar mobility μ_a tends to zero (see Eq. (2.94)). This means that the electric field term in the ambipolar transport equation (2.93) may be neglected. This equation than reduces to the form of Eq. (2.59), except that the coefficients D, τ, and L are the *ambipolar* coefficients, rather than the minority carrier ones. This may be used beneficially for extracting the ambipolar diffusion length in samples where the doping level is very low and the Dember effect is expected to be significant. For example, Liu et al. [118] showed (both theoretically and experimentally) that in semi-insulating GaAs samples, the SCR-related SPV is negligible with respect to the Dember-related SPV. Due to the similarity between Eqs. (2.93) and (2.59), the Dember-related SPV obeys an equation which is just like Eq. (5.3), except that L_n is replaced by L_a. Therefore, it is the latter which is extrapolated from an appropriate plot.

The most controversial aspect of condition (5.7e) has to do with undoped a-Si:H films. These films typically exhibit very low equilibrium carrier concentrations. Therefore, it has been argued, starting from the earliest papers dealing with SPV measurements of such films, that the extrapolated L is equal to L_a [464–466]. Some doubt has been cast on this 'standard' conclusion by McElheny et al. [553]. Using detailed numerical simulations, they showed that in the presence of significant trapping (which is ubiquitous in a-Si:H), the SPV is due to various drift and diffusion current components which depend on the excitation level in a non-trivial manner. In some cases, the calculated current components were not even in the same direction. Moreover, these authors claimed that the obtained L cannot even be used as a *qualitative* criterion for cell performance because in some of the simulations samples which yielded a smaller L_{app} were calculated to exhibit a better, rather than worse, solar cell performance. McElheny et al. suggested that the SPV method can be trusted only if trapping is greatly reduced, e.g., in samples with deliberate n-type doping and trap densities below 10^{13} cm^{-3}.

Shortly thereafter, Hegedus et al. [477] pointed out that no physical reason accounting for the different direction of drift and diffusion currents was provided by McElheny et al. They also pointed out that the significant empirical success of SPV measurements in predicting the performance of a-Si:H-based solar cells was difficult to reconcile with the pessimistic findings of McElheny et al. Hegedus et al. therefore called for a comparison between the results of SPV and those of a different L-measuring technique, which had emerged at that time – the steady-state photocarrier grating (SSPG) approach [554]. This is because of the immunity of SSPG to electric field effects. This call was answered by Balberg et al. [481]. They concluded that SPV measurements do not yield the true L_a, but rather a quantity which depends on it in a non-trivial manner. This is probably because even at the highest photo-bias intensities used by Balberg et al. a complete collapse of the SCR was not obtained. Nevertheless, these authors concluded that the predictive power of SPV is much better than that expected from the numerical simulations of McElheny et al. On the other hand, van den Heuvel et al. [484] maintained that the drift currents found by McElheny et al. are simply a manifestation of the Dember field and that the SPV method does yield L_a and can be used safely. In our opinion, the issue has not been fully settled. Unfortunately, it has not been studied further. This is because the doubts cast on the SPV technique on the one hand, and the success of SSPG in circumventing similar difficulties on the other hand, caused the a-Si:H community to almost invariably prefer the latter approach. Thus, the application of SPV to a-Si:H was practically abandoned in the 1990s.

In conclusion, we note that diffusion length measurements are a highly evolved, useful, and successful area of the SPV technique. If due attention is paid to limiting conditions and proper interpretation, results of both scientific and technological importance are obtained.

5.2. Surface band bending and dipole

Detailed information on the electronic band structure at semiconductor surfaces, expressed in the form of a schematic band diagram (see Fig. 4), plays a central role in many studies of surface chemical reactions, e.g., studies of adsorption/desorption and oxidation/reduction processes. Similar information is extremely important for studies on the formation of semiconductor interfaces, where, typically, the properties of a substrate with a very thin (metallic or semiconducting) overlayer are studied [23,24,555].

If the *bulk* band-diagram is known, information on the equilibrium surface band-bending, V_s^0, and the surface dipole, $\Delta\phi_s$, makes possible the construction of the *surface* band-diagram, shown in Fig. 4. We note that (if the bulk doping is known) knowledge of V_s^0 is equivalent to knowledge of the equilibrium surface charge, Q_{ss}. This is a result of the charge neutrality condition, $Q_{ss} = -Q_{sc}$, and the one-to-one correspondence between Q_{sc} and V_s^0, expressed in Eq. (2.30). The SPV-based extraction of the surface band-bending/charge and of the surface dipole are discussed in detail in this section.

5.2.1. Surface band bending – photosaturation

The most used SPV-based tool for determining V_s^0 is the photosaturation technique. This method, which is very simple in nature, is based on assuming that application of sufficiently intense super-bandgap illumination to the semiconductor surface results in complete flattening of the surface band bending. The basis for this assumption lies with Eq. (2.52), which describes Q_{sc} under illumination as a function of the injection ratio, Δ_n. This equation predicts that for $\Delta_n \to \infty$, $Q_{sc} \to 0$, and hence $V_s \to 0$, regardless of V_s^0. Thus, V_s^0 is obtained experimentally as equal and opposite to the SPV measured under intense illumination.

Williams seems to have been the first to utilize the photosaturation technique (as early as 1962), in the course of studying oxygen adsorption and desorption on CdS surfaces [556]. Since the photosaturation approach is relatively easy to implement and very simple to interpret, many other studies have utilized it for determining V_s^0 values at various semiconductor surfaces. These studies include further investigations of oxygen adsorption/desorption at CdS surfaces [557]; CdS/insulator interfaces [558]; a-Se/organic polymer interfaces [559]; Ambient effects on GaAs(111) surfaces [560–562]; Effects of different etching reagents on (100) InP surfaces [563]; Effect of organic molecule adsorption on various semiconductors [50–57]; Temperature-dependence of the surface potential in Si [564,565], Ge [567,568], GaAs [569] and SiC [570]; Laser-induced modification of the Si/SiO_2 interface [565]; Band-diagrams of Cd-based II–VI semiconductors [571]; Band-diagrams of various clean [11,289] and real [572–574] Si surfaces; Band-diagrams of a-Si:H surfaces [303,575–577]; Band-diagrams of organic semiconductors [412–414]; and band-diagrams of Ge [573], CdTe [384], CdMnTe [393], and NiO [578] surfaces. In addition, Brillson et al. have used the photosaturation technique extensively for characterizing the influence of metallic overlayers on the band bending at CdS [372,373,579,580], GaAs [579,581,582], and ZnO [583] surfaces.

In the early 1990s, Edelman et al. introduced wafer scale mapping of the surface charge at Si wafers, which is based on scanning the saturation SPV using the machine shown in Fig. 29 [584–586]. This produces surface charge maps, which can complement the diffusion length and Fe concentration maps shown in Fig. 64. Surface charge mapping has been successfully adopted, extended, and applied to monitoring of a wide variety of wafer processing steps by Nauka et al. [506,587–591] and Lowell et al. [507–509,592–601]. The SPV-measured charge at dielectric covered Si wafers has been shown to be in very good agreement with the charge deduced from C–V measurements [587]. This agreement was obtained even though the two results do not have to agree *completely* because of the additional processing steps needed for the C–V measurements. However, the contactless, non-destructive nature of the SPV-based approach makes it much more suitable for in-line monitoring and process control. Nauka has also extended the approach to mapping of the charge at the *buried* Si/dielectric interface of silicon-on-insulator wafers [589].

Photosaturation has also been used for performing a V_s^0-determining step in SPV-based algorithms for extracting surface state energy distributions [565,568,569,572,602,603] and surface-state properties [110,319,604], which are described in Section 5.4. Similarly, it has been used as a step in an algorithm for constructing the band diagram of semiconductor heterojunctions, discussed in Section 5.5.3 [19,403,605]. It was also used for calibration of barrier heights in field-effect measurements [562,606].

Despite the host of applications described above, many of which have been very successful, one should bear in mind that photosaturation is one of the most controversial and pitfall-laden quantitative SPV-based approaches. Therefore, much room is devoted in this section to a detailed discussion of its limitations and the conditions for its validity.

It is usually agreed that in order to ascertain experimentally that band flattening has been achieved, the SPV must be measured as a function of incident illumination intensity. A saturation of the resulting $\mathrm{SPV} = f(I)$ curve at the highest illumination intensities is taken as evidence of flat bands (hence the name photosaturation). The source of the controversy is that examinations of the $\mathrm{SPV} = f(I)$ curves have produced mixed results: In some studies photosaturation was consistently obtained (see, e.g., [303,384, 557,563,572,573,576,602]), whereas in others it was consistently *not* obtained (see, e.g., [214,607–610]).

In yet a third group of studies, photosaturation was obtained for some, but not all, surface conditions [412,556,558,561,575]. This third kind is the most interesting, as it provides a key for understanding the effects which govern the elusive photosaturation behavior. An example is given in Fig. 69, which shows the photosaturation measurements of Flinn and Briggs on *n*- and *p*-type GaAs(1 1 1) samples, exposed to different gases [561]. It is readily observed that the SPV does not saturate for any of the *p*-type samples or for the nitrogen exposed *n*-type samples. Saturation *is* obtained for the *n*-type oxygen-exposed sample and perhaps also for the oxygen and ozone exposed *n*-type sample, although in the latter case the saturation is somewhat less pronounced and is not necessarily complete.

The general validity of the photosaturation technique, as well as the conditions under which it is expected to succeed experimentally, have been recently examined theoretically by Aphek et al. [611]. They used a simple analytical model, based on the quasi-Fermi level approximation and on the 'Goodman' (Moss) equation (see Section 2.2.2), as well as a rigorous numerical solution, to construct steady-state $\mathrm{SPV} = f(I)$ curves. The results of these calculations are shown in Fig. 70. A constant k_n was used in the calculations because k_n was found to govern the SRV in this case. Since the SRV was maintained at a constant value, the $\delta p(w)/I$ ratio was approximately equal in all curves (see Eq. (2.61)), which facilitated a comparison of different curves on the same $\mathrm{SPV} = f(I)$ plot. Furthermore, for a fixed $\delta p(w)/I$ ratio, the variation between the different curves was found to depend on k_p/k_n, rather than their individual values. Fig. 70 allows much useful insight into photosaturation mechanisms and is used as a basis for our discussion.

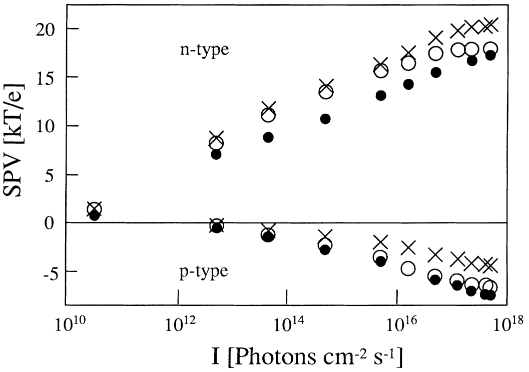

Fig. 69. SPV $=f(I)$ curves at GaAs(111) surfaces in various ambients. Full circles: nitrogen; empty circles: oxygen; crosses: oxygen and ozone (after Flinn and Briggs [561]).

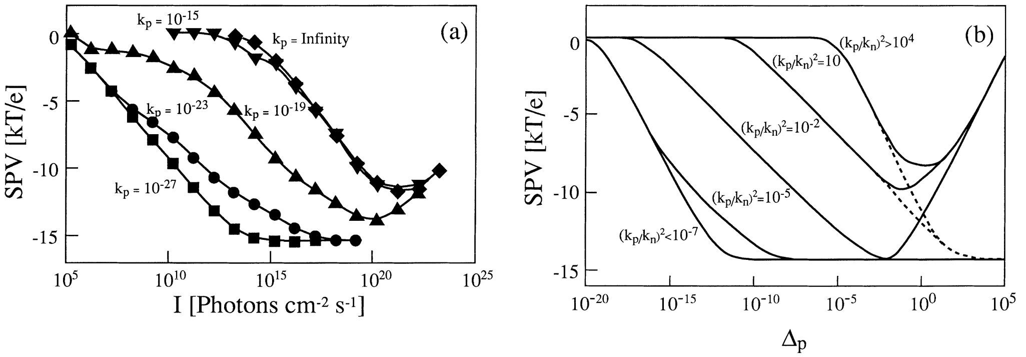

Fig. 70. Calculated steady state SPV $=f(I)$ curves for a $5\cdot 10^{16}$ cm^{-3} p-type GaAs sample, having a surface state located 0.87 eV above the valence band edge, with a density of $5\cdot 10^{11}$ states/cm^2, $k_n = 10^{-19}$ cm^2, and various k_p values (in cm^2). (a) Numerical calculations. (b) Analytical calculations (after Aphek et al. [611]).

An interesting and general observation is that all curves shown in Fig. 70 are bound between two envelope (i.e., limiting) curves on the left and right, corresponding to very small and very large values of k_p, respectively. Several asymptotic SPV regimes are common to all curves shown in the figure: For very low injection, the SPV is very small (i.e., less than kT/e). We refer to this regime as the 'null regime'. At some critical point, which is in the low-injection regime, but the value of which is different for the different curves, the (absolute value of the) SPV starts to rise in an approximately logarithmic manner. We refer to this regime as the 'logarithmic regime'. For large enough illumination intensities, the SPV of the low k_p curves saturates at a value which is indeed equal and opposite to V_s^0 over a certain interval of I values (the 'saturation regime'). For all curves, the (absolute value of the) SPV diminishes at very high intensities (the 'Dember interference regime').

The behavior of all different curves in Fig. 70 may be explained physically. Photo-excited excess carriers have been suggested to induce flattening of the surface band-bending via two distinct mechanisms: The first mechanism is screening of the surface charge by free carriers [22,66]. Namely, the photo-injection of majority carriers allows for a compensation of the surface state charge over a narrower SCR, i.e., the necessary Q_{sc} is accumulated over a smaller SCR width. The narrower the SCR, the smaller the band-bending is. Finally, under sufficiently intense illumination, the SCR width is expected to be negligible and the bands should become flat. The second mechanism is direct modification of the surface charge through carrier trapping [556,582]. The extent of this process is strongly dependent on the ratio of the surface state hole and electron capture coefficients, k_p/k_n. If the latter is large, the surface state captures holes more effectively than electrons and its charge tends to become more positive upon illumination. Similarly, if k_p/k_n is small, the surface charge tends to become more negative upon illumination.

The dependence of the second mechanism on k_p/k_n is the cause for the 'family of curves' in Fig. 70. For large k_p, the surface charge *increases* upon illumination, so band flattening may proceed only via screening, which necessarily requires high injection [611]. The smaller k_p is, the more effectively can the surface donor state capture electrons and hence diminish the surface charge. Thus, band-flattening is assisted (and at low enough k_p/k_n ratios dominated) by direct surface charge modification, which makes photosaturation obtainable at fairly low injection levels.

Not all curves in Fig. 70 saturate at the correct value for sufficiently high illumination intensity, due to the Dember effect [79,611]. As easily verified using Eq. (2.92), under high injection conditions, where the excess carrier density approaches the equilibrium majority carrier density, the Dember contribution to the measured SPV is non-negligible. The Dember contribution to the SPV is always positive (see Section 2.2.4). When it interferes with p-type SPV $= f(I)$ curves, a pseudo-saturation, at a value that is different from $-V_s^0$, should be observed over some intensity range. In the case of n-type samples, the Dember contribution should mask the photosaturation because the Dember voltage continues to increase even after the SCR-related SPV saturates.

Based on Fig. 70, the following picture emerges: In principle, sufficiently intense illumination *does flatten* the surface band bending, so that the theoretical concept behind the photosaturation approach *is valid*. However, important basic limitations arise, which preclude the attainment of V_s^0 from SPV $= f(I)$ curves in many practical cases. We now turn to analyzing the limitations of the photosaturation technique and the results of past photosaturation experiments, based on the foregoing discussion.

One problem associated with high-intensity illumination is that in many cases sample heating and/or surface photochemical processes may hinder the attainment of photosaturation, due to irreversible illumination-induced changes in the sample physical properties. Bruening et al. have estimated the error introduced by such changes by measuring SPV $= f(I)$ curves using both increasing and decreasing illumination intensity, and estimating the ensuing hysteresis [52]. This may limit the maximal illumination intensity which may be used. A practical limitation to the maximal intensity is imposed by the light sources available. As shown in Fig. 70, the illumination intensity required for the attainment of photosaturation varies over many orders of magnitude, depending on the surface state properties. The latter are seldom well-known a priori. Therefore, *the attainment of photosaturation cannot be guaranteed a priori and the experiment may fail.*

Many of the total or partial failures of the photosaturation technique can be understood on the basis of an inadequate illumination intensity coupled with an unfavorable k_p/k_n value. For example, analytical calculations similar to those behind Fig. 70 were performed in [610]. These calculations, which were restricted to a limited range of illumination intensities and cross-section ratios, predicted a *total* failure of the photosaturation technique. Let us consider the experiments of Flinn and Briggs, shown in Fig. 69, as another illustrative example. An upper limit for $\Delta p/I$ in their experiment may be found from Eq. (2.61), assuming $S = 0$, $\alpha L(1 + \alpha L) \rightarrow 1$, and using typical values for carrier mobility and lifetime in GaAs. Given the maximal illumination intensity used in their experiment (10^{18} $\mathrm{cm}^{-2}\,\mathrm{sec}^{-1}$), it turns out that the excess carrier density in the experiment was at least two orders of magnitude below the doping level (which was $3{\cdot}10^{15}$ cm^{-3}). It is therefore evident that strong injection was not obtained by Flinn and Briggs. Thus, band flattening by screening, as well as Dember-related effects, can be ruled out in the Flinn and Briggs experiment. Hence, it is clear that in those curves of Fig. 69 where saturation *was* observed, direct surface-charge modification, enabled via a favorable k_p/k_n ratio, was the saturating mechanism.

More information on the saturation mechanism at work can be obtained from considering the logarithmic regime, where the SPV is approximately given by [612]:

$$|\mathrm{SPV}| = \eta(kT/e)\ln(\mathrm{BI}), \tag{5.13}$$

where η and B are proportionality factors. Interestingly, a relation of the form of Eq. (5.13) is predicted for some illumination regime by all theoretical approaches, including calculations based on the depletion approximation [556], on barrier SPV [557], on a Schottky-diode approach [193,214], on the constant quasi Fermi level approximation [610,611], and even on the Dember effect [79,116]. Aphek et al. [611] have found that if k_p/k_n is either very large or very small, η will be approximately 1 (and in practice somewhat smaller [214]), whereas for intermediate values of k_p/k_n, η is approximately 0.5. These findings are in agreement with the physical prediction of Bednyi and Baidus [612], who interpreted η as being equivalent to the ideality factor in a Schottky diode. Accordingly, η should be ideal (i.e., 1) for a pure barrier SPV, and smaller than 1 when surface trapping of excess carriers is present. Similarly, $\eta \sim 2$ in the presence of significant bulk trapping, just like in a Schottky diode [366,612].

Since η is the slope of the $\mathrm{SPV} = f(I)$ curve on a semi-logarithmic plot, its value can be easily deduced from a given experiment and used to assess the dominating photosaturation mechanism. For example, the slopes of all $\mathrm{SPV} = f(I)$ curves in Fig. 69 related to *n*-type samples are within ±10% of 1. Since saturation is obtained for the oxygen-exposed sample and since screening is ruled out, we conclude that this curve, and probably the other two as well, are left (large k_p/k_n) envelope curves. As noted above, the curve of the oxygen and ozone exposed sample also seems to saturate, but this somewhat less pronounced saturation is not necessarily true. It may also be due to a cross-over from the large k_p/k_n to the intermediate k_p/k_n regime (compare with the $k_p = 10^{-23}$ cm^2 curve in Fig. 70). Such transitions provide another source for photosaturation misinterpretations. The curve slopes of the *p*-type samples in Fig. 69 are all within ±20% of -0.5. Therefore, they are probably intermediate k_p/k_n curves. Since saturation is harder to obtain at intermediate k_p/k_n curves than at left envelope curves, it is no surprise that saturation was not obtained at the *p*-type samples. Moreover, the illumination intensity at the rise point of the *p*-type curves is approximately four orders of magnitude larger than that at the rise points of the *n*-type curves. This is consistent with the predictions of Fig. 70, although the difference may also be due to a different injection ratio.

It is important to distinguish between direct- and indirect-gap materials in photosaturation attempts. The diffusion length in the former is usually considerably smaller than in the latter. Hence, using Eq. (2.61), we conclude that $\Delta p/I$ in direct-bandgap materials is such that large injection ratios are very difficult to obtain. In indirect-bandgap materials large injection ratios are easier to obtain, as long as S is not too large. Indeed, many photosaturation measurements of Si or Ge samples feature complete saturation [572,573,602], or at least a departure from the logarithmic regime at the highest intensities, which may indicate an approach to saturation [11].

Photosaturation is expected to be easier to obtain the smaller V_s^0 is. However, at very low band-bending, the SPV due to selective trapping of carriers at the surface may become dominant, in which case the SPV does not necessarily reflect V_s^0 even in sign (see Section 4.1). Kumar and Agarwal have calculated the importance of this effect for a-Si:H samples. They concluded that because of significant bulk trapping, Q_{sc} was not altered significantly and most of the SPV signal was due to selective carrier trapping at the surface, rather than due to a change in Q_{sc} [613]. This was demonstrated by various surface treatments which produced SPV changes uncorrelated with conductivity changes. They therefore concluded that the photosaturation technique is not suitable for a-Si:H at all. However, as noted above, Fig. 70 suggests that selective carrier trapping does not necessarily contradict photosaturation and that indeed it is frequently the dominating photosaturation mechanism. Moreover, the extent of the change in Q_{sc} is not necessarily negligible for *any* trap distribution envisaged or for *any* reasonable illumination intensity. Nevertheless, the work of Kumar and Agrawal does suggest that photosaturation measurements of amorphous semiconductors should be approached with even more caution than usual.

As discussed in Section 2.2.2, the SPV increases with decreasing temperature because thermal transitions, which compete with the optically-induced transitions, are suppressed. Thus, photosaturation should be easier to obtain at lower temperatures. For example, Mönch has shown that the SPV $= f(I)$ curve at the Si(111)-(7×7) surface, which is metallic in nature, does not saturate completely at room temperature, but features a very pronounced saturation at 85 K [11]. Similar trends have been observed at a-Si:H films by Foller et al. [577].

Much of the controversy surrounding the photosaturation technique is due to the work of Brillson et al., who studied the evolution of both CPD and SPV with metal overlayer thickness at different semiconductor surfaces [372,579–583]. Specifically, the results obtained at the Al/GaAs(1 1 0) interface [579,581,582], shown in Fig. 71 [582], were the source of a significant debate between Spicer et al. and Brillson [614–616]. Brillson interpreted the SPV obtained at the maximal photon intensity in Fig. 71(a) as indicative of $-V_s^0$. He therefore interpreted the increase of the SPV up to ~6 Å as indicating that the band bending at the Al/GaAs(1 1 0) interface does not reach its maximum value at sub-monolayer Al coverages. This was in direct conflict with the results of Spicer et al., obtained using PES [617]. In response, Spicer et al. [614] argued that, in the presence of a metallic overlayer, the SPV should be analyzed in terms of an illuminated Schottky barrier, rather than in terms of a free surface. They then argued that this precludes the achievement of photosaturation at the maximal illumination intensity used in Fig. 71(a). Moreover, Spicer et al. considered the lowest-intensity value in each of the curves in Fig. 71(a) as being due to surface states and not due to the bulk effect. Subtracting this value out produced a fairly constant SPV value, which Spicer et al. took as representing a constant V_s^0.

A closer look at the photosaturation data of Fig. 71(a) and at the debate between Spicer et al. and Brillson sheds some more light on photosaturation interpretations and misinterpretations: In Fig. 71(a), the low-coverage curves (e.g., the 0.7 Å overlayer curve) seem to approach saturation, which suggests that V_s^0 may be assessed. While this may indeed be the case, a different explanation should also be considered [611]. The most significant difference between the analytical model and the numerical simulations in Fig. 70 is that the numerically calculated $k_p = 10^{-19}$ cm^2 and $k_p = 10^{-23}$ cm^2 curves deviate rather strongly from the analytical ones. In the logarithmic regime, they feature an additional 'shoulder'. This is because in this region, the assumption of constant quasi-Fermi levels is not quite adequate. The 'shoulder' at the 0.7 Å in Fig. 71(a) is very reminiscent of the curve corresponding to

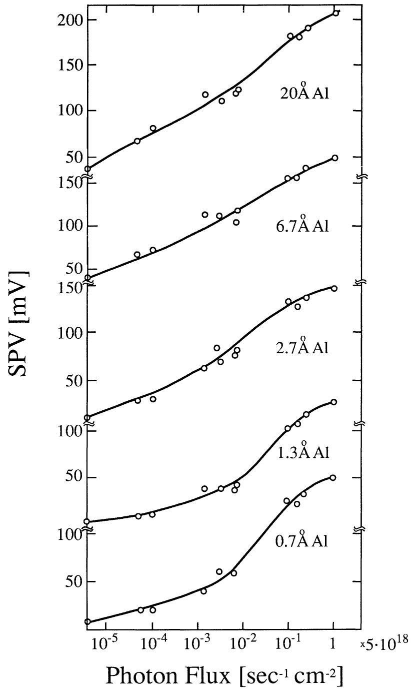

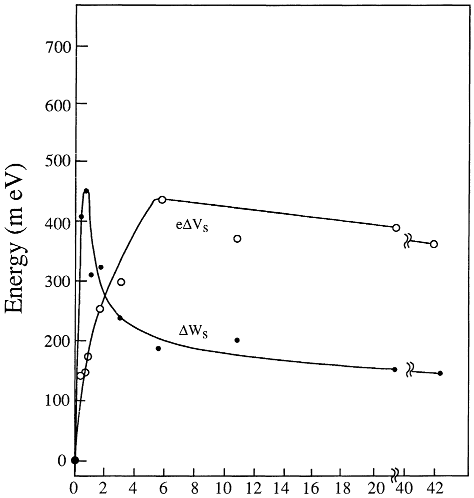

Fig. 71. (a) (top) Steady state SPV $= f(I)$ curves measured at a UHV-cleaved GaAs(110) surface, for various Al overlayer thicknesses. (b) (bottom) Variation of surface work function and saturated SPV signal vs. Al overlayer thickness (after Brillson and Kruger [582]).

$k_p = 10^{-19}$ cm^2 in Fig. 70(a). According to this explanation, the decreasing slope of the experimental curve at high intensities may be related to a return to the constant quasi-Fermi level approximation conditions, rather than to the attainment of 'real' photosaturation.

The saturation in Fig. 71(a) is more and more marginal with increasing overlayer intensity, until it is positively absent at the highest coverages (e.g., 20 Å), where the SPV $= f(I)$ curves do not deviate from the logarithmic regime even at the highest illumination intensities used. Accordingly, Brillson et al. have not considered the SPV values for thicknesses over ~6 Å as representing true saturation [582,615]. The attainment of photosaturation is indeed expected to be particularly difficult in the presence of a metallic overlayer. First, metal deposition typically increases the SRV and reduces the net photon flux entering the sample. Both effects decrease the $\Delta p/I$ ratio. Second, as the overlayer thickness increases, its properties are increasingly more 'metallic'. Therefore, in the case of a thick enough metal overlayer it is indeed more appropriate to analyze the SPV in terms of an illuminated Schottky junction, as suggested by Spicer et al. Nevertheless, an analysis in terms of surface state repopulation was correctly suggested by Brillson for thin overlayers, where metallic behavior is not established. Since, as argued above, photosaturation is frequently *dominated* by surface state repopulation, a subtraction of some of the surface state contribution, as performed by Spicer et al., is strictly forbidden. Accordingly, it seems that much of the debate between Spicer et al. and Brillson can be reduced to whether the overlayers can be considered as 'metallic' or not. Unfortunately, the onset of 'metallic behavior' is ill-defined and is frequently a subject of debate [618]. It can, however, be said that the thicker the overlayer is, the more difficult surface state repopulation (and hence the attainment of photosaturation) becomes. This is well reflected in Fig. 71(a). Since we have already concluded that photosaturation via screening is virtually impossible in steady-state measurements of GaAs, the effectiveness of the photosaturation technique for metal-covered GaAs surfaces is indeed very limited, and its use should be treated with the utmost caution.

As noted above, if strong injection *can* be obtained, saturation may be obscured by a 'parasitic' contribution of the Dember potential. This was already noted in the early studies of Williams. He noticed that the SPV $= f(I)$ taken at high-resistivity CdS samples (for which the Dember effect is more dominant – see Section 2.2.4) were insensitive to surface treatments. Upon calibrating Δ_p and subtracting the Dember contribution, he discovered that the SCR-related SPV was practically negligible at all illumination intensities. He therefore concluded that, under the conditions studied, the band bending at such samples was negligible.

Zuev et al. used high-intensity, pulsed illumination for constructing SPV $= f(I)$ curves at high-resistivity indirect bandgap semiconductor (Si and Ge) surfaces [573]. This combination allowed them to obtain very high injection ratios. Thus, they observed the logarithmic regime, the saturation regime, and at very high intensities a Dember interference, just like in Fig. 70. In the Dember interference regime, the (absolute value of the) SPV response decreased for *p*-type samples and increased for *n*-type samples, as appropriate.

While in the measurements of Zuev et al. a saturation regime could be clearly identified, Fig. 70 shows that this is not necessarily the case. In principle, if a Dember interference is observed, it may be subtracted, with the ensuing curve re-examined for saturation [562,574]. This subtraction requires knowledge of Δ_p for any illumination level, which is usually achieved via extra photoconductivity measurements. Unfortunately, measurements or calculations of Δ_p in intermediate and strong injection are often complicated by, e.g., changing lifetimes and various ambipolar effects [90,573]. Thus, Dember-contribution subtraction is not fail-safe either.

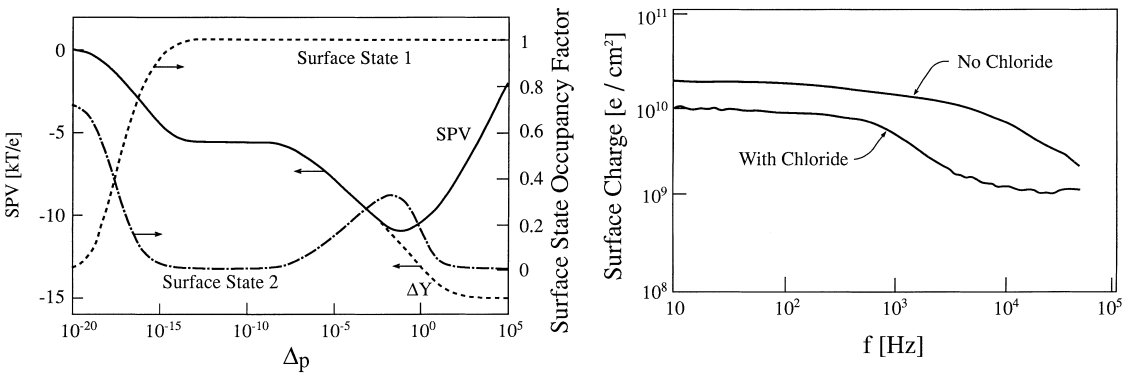

Fig. 72. (a) Intensity-resolved pseudo-saturation: Calculated steady-state SPV $=f(\Delta_p)$ curve for a p-GaAs sample with surface states at two energy levels (0.65 and 0.45 eV above the valence band edge), which have an equal density of $4 \cdot 10^{11}$ cm^{-2} and different k_p/k_n ratios (10^{-4} and 10, respectively). Solid line – SPV. Dashed line – fractional population of surface state 1. Dash-dotted line – fractional population of surface state 2 (after Aphek et al. [611]). (b) Frequency-resolved pseudo-saturation: frequency dispersion curves of the surface charge, measured by saturation SPV, at Si wafers, with and without chloride treatment (after Sherry et al. [598]).

Foller et al. suggested another means for detecting a Dember contribution [577]. They measured SPV $=f(I)$ curves of a-Si:H films at various temperatures and discovered that the *x-axis* intercept of these curves depended exponentially on the temperature. For strongly absorbed light, the activation energy of this intercept was the same as the activation energy of the dark conductivity. This suggests a Dember contribution because of the dependence of the latter on the dark conductivity (see Eq. (2.92)).

So far, only surfaces dominated by a single surface state were considered. However, more complicated situations may arise. A calculated SPV $=f(\Delta_p)$ curve for a p-GaAs sample with two surface states, which have very different k_p/k_n ratios, is shown in Fig. 72(a) [611]. Under low injection conditions, a *pseudo-saturation* at which SPV $= -15 \cdot (kT/e) \neq -|V_s^0|$ is easily observed. The SPV remains constant for several orders of magnitudes of Δ_p before the second surface state influences the SPV $=f(\Delta_p)$ curve. Eventually, the real saturation, supposed to be obtained at Δ_p values which are about 15 *orders of magnitude* higher than those of the pseudo-saturation, is interfered by the Dember potential. This extreme pseudo-saturation is a direct result of the drastically different k_p/k_n ratios used in the calculation. At relatively low values of Δ_p, the state with $k_p/k_n = 1 \cdot 10^{-4}$ is filled entirely with electrons, so that its effect on band-bending is canceled. However, in the same injection range, the charge of the $k_p/k_n = 10$ state has neither been modified significantly nor screened effectively, so that complete flattening cannot be attained. (This is readily seen in the dependence of the states' fractional electron population on Δ_p, also shown in Fig. 72(a)). Note that the contributions of the two states to the band bending are *not* additive. Therefore, the pseudo-saturation value *cannot* be interpreted as the band-bending induced by the $k_p/k_n = 1 \cdot 10^{-4}$ state alone.

Since the 'temporary' flattening of the SPV $=f(\Delta_p)$ curve in Fig. 72(a) can be misinterpreted as a saturation, leading to a (possibly very significant) underestimate of V_s^0, saturated SPV values may indeed be interpreted as V_s^0 if and only if pseudo-saturation can be ruled out. Thus, one has to obtain complementary information about the surface state properties in order to assess whether such a scenario is realistic. Alternatively, if at all possible, it is preferred to measure the SPV $=f(\Delta_p)$ curve all the way to strong injection even if saturation of the curve is observed prior to that.

To the best of our knowledge, an SPV $=f(I)$ curve as in Fig. 72(a) has not been observed experimentally yet. However, a different kind of pseudo-saturation may explain errors in previously published investigations. Consider again a surface having two distinct surface states types, where the response of one state is slow and that of the other is fast. If the time between illumination and SPV measurement is such that steady-state conditions are not obtained, the fast surface state may be completely neutralized, whereas the slow surface state will retain its original charge. Under such conditions, the SPV $=f(I)$ curve will saturate due to the filling of the fast state. However, this saturation value will not be equal to $-V_s^0$ because the slow state is still charged and thus the bands are not flattened. Moreover, the *shape* of the SPV $=f(I)$ curve may change, so that an analysis of η can become misleading [331,353].

Even if band-flattening is achieved via screening, in which case the surface population under illumination is not important, photosaturation measurements obtained with pulsed or chopped illumination may still produce erroneous results. If the sample does not relax completely in the *dark* between consecutive illumination periods, the band bending measured by all but the first illumination pulse may be smaller than V_s^0. This effect has been demonstrated in several materials and dubbed the 'photo-memory' effect [564–570]. It should be particularly troublesome at low temperatures, where charge relaxation is more difficult.

A dependence of the saturation SPV on the illumination chopping frequency is indeed regularly observed (and used – Section 5.4 below) in Si wafers [509,586,595–601]. A typical dependence is shown in Fig. 72(b) [598], where the saturation SPV has been converted into an equivalent surface charge. Here, the decrease of the SPV with increasing chopping frequency is due to a mechanism similar to the 'photo-memory' effect. During illumination, the surface states trap minority carriers, which reduce the surface charge and surface band-bending. At higher frequencies, the surface states do not have sufficient time in the dark to re-emit these charges. Therefore, measurements which are slow enough with respect to the surface state response are *essential* to obtaining meaningful photosaturation data.

The most simple means of avoiding temporal problems in photosaturation curves is to ascertain that all SPV measurements are conducted under steady-state conditions, possibly by studying the transient SPV response. However, this apparently simple solution has some significant disadvantages as well. First, higher illumination intensities may be obtained with pulsed illumination. Second, heating and photochemistry effects are reduced due to the limited light–sample interaction time. Thus, if steady-state SPV measurements do not yield satisfactory results, non-steady-state SPV measurements may be attempted. However, in the latter case the frequency-dispersion of the saturated SPV taken using non-steady-state SPV, as well as possible 'photo-memory' effects, have to be investigated.

Many of the past photosaturation measurements may have suffered from the 'temporal pseudo-saturation' problem. For example, in the measurements shown in Fig. 69, Flinn and Briggs used 5 ms illumination pulses because the use of pulsed illumination greatly reduced sample heating. However, they reported a SPV relaxation time of the order of minutes [561]. Thus, the V_s^0 values reported by them may underestimate the real ones, even in curves where good saturation with illumination intensity was observed.

Having understood the difficulties associated with obtaining a 'true' photosaturation, the question arises whether V_s^0 can be found even from an 'incomplete' photosaturation curve. If photosaturation is *not* obtained, the only information in the SPV $=f(I)$ curves of Fig. 70 is in the rise point. This is because identical curve slopes correspond to many different surface conditions, as explained above.

Unfortunately, the same rise point can be obtained for different combinations of V_s^0, k_p/k_n, and surface state density. Therefore, a rigorous extraction of V_s^0 in the absence of photosaturation is, in general, impossible. Aphek et al. [611] suggested that one possibility for 'forcing' the SPV $= f(I)$ curve to saturate is the 'artificial' manipulation of k_p/k_n through the simultaneous use of super- and sub-bandgap illumination. The latter may add illumination-induced transitions to/from the surface state, thereby assisting in surface charge neutralization. If the sub-bandgap illumination wavelength and intensity are properly selected, it may change the effective k_p/k_n so as to be more favorable with respect to photosaturation. This approach has yet to be tested experimentally.

Finally, we note that due to the significant limitations discussed above, the photosaturation technique has fallen into disrepute, despite its numerous successes. This section shows that, while photosaturation results should indeed be interpreted very carefully, they *can* be used successfully in a wide array of applications, if analyzed with sufficient care.

5.2.2. *Surface band bending – other methods*

Many of the problems associated with steady-state photosaturation measurements can be circumvented if the measurements can be made at a constant Q_{ss}. The principal motivation for holding Q_{ss} 'artificially' constant is that under these conditions the SPV depends *only* on V_s^0 and Δ_n because it is reduced to a 'barrier SPV' (see Section 2.2.2). This condition can be realized experimentally if the surface potential is dominated by 'slow' surface states. Namely, the effective response time of surface potential variations due to surface state repopulation is much slower than that due to the bulk lifetime. In many direct bandgap materials this is a fair assumption since non-radiative lifetimes are typically significantly longer than radiative ones.

An elegant algorithm for extracting SPV $= f(I)$ by comparing constant-Q_{ss} and steady-state measurements has been suggested and demonstrated by Bednyi et al. [619]. These authors considered the case where the 'light-on' and 'light-off' transient SPV response has an initial fast component followed by a slow component, as in Fig. 73(a). Assuming that no change in Q_{ss} occurs during the initial, fast, SPV component, four critical points on the SPV transient curve can be defined. Two, denoted '0' and '2', correspond to steady-state conditions, in the dark and under illumination, respectively. The other two, denoted '1' and '3', correspond to 'barrier SPV' conditions, i.e., the bulk has already achieved steady-state, but Q_{ss} could not change yet. These four points can be placed on

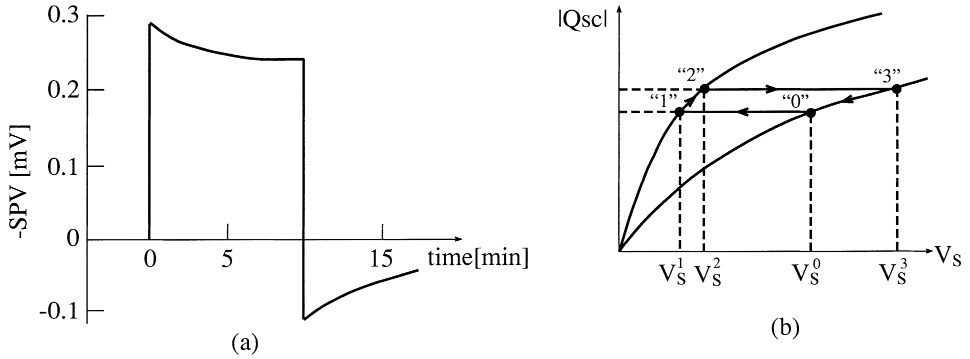

Fig. 73. Extraction of V_s^0 from a combination of constant-Q_{ss} and steady state measurements: (a) Super-bandgap SPV kinetics in p-type InP. (b) Space charge curves corresponding to the critical points in (a) (after Bednyi et al. [619]).

appropriate space charge curves, as in Fig. 73(b). Since Q_{ss}, and hence Q_{sc}, do not change between points ‘0’ and ‘1’, as well as between points ‘2’ and ‘3’, we obtain:

$$Q_{\mathrm{sc}}(0) = Q_{\mathrm{sc}}(1), \tag{5.14a}$$

$$Q_{\mathrm{sc}}(2) = Q_{\mathrm{sc}}(3). \tag{5.14b}$$

With Q_{sc} at the various points given by Eq. (2.52), the two equations (5.14) contain only two unknowns – V_{s}^0, the sought-after band-bending, and Δ_p, the injection level. Moreover, the reliability of the obtained V_{s}^0 value can be checked by using several illumination intensities, which induce different Δ_p values.

The success of Eq. (5.14) depends on the experimental identification of fast and slow SPV transient components, which is not always the case [620]. For example, if the slow component is missing, i.e., Q_{ss} does not change at all, Eq. (5.14) become dependent. In this case, we again suggest using sub-bandgap illumination for forcing changes in Q_{ss}.

An alternative approach, suitable for the case of constant-Q_{ss} measurements only, was suggested by Dittrich et al. [621]. They assumed the measured SPV to be the sum of a constant-Q_{ss} (i.e., ‘barrier SPV’) term and a Dember term. Using two light intensities and assuming a constant $\Delta n/I$ ratio, they obtained three equations for three variables – V_{s}^0, and Δ_n at the two illumination intensities. While elegant, this algorithm also has some drawbacks: Aphek et al. have shown that before saturation is approached, and where the Dember effect is negligible, these three equations become practically dependent, and no solution can be obtained [611]. Therefore, the attainment of Dember interference is a must in this approach. As shown above, a non-negligible Dember term requires a substantial injection ratio. Fortunately, such injection is easier to achieve in the non-steady-state measurements, aimed at preserving the value of Q_{ss} because pulsed illumination sources can be used. However, the assumption of a constant $\Delta n/I$ ratio at injection levels, which are high enough for Dember interference to be significant, is problematic and should be approached with caution.

A precursor of the approach of Dittrich et al. was suggested many years earlier by Heilig [622]. Heilig noted that if V_{s}^0 is not too small, a *minimum* is found in the transient SPV response obtained after excitation with a high-intensity laser pulse of *p*-type samples. This was due to the opposite signs of the Dember voltage and the SCR-related SPV in *p*-type samples, and the change of the relative contribution of the two with decreasing excess carrier density. From the value of the SPV at the minimum, V_{s}^0 could be inferred if a constant Q_{ss} (or, alternatively, a specific surface trapping model) was assumed. The limitations of Heilig's approach are essentially very similar to that of suggested by Dittrich et al., but Heilig's approach is also limited to *p*-type samples where a minimum in the SPV transient is experimentally obtained.

In general, approaches which utilize a constant Q_{ss} alleviate most of the difficulties associated with the photosaturation technique. First, complete flattening of the bands is no longer required for extraction of V_{s}^0. Second, due to the use of pulsed illumination higher intensities may be achieved and parasitic effects (photochemistry, heating) are diminished. Third, Dember interference may become an asset rather than a liability. Finally, pseudo-saturation is inherently eliminated. Thus, these methods are more robust than steady-state photosaturation, at least for direct-bandgap semiconductors with slow surface states. The major disadvantage of constant Q_{ss} approaches is that they inherently assume a negligible density of fast surface states (i.e., states whose response time is similar to that of the bulk lifetime). This assumption is very difficult to verify. If this assumption is not valid, and the steady-state photosaturation method fails as well, we suggest that the best hope for extracting V_{s}^0 from ‘pure’ SPV measurements lies with analyzing *sub-bandgap* measurements (where the fast surface states may be probed directly), and using V_s^0 as a fitting parameter. One preliminary algorithm, which proves that the concept may in principle work, has been suggested by Kronik and Shapira [623]. This algorithm is described in Section 5.4 in the context of extracting surface state properties.

Several other SPV-based approaches, based on neither photosaturation nor a constant Q_{ss}, have been suggested. These techniques, described below, are less universal then those discussed so far, but provide relatively simple means for extracting V_s^0 where applicable.

An ac-SPV-based approach for determining the surface band-bending has been suggested by Kamieniecki [624,625] According to Eqs. (2.71b) and (2.80) of Section 2.2.2, if high-absorption, high-frequency, super-bandgap illumination is used in a MIS-structure-based measurement, the obtained SPV is given by [97]

$$|\mathrm{SPV}(\omega)| = \frac{eI}{C_{sc}\omega}. \tag{5.15}$$

Thus, if the effective photon flux, I is calibrated, the measured SPV directly yields the space-charge capacitance, C_{sc}. Since $C_{sc} = \epsilon/w$, where w is the SCR width, V_s^0 (and hence the total surface charge) can be immediately extracted, based on Eq. (2.33).

Kamienicki's approach is limited by the assumption that the equivalent capacitance, C_{eq}, in Eq. (2.73), is entirely due to the space charge capacitance. Thus, its use is limited to samples where other capacitance factors, e.g., surface states, can be neglected.

As ac-SPV-based measurements of w are contactless and non-destructive, they are at the heart of two commercial devices used for in-line inspection of Si wafers: the surface charge analyzer [234] (the discussion of which is deferred to Section 5.4.1) and the surface charge profiler [235]. The latter offers the possibility of measuring changes in w following various treatments as a means of estimating changes in the surface charge. This can be used for quality control of various processing steps. A key application is the in-line monitoring of various wafer cleaning steps [625–627], especially HF cleaning sequences. Other applications include the monitoring of surface metal contamination, investigation of surface stability (via time-resolved w measurements), and the investigation of oxide charge in oxidized Si wafers [626]. Another advantage of this approach is that because only low-intensity illumination is used, a possible influence of the illumination on the measured results (via, e.g., surface photochemistry or photo-desorption) is ruled out [625,628].

If the sample surface is in inversion, Kamieniecki's method no longer yields the surface potential, V_s^0 because w reaches a maximal, fixed value in the inversion regime [25]. This maximal value, however, can be used for determining the doping of the sample [628–630], using standard MIS-related formulas [25]. Assuming that a given sample surface is in inversion both before and after a certain treatment, any changes in w must indicate a change in the sub-surface contamination level [628–630]. In a recent example, Roman et al. monitored the effective sub-surface p-type doping concentration in boron-doped Si wafers [630]. Boron can be deactivated by pairing with hydrogen or metals, particularly Cu and Fe, all of which may originate from surface polishing processes. The degree of deactivation can be quantified based on the increase in w following the polishing step. Roman et al. found this deactivation to decay exponentially with increasing annealing temperature. The obtained activation energy was equal to the boron-hydrogen dissociation energy, indicating the latter contaminant as responsible for the sub-surface doping decrease. Use of the same approach with metal-contaminated 1% HF solutions yielded a detection limit as low as 1 ppb for silver and gold and 10 ppb for copper [628].

A different approach for extracting w, and hence V_s^0, relies on the diffusion length measurements discussed in the preceding section: As discussed there, L_{app} is influenced by w if condition (5.7b), $w \ll L$, is not satisfied. Several groups have demonstrated that if a sophisticated enough mathematical analysis of L_{app} is applied, both L and w can be extratced [467,472,523].

For metal–semiconductor junctions, Schlaf et al. [248] suggested that the Schottky barrier height, ϕ_{b} (see Section 2.1.5), and hence V_s^0 (see Fig. 7), can be deduced from SPV measurements, based on the thermionic emission equation [25]:

$$J = A^* T^2 \exp\left(-\frac{e\phi_b}{kT}\right)\left[\exp\left(\frac{eV}{kT}\right) - 1\right], \tag{5.16}$$

where J is the minority carrier current density and A^* the Richardson constant. Schlaf et al. assumed that under open-circuit conditions, V is the SPV and J is J_{ph} (the limitations of this assumption were already discussed at length in Section 2.2.2). Thus, both ϕ_{b} and J_{ph} can be fitted using Eq. (5.16) based on the temperature dependence of the SPV (assuming that the fitted quantities are temperature-independent).

Recently, Yan applied the same approach to the study of V_s^0 at a free semiconductor surface [631]. However, it is very important to realize that due to the different nature of the boundary, the temperature dependence of the SPV at a free and metallized surface is *not* the same. For example, for SPV$\ll kT/e$, Eq. (5.16) reduces to:

$$\ln(T\text{SPV}) = \ln\left(\frac{kJ_{\text{ph}}}{eA^*}\right) + \frac{e\phi_{\text{b}}}{kT}, \tag{5.17}$$

whereas a combination of Eq. (2.61) with the small-SPV approximation of Eq. (2.52), yields [12]:

$$\text{SPV} = I \cdot \frac{kT \exp(-eV/kT)\alpha L}{en_{\text{b}}(S + D/L)(1 + \alpha L)} \quad \text{for a depleted surface,} \tag{5.18a}$$

$$\text{SPV} = I \cdot \frac{kTn_{\text{b}}\alpha L}{en_{\text{i}}^2(S + D/L)(1 + \alpha L)} \quad \text{for an inverted surface.} \tag{5.18b}$$

Since $\delta n(w)$ is proportional to J_{ph} (Eq. (2.69)), it is readily observed that the temperature dependence of the SPV in Eq. (5.18) is somewhat different than that of Eq. (5.17) even for a depleted surface, and very different for an inverted surface.

Several other V_s^0-extracting techniques, which combine SPV with additional *contact* measurements have also been suggested. For example, Johnson suggested early on that if Q_{ss} is assumed to be constant, additional photoconductivity measurements may be used in order to directly calibrate Δ_n [66]. Then, V_s^0 is easily extracted from Eq. (2.52) [632]. However, Ewing and Hunter have shown that this simple approach will rarely yield the true V_s^0 in the presence of surface states [633]. More recently, Karpovich et al. suggested that V_s^0 can be found by combining *surface* photoconductivity and SPV measurements [341]. The surface conductivity depends on the SCR width, which, in turn, depends on $V_s \equiv V_s^0 + \text{SPV}$. Therefore, the measured difference in surface conductivity values in the dark and under illumination yields an algebraic equation for the single unknown, V_s^0. These simple approaches naturally require additional contacts.

Other authors have offered to use SPV in conjunction with additional *contactless* measurements. For example, it has been shown that the SPV signal can be used to assess the attainment of flat-band conditions imposed by an external bias [634,635]. This approach, however, is expected to have a fairly large measurement error in the presence of preferential surface trapping because, as discussed in Sections 2.2.2 and 4.1, the SPV at flat-band conditions is not necessarily zero under such conditions. (We note in passing that by measuring the SPV at *extreme* bias-induced band-bendings, i.e., accumulation and strong inversion,the doping and mobility ratio of the sample under study can also be assessed [636].) Galbraith and Fischer combined SPV and CPD measurements at room temperature and at low temperature for extracting V_s^0 [193]. However, their approach, which assumed (among other things) a Schottky-like mechanism of thermionic emission and a constant surface charge, is very non-general in nature. Further approaches which combine SPV and CPD measurements to extract V_s^0 are given in the following section, within the context of the surface dipole.

So far, we have discussed why photosaturation is not always obtained, what misinterpretations should be avoided, and what alternative measures for extracting V_s^0 may be taken. However, in many studies (see, e.g., [55,607–609,637]) the exact value of V_s^0 was not very important. Instead, SPV changes upon different surface treatments were taken to reflect the trends of V_s^0 even if complete saturation was not ascertained. It is very important to realize that this is not necessarily true. The essential problem, already mentioned in Section 4, is that SPV changes may also arise, at least partly, from changes in the SRV.

The assignment of SPV changes to changes in V_s^0 is valid only if additional information on the SRV is available. Several examples follow. Koenders et al. found that the SPV at cleaved InP(110) surfaces increases monotonously with increasing oxygen exposure [637]. The latter is well-known to *increase* the SRV, which should have *decreased* the SPV. Therefore, an increase in the SPV can be safely associated with an increase in V_s^0. Similar conclusions apply to the data of Brillson and Kruger [582], shown in Fig. 71. Since Al deposition is known to increase the SRV, the SPV increase with increasing overlayer thickness reflects an increase in V_s^0 even if the SPV is not saturated. Cohen et al. augmented SPV measurements with independent time-resolved PL measurements [55]. The latter showed that the SRV did not change appreciably with surface treatment, which made the assignment of the SPV changes to V_s^0 changes legitimate. Munakata et al. devoted a series of studies to the effect of various contamination sources on the ac SPV in Si wafers [228–231,638–647]. Although in their studies no attempt at saturation was made, and no specific tests of SRV effects were made, an overwhelming correlation between the measured SPV and the concentration of the contaminating species was found. This strongly supports that the increase in SPV is due to an increase of surface charge (and hence V_s^0), as suggested by the authors.

So far, our discussion here has been devoted solely to SPV-based means of extracting V_s^0. However, as already noted in Section 3.3.2, most experimental determinations of V_s^0 are actually performed using PES (see Fig. 32). As long as we are concerned with the *equilibrium* band bending, such measurements do not rely on the surface photovoltaic effect. Therefore, they are not covered here, despite their obvious usefulness. It should be noted, however, that PES has several important disadvantages as well. First, due to the need for electron emission it may only be operated in sufficiently high vacuum, which limits the range of surfaces it may be applied to. Second, its accuracy is typically limited to 100–150 mV.

Combining PES and PES-based SPV, Jaegermann et al. have simultaneously measured both V_s^0 and the SPV as a function of various adsorbates, especially on layered metal chalcogenide semiconductors [248,648–654]. The comparison of the two quantities made it possible to obtain *direct* information on the relative importance of band-bending and recombination effects in determining the SPV. Somewhat similarly, Alperovich et al. used photoreflectance for quantitative and qualitative assessment of V_s^0 and SPV trends, respectively, upon Cs and O adsorption on GaAs(100) [254].

A different interesting link between PES and SPV was established in recent years: Although observed at times before that [655,656], in the early 1990s it has been systematically shown that PES results may be influenced by a *parasitic* surface photovoltaic effect [16–18]. Namely, the exciting UV or X-ray radiation source causes changes in the surface potential and therefore the measured band-bending is smaller than the true equilibrium value, possibly very significantly. This is especially true at low temperatures, where the SPV is more sizable in general. Neglecting to take this effect into account can lead to serious misinterpretations of experimental data. Therefore, a sizable body of literature devoted to observing this effect, correcting for it, and even exploiting it has evolved. A detailed discussion of the parasitic SPV effect is outside the scope of the present text. The interested reader is referred to, e.g., [16–18,655–674] for further details. Similar parasitic SPV effects in photoreflectance, i.e., an influence of the probe beam on the band-bending, have also been noted. The reader is referred to [675,676] for a detailed discussion.

5.2.3. Surface dipole

In general, any surface chemical reaction can induce changes in both the surface band-bending, V_s^0, and the surface dipole, $\Delta\phi_s$. Both changes contribute to changing the surface work function, W_s (see Fig. 4 and Eq. (2.36)). Therefore, surface-induced changes in W_s can be expressed as:

$$\Delta W_s = \Delta V_s^0 + \Delta(\Delta\phi_s). \tag{5.19}$$

Any changes in W_s can be measured with the Kelvin probe by detecting CPD differences before and after surface reaction. In addition, V_s^0 can be measured before and after the reaction, either by photosaturation or by any of the other means discussed in the preceding sub-section. Thus, $\Delta(\Delta\phi_s)$ can be determined by simple subtraction using Eq. (5.19).

A few comments are in order. First, unlike the surface band-bending, the surface dipole is generally not influenced by illumination. This is because the inherently small width (ideally a monolayer) of the latter and the strong bonding of its charge lead to its stability under external excitation [24]. Thus, SPV measurements are 'blind' to $\Delta\phi_s$. It is this property which makes it possible to consider SPV-based approaches for extracting V_s^0 without having to worry about the surface dipole. Second, several authors interpreted treatment-induced W_s changes at GaAs [677,678], InP [679], and diamond [680,681] surfaces as being due to changes in the band-bending *alone*. While this may be true in some cases, surface dipole changes *cannot* be ruled out in the general case. Thus, such interpretation can be trusted only if it accompanied by complementary evidence, e.g., of PES measurements [681]. Third, usually only *changes* in $\Delta\phi_s$, rather than its absolute value, are sought. This is because, as explained in Section 2.1.4, the absolute value of $\Delta\phi_s$ has to do with the value of the 'ideal' (as opposed to the surface) affinity, χ, which is almost always unknown. Fourth, the above-explained approach was frequently utilized by employing Kelvin probe and PES measurements for measuring ΔW_s and ΔV_s^0, respectively. A review of such studies may be found in [11]. Here, we naturally concentrate on studies which employed SPV measurements.

Combined SPV and work function measurements have been used in the context described above as early as the 1960s by Campbell and Farnsworth, who studied the effects of oxidation on the band-diagram of CdS surfaces [609]. This approach was put to much use by Brillson et al. for their studies of the formation of metal-semiconductor interfaces, already mentioned in Section 5.2.1. An example of the evolution of the saturated SPV and the surface work-function (measured by a Kelvin probe) is given in Fig. 71(b). When studying *interfaces*, rather than *surfaces*, Eq. (2.36) must be used with caution because the overlayer may have both a surface and an interface dipole. Brillson et al. therefore assumed that the magnitude of the *interface* dipole is best approximated by the $\Delta W_s - \Delta V_s^0$ value found where ΔW_s is maximal ($\sim$1/2 monolayer in the case shown in Fig. 71(b). This is because the distinction between surface and interface is not in effect yet for such thin overlayers. Using this approach, Brillson et al. detected significant changes in both SPV and CPD evolution between, e.g., the Al/GaAs and the Al/CdS interfaces [580], or the Al/ZnO and the Au/ZnO interfaces [583]. These differences were correlated with significant differences in the chemistry of III–V versus II–VI semiconductors and of reactive versus unreactive metals, respectively.

One of the key arguments against Brillson's claims of achieving photosaturation was that the measured V_s^0 values in Fig. 71(b) do not yield the correct Schottky barrier height of the Al/GaAs interface (with a similar problem in other interfaces as well) [614]. Interestingly, the sum of the SPV-measured V_s^0 and the interface dipole *did* yield the correct barrier height [615] This is intriguing since in the abrupt metal/semiconductor band-diagram, shown in Fig. 7, the Schottky barrier height should *not* depend explicitly on the interface dipole. This independence, easily confirmed graphically from Fig. 7(b), is also physically reasonable because the abrupt interface dipole should be transparent to electron tunneling and therefore should not pose a barrier to transport [614]. Brillson suggested that the interface dipole is *not* atomically abrupt, but is still insensitive to illumination, due to a high density of states associated with the local charge redistribution [582]. A more detailed discussion of the true nature of this interface is outside the scope of the present text. It is interesting to note, however, that a somewhat similar argument was used by Jaegermann et al. to explain an SPV which was much smaller than that anticipated from the band bending at the Cu/*p*-WSe_2(0001) interface [651]. There, it is argued that Cu intercalation may result in a thin near-surface layer which contributes to the band-bending, but not to the SPV.

A combination of CPD and saturated-SPV measurements was used in recent years by Cahen et al. for deducing the systematic effects of various organic ligands to semiconductor surfaces on the band-bending and surface dipole at $CuInSe_2$ [50,51,54], CdTe [50,51,55,56], CdSe [52], GaAs [53], and Si [57] surfaces. Organic ligands are an attractive alternative to the inorganic treatments usually used for surface control. This is because organic ligands feature structural versatility and flexibility, may be designed to incorporate several properties simultaneously, and potentially allow systematic modifications of one specific property independent of the others [54,56].

As an illustrative example of the above concepts, consider the modification of a CdTe surface upon adsorption of dycarboxylic acid derivatives which include a polar group, consisting of para-subsituted phenyl rings [56]. Fig. 74(a) shows that the changes in the surface dipole are linearly correlated to the average dipole moment of the ligand polar group. A linear correlation between the change in surface dipole and the dipole moment of the adsorbed ligands, expected from Eq. (2.39), was found in all cases studied. However, when ligand molecules more complicated than simple benzoic acids were used, a *constant* offset, not predicted by this equation, was also found. This offset was attributed to an additional dipole moment due to the binding group of the ligands and/or to the dipole due to the bond formed between the surface and the ligand. The latter can often be calculated from known eletronegativities [54]. Fig. 74(b) shows that changes in the band-bending at the same surface are related to the position of the lowest unoccupied molecular orbital (LUMO) of the phenyl substituents. The closer the energy position of the LUMO to the CdTe surface states, the stronger is the molecule–

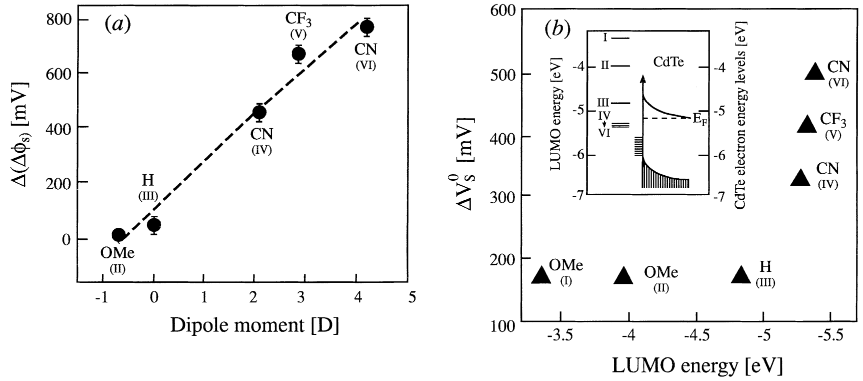

Fig. 74. (a) Changes in surface dipole of a CdTe crystal upon adsorption of dycarboxylic acid derivatives as a function of the average dipole moment of the polar group of the ligand, consisting of para-substituted phenyl rings (ligand dipole moment given in Debye – $1D \equiv 3.336 \cdot 10^{-30}$ C· m). (b) Changes in surface band-bending of the same surface upon adsorption of the same set of molecules (with respect to $V_s^0 = -610$ mV), as a function of the LUMO energies of the phenyl substituents (which are shown for clarity in the inset) (after Cohen et al. [56]).

surface-state orbital interaction. As a result, occupied surface states are pushed down in energy so that some of them move inside the valence band. This decreases the localized surface charge and hence the band bending. Thus, Fig. 74 shows that an organic molecule which provides a desired surface band-bending and dipole can potentially be *designed* on the basis of its dipole moment and ionization potential.

Interestingly, organic molecules sometimes exhibit a *photo-dipole*, i.e., photo-induced changes in their dipole moment. Then, any photo-induced change in the CPD may partly reflect a photo-dipole, in addition to changes in band-bending. This has been elegantly demonstrated by Gatos et al., who measured a non-zero change in CPD upon illumination of an Au surface adsorbed with dye molecules [374]. Since there is no band-bending in a metal, the observed changes were clearly due to change in the surface dipole. If photo-dipole effects are present, the approach outlined above for separating between ΔV_s^0 and $\Delta(\Delta\phi_s)$, which assumes an illumination-independence of the latter, is invalid.

In all studies mentioned so far, the combination of SPV and CPD approaches was always performed before and after some surface reaction, but never *during* the reaction. This is because, obviously, one cannot follow the evolution of the work function in the dark and under intense illumination simultaneously. Fefer et al. removed this obstacle by suggesting a ‘time sharing’ between dark and illumination during the response [682]. Their approach is shown schematically in Fig. 75. As long as the illumination response time is short with respect to the chemical response time (which is frequently the case), periods of darkness can be punctuated by periods of intense illumination, resulting in a W_s evolution which resembles a pulse train. The evolution of the work function in the dark is then deduced from the periods of non-illumination, whereas the evolution of the band-bending is deduced from the magnitude of the individual ‘pulses’ (subject, of course, to the limitation that photosaturation is reasonably approached).

Fig. 75 schematically shows three surface work function curves as a function of time: In Curve (a) the surface reaction changes the surface dipole, but not the band bending. Hence, the dark value of the work function changes, but the height of the illumination-induced ‘pulses’ does not. Visually, the ‘pulse envelope’ (dashed curve) follows the ‘dark’ Curve. In curve (b), the surface reaction changes the band

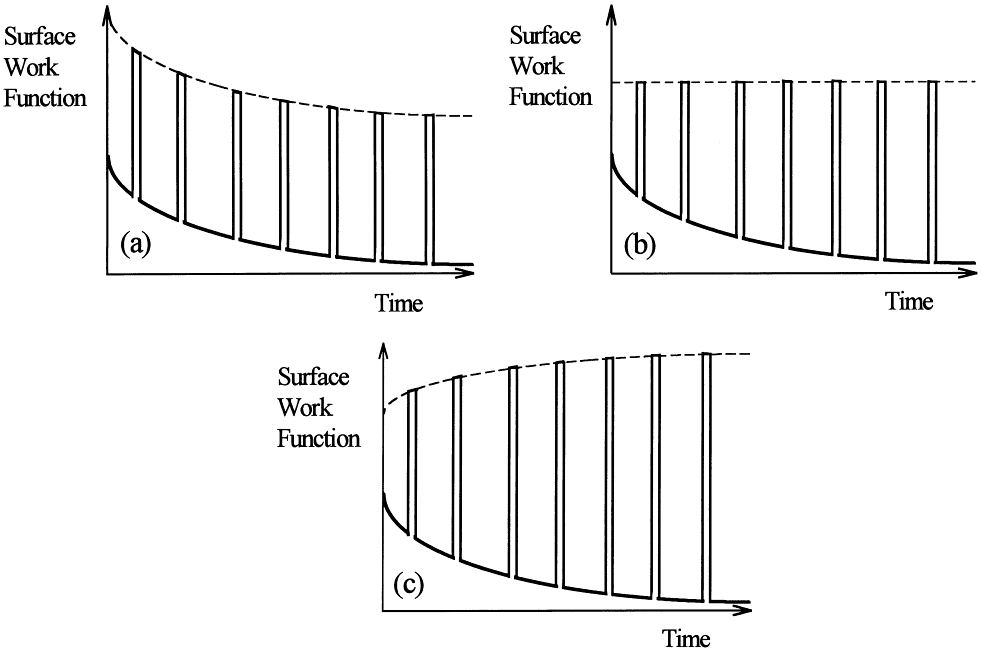

Fig. 75. Schematic work function vs. time curves during a surface reaction, with periodic illumination: (a) Change in surface dipole, no change in surface band bending. (b) No change in surface dipole, change in surface band bending. (c) Change in both surface dipole and surface band bending (afer Fefer et al. [682]).

bending, but not the surface dipole. Hence, the change in the 'dark' work function is equal and opposite to the change in 'pulse' height. Visually, the 'pulse envelope' is constant. Curve (c) depicts a general case where both dipole and band bending change.

In some special cases, a separation between the relative contribution of ΔV_s^0 and $\Delta(\Delta\phi_s)$ to CPD changes (see Eq. (5.19)) can be made *without* resorting to photosaturation experiments. This direction has been pursued by Lassabatere et al., who used scanning CPD and SPV measurements to characterize cleaved, metal- and oxygen-adsorbed surfaces of III–V semiconductors [610,683–692].

As already mentioned in Section 4.2 (see Fig. 42 and its discussion), the clean, UHV-cleaved surface of GaAs and InP is supposed to be unpinned, i.e., have a negligible band-bending. In practice, some residual band-bending, which is due to imperfect cleavage, remains. CPD mapping, performed by Lassabatere et al., confirmed that indeed work function differences of many hundreds of meV do exist across the cleaved surface at both *n*- and *p*-type GaAs and InP samples [683–689]. The corresponding (unsaturated) SPV map was linearly correlated to the CPD changes, as shown in Fig. 76 for the case of the GaAs(110) surface [689]. This linearity suggests that most of the change in work function is due to a change in band bending, rather than in surface dipole. Moreover, changes in $\Delta\phi_s$ are expected to be independent of the sample type, and hence cause opposite deviations from linearity in *n*- and *p*-type samples. Such opposite deviations were not observed. The authors therefore concluded that the surface dipole did not change appreciably across the cleaved surface. This made it possible to assign the (extrapolated) CPD, at which the SPV is zero, to the flat-band point. The validity of this assignment is strongly supported by the fact that the difference between the flat-band CPDs at the *n*- and *p*-type

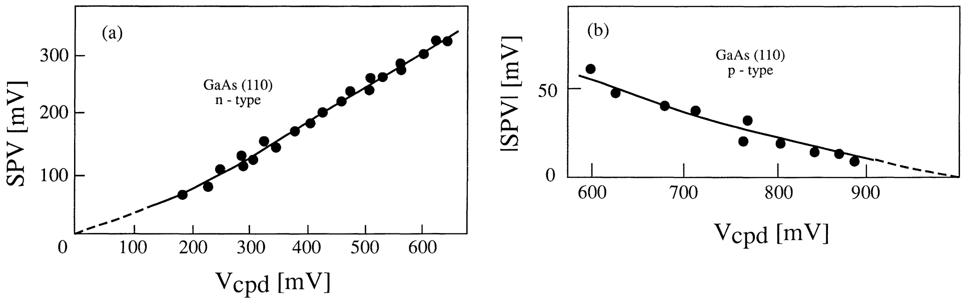

Fig. 76. SPV vs. CPD along the surface of (a) n-type and (b) p-type GaAs(110) UHV-cleaved samples. Zero CPD corresponds to an n-type sample with no band-bending (after Ismail et al. [689]).

surfaces is in excellent agreement with the difference of the *bulk* Fermi level positions of the n- and p-type samples.

Interestingly, an extension of this approach to UHV-cleaved n-GaP surfaces, generally assumed to be pinned, yielded very similar results [691]. This suggests that the GaP surface may be more similar to the GaAs and InP surfaces then previously assumed, but is perhaps more sensitive to cleavage- and contamination-induced damages than the latter surfaces [691]. Lassabatere et al. generally observed a homogenization of the SPV after metal-deposition or oxygen-adsorption, so that the above-discussed approach could not be directly extended to these surfaces [683–689,692]. Usually, they assumed that the calibration factor between SPV and CPD found at the clean surface remained unaltered following deposition/adsorption. This made it possible to assess treatment-induced changes in V_s^0, and hence $\Delta\phi_S$. While this procedure led at times to good agreement with independent PES results [689], we note that it must be used with caution. As already observed several times, surface treatments frequently cause significant changes in the SRV, which should alter the dependence of the SPV on V_s^0.

We close this section by describing combined SPV and CPD measurements, used to distinguish between charges located at the Si/dielectric interface and the dielectric external surface at Si wafers. While not strictly a surface-dipole-type problem, it utilizes concepts which are very similar to those discussed above. According to Gauss's law, the surface charge calculated from the saturated SPV at Si dielectric-covered wafers is a measure of the *total* dielectric charge (at both its internal and external surfaces, as well as in its volume). Edelman et al. suggested that, neglecting volume charges, a distinction between internal and external surface charge is made possible by means of CPD measurements [585]. This is because further simple Gauss law considerations show that:

$$\mathrm{CPD} = \mathrm{const.} + V_s^0 + V_{\mathrm{ins}} = \mathrm{const.} + V_s^0 + Q_{\mathrm{ins}}/C_{\mathrm{ins}}. \tag{5.20}$$

Since V_s^0 can be found by saturated SPV mapping, Eq. (5.20) shows that the distribution of Q_{ins} can be easily determined by subtracting CPD and SPV maps. This approach was found to be highly useful by Nauka et al. [506,588,590] and Lowell et al. [594,598] in assessing the impact of various processing steps on the dielectric charge. Interestingly, an ostensibly similar approach (less scanning) was suggested by Buchheim et al. as early as 1977 [632]. These authors also suggested CPD and SPV *profiling* after successive etches of the dielectric as a means of determining the volume distribution of charges in the dielectric film.

5.3. Recombination rates

Carrier recombination rates, both in the bulk (expressed in terms of the excess carrier lifetime, τ) and at surfaces or interfaces (expressed in terms of the SRV), are extremely important for the characterization of semiconducting materials. Moreover, they are crucial for the design and analysis of semiconductor devices. In this section, we describe how SPV measurements can be used for the extraction of these important parameters.

The most obvious method for obtaining *direct* information on carrier recombination is to observe the relaxation of the SPV signal after switch-off of super-bandgap illumination. Such monitoring of the SPV decay provides a contactless alternative to conventional, contact-requiring PCD measurements. In addition, SPV monitoring is much simpler than contactless PCD versions, e.g., μPCD. This approach has been suggested and used as early as 1957 by Johnsnon [4], who extracted the same lifetime from SPV relaxation and PCD measurements on Ge samples. Interestingly, Johnson also measured the time-dependence of the SPV when the sample was illuminated from the back, in order to estimate the *transport* time across the sample. This is, in a sense, a contactless analogue of the well-known Haynes–Shockley experiment [90].

Johnson used a MIS structure for measuring the SPV relaxation. This is because the response time of Kelvin probe, with is typically a fraction of a second (see Section 3.1), is clearly inappropriate for following rapid transients. However, the minimum time resolution available with a MIS structure is ~0.1 μs at best (see Section 3.1). This value is still too large for many semiconductors, especially direct-bandgap ones. Thus, Johnson's work was not followed by other scientists. Only in 1996, Hlávka and Švehla attempted such measurements again, in the context of presenting improvements to the temporal resolution of MIS structures, already discussed in Section 3.2 [216].

In an important extension of Johnson's approach, Long et al. monitored the SPV relaxation of a Si(111) sample using PES [249]. With a temporal resolution of tens of ns, these authors had no difficulty in determining a bulk lifetime of 1.7 μs. Recently, Marsi et al. improved the temporal resolution of such experiments to a fraction of a ns [693]. This was achieved by using free electron laser illumination and synchrotron radiation, which are inherently synchronized, as the SPV excitation and measurement sources, respectively. We note in passing that the monitoring of signal relaxation at specific photoemission energies [694,695] is strongly influenced by SPV variations and serves as an indirect measure of typical relaxation times of the latter. However, such experiments are not strictly SPV measurements and are not discussed further here.

Just like PCD measurements, SPV relaxation curves involve both bulk and surface relaxation contributions, with no straight-forward means of separating the two. In fact, this problem is more severe in SPV than in PCD because the former is inherently more sensitive to surface effects. Surface effects in SPV relaxation curves were indeed found by several groups: Hlávka and Švehla clearly demonstrated the impact of surface-trapping effects on the SPV relaxation by showing that background illumination, which eliminated long relaxation times associated with surface trapping, reduced the apparent lifetime from 700 to 5 μs [216]. Long et al. found that the bulk-related SPV relaxation is followed by a long 'tail' of surface-related relaxation [249]. Using numerical fitting of the measured data, they were able to use this surface interference beneficially for deducing the SRV at the measured Si(111) surface. Marsi et al. found that the SPV relaxation on the sub-nsec scale at Si(111)-(2×1) samples is non-monotonous [693]. This was attributed by them to band-bending fluctuations, brought about by the different rate of charge flow to donor and acceptor surface states.

The distinction between bulk and surface recombination rates from the observation of SPV relaxation curves is difficult (both theoretically and experimentally). Therefore, several approaches which *directly* yield one or the other have been suggested. For a rigorous extraction of the *bulk* carrier lifetime, Munakata et al. developed an approach which is based on frequency-resolved, rather than time-resolved, ac SPV measurements [696]. These authors have limited their studies to Si, where diffusion lengths are relatively long. They therefore assumed that the effective SCR-edge SRV, S (which is not to be confused with the real SRV – see below), is much higher than the diffusion velocity, D/L. By using low-absorption illumination, they were therefore able to use Eq. (2.71a) for the photocurrent density, J_{ph}. They then used Eqs. (2.72) and (2.73) to express the SPV as:

$$\mathrm{SPV} = J_{\mathrm{ph}} Z_{\mathrm{eff}} = J_{\mathrm{ph}} \frac{1}{1/R_{\mathrm{eq}} + i\omega C_{\mathrm{eq}}} = eI\alpha \frac{1}{1/R_{\mathrm{eq}} + i\omega C_{\mathrm{eq}}} \cdot \frac{L(\omega = 0)}{\sqrt{1 + i\omega\tau}}. \tag{5.21}$$

A schematic, logarithmic scale drawing of the SPV versus frequency dependence, deduced from Eq. (5.21), is shown in Fig. 77(a) [696]. It features two 'knees'. The first, $\omega_{\mathrm{a}} = 1/R_{\mathrm{eq}}C_{\mathrm{eq}}$, is due to the effective impedance term, and is usually dominated by the SCR capacitance. The second, $\omega_{\mathrm{b}} = 1/\tau$, typically occurs at a higher frequency and can be used for *direct* determination of τ.

The above-derived approach implicitly assumes that R_{eq} and C_{eq} are frequency-independent. However, Munakata et al. have observed that this is not necessarily true, especially in the presence of a significant surface-state density [697,698]. Depending on sample properties, the above-described approach therefore ranged between being highly useful and completely useless, depending on the ability to identify ω_{a} and ω_{b} from an experimental curve. An example of the latter case is shown in Fig. 77(b) [697]. Even in this more difficult case, ω_{b} can still be extracted using a somewhat more complicated approach [697]. If high-absorption illumination, such that $\alpha L \gg 1$, is used, Eq. (2.71b)

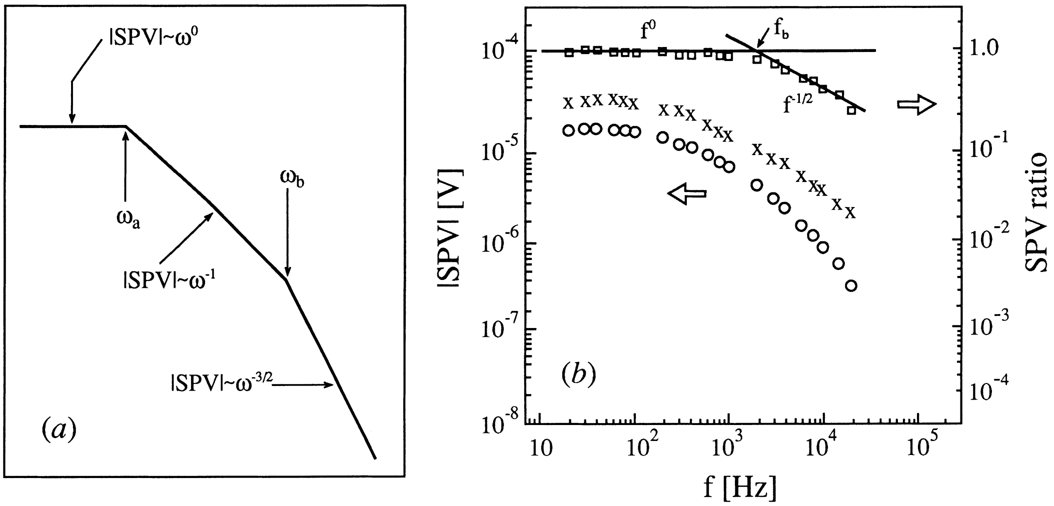

Fig. 77. (a) Schematic drawing of the SPV vs. modulation frequency (after Munakata et al. [696]). (b) Experimental SPV vs. modulation frequency curves at a Si sample with many surface states: x's – large α, circles – small α, squares – ratio of the two SPVs (after Honma et al. [697]).

can be used. The SPV is then given by:

$$\mathrm{SPV} = J_{\mathrm{ph}} Z_{\mathrm{eff}} = eI \frac{1}{1/R_{\mathrm{eq}} + i\omega C_{\mathrm{eq}}}. \tag{5.22}$$

Dividing Eq. (5.21) by Eq. (5.22), we obtain:

$$\frac{\mathrm{SPV}(\text{small}\,\alpha)}{\mathrm{SPV}(\text{large}\,\alpha)} = \text{const.} \cdot \frac{L(\omega = 0)}{\sqrt{1 + i\omega\tau}}, \tag{5.23}$$

i.e., the problematic impedance term is eliminated. As shown in Fig. 77(b), τ can be accurately determined from the SPV ratio even when no 'knee'-points are discernible in the normal low-absorption SPV versus frequency plot.

More recently, the same basic approach has been extended towards high-speed measurement of lifetime distribution *maps* [227]. If the detailed SPV versus ω plot is recorded at several points, so that the general position of ω_a and ω_b is fairly well known, ω_b at all other locations can be calculated by interpolation from the SPV at two frequencies only – one such that $\omega_a < \omega < \omega_b$, the other such that $\omega > \omega_b$.

The lifetime extraction technique of Munakata et al. is subject to the same set of limitations (Eq. (5.7)) as Goodman's diffusion length extraction technique. This is because both are based on the same equations, namely, Eqs. (2.60) and (2.61). Specifically, the obtained lifetimes have been shown to be prone to back surface effects if the sample is not much thicker than L [699–701]. Moreover, calibration charts for converting the apparent τ into the true one have been suggested [700], just like in L measurements.

While providing for an elimination of surface recombination contribution to the bulk recombination rate, the frequency-resolved approach of Munakata et al. does not remove the temporal resolution limitation, from which Johnson's original approach has suffered. Both measurements utilize the MIS structure and are thus limited by the same time-constants. Thus, it is no surprise that most scientists have preferred to extract τ by determining L using Goodman's approach and the using the relation $L \equiv \sqrt{D\tau}$.

An interesting means of surpassing the time-resolution limitations of the measurement device by utilizing the inherently non-linear dependence of the SPV on the illumination duration was suggested by Hamers and Cahill [702]. When using *pulsed* illumination, the longer the delay between subsequent pulses, the more time the excess carriers have to relax and the smaller the ensuing SPV signal is. Using a fast (ps) pulse train from a laser source, Hamers and Cahill measured the SPV as a function of pulse separation. The obtained dependence contained all information about the transient processes, even though all measurements were taken under steady-state conditions! This approach has been used by Hamers and Cahill only in the context of scanning probe microscopy and for extracting the lifetime associated with the junction impedance (i.e., $1/\omega_a$) at Si(111)–(7×7) surfaces. However, it is conceivable that with further research this elegant technique could be adapted to measurements of the *bulk* lifetime, using other experimental tools, in Si as well as in other materials.

We now turn our attention to techniques intended for extraction of the surface recombination rate. These can be broadly divided into methods which measure the *effective* SRV at the back SCR-edge, S (defined in Eq. (2.60)), and methods which measure the *real* SRV at the free semiconductor surface, s (defined in Eq. (2.21)). Both SRVs are similar in the sense that they are defined as a ratio of carrier current to the excess carrier density. However, s relies on the surface recombination rate and excess carrier density (for either type of carrier), whereas S relies on the *overall* minority carrier current and excess density at the back SCR-edge.

In order to get an idea on the relation between the minority carrier S and s, let us consider a p-type material, where we employ many of the simplifying assumptions used in previous developments: First, we neglect SCR generation-recombination processes, so that $J_n(0) = J_n(w)$ (see Eq. (2.62)). Then:

$$S = \frac{J_n(w)}{e\delta n(w)} = \frac{J_n(0)}{e\delta n(w)} = \frac{es\delta n(0)}{e\delta n(w)} = s \cdot \frac{\delta n(0)}{\delta n(w)}. \tag{5.24}$$

Using Eq. (2.8), Eq. (5.24) may be recast in the form:

$$\frac{S}{s} = \frac{\delta n(0)}{\delta n(w)} = \frac{\{\exp[(F_n(0) - E_{\mathrm{Fi}}(0))/(kT)] - 1\}}{\{\exp[(F_n(w) - E_{\mathrm{Fi}}(w))/(kT)] - 1\}}. \tag{5.25}$$

If $\delta n \gg n_i$, Eq. (5.25) is further reduced to:

$$\frac{S}{s} \simeq \exp\left[\frac{(F_n(0) - F_n(w)) - (E_{\mathrm{Fi}}(0) - E_{\mathrm{Fi}}(w))}{kT}\right]. \tag{5.26}$$

Assuming that the region at $x > w$ is quasi neutral, $E_{\mathrm{Fi}}(0) - E_{\mathrm{Fi}}(w) = eV_{\mathrm{s}}$, where V_{s} is the *non-equilibrium* surface potential. Using the QFL approximation, $F_n(0) = F_n(w)$. Inserting these relations into Eq. (5.26) yields a very simple result:

$$\frac{S}{s} = \exp\left(\frac{eV_{\mathrm{s}}}{kT}\right). \tag{5.27}$$

Eq. (5.27) shows that, in general, S may be significantly larger than s. Howland and Fonash studied the relation between S and s for a Schottky barrier [545]. (As discussed in Section 2.2.2, this requires different assumptions on the quasi-Fermi levels than those used for deriving Eq. (5.27).) These authors studied the S/s ratio for different Schottky barrier heights and concluded that S is, in general, *not* a direct measure of s, in agreement with our simple calculation. Furthermore, they theoretically studied SCRs with a surface defect layer, so that generation/recombination processes in the SCR were included in S. In this case, they concluded that S is not necessarily even a simple qualitative figure of merit for surface quality. Thus, extraction of S and of s are discussed below separately.

Before proceeding to discuss quantitative procedures, we note that the sensitivity of the SPV to a surface defect layer is not necessarily a disadvantage. For example, Chiang et al. used SPV measurements in conjunction with successive electrochemical etching. This enabled them to determine the width of the surface defective layer by measuring the etch depth for which the SPV signal stabilized [703]. It should be noted, however, that the magnitude of the SPV variations *does not* directly reflect the changes in S. This is because, as already emphasized in Sections 4.2 and 5.2.1, the SPV is also sensitive to the equilibrium surface band-bending, which also changes with etching.

The most common approach for quantitative extraction of S relies on measuring Goodman plots (discussed in Section 5.1) [12,232,233,428,506,509,628,704,705]. The value of S affects the slope of the Goodman plot used to extract L (in both the constant SPV and the linear SPV approaches), due to the $(S + D/L)^{-1}$ coefficient in the dependence of $\delta n(w)$ on I (Eq. (2.61)). Qualitatively, this is apparent in, e.g., Fig. 63 [425], where the slope of the $I(\lambda)$ versus $1/\alpha(\lambda)$ curve increases with decreasing surface quality. If D/L is known, then the slope ratio before and after some surface treatment can be directly translated into the S ratio before and after the same treatment [704].

Lagowski et al. [12] noted that Eq. (5.18) show that if the surface band-bending is known, S and L may be extracted simultaneously, from the slope and intercept of a Goodman plot, respectively. This approach has indeed been used successfully in several studies [12,428,506,509]. Specifically, Hoff et al. used scanning SPV and work function measurements for simultaneous wafer-scale maps of L, [Fe], V_s^0, Q_{ins}, and S, thus combining several approaches discussed above for comprehensive characterization of surface and bulk properties of Si wafers [506].

Faifer et al. suggested a novel approach to measuring S in samples which obey all limitations of the Goodman technique (Eq. (5.7)), except for limitation (5.7)d, i.e., $L \ll l$. As explained in Section 5.1, violation of the latter assumption causes an SPV to develop on the *back* surface of the wafer, if illuminated from the front (and vice versa). By solving the continuity equation with the front and back effective SRV boundary conditions (Eqs. (2.60) and (5.9), respectively), they have shown that:

$$\mathrm{SPV}_{\mathrm{bf}} = \mathrm{const} \cdot I_{\mathrm{f}} \cdot \left(\frac{S_{\mathrm{f}}}{\alpha} + D\right), \tag{5.28a}$$

$$\mathrm{SPV}_{\mathrm{fb}} = \mathrm{const} \cdot I_{\mathrm{b}} \cdot \left(\frac{S_{\mathrm{b}}}{\alpha} + D\right), \tag{5.28b}$$

where ‘f’ (‘b’) refer to the front (back) surface and indexes ‘bf’ (‘fb’) refer to the back (front) SPV due to front (back) illumination. Thus, if the experimental setup is such that the front and back SPV can be measured *independently* (see Section 5.1), then S at both the front and back surface can be extracted from a ‘Goodman-like’ plot of $\mathrm{SPV}_{\mathrm{bf}}$ or $\mathrm{SPV}_{\mathrm{fb}}$, as a function of I_{f} or I_{b}, respectively. We note that the measured S_{b} can then be used to calibrate the measurement of L, via Eqs. (5.10) and (5.11).

If J_{ph} and $\delta n(w)$ can be calculated and/or measured, S can be found directly from Eq. (2.69). For example, Lile used the simplified formula of Eq. (2.71b) for J_{ph} and estimated $\delta n(w)$ using auxiliary C–V measurements in order to assess S at the InSb/$\mathrm{In_2O_3}$ interface of an InSb-based MIS structure [74]. More recently, Yan extracted J_{ph} from the intercept of a $\ln(T \cdot \mathrm{SPV})$ versus $1/T$ curve (Eq. (5.17)) and $\delta n(w)$ from a solution of the continuity equation which is somewhat less restrictive than Eq. (2.61). The limitations of the latter analysis were already discussed in Section 5.2.2.

Many attempts at the extraction of the *majority carrier s* rely on the extraction of τ_s (from which s can be calculated), based on the Kamieniecki model for the ac SPV response, described in Eqs. (2.79) and (2.80). Because the real part of $1/Z_{\mathrm{eff}}(\omega)$ contains τ_s, the latter can be easily found by analyzing the real and imaginary components of the ac SPV response [625]. Measurements of τ_s are performed together with w measurements in the surface charge profiler [235] mentioned in Section 5.2.2 and are also used in detecting the effects of various cleaning procedures on the state of Si wafer surfaces [625–630].

A cursory version of τ_s measurements is already found in the work of Nakhmanson et al. [706], who studied the dependence of both the real and imaginary parts of the SPV on the measurement frequency. It has been further developed by Ukah et al. [482], who also studied the dependence of the ac SPV on bias illumination. A somewhat different approach to the extraction of τ_s has been suggested by Goldfarb [707] as part of the surface charge analyzer, discussed in Section 5.4.1 below. He noted that in Eq. (2.73), the SCR width, w, is assumed to be a constant. However, this is clearly a first-order approximation because the illumination tends to reduce w. Since this reduction depends on the surface recombination (i.e., on τ_{s}), τ_{s} can be reliably extracted from the ac SPV dependence on the illumination intensity. Goldfarb used τ_{s} measurements for comparing the surface quality of different Si wafers. Because τ_{s} also depends on V_{s} (Eq. (2.79)), a reliable quantitative comparison between different wafers is obtained only if all wafers are brought into a controlled V_s via application of a gate bias or an appropriate cleaning agent. The most convenient value for this controlled V_s is in the inversion regime, where the SPV signal is large and both τ_s and w are insensitive to the exact value of V_s [627,707]. However, for qualitative monitoring of different trends, τ_s can be used even in the absence of inversion.

Several comments are in order: First, as already noted in Section 5.2.2, by using Eqs. (2.79) and (2.80) for extracting τ_s, we implicitly assume that the SCR capacitance is the dominant capacitance term in the ac-SPV response. This assumption should always be treated with caution. For example, Munakata has suggested that the SRV at strongly inverted Si wafers may actually be determined from studying the capacitance term which is due to the *inversion layer*, rather than the depletion layer [708]. Second, we note that τ_s is sometimes erroneously referred to as the '*minority carrier* surface recombination lifetime' [625,707], although the development leading to Eq. (2.79) clearly shows τ_s to be related to the *majority* carriers. The true *minority* carrier s can be extracted, along with L and w, from Goodman plots where $w \sim L$ (see Sections 5.1 and 5.2.1), assuming one has a sufficiently detailed and appropriate model for the charge balance in the SCR [523].

Takahashi and Yoshita defined a surface time-constant different from τ_s, in the form $\tau \equiv \delta Q_{ss}/(eI)$, where δQ_{ss} is the photo-induced change in surface charge, as a simple indicator of surface quality. This measure is, of course, related to the SRV. However, in calculating δQ_{ss} Takahashi and Yoshita assumed that SPV changes are *only* due to surface charge changes, i.e., that photo-induced changes in Q_{sc} are negligible. The theory in Section 2.2.2. and, e.g., Fig. 70, show that this is not necessarily the case, especially at high illumination intensities. Thus, this approach must be used with caution.

To conclude this section, we note that the different techniques surveyed here for the extraction of τ, S, and s, seem to have been developed independently with little interaction between the groups involved. Thus, a comparative *experimental* study of the relative strengths and weaknesses of the different approaches has yet to be performed. Here, we have outlined the major advantages and disadvantages of the approaches from a theoretical standpoint.

5.4. Surface states

A key strength of SPV-based methods is their inherent sensitivity to surface states. In Section 4.2, we have demonstrated how this is used for (mostly) qualitative surface state spectroscopy. In this section, we present quantitative SPV-based analyses, which make it possible to extract surface state energy distributions, as well as other properties (e.g., thermal and optical cross-sections). We also discuss how surface gap states may be distinguished from bulk gap states.

5.4.1. Energy distribution

Many SPV-based methods for determining the surface state energy distribution, $N_t(E)$ (defined in Eq. (2.23b)), are based on determining $Q_{ss}(E_{Fs})$, i.e., the dependence of the surface charge on the position of the surface Fermi level. In order to understand why that is so, let us combine Eq. (2.11) with Eq. (2.23b), which yields:

$$Q_{ss} = e\int [N_t^d(E)(1-f(E)) - N_t^a(E)f(E)]\,dE, \tag{5.29}$$

where $f(E)$ is the Fermi–Dirac distribution. We *approximate* the latter to be equal to one below the surface Fermi level, E_{Fs}, and to zero above it (i.e., our calculation is accurate only in the limit of negligible absolute temperature). Then, Eq. (5.29) reduces to:

$$Q_{\mathrm{ss}} \simeq e\int_{E_{\mathrm{Fs}}}^{\infty} N_{\mathrm{t}}^{\mathrm{d}}(E)\,\mathrm{d}E - e\int_{-\infty}^{E_{\mathrm{Fs}}} N_{\mathrm{t}}^{\mathrm{a}}(E)\,\mathrm{d}E, \tag{5.30}$$

which yields:

$$N_{\mathrm{t}}^{\mathrm{d}}(E_{\mathrm{Fs}}) + N_{\mathrm{t}}^{\mathrm{a}}(E_{\mathrm{Fs}}) = N_{\mathrm{t}}(E_{\mathrm{Fs}}) \simeq -\frac{1}{e}\frac{\mathrm{d}Q_{\mathrm{ss}}}{\mathrm{d}E}\,|_{E=E_{\mathrm{Fs}}}. \tag{5.31}$$

Eq. (5.31) shows that $N_t(E)$ can be measured at the energy range over which E_{Fs} can be swept. By definition:

$$E_{\mathrm{Fs}} = E_{\mathrm{Fb}} + eV_{\mathrm{s}}^{0}, \tag{5.32}$$

where E_{Fb} is the Fermi level in the quasi-neutral bulk (see, e.g., Fig. 4). At a first glance, modifying V_{s}^{0} via some surface treatment seems to be the obvious choice for changing E_{Fs}. However, this is unacceptable since one must change E_{Fs} *without* disturbing the electronic properties of the surface. Eq. (5.32) was used by Allen and Gobeli as early as 1962 for modifying E_{Fs} via using samples with different E_{Fb} [710]. By studying both *p*- and *n*-type samples over the entire doping range available to them, they were able to modify E_{Fs} at the clean Si(111) surface over a ~0.2 eV range slightly below midgap. By calculating Q_{sc} from Eq. (2.30) and using $Q_{\mathrm{ss}} = -Q_{\mathrm{sc}}$, they constructed a $Q_{\mathrm{ss}} = f(E_{\mathrm{Fs}})$ curve. Finally, $N_t(E)$ over the probed energy range was determined using Eq. (5.31).

In the above analysis, the role of SPV measurements is limited to determining V_{s}^{0} using any of the techniques discussed in Section 5.2. Allen and Gobeli did not actually use SPV measurements at all for that purpose. Rather, they used a combination of work function and photoemission measurements [710]. Later, Yamagishi used the same approach in conjunction with photosaturation for a renewed study of (oxidized and nitridized) Si(111) surfaces [572]. In addition to using samples with different doping types and levels, Yamagishi also changed the measurement temperature over a wide range. Thus, he was able to extend the range over which $N_t(E)$ was measured to ~0.8 eV, situated symmetrically about midgap.

The above approach has only been used scantily [565,711]. This is because it has several significant disadvantages. First, for using a *set* of samples with different doping, one must assume that the surface state distribution is the same for all samples, within experimental error. Second, one must also assume that the surface does not undergo any reconstruction (which may modify the surface state distribution) with decreasing temperature. However, detailed investigations of the temperature dependence of V_{s}^{0} revealed that such restructuring *does* take place at various semiconductor surfaces [566,568–570]. Last, but not least, the use of different samples and different temperatures requires many measurements (of both E_{Fb} and E_{Fs}) and is quite tedious. Therefore, an approach which makes it possible to obtain many E_{Fs} values at *the same sample* was clearly called for.

In 1971, Lam suggested that the necessary modification may be obtained by sweeping the gate bias of a MIS structure [712], i.e., by modulating E_{Fs} via the field effect. As explained in Section 2.1.5, the simple charge conservation rule, $Q_{\mathrm{ss}} = -Q_{\mathrm{sc}}$, is no longer valid in this case and a more elaborate analysis must be used. By taking the differentials of Eqs. (2.40) and (2.42), we obtain [712]:

$$\mathrm{d}Q_{\mathrm{m}} + \mathrm{d}Q_{\mathrm{sc}} + \mathrm{d}Q_{\mathrm{ss}} = 0, \tag{5.33a}$$

$$\mathrm{d}V_{\mathrm{G}} = \mathrm{d}V_{\mathrm{ins}} + \mathrm{d}V_{\mathrm{s}}^{0}. \tag{5.33b}$$

Inserting these differential relations, as well as Eq. (2.41), into Eq. (5.31) yields:

$$eN_t(V_s) = C_{\text{ins}}\left(\frac{\mathrm{d}V_G}{\mathrm{d}V_s^0} - 1\right) + \frac{\mathrm{d}Q_{sc}}{\mathrm{d}V_s^0}, \tag{5.34}$$

where $N_t(E)$ is related to $N_t(V_s)$ using Eq. (5.32). Lam measured V_s^0 using photosaturation for different gate voltages. He then calculated the first term in Eq. (5.34) by numerically deriving the obtained $V_s^0 = f(V_G)$ dependence and the second term from Eq. (2.30) [712].

Lam's SPV-based approach is essentially an extension of previous capacitance analyses [712]. However, it features several significant advantages over traditional *C–V* methods. First, it may be performed in a contactless manner (see below). Second, it is easily applicable to structures with thick insulators, where *C–V* methods fail due to the decreased insulator capacitance [713]. Finally, it is easier to interpret than *C–V* data as it avoids frequency–dispersion difficulties [714]. Interestingly, the dependence of the SPV on the gate bias in MIS structures as a function of different surfaces and/or prior illumination was used by Snitko to *qualitatively* detect changes in surface state distributions as early as 1959 [715]. However, no attempt at quantification was made in those early measurements.

Lam's approach has found several useful applications. First, Lam himself used his approach for studying the influence of different technological steps (e.g., oxidation temperature, annealing temperature and ambient, type of furnace, etc.) on the distribution of gap states at the Si/insulator interface of various commercial MIS capacitors, based on both SiO_2 and Si_3N_4 [716]. In all cases, reasonable agreement with ac conductance data (where that method was applicable) was obtained. Consequently, Flietner, Heilig, et al. extended the field modulation approach to the study of free Si surfaces and non-metallized Si/insulator interfaces by employing an 'artificial' MIS structure (i.e., a contactless gate electrode – see Section 3.2) in conjunction with SPV-based V_s^0-determining methods discussed in Section 5.2.2 [717]. For example, the analysis based on Eq. (5.34) has been applied to the study of HF and H_2O treated Si(111) surfaces [717,718], Si(111)/lead-boro-alumino-silicate glass [713] and Si/porous Si [719], and mostly chemically [720–725] and electrochemically [714,726,727] H-terminated Si (111) surfaces. The same approach was used by Venger et al. to study the surface state distribution at real Ge [568] and GaAs [569] surfaces.

As an illustrative example, consider the evolution of the surface state distribution with progressive electrochemical H-termination of *n*-Si(111), shown in Fig. 78(a) [726]. It is readily observed that the density of gap states decreases and that the state distribution shifts and widens with increasing electrochemical treatment time. A striking correlation is found between the time at which changes in $N_t(E)$ are most dramatic and the time at which a pulse in the dark current of the electrochemical cell occurs, as shown in Fig. 78(b). This indicates that the surface response is indeed *electro*-chemical, rather than chemical.

The results shown in Fig. 78 are generally consistent with other investigations of Flietner et al. [717,718,720,721,723], as well as with the earlier analyses of Allen and Gobeli [710], Yamagishi [572], and Lam [716]. All of these show that well-passivated Si surfaces feature a 'U-shaped' distribution of surface states, which is typically symmetric about midgap. This distribution is usually related to intrinsic defects, i.e., strained Si–Si bonds and dangling bonds, which are back-bonded to Si atoms only [722,728]. On the other hand, peaks in the surface state energy distribution are usually interpreted as indicating Si atoms with lower states of oxidation [728]. Thus, the transition from a narrow and large density of surface states, situated above midgap, to a wide, smaller, and symmetric distribution of surface states (Fig. 78(a)), clearly indicates the passivation of the Si(111) surface under study.

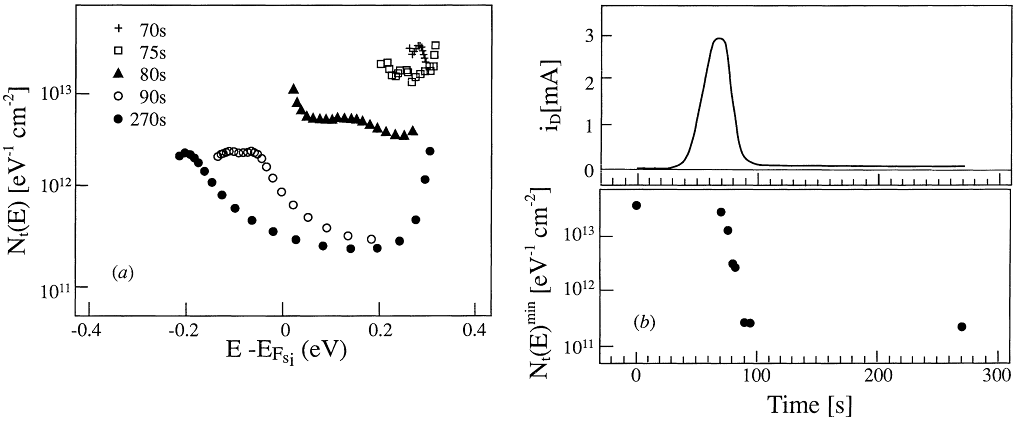

Fig. 78. (a) Surface state distributions at the n-Si(111) surface, obtained after various interruption times of the dark current in an electrochemical cell. (b) Dark current and minimal $N_t(E)$ as a function of time (after Dittrich et al. [726]).

In Lam's field modulation approach, the minimum resolvable density of surface states is determined by the opposing signs of the two additive terms on the right hand side of Eq. (5.34): $\mathrm{d}Q_{\mathrm{sc}}/dV_{\mathrm{s}}^{0}$ is always negative (see Eq. (2.30)) and the first term must therefore be always positive to result in a positive $N_{\mathrm{t}}(E)$. If the terms are very close in value, the difference signal may be obscured by noise, resulting in an unreliable measurement. Lam calculated that if the difference between the two terms is taken as at least 10% of $\mathrm{d}Q_{\mathrm{sc}}/\mathrm{d}V_{\mathrm{s}}^{0}$, then the minimum resolvable density increases with decreasing doping, and is $\sim 10^{10}$ cm^{-2} eV^{-1} for a $\sim 10^{15}$ cm^{-3} doping level (at room temperature) [712]. Lam and Rhoderick have also devised a *second* field modulation, SPV-based $N_{\mathrm{t}}(E)$ determining tool, where the minimum resolvable density was smaller [716,729]. However, that approach, based on analysis of *small-signal* SPVs, assumed that all gap states only trap *one* type of free carriers – a rather restrictive assumption. Thus, this second approach has not been in much use. In another variant of small-signal SPV analysis, Adamowicz and Kochowski [574] complemented SPV measurements with photoconductivity ones to plot the SPV/Δn ratio versus temperature. By *assuming* a distribution of donor and acceptor states which decay exponentially from midgap, they obtained a reasonable qualitative fit with the experimental data. However, this approach is not suitable for *direct* extraction of surface state energy distribution.

Just like the doping/temperature modulation approach, the field modulation approach relies on SPV tools only in determining V_{s}^{0}. Nevertheless, studies where other V_{s}^{0}-determining techniques mentioned in Section 3.3.2 were utilized in conjunction with Eq. (5.34) were not reported until quite recently. Kwok et al. [730] and Kobayashi et al. [731] used PES analysis to probe semiconductor/dielectric structures, where bias was applied either by electron charging or by a biasing a thin metallic overlayer, respectively. The main limitation of this approach has to do with the thickness of the dielectric. On the one hand, it must be thin enough to allow the semiconductor interface to be within the probing depth of PES. On the other hand, it must be thick enough to avoid breakdown upon bias. For example, Kwok et al. found that reliable results could be obtained at the Si/SiO$_2$ interface for SiO$_2$ thicknesses of only ~20–150 Å [730]. Electroreflectance has also been used successfully for determining the surface state distributions at the GaAs/SiO$_2$ interface [732]. There, the main limitation was the need for a special *i/n*$^+$ GaAs structure.

We now consider the limitations of analyses based on E_{Fs} modulation by either doping/temperature or by electric field. The energy resolution with which $N_{\mathrm{t}}(E)$ can be determined is limited by the negligible-temperature approximation underlying Eq. (5.31), which is the basis of all our quantitative analyses so far. Therefore, the energy resolution is only several kT at best [710,712]. This was vividly demonstrated in the early work of Allen and Gobeli [710]. Based on a simple derivative of the experimental $Q_{\mathrm{ss}} = f(E_{\mathrm{Fs}})$, they have obtained a 'U-shaped' (hyperbolic cosine) $N_t(E)$ distribution over the ~0.2 eV range probed. However, using direct integration, Allen and Gobeli found that the same $Q_{\mathrm{ss}} = f(E_{\mathrm{Fs}})$ curve could be obtained from many other distributions, as long as the *qualitative* trend (increasing density of states away from the middle of the energy range probed) was maintained. These distributions included two uniformly-distributed minibands, separated by $\sim 8kT$, and two discrete surface states, separated by $\sim 6kT$.

Both E_{Fs}-modulating approaches are expected to fail if the sample under study has an excessive density of either surface or bulk gap states. If the surface state density is very high, the surface Fermi level will be pinned. Then, modifications of gate bias, temperature, or doping will only modify E_{Fs} by very little, resulting in a very small energy range over which $N_t(E)$ can be determined. For example, Kwok et al. had to settle for a qualitative investigation of the InP/silicon nitride interface because Fermi level pinning precluded a quantitative analysis [730]. This immediately explains why most successful investigations described so far were limited to unpinned Si surfaces. In addition, possible hysteresis effects due to capture of charge in surface states must be taken into account when performing measurements as a function of gate bias [568,712,717]. If the bulk state density is very high, Q_{sc} (and hence Q_{ss}) can no longer be calculated from Eq. (2.30) and more general expressions must be used (see Section 2.1.3). These, however, require detailed knowledge of bulk state energy positions and densities, which is not necessarily available.

By studying Ge/Al_2O_3 interface states, Venger et al. demonstrated that even if E_{Fs} can be modified by both temperature and field, the surface state energy distribution measured by the two techniques is not necessarily identical [568]. They reasoned that the state density is lower in the temperature-based measurements because the sample does not reach complete thermal equilibrium during thermal cycling. Instead, only the fast surface states (the density of which is lower) react. They further reasoned that the slow states probed by the field modulation method are located slightly inside the Al_2O_3 film, so that tunneling is required. This makes the measured density of states an *effective* one because the accessible states depend on the electric field in the Al_2O_3 film.

A different type of field modulation tool, intended for the Si manufacturing industry, was introduced by Kamieniecki and dubbed 'surface charge analysis' (SCA) [624]. Kamieniecki combined the ac-SPV approach used in the surface charge profiler (SCP) for measuring the surface space charge capacitance (see Section 5.2.2) with gate-bias modulation. (Note that although it is somewhat more complex, the SCA precedes the SCP historically, for reasons given below). Kamieniecki used a fairly thick spacer (~10 μm) as the insulator in his 'artificial' MIS structure, which required using fairly large biases (~ 1000 V). As a result, any built-in potential drops on the insulator (e.g., due to the CPD between metal and semiconductor) were negligible and the charge on the gate was given simply by $Q_{\mathrm{m}} = C_{\mathrm{ins}} V_{\mathrm{G}}$. By modulating the gate bias, Kamieniecki was able to construct a complete w versus Q_{m} curve, extending over the accumulation, depletion, and inversion regimes.

The Si/insulator interface state distribution is derived from the w versus Q_{m} curve in a manner which is similar to that of the Lam approach, but which is more simple: From the value of w, both Q_{sc} and E_{Fs} are easily calculated using Eqs. (2.32) and (2.33), respectively. Since Q_{m} is directly obtained from the measurement, dQ_{ss} can be immediately obtained from Eq. (5.33a) over any energy range dE and inserted into Eq. (5.31) for obtaining $N_t(E)$.

We note that SCA can yield additional important information other than the interface state charge. This is because it is, essentially, a contactless, non-destructive analogue of standard C–V analysis. This is highlighted by, e.g., ac-SPV measurements which were used in conjunction with algorithms originally devised for *capacitance* measurements in order to deduce the spatial variation of the space charge density at Pt/a-Si:H samples [733]. Going back to crystalline Si wafers, the *bulk* type and doping may be easily obtained from the w versus Q_m curve [624]. First, the type of the sample (p or n) is determined from the direction of the curve because for p- (n-)type samples, inversion is obtained for positive (negative) gate charge; Second, as already discussed in the context of the SCP and just like in textbook C–V analysis (see, e.g., [25] and [30]), the doping level can be easily calculated from the maximal value of w. The induced charge necessary for obtaining flatband conditions is also easily read off w versus Q_m curves by identifying the cross-over between the depletion and accumulation regimes. We also note that the cross-over between different regimes can be identified even using dc SPV (and corona-discharge-induced biasing) [734], but the possibilities for quantitative analysis are more limited.

In all analyses so far, we have assumed that there is no fixed charge in the insulator – an assumption which incorrect for industrial Si-based MIS structures. Fortunately, this does not affect the results presented because a fixed, additive surface charge term (which can be lumped into Q_{ss}) does not modify the $N_t(E) \simeq dQ_{ss}/dE$ calculation. It is reasonable to assume that if E_{Fs} is where the minimum of the 'U-shaped' distribution is obtained (typically around midgap for passivated Si wafers), the net interface state charge is negligible, due to the symmetry of donor and acceptor states on the two sides of the 'U-curve'. Thus, if the insulator is thick enough so that Q_m can be determined directly, Q_{ins} is simply given by $Q_m - Q_{sc}$. This type of calculation is usually performed in the context of SCA [624], but can used in conjunction with other means of determining Q_{sc} [713,735].

SCA ('contactless C–V analogue') offers several advantages over the use of *standard* C–V analysis. This is because many difficulties are encountered when attempting to apply the latter approach to industrial monitoring of Si wafers [736]. The most important problem is that post-processing steps are required in order to fabricate test MIS structures on the Si wafer. This is time consuming and costly and cannot be performed regularly. Thus, problems may go undetected for several production lots. Moreover, the source of contamination and/or intrinsic defects may be obfuscated by the additional processing steps and wafers with only native oxides cannot be studied using C–V analysis. Finally, in the latter analysis the insulator charge inferred from the flat-band voltage is *weighted* [25], i.e., charges closer to the Si/SiO$_2$ interface are weighted more than those close to the SiO$_2$/metal interface. In SCA, measurements do not require any further processing. Moreover, since the SiO$_2$ layer is only a small fraction of the total insulating spacer used, the measured charge is practically unweighted because all of it is effectively very close to the Si/SiO$_2$ interface.

Due to its advantages, SCA was introduced in 1989 by Kamieniecki [624] as a commercial tool [234]. In the same year, Kamieniecki and co-workers from Digital demonstrated its usefulness for studying the effect of Si wafer cleaning [737] and of ambient air infiltration [738] on surface passivation and oxide charge. Soon thereafter, Murali et al. of Intel published a comprehensive study which established SCA as a valid and useful technique for *in-line* monitoring of micro-contamination and process-induced damage [736]. Ajuria et al. of Motorola directly compared SCA and C–V measurements as methods for detecting ionic impurities in Si/SiO$_2$ structures [739]. They concluded that the two do not necessarily yield the same results because the additional processing steps required for the *C–V* analysis may modify the oxide charge. However, both techniques show the same trends in surface charge with respect to any process studied. Of the two tools, SCA was determined to be far more sensitive and less erratic than *C–V*.

Today, SCA is a well-established industrial tool. Some notable recent publications of its use by semiconductor manufacturing companies include: Studies of the activity of HF/H_2O treated silicon surfaces in ambient air [740] (Digital), Real time oxidation monitoring [741] and damage evaluation of reactive ion etching [742] (IBM), evaluation of pre-cleaning effects on thermal oxide films [743] (Seiko-Epson), characterization of rapid thermally grown dielectrics [744,745] (Sharp), and in-line monitoring of oxide charge [498] (SGS-Thomson).

Naturally, the SCA is not without disadvantages: It is not well-suited to the study of bare Si wafers, mostly due to surface-state-related hysteresis encountered in the w versus Q_m curves [737]. In addition, the high bias required for its operation, as well as the mylar spacer used in the device, may modify the bare surface. These disadvantages are overcome by using the more simple surface charge profiler (see Section 5.2.2), which does not use gate biases or spacers. Thus, the latter device *can* be easily used for the study of bare surfaces, at the expense of sacrificing some of the SCA capabilities.

For completeness, we note that in a different ac-SPV based approach, Shimizu et al. determined the surface charge by analyzing the frequency dispersion of the ac-SPV and extracting the capacitance terms which are due to interface states, instead of assuming that all capacitive response is due to the depletion region [735]. If in doubt about the source of the effective capacitance in the ac-SPV response, studying the frequency–dispersion of the SPV signal before proceeding with quantitative analyses is always a good idea.

We briefly describe a different tool for the distinction between ionic and surface-state charge at Si wafer surfaces – the frequency dispersion of saturated-SPV measurements, as in Fig. 72(b) [509,586,595–601]. In Section 5.2.1, we have already noted that characteristic 'knees' can be observed in the SPV versus frequency curves, which are associated with insufficient re-emission of trapped charge in the dark. If all surface charge is ionic, this effect is absent and the frequency dispersion curve should remain flat up to $f \sim 1/\tau_{\text{bulk}}$. Any decrease in the SPV indicates a partial contribution of surface trapping, and hence surface states. If (and only if!) all surface charge is compensated by trapping, it can be calculated from the difference of the SPV before and after the 'knee'. This interpretation is in disagreement with that of Lowell et al. (see, e.g., [596]), who interpreted a flatter gradient at a 'knee' as indicating that surface-state charge dominates over ionic charge.

All the methods reviewed in this sub-section so far relied on *indirect* modification of the surface state population, by means of temperature, electric field, or super-bandgap illumination. In Section 4.2, we have shown that direct excitation of surface states with sub-bandgap illumination has been very successful in determining the approximate energy position of surface states. Thus, it seems natural to extend these methods for quantitative characterization of surface state distributions, by considering the derivative of the SPV signal with respect to the exciting photon energy. As already noted in Section 4.2, the inherent difficulty with such an approach is that the sub-bandgap SPV signal is always affected by both the density of states and the optical cross-section of the states, with the separation between the two being very problematic.

Kronik et al. demonstrated theoretically and experimentally that derivative sub-bandgap SPS *can* be used for extracting the surface state distribution, if the SPV signal is saturated at each photon energy used [603]. This typically requires the use of a high-intensity tunable source, e.g., a tunable laser.

Consider, for example, a depleted *n*-type semiconductor surface, where the surface band-bending is due to trapping of electrons in surface states. Let us assume that the surface states in question have non-negligible optical cross-sections only with the conduction band. A saturated SPV signal then indicates that all states whose energy separation from the conduction band is smaller than $h\nu$ have been emptied out. Then, any small change in the surface potential (i.e., an SPV), due to a small increase, $\Delta(h\nu)$, in the incident photon energy, is due to the evacuation of an additional charge, Δn_t, whose excitation energy is between $h\nu$ and $h\nu+\Delta(h\nu)$. In other words, the change in surface potential with increasing photon energy *must* be attributed to changes in the density of states probed *alone*. Changes in the optical cross-section (which reflects the probability of absorption) are made irrelevant because the state is completely emptied out regardless of the value of the optical cross-section. Thus, the surface electron density over the energy range $\mathrm{d}(h\nu)$ is given by the simple relation:

$$\mathrm{d}n_\mathrm{t} = n_\mathrm{t}(h\nu + \mathrm{d}h\nu) - n_\mathrm{t}(h\nu), \tag{5.35}$$

where an independent measurement of V_s^0 is required for calculating n_t from V_s via the depletion approximation expression, $n_\mathrm{t} = \sqrt{2\epsilon n_\mathrm{b}|V_\mathrm{s}|/e}$. Then, $N_\mathrm{t}(E)$ can be obtained from $n_\mathrm{t}(E)$ via the Fermi-Dirac distribution. Note that the analysis of Kronik et al. shows that the derivative of the SPV *does not* reflect the surface state distribution even if the optical cross-section is constant, due to the square root dependence of n_t on V_s.

The chief advantage of this approach is that since it does not assume a negligible temperature, its energy resolution is much better than that of the previous approaches [603]. Another reason for the improved accuracy is that due to the square root dependence on V_s, even relatively large errors in determining V_s^0 are translated into small errors in n_t. A significant disadvantage, however, is that it is strictly valid only for unipolar excitation. For optical interaction with both bands, Eqs. (2.13) and (2.18) show that a given surface state does not empty out at high illumination intensity. Rather, its population reaches a steady-state value of $n_\mathrm{t} = \sigma_n N_\mathrm{t}/(\sigma_n + \sigma_p)$. However, if this complication is ignored and the analysis of Eq. (5.35) is pursued nevertheless, the results are still expected to approximate the true distribution reasonably well because the dependence of the optical cross-section *ratio* on the photon energy is very frequently weaker that that of the optical cross-section itself [603]. Thorough investigations of this approach, or detailed comparisons with the other tools discussed in this section, have yet to be performed.

5.4.2. Properties

Apart from the surface state energy position (if discrete) or distribution (if continuous), many other important surface state properties can be determined. These include the surface state density, N_t, its electron (hole) density, n_t (p_t), its thermal cross-sections for electrons and holes, k_n and k_p, and its optical cross-sections for electrons and holes, σ_n and σ_p. (All quantities have been defined in Section 2.1.2). Many approaches for extracting surface state parameters from various SPV measurements, especially time-resolved ones, have been devised. These approaches can be broadly categorized into two groups. The first group involves direct excitation of the surface-states under study via sub-bandgap excitation. The second group involves indirect modification of surface state population via trapping of free carriers induced by super-bandgap illumination. Many of the approaches given here can be modified to the study of bulk states, taking into account that the free carrier density is that of the bulk (or the SCR), rather than that of the surface.

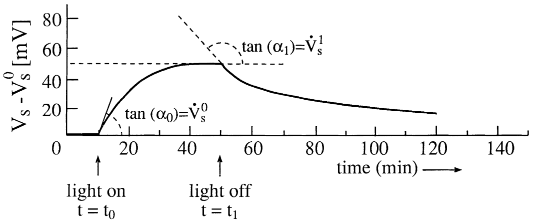

Fig. 79. Sub-bandgap ($h\nu \simeq 0.5$ eV) transient SPV curve, obtained at a basal *n*-CdS surface. Specific quantities pertinent to quantitative analysis are noted (after Lagowski et al. [110]).

Lagowski et al. were the first to use time-resolved SPV measurements for a quantitative extraction of surface state properties, soon after the introduction of SPS [110]. A typical transient SPV curve, obtained at a basal CdS surface, where some specific quantities pertinent to the analysis of Lagowski et al. are highlighted, is given in Fig. 79 [110].

Many analyses of transient curves as in Fig. 79 (including that of Lagowski et al.) make two significant assumptions. The first assumption is that of unipolar excitation. Namely, transitions involving minority carriers are neglected (see Section 2.2.3 above). We continue our discussion assuming an *n-type* material with electron transitions between the conduction band and the surface state. A similar analysis may be performed for hole transitions involving the valence band. The second assumption is that all generation *and* recombination transitions are assumed to involve only *one* surface state.

Under these assumptions, it may seem at a first glance as though k_n and σ_n can be obtained immediately by fitting the transient 'light-on' and 'light-off' curves with exponential curves. However, this is usually *incorrect*. To understand why, let us reconsider the unipolar rate equation (Eq. (2.81)), reproduced here for convenience:

$$\frac{\mathrm{d}n_\mathrm{t}}{\mathrm{d}t} = -g_n^{\mathrm{th}} - g_n^{\mathrm{opt}} + r_n^{\mathrm{th}} = -\sigma_n^{\mathrm{opt}} I n_\mathrm{t} - c_n n_1 n_\mathrm{t} + c_n (N_\mathrm{t} - n_\mathrm{t}) n_\mathrm{s}. \qquad (5.36)$$

As opposed to the generation terms, the recombination term in the above equation is *not* proportional to the surface state occupation. The reason is that n_s, the electron (volume) density at the surface, depends on V_s (via Eq. (2.27)) in the case of the FQL approximation). V_s obviously changes during the SPV transient, which makes Eq. (5.36) a non-linear differential equation.

Inspection of Eq. (5.36) shows that the 'light-on' part of the transient SPV curve can yield the optical cross-section *only* if the problematic recombination term (as well as the less problematic thermal generation term) are negligible with respect to the optical generation. This may require high-intensity illumination, depending on the σ_n / c_n ratio. If the optical generation term can be made to dominate, then n_t decreases with a time constant of $\tau_n^{\mathrm{on}} = 1/(\sigma_n I)$, from which σ_n can be extracted. This approach was used by Kronik et al. [746], who observed that in the initial part of the 'light-on' SPV transient (where the excess carrier density was not very large), obtained at the CdTe(100) surface using high-intensity illumination, an exponential rise was indeed observed. Moreover, they fitted the transient SPV curve for several illumination intensities and obtained a τ_n^{on} which was inversely proportional to I, as appropriate.

The time-constant fitted to the SPV curve can be equated with τ_n^{on} *only* if the SPV is small enough to assume that it is proportional to $\mathrm{d}n_t$. For example, combining the depletion approximation (square root) form of Eq. (2.30) with Eq. (2.23) yields [110]:

$$V_s = C_1 - \frac{n_t^2}{C_2^2}, \tag{5.37}$$

where C_1 is the contribution to the surface potential of other surface states (the charge of which was assumed above to remain constant even under illumination), and $C_2 \equiv \sqrt{2\epsilon n_b/e}$. If C_1 is negligible, the SPV(t) curve can be converted to a $n_t(t)$ curve provided that V_s^0 is known [603]. In any case, the relation between the time-constants of the SPV(t) and $n_t(t)$ curves must be examined.

In the 'light-off' part of the SPV response, the recombination term in Eq. (5.36) dominates by definition, so that the relaxation of the sub-bandgap SPV is not expected to be exponential. An elegant demonstration of this non-exponential nature was given by Kuhlmann and Henzler, who studied sub-bandgap SPV transients at the Si(111) surface [747]. These authors defined a time-dependent relaxation time-constant, $\tau(t)$, in the form:

$$\tau(t) = -\frac{\mathrm{SPV}}{\mathrm{d(SPV)}/\mathrm{d}t}, \tag{5.38}$$

which can be directly calculated from the experimental SPV decay curve. By plotting $\tau(t)$ versus the SPV, they noticed that $\tau(t)$ *increases* as the SPV decay proceeds. This observation is an immediate consequence of the mathematical form of the recombination term in Eq. (5.36). As the SPV decays, the surface barrier increases, so that n_s is reduced, the surface recombination is slowed, and its effective time constant increases. Kuhlmann and Henzler further noted that $\tau(t)$ did approach a constant value towards the end of the relaxation, where only a residual SPV (~0.1 mV) remained. This is also expected from Eq. (5.36) because the deviation from the linearity of the equation, introduced by the SPV, may be neglected if the latter is much smaller than kT/e. Therefore, the constant value of $\tau(t)$, obtained towards the end of the SPV relaxation (if observed), *can* be used as a reliable indicator of surface recombination rates. Unfortunately, using Eq. (5.36), we obtain a relaxation time constant of $\tau_n^{\mathrm{off}} = 1/c_n(n_1 + n_s)$. Thus, c_n (and hence the thermal cross-section, $k_n \equiv c_n/v_n$ – see Eq. (2.17)) can be obtained only if n_s can be estimated.

We now consider the approach suggested by Lagowski et al. for a complete extraction of surface state properties [110,748]. In the following, the superscripts '0' and '1' denote steady-state conditions in the dark (i.e., equilibrium) and under illumination, respectively. Lagowski et al. measured V_s^0 using photosaturation, so that V_s^1 was also immediately known because, by definition, SPV $\equiv V_s^1 - V_s^0$. They then built an additional set of equations for the remaining five unknown surface state properties of interest – N_t, k_n, σ_n, n_t^0, n_t^1. Two equations for these quantities are obtained from the steady-state solutions of Eq. (5.36) in the dark and under illumination, using the FQL approximation. They are:

$$(N_t - n_t^0)n_b \exp\left(\frac{eV_s^0}{kT}\right) = n_t^0 N_c \exp\left(\frac{E_t - E_c}{kT}\right), \tag{5.39a}$$

$$\sigma_n I n_t^1 = c_n(N_t - n_t^1)n_b \exp\left(\frac{eV_s^1}{kT}\right) - c_n n_t^1 N_c \exp\left(\frac{E_t - E_c}{kT}\right). \tag{5.39b}$$

Two more equations are obtained from the specific form of the Poisson equation used above, Eq. (5.37), in equilibrium and under steady-state illumination, which introduces a sixth unknown constant – C_1.

Due to the additional unkown, *two* more equations, which must rely on the transient parts of the curve in Fig. 79, not used so far, must be introduced.

As both the 'light-on' and the 'light-off' transients are non-exponential, Lagowski et al. concentrated instead on the measured *slopes* of the SPV curve, obtained immediately after switching the light on and off (see Fig. 79). Inserting Eqs. (5.39) into the rate equation (Eq. (5.36)), and using the derivative of Eq. (5.37), they obtained:

$$\left.\frac{\mathrm{d}n_\mathrm{t}}{\mathrm{d}t}\right|_{t=t_0^+} = -\frac{C_2}{2|V_\mathrm{s}^0|^{1/2}}\left.\frac{\mathrm{d}V_\mathrm{s}}{\mathrm{d}t}\right|_{t=t_0^+} = -\sigma_n n_\mathrm{t}^0 \dot{I}, \tag{5.40a}$$

$$\left.\frac{\mathrm{d}n_\mathrm{t}}{\mathrm{d}t}\right|_{t=t_1^+} = -\frac{C_2}{2|V_\mathrm{s}^1|^{1/2}}\left.\frac{\mathrm{d}V_\mathrm{s}}{\mathrm{d}t}\right|_{t=t_1^+} = \sigma_n n_\mathrm{t}^1 \dot{I}, \tag{5.40b}$$

where t_0^+ (t_1^+) refers to the time immediately after illumination switch-on (switch-off).

By simultaneously solving Eqs. (5.37), (5.39) and (5.40), a complete characterization of the surface state is obtained. This approach has indeed been used for the complete characterization of surface states at CdS [110,362], GaAs [319], ZnO [401], CdSe [377] and CdTe [749] surfaces. Moreover, if the SPV transients are analyzed at many different wavelengths, the dependence of the optical cross-section on the photon energy can be constructed [378,623].

As always, the above analysis is not without limitations. When several surface states are detected using SPS, the assumption that each one may be selectively excited is very problematic. This casts a significant doubt over the application of the algorithm in such cases and has probably limited the actual use of the approach. Even if only one state is optically excited, other states may still influence the results via trapping of the excited carriers (see Section 2.2.3). We have shown theoretically that the analysis can be extended by: [623] (a) replacing the constant C_1 in Eq. (5.37) with a detailed accounting of all surface charge, (b) writing a rate equation of the form of Eq. (5.36) for each of the states involved, and (c) recording as many SPV transients as there are types of surface states. Thus, the properties of *all* surface states may be extracted. Moreover, as C_1 is eliminated from the equations, V_s^0 may also be determined along with the other parameters, resulting in yet another technique for its extraction. This extension has not been tested experimentally yet. As explained in Section 2.2.3, if surface transitions involving the *minority* carriers are identified in the SPV spectra (i.e., the unipolarity assumption is invalidated), analytical results are difficult to obtain. Nevertheless, judging by the above developments it seems that the information *can* be extracted from a sufficient number of SPV transients, with the aid of numerical simulations. This has not been performed yet either.

A different assumption behind the algorithm of Lagowski et al. is that steady-state conditions are indeed obtained in the dark and under illumination. If the surface states are in poor communication with the bulk, this is not necessarily true. However, Balestra et al. have shown that the approach is easily extended to this case by making the necessary modifications in the rate equation [748]. Experimentally, the success of the approach critically depends on the ability to obtain an accurate reading of the slopes. This explains why it has been mostly applied to II–VI compounds, where transients are typically slow enough to be followed with a Kelvin probe. If a MIS capacitor, or other faster approaches, are used, one must ascertain that the illumination is chopped with a frequency low enough to retain the true steady-state value of the SPV.

Several attempts at extracting the optical cross-section from *steady-state* sub-bandgap SPV measurements have also been reported. Musatov and Smirnov [338] suggested that if the SPV is small enough, it is expected to be proportional to the photo-current, where the latter is simply equal to eg_n^{opt}. Assuming further that the population of the surface states is approximately constant, the dependence of the SPV on the photon energy is then expected to directly follow the dependence of σ_n on $h\nu$. This enables the measurements of the latter dependence, at least in arbitrary units. There are two very significant assumptions behind this approach. First, the surface state involved must be discrete, or some of the SPV may be due to an increase in the density of states accessible to excitation with increasing photon energy (see Section 5.4.1). Second, the optical current is expected to reflect eg_n^{opt} *only if* recombination can be neglected, which is a strong assumption. We also note that the σ/k ratio has been extracted from analyzing the dependence of the SPV on photon energy [296] or illumination intensity [113]. Note that this requires detailed knowledge on other parameters (e.g., defect density) and thus is not very general.

We now consider the quantitative analysis of *super-bandgap* SPV data. In this case, the surface states are not excited directly. Rather, their population is modified via trapping of photo-induced excess carriers from the bands. Accordingly, they are used mostly for assessing the thermal cross-section (which controls thermal generation and recombination), as well as the state energy position, which also influences emission rates. Again, the most significant algorithm has to do with the analysis of the SPV transient. In many cases, the SPV relaxation is composed of a fast component, followed by much slower 'tail'. A typical example is shown in Fig. 80(a) [604]. The slow SPV tail can be explained as follows [295,604,750–752]. During illumination, minority carriers, which are swept in the direction of the surface by the electric field in the SCR, are trapped in surface states. The fast decay immediately after illumination switch-off is due to electron-hole recombination in the bulk. In its wake, the trapped minority carriers must be emitted in order to re-establish thermal equilibrium. This is a much slower process than inter-band recombination, resulting in the SPV 'tail'.

If re-trapping of charge can be neglected, then according to Eq. (5.36), the typical time-constant of the slow SPV decay would be:

$$\tau = 1/c_n n_1, \tag{5.41}$$

where again we assume electron emission with no loss of generality. Just like in the case of optical emission of surface carriers, here too the assumption that recombination is negligible and the process it truly exponential must be examined with caution. It is typically found that for times which are long compared to the inter-band recombination, but at which a significant re-trapping of charge has not taken place yet, the SPV is indeed reasonably exponential, as shown in Fig. 80(a). Thus, τ can indeed be defined and extracted.

The time constant τ does not have to be extracted directly from time-resolved measurements. Alternatively, it may be found by performing frequency-resolved measurements, as in Fig. 72(b). As discussed in Section 5.2.1, if the chopping frequency exceeds $1/\tau$, trapped minority carriers are not re-emitted in the dark, so that the overall SPV is reduced. Thus, τ may be found from the inverse of characteristic knees in the SPV versus frequency curve. This approach has been used successfully with both saturated [509],[586],[595–601] and non-saturated [294,295] SPV.

The direct monitoring of SPV relaxation transients is an extension of similar ideas commonly applied for characterizing bulk states [30]. In the latter case, the population of the bulk states is typically driven away from equilibrium using an electrical or optical pulse, and the charge emission process is followed

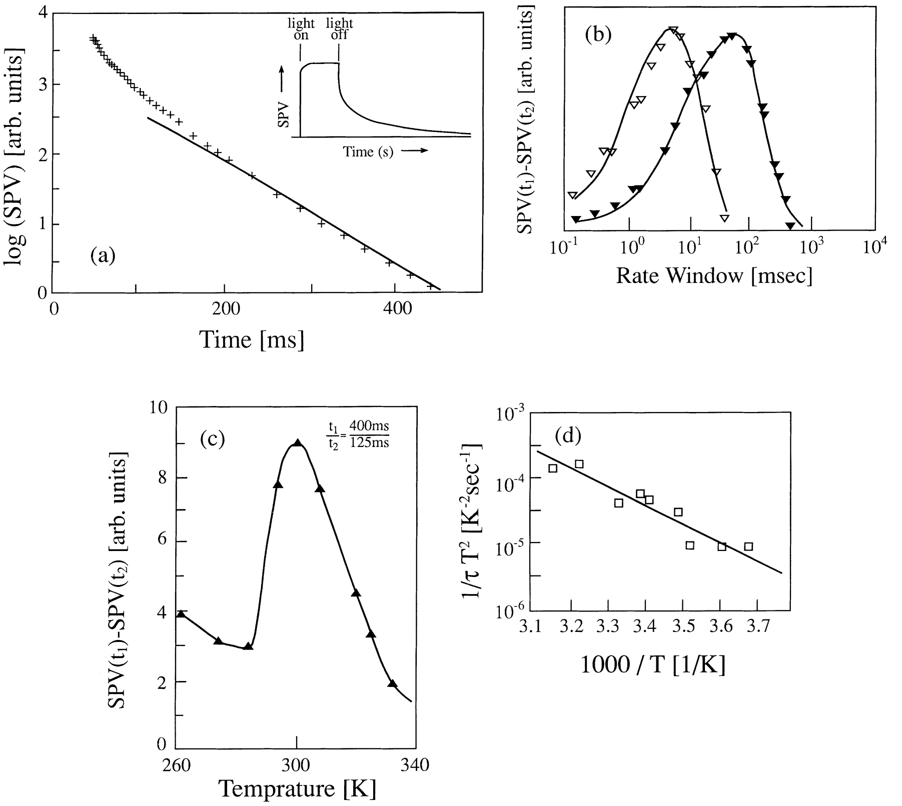

Fig. 80. (a) Super-bandgap transient SPV curve, obtained at an n-type GaAs wafer at room temperature. (b) DLTS analysis of the SPV relaxation – fixed temperature, variable 'rate window'. (c) DLTS analysis of the SPV relaxation – fixed 'rate window', variable temperature. (d) Thermal activation plot of the 'tail' time-constant extracted from the SPV relaxation (after Lagowski et al. [604,750]).

by monitoring capacitance or current transients. Lagowski et al. [604,750] and independently Estrada [751] have suggested that the identification of gap states based on the SPV transients may be facilitated by the use of the 'rate window' concept, known as deep level transient spectroscopy (DLTS) [30]. In 'rate window' analysis, one monitors the difference signal:

$$\mathrm{SPV}(t_2) - \mathrm{SPV}(t_1) = \mathrm{const} \cdot [\exp(-t_2/\tau) - \exp(-t_1/\tau)], \tag{5.42}$$

where t_1 and t_2 are pre-selected. It is easy to show that this difference signal is maximal when $\tau = (t_2 - t_1)/\ln(t_2 - t_1)$. Therefore, characteristic peaks, indicating individual gap states, appear when $t_2 - t_1$ is varied (typically keeping t_2/t_1 constant), as in Fig. 80(b), or when the temperature, and hence τ, are varied for a fixed t_1 and t_2, as in Fig. 80(c). Hybrid SPV-DLTS analysis was also used successfully in conjunction with a scanning MIS capacitor in order to detect gap state distributions in GaAs [750] and areas with different gap state characteristics in CdTe [753]. Recently, a high-resolution SPV-DLTS map, using STM-based sensing of the SPV, was also demonstrated [754].

By inserting Eqs. (2.16) and (2.17), which express n_1 and c_n, respectively, into Eq. (5.41) and by explicitly expressing the thermal velocity, v_n, in terms of temperature and electron mass, we obtain [30]:

$$\frac{1}{\tau T^2} = \gamma_n k_n \exp[(E_c - E_t)/kT], \tag{5.43}$$

where $\gamma_n \equiv v_n N_c/T^2 = \text{const}$. Thus, just like in conventional DLTS, a logarithmic plot of $1/(\tau T^2)$ versus temperature should yield a straight-line, as in Fig. 80(d), from which both the energy position and the thermal cross-section of the gap state involved can be easily derived [295,604,750,751].

Several important comments on Eq. (5.41) are in order. First, it has been used successfully long before 'rate window' concepts were introduced to SPV (see, e.g., [295]). Second, a similar analysis may in principle be applied even if the surface states trap *majority* carriers. This case is less frequent since majority excess carries are typically swept *away* from the surface. However, they may still be preferentially trapped, depending on the ratio between the electron and hole thermal cross-sections (see Section 5.2.1). If that is indeed the case, the slow and fast components of the SPV relaxation must have opposite signs, as in Fig. 73(a). Third, SPV–DLTS, like all SPV tools, is sensitive to both surface and bulk states. Accordingly, SPV–DLTS can be used as a contactless alternative to conventional DLTS. Fourth, the dependence of the steady-state SPV on temperature, using both super-bandgap [295,303] and sub-bandgap [294,295,303] illumination, is also frequently exponential and can be used to yield an 'activation energy'. However, since the steady-state SPV depends on many factors, the precise physical meaning of this activation energy must be examined with caution. For example, if the SPV is proportional to the excess carrier density, it may indicate the activation energy of shallow acceptors [294]. If it is governed by the surface charge, it may indicate a surface state energy [303], etc. Fifth, as mentioned above, if carrier trapping during the slow SPV relaxation is not outright negligible, Eq. (5.41), and hence Eq. (5.43), cannot be used. It was shown that even in the presence of trapping the transient might still be approximately exponential, albeit with a modified τ [755].

Liu and Ruda reported an interesting 'pump-probe' two beam extension of transient SPV analysis, applied to the study of semi-insulating GaAs films, where the Dember potential dominates the SPV response [755]. They noted that in the limit of a small-signal SPV, Eq. (2.92) reduces to:

$$\text{SPV} = \frac{kT}{e}(\mu_n - \mu_p)\frac{\delta n}{\sigma_0}, \tag{5.44}$$

so that the small-signal, Dember-related SPV is inversely proportional to the dark conductivity of the sample. If a simultaneous 'optical bias' illumination pulse is applied, σ_0 shall reflect the conductivity of the sample under this illumination. Therefore, in this case SPV measurements can be used for contactless monitoring of the photoconductivity.

Liu and Ruda have recorded the 'light-on' and 'light-off' response of the SPV signal to the (independent) optical bias illumination, as shown in Fig. 81(a). It is readily observed that the Dember-related SPV decays rapidly upon illumination, due to the sudden photo-induced increase in conductivity. However, its increase upon switch-off of the optical bias is much more gradual due to the slow release of captured carriers. The ensuing activation energy of the process was determined using a $\tau(T)$ plot. At some range of low temperatures, it has been found that after the optical bias is switched-off, the SPV increases rapidly to a value which is much larger than that found before the bias was applied and slowly decreases towards that value afterwards. This is shown in Fig. 81(b). As this phenomenon *cannot* be explained using the trapping mode, it was interpreted in terms of an optically-induced metastable transformation of the EL2 defect, which decays thermally after bias switch-off.

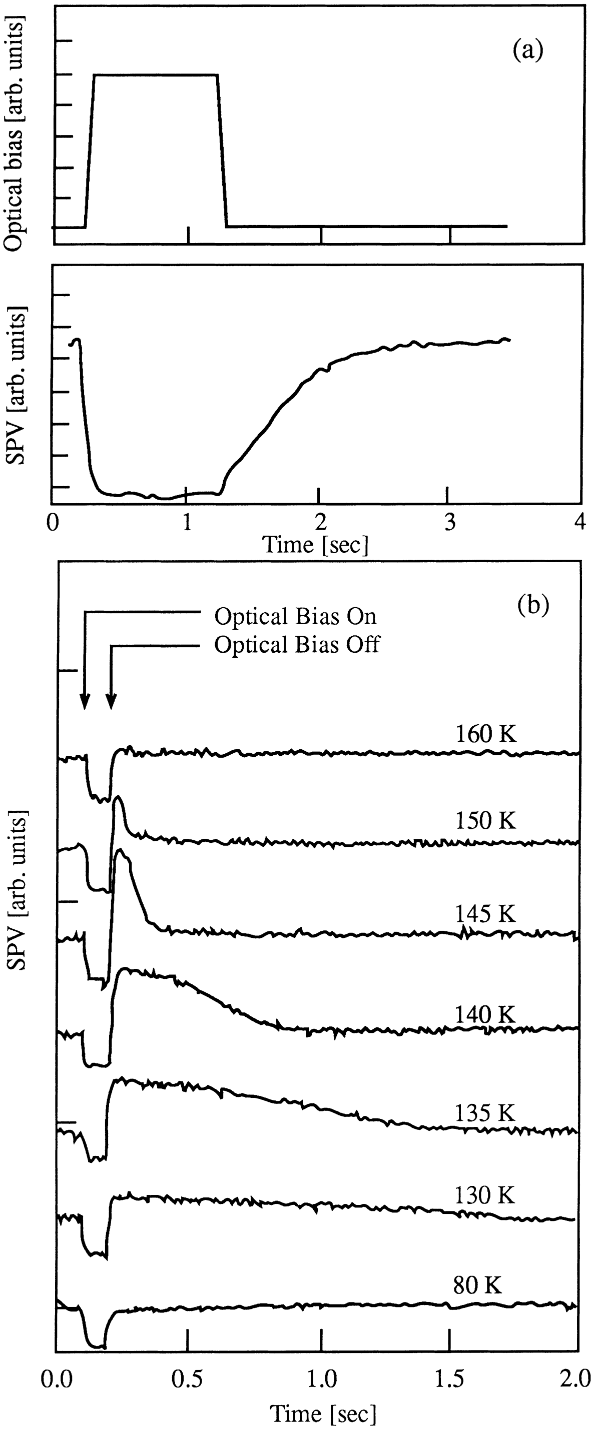

Fig. 81. Pump-probe SPV measurements of semi-insulating GaAs samples: (a) Optical bias illumination (top) and a characteristic SPV transient response to it (bottom), recorded at 280 K. (b) Optical-bias-induced SPV transients at various low temperatures (after Liu and Ruda [755]).

All super-bandgap SPV based approaches presented so far assumed unipolarity. This assumption is eminently suitable for studying the thermal cross-section of surface traps, but is obviously not suitable for studying the thermal cross-sections of surface recombination centers, which by definition interact with both bands. In one of the earliest quantitative parameter extraction from SPV data, Brattain and Garrett combined SPV, field effect, conductivity and photoconductivity measurements for extracting the k_n/k_p ratio at Ge surfaces, based on the small-signal SPV equation (Eq. (2.57)) [68]. Using field effect and conductivity measurements to assess $\partial Q_{\mathrm{ss}}/\partial V_{\mathrm{s}}$, photoconductivity measurements to assess Δ_p, and calculating $\partial Q_{\mathrm{sc}}/\partial \Delta_p$ and $\partial Q_{\mathrm{sc}}/\partial V_{\mathrm{s}}$, they were able to determine the remaining term in Eq. (2.57), $\partial Q_{\mathrm{ss}}/\partial \Delta_{\mathrm{p}}$. The latter strongly depends on the k_n/k_p ratio, which was thus found. Measuring the SRV as well, Barattain and Garrett were able to give absolute numbers for k_n and k_p. In the 1970s, the k_n/k_p ratio was also determined from the dependence of the small signal SPV on temperature [756] and by fitting the SPV=$f(\Delta_p)$ curve [366].

To conclude this sub-section, we note that in simple situations (one dominant surface state, unipolar interaction), surface state parameters may be extracted using relatively simple, analytical approach. Such extraction is considerably more complicated in more complex scenarios. Nevertheless, the examples given above show that with a sufficient number of well-designed SPV measurements, backed with numerical simulation, quantitative characterization of surface states can be performed even in difficult cases.

5.4.3. Distinction between surface and bulk states

In most quantitative approaches outlined in Sections 5.4.1 and 5.4.2, it was tacitly assumed that all gap states probed reside at the semiconductor surface. It has been already emphasized in both the theoretical (Section 2.2.3) and qualitative (Section 4.2) discussion of gap-state-related SPV data, that this is not necessarily true. In fact, most of the surface-state-related tools explored in the preceding sub-section can and have been applied to the investigation of bulk states, with little or no modification. However, the distinction between surface and bulk states is very important because a misassignment of the gap-state site may result in mistaken conclusions as to the performance of the tested material or structure. Two *qualitative* tools were suggested in Section 4.2 for distinguishing between surface and bulk states: (a) comparison of SPS features before and after various surface or bulk treatments, attributing persistent features to the bulk or surface, respectively. Specifically, reversals of the sign of the SPV at the same energy position were taken as indicating bulk states. (b) Assignment of SPS features to the bulk or surface according to whether or not they also appear in photoconductivity spectra, respectively. Here, we discuss some *quantitative* criteria for distinguishing surface states from bulk states.

One *indirect* quantitative tool for detecting bulk states, already suggested in Section 5.2.1, is the identification of an ideality factor of $\eta \sim 2$ in SPV$=f(I)$, as in $I-V$ analysis [366,612]. There are two significant problems with this approach: (a) The SCR recombination must be high for η to change significantly. Thus, such analysis is unsuitable for discerning the origin of subtle features in SPS, which may correspond to fairly low defect densities. (b) Even when $\eta \sim 2$ is observed, it is not linked to any specific state.

An interesting *indirect* analysis of the recombination paths in $\mathrm{FeS_2}$ was presented by Bronold et al. [757]. These authors measured the temperature dependence of the super-bandgap SPV and attempted to fit the measured data using the known metallic nature of the free $\mathrm{FeS_2}$ surface. However, use of thermal emission models resulted in SPV values which were more than twice the measured ones. Additionally, if SCR recombination was included, a fitting of the temperature dependence was obtained only for a bandgap value of about half its true size. Bronold et al. have therefore suggested that due to the defect chemistry of the FeS_2 surface, there exists a thin surface layer which is effectively very highly doped. Thus, they have suggested that the results may be rationalized only if excess carriers are lost via both SCR recombination and tunneling across the thin, highly-doped surface barrier. While elegant, this analysis is clearly case-specific.

It is reasonable to expect that for obtaining more *direct* information on the site of the state, the population of the state must be modified via direct excitation. Let us examine the quantitative difference between such charge modification in surface and in bulk states: In the depletion approximation, a combination of Eqs. (2.24), (2.32) and (2.33) yields $V_s = -Q_{ss}^2/(2\epsilon\rho)$. Thus, if the illumination induces a surface and bulk change of δQ_{ss} and $\delta\rho$, respectively, the SPV is given by:

$$\mathrm{SPV} = -\frac{1}{2\epsilon}\left[\frac{(Q_{ss}^0+\delta Q_{ss})^2}{\rho^0+\delta\rho} - \frac{(Q_{ss}^0)^2}{\rho^0}\right], \tag{5.45}$$

where the index '0' denotes equilibrium, as usual. If the illumination modifies only the surface charge or the bulk charge, Eq. (5.45) can be further reduced to:

$$\mathrm{SPV} = -\frac{\delta Q_{ss}(2Q_{ss}^0+\delta Q_{ss})}{2\epsilon\rho_0}, \quad \text{for fixed bulk charge,} \tag{5.46a}$$

$$\mathrm{SPV} = \frac{(Q_{ss}^0)^2\delta\rho}{2\epsilon\rho_0(\rho_0+\delta\rho)}, \quad \text{for fixed surface charge.} \tag{5.46b}$$

Leibovitch et al. suggested that Eqs. (5.46) can be used as a basis for distinction between surface and bulk states, by relying on the dependence of the SPV on illumination intensity [116]. Their arguments follow. Whereas in Eq. (5.46a) the $\mathrm{SPV} = f(\delta Q_{ss})$ dependence is super-linear, the $\mathrm{SPV} = f(\delta\rho)$ dependence in Eq. (5.46b) is sub-linear. Since the dependence of δQ_{ss} and $\delta\rho$ on I, the illumination intensity, may itself be sub-linear, the overall $\mathrm{SPV} = f(I)$ dependence may be sub-linear even in the case of surface excitation. Thus, observation of a sub-linear $\mathrm{SPV} = f(I)$ dependence does not tell us anything about the surface state site. However, identification of a super-linear dependence, even over a limited portion of the $\mathrm{SPV} = f(I)$ curve, is a definite indicator of surface states. For confirming this approach experimentally, Leibovitch et al. compared the $\mathrm{SPV} = f(I)$ curve of a device grade InP sample with a damaged surface (which is dominated by surface states) with the $\mathrm{SPV} = f(I)$ curve of a Fe-doped sample, dominated by bulk states, as shown in Fig. 82. A super-linear response is clearly observed for the surface states, but not for the bulk states, as appropriate.

In a somewhat similar approach, Lagowski et al. suggested earlier that Eqs. (5.46) can be used for site assignment based on monitoring the super-bandgap SPV transient curve [604]: due to the square dependence of the SPV on δQ_{ss} in the case of surface excitation, an exponential decay of n_t due to carrier emission, with a time constant of τ, would result in both τ and $\tau/2$ exponential components in the SPV curve. Conversely, only a τ component would be observed in the case of bulk excitation, due to the lack of a non-linear term.

Leibovitch et al. have further suggested that the high intensity end of the sub-bandgap $\mathrm{SPV}=f(I)$ curve can also be used for site assignment [116]. For bulk states, the shift of the SCR edge with increasing illumination is expected to modify the density of bulk states accessible to excitation which

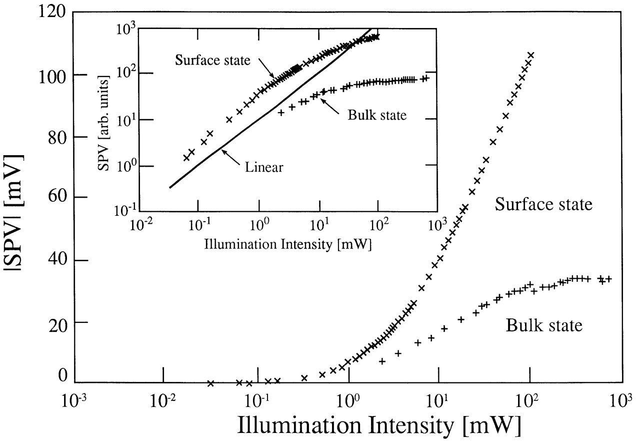

Fig. 82. Sub-bandgap SPV=$f(I)$ curves of InP samples. '×' – device grade sample with damaged surface. '+' – Fe doped sample. Inset: Logarithmic plot of the same curves, in arbitrary units, used for determining the super- or sub-linear nature of the curves (after Leibovitch et al. [116]).

produces a SPV signal (i.e., which is in the SCR). This should result in a gradual ('soft') saturation, whereas for surface states a 'hard' saturation is expected. This conclusion was also backed by numerical simulations. In Fig. 82, a 'soft' saturation is indeed observed for the bulk state. For the surface state, saturation is not achieved. However, in a subsequent study Kinrot et al. verified that a 'hard'-saturation producing state was indeed a surface state, as it disappeared after surface modification [357]. This criterion should nevertheless be used with caution as it is somewhat subjective, with the terms 'soft' and 'hard' not being strictly defined.

For scenarios involving *one* gap state, with selective excitation of either the bulk or the surface, the approaches given above seem to offer a clear method for site assignment. However, calculations or experiments which attack more complicated scenarios, (e.g., multiple states, surface trapping of bulk excited carriers and vice versa, etc.), have not been performed yet.

5.5. Thin films and heterostructures

In Section 2.2.5, we have shown theoretically that SPV measurements are sensitive not only to the surface SCR, but rather to any region within the sample, where absorption followed by charge separation may take place. Surprisingly, until recently this effect has found little use in SPV analyses, as almost no attempt at studying homojunctions, heterojunctions, or multilayer structures has been made. Thus, the only buried SCR to be studied, if any, has been due to non-Ohmic back contacts.

An elegant example of such a study is that of Kramer et al. [758], who investigated the SPV of semi-insulating CdS crystals by mounting a transparent electrode on a thin spacer on *both sides* of the sample. This formed a 'double MIS structure', which made it possible to illuminate the structure on either side. By systematically modifying the temperature, ambient, and illumination penetration depth, as well as making use of complementary photoconductivity measurements, Kramer et al. were able to separate the contribution of the front SCR, back SCR, and the Dember effect to the overall measured SPV signal. Some additional examples of back-contact effects were discussed in Section 5.1, in the context of diffusion length measurements. However, there these effects were generally considered as a nuisance and suppressed as much as possible. SPV-based charge mapping at the buried interface of silicon-on-insulator wafers was mentioned in Section 5.2.1 [589].

Some significant, yet isolated, SPV studies which were designed to study *buried* interfaces were presented in the early 1980s [759–761] and are discussed in more detail below. However, a concentrated effort at applying SPV measurements to the analysis of bi- and multi-layer structures was made only in the 1990s, mostly by the research group of the authors.

This section, which is devoted to the SPV analysis of films and heterostructures, begins with a detailed discussion of the principles and capabilities of SPS analyses of multilayer structures. This discussion is followed by reviewing the applications of SPS to the study of quantum structures and by showing how SPV measurements can be used for obtaining quantitative information on interface and heterostructure band diagrams.

Before proceeding, we note that it could be argued that the term '*surface* photovoltage' is no longer appropriate for a photovoltage related to buried interfaces. We shall nevertheless continue to use this term here because while the photovoltage is not necessarily *generated* at the surface, it is *measured* there.

5.5.1. Spectroscopy of multilayer structures

We start our discussion of the SPS of multilayer structures by considering an illustrative example, shown in Fig. 83. This figure features SPV spectra of a ZnO:Al/u-ZnO/CdS/Cu(In,Ga)Se$_2$ layered structure, used for the fabrication of thin film solar cells ('u' denotes unintentional doping) [402]. Distinct spectral 'knees' at $\sim$1 eV, $\sim$2.4 eV, and $\sim$3 eV, corresponding to the bandgaps of Cu(In,Ga)Se$_2$ (CIGS), CdS, and ZnO, respectively, are clearly observed. The unequivocal identification of all three bandgaps confirms the above mentioned theoretical prediction of SPS sensitivity to buried interfaces (see Fig. 18).

While spectral 'knees' are assigned to the various bandgaps as in the simple SPS analysis discussed in Section 4.1, the interpretation of the *slope sign* of these 'knees' is considerably more complicated than that offered in Section 4.1. There, we have argued that, as long as the SPV can be associated with a decrease in surface band-bending and that the surface SCR is in depletion or inversion, positive and negative super-bandgap SPVs necessarily correspond to *n*- and *p*-type materials, respectively. In the SPS of multi-layer structures, this simple rule is no longer necessarily valid for two distinct reasons.

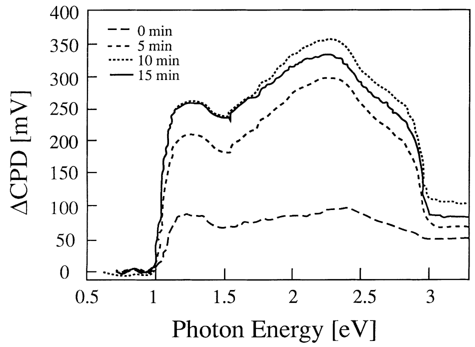

Fig. 83. SPV spectra of ZnO:Al/u-ZnO/CdS/CIGS structures for various annealing times (after Gal et al. [402]).

The first reason for deviation from the type assignment rule of Section 4.1 can be easily understood with the aid of Fig. 18. In this figure, the *n*-type thin film has *two* SCRs, related to the surface and the interface, both of which are in depletion. However, a decrease of the *surface* band-bending results in a positive SPV (Fig. 18(a)), whereas a decrease in the *interface band-bending* results in a negative SPV (Fig. 18(b)). This is a direct result of the different direction of the band-bending in the two SCRs with respect to the back contact. Therefore, an assignment of layer type which is based on the sign of the SPV slope can be made *only* if the dominating SCR can be identified. For example, Moons et al. measured the SPV response of the organic/inorganic *p*-dithioketopyrrolopyrrole (DTPP)/SnO_2:F heterojunction [414]. They used both front- and back-side illumination, which selectively excited the DTPP/air and the DTPP/SnO_2 depletion regions, respectively. Indeed, the SPV from the two depletion regions featured opposite signs, in agreement with the above explanation.

A special class of semiconductors, known as layered metal chalcogenides, feature basal plane surfaces which are free of dangling bonds and are therefore not expected to exhibit any band-bending under UHV conditions [762]. Consequently, the SPV of structures based on these materials should be governed by their buried interfaces, rather than by their surfaces. This provides a particularly good opportunity for experimentally confirming the SPV signs expected from a back SCR. Such a study was performed by Lang et al., who investigated the SPV of GaSe/WSe_2 structures under UHV conditions [762]. When studying the SPV of a *p*-GaSe/*n*-WSe_2 structure as a function of overlayer thickness, Lang et al. found a monotonously increasing *positive* SPV, attributed to the build-up of the depletion region at the buried *p–n* heterojunction. The SPV sign is in agreement with the direction of the band-bending at the buried depletion region and in disagreement with the SPV sign predicted for a depletion layer at the surface of the *p*-type top layer, as expected.

An even more interesting evolution of the SPV was found by Lang et al. when studying the *p*-GaSe/*p*-WSe_2 structure. After annealing (which is performed prior to GaSe growth), the surface region of the *p*-WSe_2 region is known to convert into *n*-type, so that the measured structure is really a bipolar-transistor-like *p*-GaSe/*n*-WSe_2/*p*-WSe_2 structure. In this case, a *negative* SPV, interpreted to be related to the buried *n*-WSe_2/*p*-WSe_2 homojunction, was found. The absolute value of this SPV decreased with increasing overlayer thickness, due to the counteracting effect of the *p*-GaSe/*n*-WSe_2 heterojunction, but the SPV sign was not inverted, indicating a dominance of the deeper junction throughout.

As the magnitude of equilibrium band-bending is not the only factor influencing the SPV magnitude, the SPV-dominating SCR is not necessarily where the equilibrium band-bending is larger. This point has been recently demonstrated by Moons et al., who studied *n*- and *p*-type porphyrin semiconducting layers which were (separately) deposited on Indium Tin Oxide (ITO) [413]. In this structure, two depletion regions in the porphyrin layer can be expected: a front one, associated with the free surface and a back one, associated with the Schottky barrier between the porphyrin layer and the highly conductive ITO. CPD measurements in the dark indicated an increase (decrease) of the surface work function of the porphyrin/ITO structure with increasing porphyrin *p*-type (*n*-type) overlayer thickness. This means that the CPD evolution is dominated by the increasing back depletion region, as domination of the front one would result in the opposite CPD trend. Nevertheless, the SPV slope change signs at the porphyrin 'bandgap' were found to be commensurate with a dominating band-bending reduction at the front depletion region, for both types of porphyrins used. This was interpreted by assuming that the recombination rate at the back SCR is larger than that at the front SCR, so that the photovoltaic effect at the back SCR is reduced. This conclusion was confirmed by independent contact *I–V* measurements in the dark and under illumination, which yielded a very small photovoltage. Similar results were obtained by Moons et al. at the *p*-DTPP/SnO_2:F heterojunction [414].

The second possible reason for deviation from the type assignment rule of Section 4.1 has to do with a reduced photon flux arriving at a buried SCR, due to partial absorption of light in the overlayer. In order to understand this effect, let us consider an extreme case where a certain layer absorbs light at its bandgap energy, but produces no photovoltaic effect whatsoever because for some reason no charge separation can take place. If at energies lower than this bandgap, a photovoltaic effect is produced at some region of the sample lying *beneath* this layer, then a decrease in the magnitude of the SPV will be noticed as soon as the layer begins to absorb. Thus, a 'knee' associated with the layer bandgap will be recorded in the SPV spectrum, even though the layer has not produced any photovoltaic effect of its own. Clearly, in this case the sign of the SPV slope change has nothing at all to do with the type of the layer.

As an experimental demonstration of absorption-related SPS features, let us consider the 'knees' of Fig. 83 in some more detail. Both the CdS and the ZnO layers are transparent to ~1 eV photons, so that the latter have no difficulty in getting to the CIGS region. At ~1 eV, the absorbed photons produce a positive ΔCPD (negative SPV), due to the reduction of the band-bending at the *n*-CdS/*p*-CIGS heterojunction. The same mechanism is also responsible for the solar cell operation of the ZnO/CdS/CIGS structure. It is much more difficult, however, to explain the CdS-related feature at ~2.4 eV in similar terms: On the one hand, if the SPV were due to additional absorption of photons at the CdS/CIGS *p–n* junction, the ΔCPD slope change would be positive, rather than negative. On the other hand, it is not reasonable to attribute the observed negative slope change to a significant depletion region at the ZnO/CdS interface because the existence of such a depletion region would severely hinder the solar cell performance of the structure. A reasonable explanation, however, is that as the CdS layer begins to absorb photons the effective photon flux at the region of the sample where charges can be separated is reduced. This, in turn, reduces the magnitude of the SPV signal. This mechanism is even more clearly at work near the ZnO bandgap, at ~3 eV, where a drastic decrease of the SPV signal is observed. After the ZnO bandgap, only a residual SPV which is independent of the photon energy remains. This is attributed to an incomplete relaxation of the CIGS-related SPV, due to non-steady-state conditions during the acquisition of the data. Thus, the agreement of the negative ΔCPD slope change signs at the CdS and ZnO bandgaps with the *n*-type nature of the CdS and ZnO layers seems to be coincidental, rather than reflecting a success of the type assignment scheme of Section 4.1.

Some recent SPV and SPS investigations of bi-layer structures have been devoted to the characterization of porous Si, using both contactless [308–312],[316],[763] and contact [313–315] measurements. Since porous Si is typically prepared by anodization of crystalline Si, a (porous-Si thin film)/(crystalline-Si substrate) structure is naturally formed. Accordingly, all SPS data of such structures revealed various features between ~2 eV and ~3 eV, related to the porous-Si layers, in addition to the crystalline-Si related 'knee' at ~1.1 eV [308,310–316]. However, the *sign* of the porous-Si related features was found to vary, depending on the technological details of porous-Si anodization and subsequent treatments [308].

In some of these studies [309–311], a complicated transient SPV behavior, including a non-monotonous relaxation of the SPV after illumination and relaxation times as long as several hours, was observed. This behavior, which is not found at surfaces of crystalline Si, indicates that significant trapping processes take place in the porous-Si layer (as can be expected from the highly non-ideal nature of this layer). As already argued in Section 4.1, this means that another mechanism for SPV generation, namely, preferential trapping, must also be taken into account and may even dominate over the usual band-bending-related SPV. When this is the case, the sign of the SPV response is again unrelated to the semiconductor type (see Section 4.1). Due to the complicated transport phenomena encountered at porous-Si layers, consensus has not been reached yet on the dominating SPV-generating mechanism in porous-Si/crystalline–Si structures. In different studies, *all* mechanisms described above have been invoked to explain the various trends observed in the different films studied. These mechanisms include the usual band-bending-related SPV (at both front and back SCRs) [311,315], preferential trapping at the porous-Si layer [311], and absorption at the porous-Si layer which reduces the crystalline-Si-related SPV [313].

We emphasize that, as in Section 4.1, the sign of the SPV *slope* at the various 'knees', rather than the sign of the SPV itself, must be analyzed. For example, Kashkarov et al. suggested that the inversion of the SPV sign at $h\nu > 3.2$ eV, observed after heating a porous-Si/crystalline-Si layer which was stored in air, reflected a change in the direction of electric field in the porous layer [311]). However, since no change in SPV slope signs was observed following this treatment, this interpretation must be rejected.

Throughout our discussion so far, we have implicitly assumed that the various SCRs in the structure are decoupled, namely, that the photovoltaic response in one SCR is independent of that of the other SCRs. For two SCRs to be decoupled, they must be separated by a quasi-neutral region which is thicker than both the Debye screening length, L_D (defined in Section 2.1.3), and the diffusion length, L. The former assures that the two SCRs cannot influence each other via electrostatic interaction. The latter assures that excess carriers cannot be injected from one SCR to the other. In semiconductors of reasonable doping and quality $L > L_D$, so that the diffusion length limitation is usually the more severe one. Mishori et al. have recently performed SPS measurements of a GaAs/AlGaAs heterojunction bipolar transistor (HBT) structure, consisting of a graded n^+-AlGaAs emitter on a p^+-GaAs base, which is itself on an n-GaAs collector [764]. This results in two depletion regions (emitter/base and base/collector) which feature opposite directions of band-bending. By design, a HBT structure must feature a significant injection of charge from emitter to collector. Accordingly, Mishori et al., using numerical calculations, have shown that the SPV spectrum undergoes significant qualitative *and* quantitative modifications with a changing electron mobility in the base (which changes the extent of charge injection between the two junctions). Thus, an explicit consideration of coupling effects is crucial for successful quantitative interpretation of coupled SCRs, but may be significant even for qualitative analyses if the coupling is substantial.

Karpovich et al. suggested an elegant experimental technique for separating between the back and front SCR contributions by means of changing the position of the back contact [341]. To understand their approach, let us consider Fig. 18 again. We have already explained that in the absence of significant Dember effects, the SPV measured at the semiconductor surface is an algebraic sum of the SPVs accumulated in the different SCRs between the surface and the back contact (see Section 2.2.5 and the discussion of back-contact effects in Section 5.1). Usually, the back contact is in the physical back of the sample so that the overall SPV is the sum of the SPVs due to both SCRs. However, if the back contact is placed on a non-illuminated edge of the *front* surface of the sample (and care is taken that it is not reached by photons or excess carriers), the measured SPV is *only* due to the front SCR. This is because the SPV due to the buried SCR changes the potential of both the 'back' and front contacts, so that it produces no net difference between them. The SPV due to the back SCR is then easily obtained by subtracting the SPV measured with the 'back' contact on the front side from the SPV

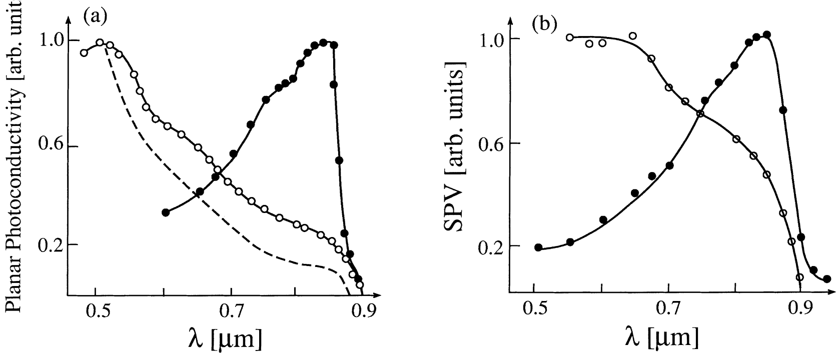

Fig. 84. (a) Spectral planar photoconductivity of GaAs layers: Filled circles – δ-doped layer. Empty circles – homogeneous layer. Dashed line – absorption spectrum. (b) SPV spectra of the δ-doped layer: Filled circles – back-SCR-related SPV. Empty circles – front-SCR-related SPV (after Bednyi et al. [342]).

measured in the usual configuration. We reiterate that the two SPVs obtained using this approach can be regarded as the SPVs obtained from each SCR had the other not existed *only* if the SCRs are decoupled.

As an illustrative example of the potential of such SPV separation, which also highlights some additional concepts discussed above, we consider the analysis of a δ-doped GaAs layer, performed by Bednyi et al. [342]. These authors compared the planar photoconductivity and SPV spectra of 0.5 µm thick n-type GaAs layers, deposited on a semi-insulating GaAs substrate, with and without a 'δ-doping' monolayer of Ge, situated 0.1 µm below the surface, shown in Fig. 84. The planar photoconductivity of the δ-doped layer is much lower than that of the homogeneous sample. Moreover, Fig. 84(a) shows that the planar photoconductivity of the δ-doped layer decreases significantly after the initial onset of GaAs absorption, whereas the planar photoconductivity of the homogeneous sample increases with increasing absorption throughout the wavelength range studied.

The key to understanding the different behavior of the planar photoconductivity in the two samples is in the SPV measurements of the δ-doped layer, shown in Fig. 84(b). In principle, the planar photoconductivity is modified mostly due to the photo-induced change in the depletion region width (at both front and back SCRs). In the homogeneous layer, the main effect is that of the front SCR. Indeed, the spectral dependencies of the front SPV and the planar photoconductivity spectrum of the homogeneous sample are strikingly similar because both are governed by the same physical phenomenon. In the presence of the δ-doped layer, the top 0.1 µm of GaAs which is above this layer is completely depleted both in the dark and under illumination. Moreover, the surface charge is screened by the δ-doped layer. Thus, no significant modulation of either the planar photoconductivity or the back SPV due to the front SCR takes place. Hence, all photoconductivity features must be due to the modulation of the back SCR, which is the cause for the striking resemblance between the back-SPV and the planar photoconductivity of the δ-doped layer. The observed relatively smaller magnitude of the back surface modulation explains why the photoconductivity is significantly reduced. Finally, the decrease of both back SPV and photoconductivity with increasing photon energy is due to the increase of absorption in the top GaAs layer, which decreases the effective photon flux arriving at the bottom GaAs layer.

As SPV analyses of multi-layer structures offer the possibility of performing *contactless and non-destructive* electrical and optical characterization of buried interfaces, they have found significant uses in the field of process monitoring and quality control. In one of the earliest applications, Munakata and

Honma demonstrated that frequency-resolved ac-SPV measurements, of the type shown in Fig. 77, may be used to measure the SCR cut-off frequency (ω_a in the figure) at a *buried p–n junction* and not just at a surface SCR [761]. This is based on assuming that the contribution of the surface SCR to the overall SPV is negligible due to the high doping of the layers.

Goldstein et al. argued that, by definition, SPV measurements are conducted under open-circuit conditions. Therefore, if the surface-related SPV in solar-cell structures is negligible, the measured SPV must be equal to the open-circuit voltage of the solar-cell, V_{oc}. Thus, a contactless measurement of V_{oc} is made possible [759,760]. By comparing contact photovoltaic measurements with SPV measurements, this was verified by these authors at both single-crystalline [759] and amorphous [760] Si-based solar cells. Moreover, by measuring the SPV as a function of illumination intensity and assuming that photo-bias can be equated to electrical bias, the ideality factor of the solar cell was found (and again confirmed by electrical measurements). Later, Rennau et al. have suggested that SPV measurements can be used for measuring the V_{oc} as a function of position in large area solar cells for a contactless assessment of homogeneity [734].

Recently, Kronik et al. have used SPS measurements for quality control of ZnO/CdS/CIGS-based solar cells [404]. In this study, the contactless nature of the measurement made it possible to eliminate defective structures after the deposition of each of the three semiconducting layers. As an example, we consider the quality control of the CdS/CIGS bi-layer structures is shown in Fig. 85. Here, samples with different Na contents (which is known to enhance the photovoltaic performance of CIGS-based cells) were examined. Fig. 85(a) shows that the SPV spectrum of the Na-poor sample is *qualitatively* different then the other SPV spectra: it features a distinct decrease of the SPV signal immediately after its initial onset, whereas the other spectra continue to increase with increasing photon energy, until ~1.7 eV (where the SPV reduction is attributed to a surface state lying at the external CdS surface). The

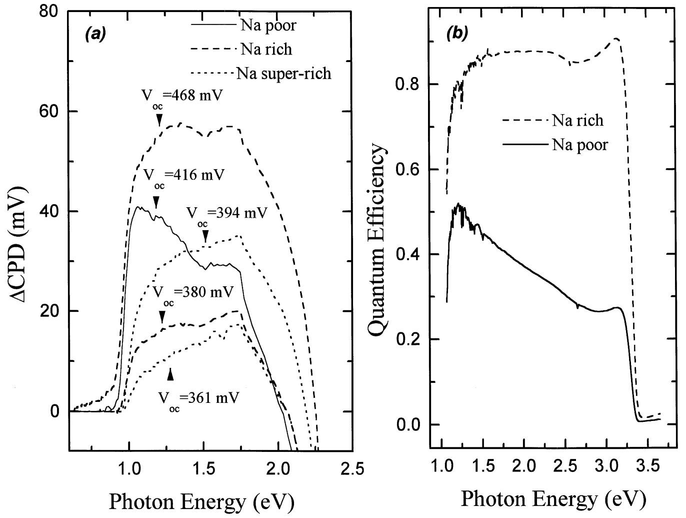

Fig. 85. (a) SPV spectra of CdS/CIGS structures with three different Na contamination levels. Open-circuit voltages of solar cells fabricated from region adjacent to the measured samples are denoted. (b) Quantum efficiency spectra of a ZnO/CdS/CIGS solar cell, based on a Na-poor and a Na-rich CIGS layer (after Kronik et al. [404]. Quantum efficiency data taken from Rau et al. [765]).

difference in the SPV response of the Na poor and Na rich layers is strikingly reminiscent of a similar difference observed in quantum efficiency spectra, shown in Fig. 85(b) [765], which were measured independently on solar cells of the same make. However, the latter measurements were performed on *complete and contacted* solar cells, whereas the SPV measurements are contactless and performed on a partial structure, allowing for early rejection of inadequate layers.

For the bi-layer structure studied, the SPV obtained with broad-band illumination (e.g., from a solar simulator) is *not* expected to reflect V_{oc} accurately, due to the influence of a significant SCR at the external CdS surface. However, Fig. 85(a) clearly shows that the magnitude of the SPV step at ~1 eV, related to absorption at the CdS/CIGS interface itself, depends monotonously on V_{oc}. Thus, pending appropriate calibration, this magnitude can be used for quantitative screening of layers predicted to result in cells with sub-standard V_{oc}. Fig. 83 provides another example of process monitoring – this time of the impact of annealing on the complete CIGS-based solar cell structure [402] In the figure, the beneficial influence of annealing on the photovoltaic response is clearly apparent. Moreover, the optimal annealing time can be easily assessed.

To date, the use of SPS of heterostructures for quality control and process monitoring purposes has been applied mostly to solar cells. One of the reasons is that solar cell structures are ideally suited for SPS studies, as they are a-priori designed so as to ensure significant photon absorption at the interfaces of interest. Two notable examples of SPS-based quality control of other structures have been reported recently: Krystek et al. used SPS for gauging the success of *p*-type doping at InGaN/GaN structures [359]; Mishori et al. used SPS for assessing the bandgap narrowing of the degenerately doped base layer in a HBT structure, from which the base doping can be assessed [764].

So far, only super-bandgap and near-bandgap SPV features were discussed. In light of the discussion in Section 4.2, it is clear that SPS should also yield significant information on gap states. However, we are aware of only two systematic SPS studies of gap states in heterostructures [20,355]. Burstein et al. studied lattice-mismatched $\mathrm{In}_x\mathrm{Al}_{1-x}\mathrm{As/InP}$ epilayers with various values of x [355]. They observed a rich spectrum of defect states, especially in highly strained samples with reduced crystalline quality. As the qualitative analysis of the sub-bandgap SPS features observed by Burstein et al. is similar to that of bulk samples discussed in Section 4.2 (except that again special care must be exercised with respect to sign conventions, due to the possible influence of back SCRs), this work is not discussed in more detail here.

Some quantitative aspects of the SPS of thin film structures were studied by Leibovitch et al. [20]. In particular, the evolution of the SPV spectra of a (thin semiconducting film)/(semiconducting substrate) structure with increasing overlayer thickness was examined. Assuming that the overlayer is thin enough to be completely depleted, the calculus of variations leading to Eq. (2.89) can be readily extended to the form appropriate for the structure at hand [20]:

$$\delta V_{\mathrm{s}} = \frac{w}{\epsilon_{\mathrm{s}}}\delta Q_{\mathrm{ex}} + \int_0^{w_{\mathrm{f}}}\left(\frac{w}{\epsilon_{\mathrm{s}}} - \frac{x}{\epsilon_{\mathrm{f}}}\right)\delta\rho_f(x)\mathrm{d}x + \frac{w - w_{\mathrm{f}}}{\epsilon_{\mathrm{s}}}\delta Q_{\mathrm{in}} + \int_{w_{\mathrm{f}}}^{w}\frac{w - x}{\epsilon_{\mathrm{s}}}\delta\rho_{\mathrm{s}}(x)\mathrm{d}x, \tag{5.47}$$

where the subscripts ‘ex’, ‘in’, ‘f’, and ‘s’ denote the external surface, interface, film, and substrate, respectively, w_{f} is the overlayer thickness, and w is the *total* width of the SCR, which includes w_{f} and the depletion region extending into the substrate.

Inspection of Eq. (5.47) shows that even under the most ideal conditions, where all (surface and volume) charge densities involved in the equation are thickness independent, modification of w_{f} will *inherently* alter the measured SPV. This is because the SPV due to a gap state situated in a SCR also

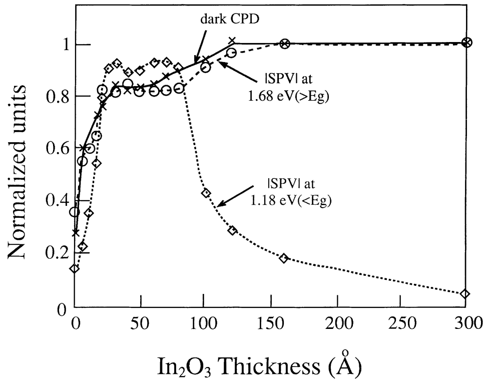

Fig. 86. Evolution of the (normalized) CPD and SPV at the In_2O_3/InP heterojunction, as a function of In_2O_3 overlayer thickness. 'x' – CPD, '○' – super-bandgap SPV, '◇ – sub-bandgap SPV (after Kronik et al. [19]).

depends on the distance between this state and the edge of the SCR (as already noted in Section 2.2.3, in the context of bulk states). In theory, if the SPV evolution is governed *solely* by this effect, then the different thickness dependence of the SPV due to states at different sites could be used for a non-destructive assignment of these sites [20].

In practice, the evolution of the SPV with changing w_f is influenced and possibly dominated by a changing interaction of the defect states with the bands, which changes their occupation. This may provide considerable insight into the formation of various semiconductor interfaces and into the relation between their defect and electrical properties. A case in point is the evolution of the super-bandgap and sub-bandgap SPVs with increasing In_2O_3 overlayer thickness, due to defect states at the n^+-In_2O_3/p-InP heterojunction [19,20], as shown in Fig. 86. Initially, both the sub- and super-bandgap SPVs increase with increasing overlayer thickness, due to the increase of the layer thickness and the build-up of the junction SCR. At higher thicknesses, the super-bandgap SPV finally saturates, indicating that the build-up of the SCR is complete. However, the sub-bandgap SPV decreases. The behavior of the super-bandgap SPV rules out a collapse of the band-bending or a significant increase of recombination rates at the In_2O_3/InP interface. Therefore, the sub-bandgap SPV decrease must be interpreted in terms of filling of the donor states by electrons supplied from the n^+ side of the junction, which impedes electron excitation into the defect state. This serves to explain the why the ideality factor of In_2O_3/InP diodes is very close to 1, despite their clearly non-ideal interface: at the final In_2O_3 film thickness, the interface defect states are primarily filled and are thus of limited electrical activity.

In the above discussion, all geometry was considered to be one-dimensional, with the buried interfaces parallel to the free surface of the sample. To conclude this section, we note that in recent years, several studies have been devoted to high-resolution KFM- [766–768] and STM- [769] based SPV mapping of structures cleaved along the growth direction of the sample. In such structures, the buried interfaces intersect the free surface of the sample and are *perpendicular* to it. Then, one must consider a *lateral* SPV effect, associated with the buried interfaces, in addition to the *vertical* one, associated with the free surface.

As an example, let us consider the CPD profile of a hypothetical cleaved *p*–*n* junction. In the dark, the junction is usually discerned as a potential drop in the CPD profile. However, the magnitude of this potential drop is usually found to be much smaller than the built-in voltage of the junction [766–768], because both the *p* and the *n* sides of the junction are depleted. (Note that in the limiting case of a completely pinned surface Fermi level, the work function is independent of the substrate doping and the *p–n* junction would not be observed). Upon illumination, the potential drop over the *p–n* interface should decrease due to the photovoltaic effect. This, in turn, should result in a further loss of the CPD contrast. On the other hand, the photovoltaic effect at the free surface should decrease the degree of depletion at both *p* and *n* sides of the junction, which should bring the surface work function values closer to their non-depleted values and increase the CPD contrast. In practice, both an illumination-induced increase [766,768] and decrease [767,768] in contrast have been observed, indicating that the dominance of a particular mechanism is a result of a complicated interplay between surface properties, interface properties, and sample geometry.

5.5.2. *Spectroscopy of quantum structures*

Quantum structures are characterized by significant changes in their absorption spectra, with respect to that of the bulk materials on which they are based. Since the photovoltaic spectrum is related to the absorption spectrum, these changes are detectable by SPS. For example, the quantum size effect in nano-crystallite films (namely, the blue shift in their apparent bandgap with decreasing crystallite size), was already discussed in Section 4.1. Most modern quantum structures are based on multilayer heterostructures. Therefore, quantum effects in their absorption features can be analyzed using the SPS principles outlined in the preceding section. Specifically, the absorption spectrum is characterized by peaks (rather than ‘knees’) which correspond to electron transitions between different quantum levels (such peaks are washed out in nano-crystallite films due to a broad size distribution of the crystallites). These characteristic peaks were indeed found in numerous *contact* photovoltage (and photocurrent) spectroscopy studies of quantum well structures (see, e.g., [770]). Similar peaks were found in some contact photovoltage spectroscopy of porous-Si/crystalline-Si structures and may be related to the quantum nature of the Si wires in the porous layer [313,314].

To the best of our knowledge, the first *contactless* SPS studies of quantum well heterostructures were conducted by Karpovich et al. [771,772]. These authors studied GaAs samples with a single InGaAs quantum well layer, ‘inserted’ at the GaAs free surface, at the surface SCR, or inside the quasi-neutral region. In these early studies, they were able to identify the lowest quantum transition (namely, 1H–1E, where 1H and 1E are the first hole and electron quantum levels, respectively) and verify its increasing energy with decreasing well size. In some cases, they were also able to observe the 2H–2E transition as well [772]. Moreover, they observed a sensitivity of the absorption spectrum to the polarization of the illumination, confirming the quantum nature of the observed transitions [773]. In a different application, they have inserted three InGaAs quantum wells of different thickness (and hence different quantum transitions) in different places inside the SCR of a GaAs sample [774]. As expected, they obtained three distinct SPS (as well as photoluminescence) features, associated with the 1H–1E transitions of the different wells. Viewing these quantum wells as ‘position markers’, they checked the effect of anodization and ion bombardment on the three peaks in order to monitor the penetration depth of the damage.

At about the same time, Wessels and Qian used STM-based spectroscopy for identifying the first two quantum transitions of an InAsP quantum well ‘inserted’ in the SCR of an InP sample [775]. These were the 1HH–1E and 1LH–1E transitions, where the ‘HH’ and ‘LH’ refer to heavy and light holes, respectively. Again, the quantum energies were found to increase with decreasing well size, as expected. In this study, the measured quantity was the tunneling photocurrent, rather than photovoltage. However, as the quantum well was situated 100 nm below the surface, the photo-induced changes in the tunneling current were related to the photovoltaic modulation of the surface potential.

Ashkenasy et al. were the first to study GaAs/AlGaAs multi quantum well (MQW) and superlattice (SL) structures using SPS [415]. The SPV spectra obtained in this case contained many interesting features and are therefore considered in detail as an illustrative example. The SPV spectra of a MQW sample and its calculated equilibrium band-diagram are shown in Figs. 87(a,b), respectively. The spectral 'knees' at 1.38 and 1.78 eV correspond to the onset of band-to-band absorption in the GaAs epilayer (beginning at energies below the nominal bandgap due to the Franz-Keldysh effect) and the AlGaAs cap layer, respectively. In between these two 'knees', the shape of the SPV spectrum resembles typical absorption spectra of MQW structures. However, the expected absorption peaks, at 1.48 eV and at 1.61 eV, are displayed as *minima*, rather than *maxima*. This indicates that most of the illumination is absorbed in the quantum wells which are situated where the bands are bent upwards towards the surface. The observed MQW-related peaks agreed well with calculated energy values of the 1HH–1E and 2HH–2E transitions. Note that before etching, a non-negligible sub-bandgap SPV signal was apparent at photon energies below 1.38 eV, indicating the presence of optically active gap states. Since no such signal was observed after etching, it was concluded that these states were located at the external AlGaAs surface and were not associated with the MQW region. Moreover, the SPV spectrum in the MQW absorption energy range has not changed at all (other than undergoing a uniform shift) after the etch, ascertaining that the SPV signal in the MQW absorption range is not interfered by surface effects.

The SPV spectra of a SL sample is shown in Fig. 87(c). Here, three minima are observed in the photon energy range of absorption in the SL region, corresponding to the 1HH–1E, 2HH–2E and 3HH–3E transitions. The 4HH–4E transition is also apparent as a shallow valley in the spectrum. Here, the peaks are broader than in the MQW sample due to the formation of minibands in the well region of SL structures and each minimum is located at the middle of the calculated miniband position.

The spectra of Fig. 87 clearly demonstrate the ability of SPS to provide unequivocal identification of many quantum-transition-related absorption features. Interestingly, in both the MQW and SL spectra *all* 'symmetry-allowed' heavy-hole-electron transition have been resolved, *at room temperature*. In contrast, photoluminescence measurements performed on the same samples at room temperatures yielded only the first quantum transition for the MQW sample and the first two for the SL sample [415]. Moreover, as opposed to transmission spectroscopy, SPS does not require any substrate thinning and it is much easier to perform than photoluminescence excitation measurements. In a similar vein, Karpovich and Filatov have shown that in the study of coupled asymmetric InGaAs wells situated in the SCR of a GaAs sample, many absorption features related to higher-lying quantum levels can be observed in the SPV spectra, but not in the photoluminescence spectra [776]. In the latter study, the lowest-energy quantum transition was also used to extract the mole fraction of the InGaAs quantum well.

Following the above demonstration of MQW and SL characterization, Aigoui et al. have used SPS in conjunction with a constant photon flux illumination source [423]. Then, assuming that the ratio $[\mathrm{d(SPV)/d}(h\nu)]/(\mathrm{SPV})$ is proportional to the ratio $[\mathrm{d}\alpha/\mathrm{d}(h\nu)]/\alpha$, they were able to fit the former ratio with a lineshape fit. This was used for the identification of many 'symmetry-allowed' and 'symmetry-forbidden' quantum transitions in ZnSe/ZnMgSSe MQW structures.

As in the case of non-quantum multilayer structures, the contactless capabilities of SPS have made it attractive for monitoring device-oriented layer structures. Two such studies have been reported recently. Aigoui et al. measured the SPV spectra of a self-assembled quantum dot (QD) InAs/GaAs laser

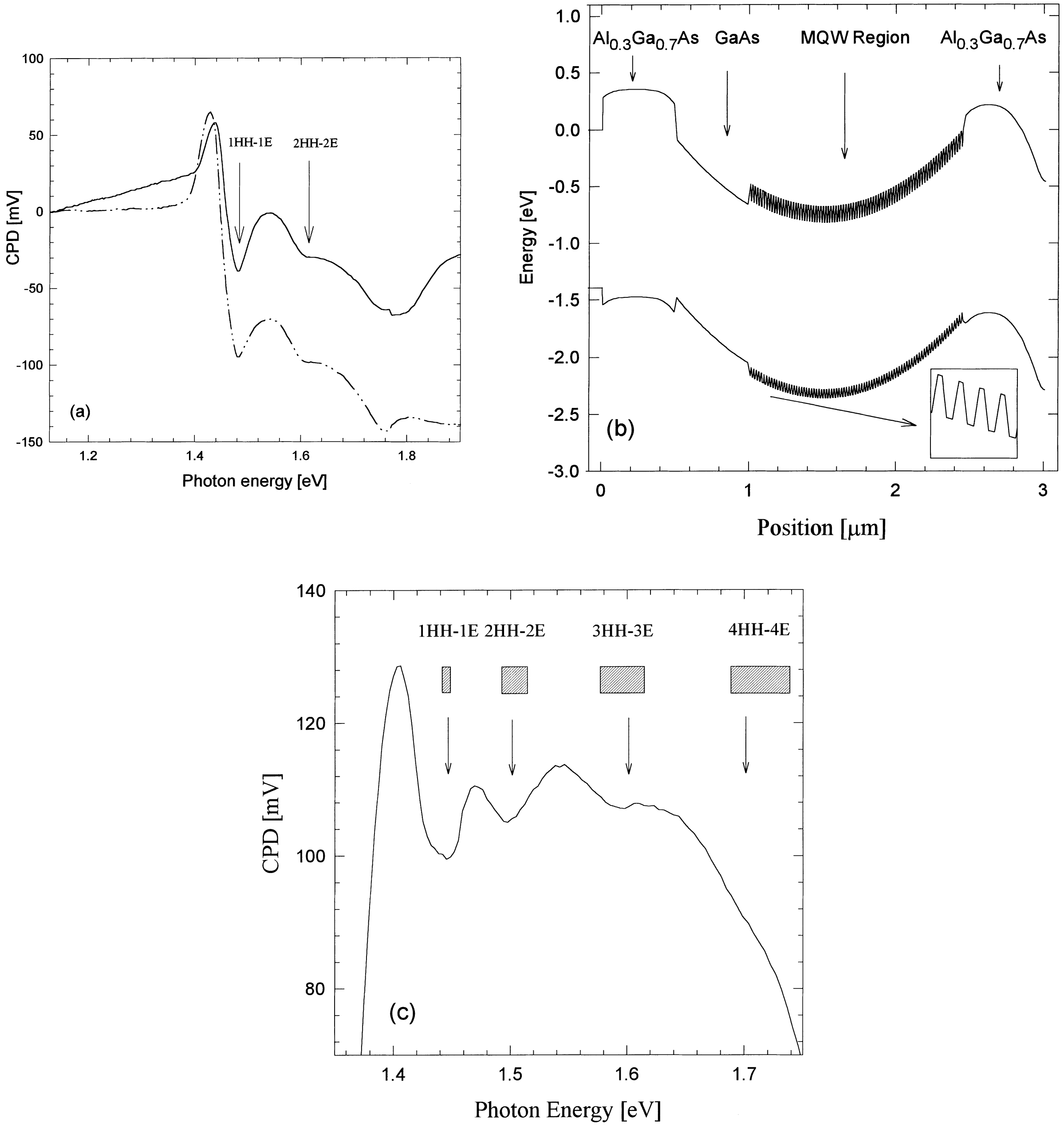

Fig. 87. (a) SPV spectra of a GaAs/AlGaAs MQW sample before (solid line) and after (dashed line) etching for 4 minutes (arrows denote minima corresponding to heavy-hole-electron transition absorption peaks). (b) Calculated equilibrium band diagram of the MQW sample (position measured with respect to substrate edge). (c) SPV spectrum of a SL sample. Arrows denote minima corresponding to heavy-hole-electron transition absorption peaks. Rectangles denote theoretical energy width of SL minibands (after Ashkenasy et al. [415]).

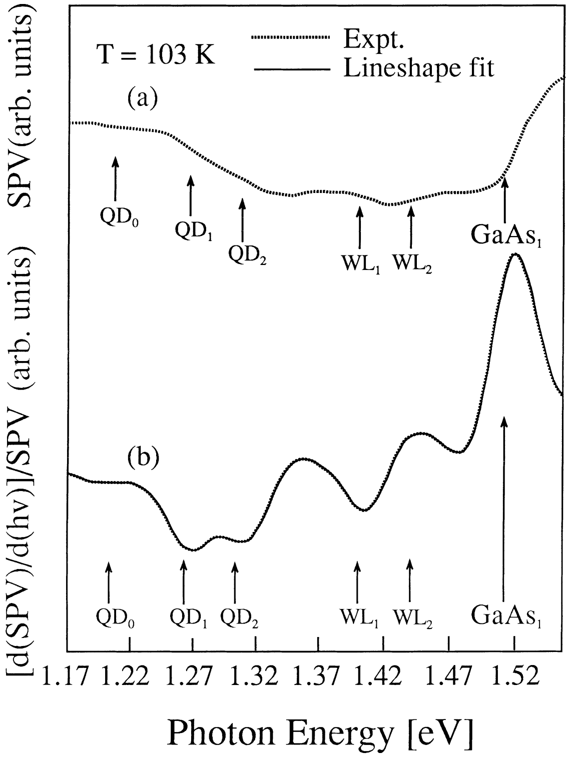

Fig. 88. SPV spectrum (a) and normalized SPV derivative spectrum (b) of an InAs/GaAs quantum dot structure. The solid line is a lineshape fit (after Aigoui et al. [777]).

structure [777]. In this structure, an InAs wetting layer (WL), which forms a quantum well, is deposited on a GaAs layer. The strong lattice mismatch between the two semiconductors induces the formation of InAs dots. These dots are then self-organized during ten cycles (in this case) of alternate short-period GaAs/InAs depositions. This active region of the structure is 'inserted' between thin GaAs layers, themselves 'inserted' between two GaAs/AlGaAs SLs and AlGaAs cladding layer and sandwiched in a GaAs *p–n* junction. Both the as-measured SPV spectrum and its normalized derivative for this structure (at 103 K) are shown in Fig. 88 [777]. With the aid of the derivative spectrum, three QD-related transitions and two WL-related transitions are extracted.

Ashkenasy et al. have studied a single quantum well graded-index-of-refraction separate-confinement heterostructure laser [778]. The studied structure consisted of a single pseudomorphic InGaAs quantum well, 'inserted' between two thin GaAs layers and two graded AlGaAs layers and sandwiched in an AlGaAs *p–n* junction. In this case, four peaks associated with the four 'symmetry-allowed' heavy-hole-electron transitions, as well as a fifth peak due to combination of several 'symmetry-forbidden' transitions were observed at room temperature. In this study, numerical simulations have shown that the energy of the 1HH-1E transition is mostly affected by the mole fraction of the InGaAs layer, whereas the energy of the 2HH-2E transition is primarily sensitive to the magnitude of the electric field in the quantum well, due to the quantum confined Stark effect. Thus, these two important parameters could be extracted from the experiment. Using the simulation, the dependence of the energy of the 1HH-1E transition on the electric field was calculated. Specifically, its value for a small electric field (such as that present during the forward bias required for lasing) was found. This enabled a contactless estimate of lasing wavelength, based on layer properties, prior to device processing. In light of the above discussion, SPS seems to be emerging as a promising tool for the characterization of quantum structures.

Having described the main developments and achievements of SPS studies of quantum structures, we conclude this section by considering some aspects of SPV generation and spectrum interpretation in quantum structures in more detail. While the absorption features of the quantum structures were examined at some length in the above examples, the charge separation mechanism – required for getting a SPV signal - was not considered so far. In the discussion of Fig. 87, we assumed that the generated electrons and holes are separated by the electric field just like in a non-quantum structure. However, this clearly requires that the excess carriers escape from the quantum well. Several temperature-resolved quantum well SPS studies revealed a decrease of the signal with decreasing temperature [423,771,772,776], whereas the simple photovoltaic effect is expected to increase with decreasing temperature (see Section 2.2.2). This indicates that carriers escape from the well by means of thermal excitation, which is insufficient at low temperatures. However, as the obtained temperature dependence is usually non-exponential [771,772], it is clear that other mechanisms, especially field-induced tunneling from the quantum well, also assist in generating the SPV signal.

As long as the cause of the SPV is the separation of charge carriers by the electric field in a SCR, the sign of the SPV signal will reflect the direction of this electric field and not the layer type, regardless of the exact escape mechanism [415,771]. As in non-quantized structures, it is necessary to consider other SPV-generating mechanisms to which this sign interpretation scheme does not apply. First, in interpreting any decrease in the absolute value of the SPV signal, an absorption-induced decrease of photovoltaic effects at a layer beneath the light absorbing one must be considered. For example, the quantum-transition-related minima in Fig. 87(a) could partially be due to modulation of the light intensity arriving at the GaAs layer by the MQW region. However, in this spectrum, recorded under steady-state conditions, the change of *sign* in the total SPV indicates that at least part of the signal is due to photovoltaic activity in the MQW region itself. Second, charge separation due to preferential trapping of charges must also be considered. For example, Cameron–Miller et al. noticed that the placement of a GaAs quantum well at the surface of an AlGaAs layer resulted in a photo-induced *increase* in surface band-bending because photo-excited electrons were preferentially trapped in the surface quantum well [779]. In addition, Karpovich et al. measured a non-negligible SPV signal related to InGaAs quantum wells embedded in the quasi-neutral region of a GaAs layer [770,774]. In this case, the only electric fields are due to the InGaAs/GaAs heterojunction and must be symmetric with respect to the quantum well. The observation of a SPV in this case must therefore indicate a *preferential escape* of one type of carriers from the well, resulting in an effective charge separation.

5.5.3. Construction of band diagrams

The construction of *interface* band-diagrams is a relatively new application of SPV measurements. A first, significant step in this direction was taken by Goldstein et al. [759,760], who performed 'depth-profiled' SPV analyses by measuring solar cell structures after repeated sputtering steps. As an example, we consider the SPV profile of an a-Si:H *p–i–n* solar cell, shown in Fig. 89 [760]. The SPV profile clearly resolves the different layers in the studied structure. Moreover, it elegantly reveals the effects of prolonged illumination ('light soaking') on the device properties: after illumination, the SCR width at the p^+–*i* junction decreases (due to an increase in the effective doping at the *i* region),

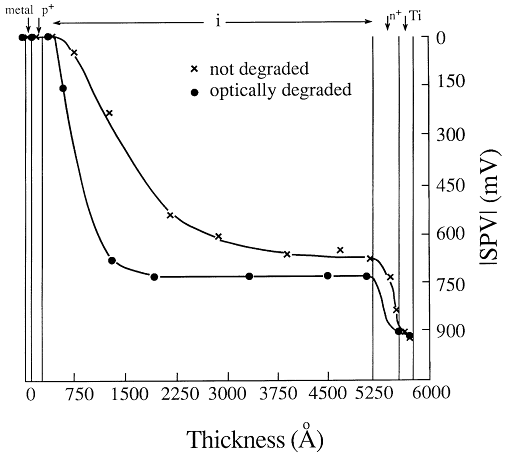

Fig. 89. SPV profiles of an a-Si:H solar cell, before and after degradation by prolonged illumination (after Szostak and Goldstein, [760]).

producing an additional ‘dead layer’, at which charges cannot be separated by an electric field. This results in a decreased solar cell performance.

While qualitatively very useful, an SPV profile of the type shown in Fig. 89 should by no means be considered as reflecting the true potential distribution in the studied structure, for several reasons. First, the etching process may introduce surface defects which may result in a non-negligible surface band-bending. Then, the measured SPV will contain a contribution which is unrelated to the SCRs of the real structure. As long as the surface and buried SCRs are decoupled, the contribution of the former may be eliminated by separately assessing its contribution to the overall signal using test structures [760,780]. The SPV data shown in Fig. 89 has been corrected against this effect. However, even if there are no surface states the obtained profile may deviate from the real one when the width of a given layer is thinner than the normal SCR width in this layer [760,780]. This is because in this case charge equilibrium cannot be obtained unless an additional potential in the thin layer is produced. The most serious limitation of SPV profiling stems from the obvious, yet crucial fact that a potential profile of a junction can be obtained only if the junction itself remains intact [760]. For junctions where one side is significantly more heavily doped, as in the structure studied in Fig. 89, most of the SCR is in the lightly doped side. Thus, the junction potential can be studied only if profiling proceeds from the lightly doped side. Accordingly, the spatial extent of the *n–i* junction in Fig. 89 cannot be studied and the junction is marked only by a sharp drop in the SPV. Finally, we recall that the SPV is also influenced by recombination rates, so that SPV modifications may be due to, e.g., varying defect densities (or defect filling), rather than due to a real change in potential.

Kronik et al. have combined CPD and SPV measurements for a complete and quantitative construction of heterojunction band-diagrams, where both sides of the junction can be assumed uniform and the junction is abrupt [19,403,605]. Their approach starts with the measurement of the built-in voltage of the heterojunction. Using Fig. 8, it is readily observed that the built-in voltage of the heterojunction can be expressed as:

$$eV_{\mathrm{bi}} = W_1 - W_2, \tag{5.48}$$

where W_1 and W_2 are the *ideal* work functions of the two sides of the heterojunction. In other words, W_1 and W_2 correspond to the distance between the Fermi level and the local vacuum level in the quasi-neutral region on each side of the heterojunction. In the case of ideal surfaces (i.e, containing no surface band-bending and surface dipole), $W_1 - W_2$ can be measured by subtracting the CPD measured at the free surface of the complete heterojunction from the CPD measured at the free surface of the substrate (prior to semiconductor deposition). In practice, the measured CPD difference will be given by $\Delta\,\mathrm{CPD} = W_1' - W_2'$, where W_1' and W_2' are the real (non-ideal) surface work functions of the substrate and overlayer. Using Fig. 4 and Eq. (2.36) for relating the ideal and real surface work-functions, Eq. (5.48) is recast in the form:

$$\begin{aligned} eV_{\mathrm{bi}} &= W_1 - W_2 = (W_1' - eV_{\mathrm{s1}} + \Delta\phi_{\mathrm{s1}}) - (W_2' - eV_{\mathrm{s2}} + \Delta\phi_{\mathrm{s2}}) \\ &= \Delta\mathrm{CPD} - (eV_{\mathrm{s1}}^0 - eV_{\mathrm{s2}}^0) + (\Delta\phi_{\mathrm{s1}} - \Delta\phi_{\mathrm{s2}}). \end{aligned} \tag{5.49}$$

Eq. (5.49) shows that the built-in voltage in a real case is still related to ΔCPD, but must be corrected by the difference in surface band-bending and surface dipole of the two free surfaces. Once V_{bi} is determined (and assuming that the bulk properties are known), the band offsets can be determined using Eqs. (2.43) and (2.46).

Experimentally, ΔCPD can be easily determined from overlayer-thickness-dependent CPD measurements, as shown in Fig. 86. When the overlayer is thick enough to contain a quasi-neutral region, the CPD reading saturates and the true ΔCPD is obtained. V_{s1}^0 and V_{s2}^0 can be determined by photosaturation, or any of the techniques described in Section 5.2.2. Then, if the surface and interface dipoles are estimated (using chemical considerations [605] and/or measurements of the type discussed in Section 5.2.3), the built-in voltage and the heterojunction band offsets can be found.

The above outlined approach seems to be of particular advantage for junctions comprising polycrystalline or amorphous materials, or for heterojunctions which are not prepared using conventional UHV fabrication tools. This is because in such junctions many other band-offset measurement techniques tend to fail, or produce inconclusive data. For establishing its validity, the SPV/CPD-based approach was first demonstrated on the In_2O_3/InP heterojunction, where its results could be easily confirmed using *I–V* analysis due to the degenerately high doping of the In_2O_3 side [19]. It was then applied to the polycrystalline CdS/CIGS heterojunction, manufactured using wet chemical methods, where the band offset values were under considerable debate [605]. Moreover, the measured CPD versus overlayer thickness curve, and hence the extracted band lineup, were found to be independent of sample annealing (within experimental error) [403].

Complete construction of the equilibrium band-diagram can be obtained by further considering the CPD and super-bandgap SPV evolution shown in Fig. 86. The overlayer thickness at which the CPD and SPV saturate is indicative of the overlayer width at which the surface and interface SCRs decouple, i.e., of the minimal overlayer thickness required to completely sustain the interface SCR. Therefore, an estimate of the SCR width at the overlayer is obtained. Then, the interface charge density (which is the only remaining independent junction parameter) can be found by fitting the CPD evolution to produce the measured SCR width in the overlayer [19,605]. Other parameters, e.g., the built-in voltage on either side of the junction and the total SCR width, can then be obtained from a solution of the Poisson equation pertaining to the heterojunction, which is based on the measured parameters.

Clearly, the weak point of the above outlined approach is that surface and interface dipoles are not measured directly, and therefore limit the experimental accuracy which can practically be obtained to ~ ±100 meV. Leibovitch et al. suggested a different approach for band offset determination, which

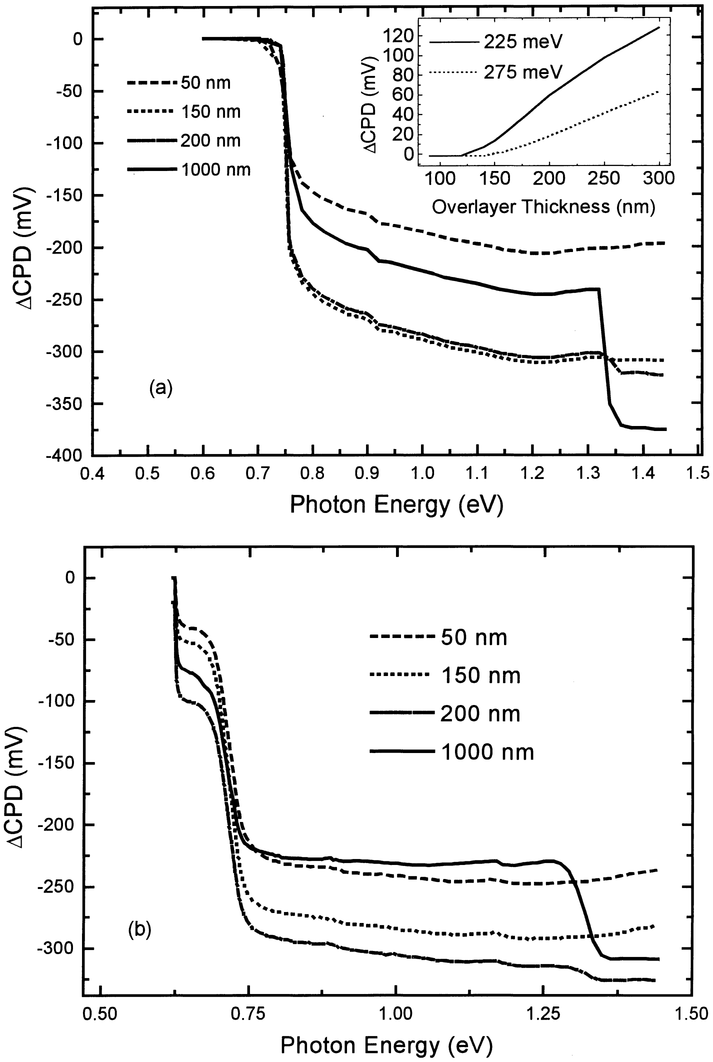

Fig. 90. (a) Numerical simulation of SPV spectra of the n^{-}-InP/n-In$_{0.53}$Ga$_{0.47}$As structure for various InP overlayer thicknesses (curve for 200 nm is shifted up by 20 mV for clarity). Inset: magnitude of the spectral ‘knee’ at 1.35 eV vs. InP overlayer thickness for $\Delta E_c = 275$ meV and $\Delta E_c = 225$ meV. (b) Experimental SPV spectra of the same structure for various overlayer thicknesses (after Leibovitch et al. [21]).

relies solely on SPS measurements and is therefore inherently immune to dipole-induced errors [21]. The principle of this approach is shown in Fig. 90, which features the numerically simulated and experimentally measured SPV spectra of the n^{-}-InP/n-In$_{0.53}$Ga$_{0.47}$As structure, for various InP overlayer thicknesses. At large InP overlayers, both simulated and experimental SPV spectra feature two distinct ‘knees’ at the InGaAs and InP bandgaps (0.75 and 1.34 eV, respectively), as expected. However, at small overlayer thicknesses, the InP-related ‘knee’ is absent. Additional simulations showed that the critical thickness at which the InP-related feature appears, w_c, is very strongly dependent on the band offsets used. For example, the inset of Fig. 90(a) shows that a change of 50 meV in ΔE_c changes w_c by 25 nm, which is a considerable thickness.

The behavior of the SPV spectra may be explained physically as follows: For small InP overlayer thicknesses, the density of excess carriers generated in the InP layer is negligible with respect to the excess carrier density injected from the InGaAs side due to the (forward) photo-bias. Therefore, no discernible SPV feature is recorded at the onset of absorption in the InP layer. At large overlayer thicknesses, this is no longer true and the InP-related feature can be identified. The strong dependence of w_c on the band offsets is obtained because ΔE_v determines the barrier height holes must overcome for crossing into the InP side.

Additional simulations (not shown) have confirmed that w_c changes very little with reasonable deviations in various bulk sample parameters (e.g., absorption coefficient, carrier lifetime, etc). The dominance of the band offsets in determining w_c is the key for the determination of the former, as their value can be fitted to correspond to the experimentally obtained critical thickness. In this case, ΔE_c was found to be 275 meV, in agreement with literature values. Moreover, the strong dependence of w_c on ΔE_c resulted in a relatively small measurement error (only ± 30 meV), which is considerably superior to that obtained with the method illustrated in Fig. 86. On the other hand, whereas the latter is in principle, applicable to *any* heterojunction interface, the method illustrated in Fig. 90 is not expected to be universal in nature.

Moons et al. have recently used a different type of SPV-based construction of the band diagrams, in the context of a study of porphyrin/ITO structures [413], already mentioned in Section 5.5.1. In this study, the porphyrin overlayer was fully depleted, so that its front and back SCR were not separated by a quasi-neutral region. Because the SPV due to the front SCR was found to dominate (see Section 5.5.1), the contribution of the back (porphyrin/ITO) SCR was assumed to be negligible. Thus, photosaturation measurements at the porphyrin bandgap were assumed to yield the band-bending at the front SCR and additional illumination at the ITO bandgap was assumed to yield the band-bending at the ITO part of the porphyrin/ITO interface. Interface charge densities could then be extracted from simple charge balance considerations.

Just like the approach of Leibovitch et al., the analysis of Moons et al. does not utilize CPD measurements and is therefore, also immune to dipole-related errors. Moreover, thickness-resolved measurements are not used so that all analysis can be conducted on the finished structure. The problem with the analysis of Moons et al., however, is that it neglects the coupling of the different SCRs in the structure. Even if absorption at the porphyrin part of the back SCR per se truly results in a negligible SPV, this SCR would still affect the other saturation measurements because excess carriers excited in the front porphyrin SCR and/or in the ITO would be injected into the back porphyrin SCR. Such coupling was indeed observed in the InP/InGaAs SPV simulations of Fig. 90(a). For, e.g., an InP overlayer thickness of 200 nm, the equilibrium band-bending in the InGaAs layer was only 50 mV, but the InGaAs-related SPV signal was well over 200 mV. As it is clearly impossible that the SPV would exceed the equilibrium band-bending by over 150 mV, charge carriers were evidently injected into the InP side of the heterojunction, as explained above. This effect makes it impossible to use (or indeed obtain) photosaturation for selective determination of the band-bending in one part of a heterojunction or in one part of coupled SCRs.

The approaches outlined above indicate the potential of SPV tools for the extraction of quantitative information on various aspects of interface band-diagrams. As this particular sub-field of SPV is relatively young, only a handful of experimental examples may be found in the literature. However, we believe that much more work can be done in this direction. Specifically, various analyses of the measurements of SPV data as a function of overlayer thickness (as in Figs. 86, 89 and 90), seem to be of particular promise.

6. Concluding remarks

In this review article, we have endeavored to provide an in-depth examination of all aspects of SPV techniques, including theory, experiment, and applications. Specifically, we have attempted to show that SPV-based analyses constitute a highly evolved tool for the characterization of semiconductor materials and structures, with a unique combination of many advantages.

SPV measurements reflect both optical properties and transport properties, because the photovoltaic effect is based on photo-generation of excess carriers which is followed by their spatial separation. The measurements are highly sensitive because even a very small optical absorption, e.g., in defect states, may result in a significant photovoltaic signal. Moreover, they can be used to probe any photovoltage developed in the sample under study, be it at its surface, at its bulk, or at any buried interface.

The unique sensitivity to many electrical and optical properties of different regions in the sample is manifested by the wide range of characterization capabilities afforded by SPV analyses. The latter can provide detailed, quantitative information on bulk properties (e.g., bandgap and type, carrier diffusion length and lifetime), on surface and interface band-diagrams, and on energy levels in quantum structures. A particular strength is that a complete analysis of surface and bulk defect state distributions and properties is afforded. A different testament to the versatility of SPV measurements is that they have been shown to emulate absorption measurements (Sections 4.1 and 5.5), capacitance measurements (Section 5.2), and even photoconductivity measurements (Section 5.4.2), depending on sample properties and experimental conditions.

Experimentally, SPV measurements feature many advantages: First and foremost, they are contactless and non-destructive. In addition, they can be performed both *in-situ* and *ex-situ*, at any reasonable temperature (from several K to many hundreds of K), at any ambient (be it air or other gases, vacuum, or even a liquid), and at any lateral resolution, down to the atomic scale. Traditionally, these characteristics have made SPV analyses attractive for basic studies of the effects of various physical and chemical processes on semiconductor properties in general and on the surface electronic structure in particular. In recent years, the same properties are being increasingly used for quality control and process monitoring of both materials and structures. This trend is especially apparent in the Si industry, where several companies now offer different kinds of SPV-based inspection stations, discussed in Section 5.

The sensitivity of SPV measurements to a plethora of physical phenomena is a double-edged sword because it requires very careful experiment design and data interpretation for the (qualitative or quantitative) extraction of specific properties. Significant strides have been made in this direction and much of this text has been devoted to presenting tools to that end.

Throughout our discussion, we have emphasized not only the advantages and achievements of any given approach, but also its limitations and shortcomings. We therefore believe that our presentation could serve as a roadmap for both current capabilities and further development of the technique.

Acknowledgements

This review has benefited from many illuminating discussions with Dr. Mark Leibovitch (Elta, Israel) and from critical reading of portions of the manuscript by Ilan Shalish, Gaby Segal, and Nurit Ashkenasy (Tel-Aviv University, Israel), and Dr. Ellen Moons (Cambridge University, England).

We wish to thank the following individuals for sharing their insight and data on specific subjects in the review (in order of appearance in the text): Dr. Guy Cohen (IBM Watson Research Center, USA) - atomic force microscopy; Dr. Gady Haase (Weizmann Institute of Science, Israel) - scanning tunneling microscopy; Prof. Jacek Lagowski (Semiconductor Diagnostics, USA) - diffusion length measurements; Prof. Isaac Balberg (Hebrew University, Israel) - SPV of amorphous silicon; Dr. John Lowell (Applied Materials, USA) and Dr. Krzystof Nauka (Hewlett Packard, USA) - photosaturation measurements of Si wafers; Dr. Emil Kamieniecki (QC Solutions, USA) - surface charge Profiling; Mr. Charles Kohn and Mr. Sergei Liberman (SemiTest, USA) - surface charge analysis; Prof. David Cahen (Weizmann Institute of Science, Israel) - surface band-bending and dipole.

Many thanks are due to Ms. Dina Levine and Mr. Oleg Tilishevsky for their expert computer help in graphics and text, respectively.

LK is deeply indebted to his family for bearing with him during the writing of this text. He also wishes to add a special, personal thank you to Dr. David Rosenfeld and to Dr. Jasmin Oz.

YS is indebted to Dinah and Henry Krongold for their generous support in establishing the Krongold Chair of Microelectronics at Tel Aviv University.

References

[1] W.H. Brattain, Phys. Rev. 72 (1947) 345.
[2] W.H. Brattain, J. Bardeen, Bell System Tech. J. 32 (1953) 1.
[3] C.G.B. Garrett, W.H. Brattain, Phys. Rev. 99 (1955) 376.
[4] E.O. Johnson, J. Appl. Phys. 28 (1957) 1349.
[5] A.M. Goodman, J. Appl. Phys. 32 (1961) 2550.
[6] H.C. Gatos, J. Lagowski, J. Vac. Sci. Technol. 10 (1973) 130.
[7] L.J. Brillson, Surf. Sci. Rep. 2 (1982) 123, and references therein.
[8] G. Heiland, W. Mönch, Surf. Sci. 37 (1973) 30.
[9] H. Lüth, Appl. Phys. 8 (1975) 1.
[10] H. Lüth, G. Heiland, Il Nuovo Cimento 39 (1977) 748.
[11] W. Mönch, in: R. Vanselow, R. Howe (Eds), Chemistry and Physics of Solid Surfaces, V, vol. 35 of the Springer Series in Chemical Physics, Springer, Berlin, 1984.
[12] J. Lagowski, P. Edelman, M. Dexter, W. Henley, Semicond. Sci. Technol. 7 (1992) A185.
[13] R.J. Hamers, K. Markert, Phys. Rev. Lett. 64 (1990) 1051; J. Vac. Sci. Technol. A8 (1990) 3524 .
[14] Y. Kuk, R.S. Becker, P.J. Silverman, G.P. Kochanski, Phys. Rev. Lett. 65 (1990) 456; J. Vac. Sci. Technol. B9 (1991) 545.
[15] J.M.R. Weaver, H.K. Wickramasinghe, J. Vac. Sci. Technol. B9 (1991) 1562.
[16] M. Alonso, R. Cimino, K. Horn, Phys. Rev. Lett. 64 (1990) 1947.
[17] M.H. Hecht, Phys. Rev. B41 (1990) 7918; J. Vac. Sci. Technol. B8 (1990) 1018.
[18] C.M. Aldao, G.D. Waddill, P.J. Benning, C. Capasso, J.H. Weaver, Phys. Rev. B41 (1990) 6092.
[19] L. Kronik, M. Leibovitch, E. Fefer, V. Korobov, Y. Shapira, J. Electron. Mater. 24 (1995) 893; M. Leibovitch, L. Kronik, E. Fefer, V. Korobov, Y. Shapira, Appl. Phys. Lett. 66 (1995) 457.
[20] M. Leibovitch, L. Kronik, E. Fefer, L. Burstein, V. Korobov, Y. Shapira, J. Appl. Phys. 79 (1996) 8549.
[21] M. Leibovitch, L. Kronik, B. Mishori, Y. Shapira, C.M. Hanson, A.R. Clawson, Appl. Phys. Lett. 69 (1996) 2587.
[22] A. Many, Y. Goldstein, N.B. Grover, Semiconductor Surfaces, 2nd ed., North-Holland, Amsterdam, 1971.

[23] W. Mönch, Semiconductor Surfaces and Interfaces, Springer, Berlin, 1993.
[24] H. Lüth, Surfaces and Interfaces of Solids, 2nd ed., Springer, Berlin, 1993.
[25] S.M. Sze, Physics of Semiconductor Devices, 2nd ed., Wiley, New York, 1981.
[26] M. Shur, Physics of Semiconductor Devices, Prentice-Hall, New Jersey, 1990.
[27] S. Selberherr, Analysis and Simulation of Semiconductor Devices, Springer, Vienna, 1984.
[28] S.G. Davison, M. Steslicka, Basic Theory of Surface States, Clarendon Press, Oxford, 1992.
[29] W. Shockley, W.T. Read, Jr., Phys. Rev. 87 (1952) 835; R.N. Hall, Phys. Rev. 87 (1952) 387.
[30] D.K. Schroder, Semiconductor Material and Device Characterization, Wiley, New York, 1990.
[31] R.F. Pierret, in: R.F. Pierret, G.W. Neudeck (Eds.), Advanced Semiconductor Fundamentals, Modular Series on Solid State Devices, Vol. VI, Addison-Wesley, Reading, 1987.
[32] J. Bonnet, L. Soonckindt, L. Lassabatere, Thin Solid Films 91 (1982) 283.
[33] R.B. Darling, Phys. Rev. B43 (1991) 4071.
[34] R.H. Kingston, S.F. Neustadter, J. Appl. Phys. 26 (1955) 718.
[35] J.R. Maltby, C.E. Reed, C.G. Scott, Surf. Sci. 51 (1975) 89.
[36] W. Jaegermann, Mod. Aspects Electrochem. 30 (1996) 1.
[37] W. Ranke, Y.R. Xing, Phys. Rev. B31 (1985) 2246; H. J. Kuhr, W. Ranke, Solid State Commun. 61 (1987) 285.
[38] R. Nicolini, L. Vanzetti, G. Mula, G. Bratina, L. Sorba, A. Franciosi, M. Peressi, S. Baroni, R. Resta, A. Baldereschi, J.E. Angelo, W.W. Gerberich, Phys. Rev. Lett. 72 (1994) 294.
[39] J. Tersoff, Phys. Rev. B30 (1984) 4874; J. Tersoff, Phys. Rev. Lett. 56 (1986) 2755.
[40] N.E. Christensen, Phys. Rev. 37 (1988) 4528.
[41] W.R.L. Lambrecht, B. Segall, O.K. Anderson, Phys. Rev. 41 (1990) 2813.
[42] A.H. Marshak, IEEE Trans. Elec. Dev. 36 (1989) 1764.
[43] A.M. Cowley, S.M. Sze, J. Appl. Phys. 36 (1965) 3212.
[44] B.L. Sharma (Ed.), Metal-Semiconductor Schottky Barrier Junctions and Their Applications, Plenum Press, New York, 1984.
[45] R.L. Anderson, Solid State Electron. 5 (1962) 341.
[46] L.J. van Ruyven, Phys. Stat. Sol. 5 (1964) K109.
[47] See, for example, F. Capasso, G. Margaritondo (Eds), Heterojunction Band Discontinuities, North-Holland, Amsterdam, 1987, and references therein.
[48] A. Franciosi, C.G. Van de Walle, Surf. Sci. Rep. 25 (1996) 1, and references therein.
[49] T. dell'Orto, J. Almeida, C. Coluzza, A. Baldereschi, G. Margaritondo, M. Cantile, S. Yildirim, L. Sorba, A. Franciosi, Appl. Phys. Lett. 64 (1994) 2111; M. Marsi, R. Houdre, A. Rudra, M. Ilegems, F. Gozzo, C. Coluzza, G. Margaritondo, Phys. Rev. B47 (1993) 6455.
[50] E. Moons, M. Bruening, L. Burstein, J. Libman, A. Shanzer, D. Cahen, Jpn. J. Appl. Phys. 32 (suppl. 32-3) (1992) 730.
[51] M. Bruening, E. Moons, D. Yaron-Marcovich, D. Cahen, J. Libman, A. Shanzer, J. Am. Chem. Soc. 116 (1994) 2972.
[52] M. Bruening, E. Moons, D. Cahen, A. Shanzer, J. Phys. Chem. 99 (1995) 8368.
[53] S. Bastide, R. Butruille, D. Cahen, A. Dutta, J. Libman, A. Shanzer, L. Sun, A. Villan, J. Phys. Chem. B101 (1997) 2678.
[54] M. Bruening, R. Cohen, J.F. Guillemoles, T. Moav, J. Libman, A. Shanzer, D. Cahen, J. Am. Chem. Soc. 119 (1997) 5720.
[55] R. Cohen, S. Bastide, D. Cahen, J. Libman, A. Shanzer, Y. Rosenwaks, Adv. Mater. 9 (1997) 746.
[56] R. Cohen, S. Bastide, D. Cahen, J. Libman, A. Shanzer, Y. Rosenwaks, Opt. Mater. 9 (1998) 394.
[57] R. Cohen, N. Zenou, D. Cahen, S. Yitzchaik, Chem. Phys. Lett. 279 (1997) 270.
[58] I.H. Campbell, S. Rubin, T.A. Zawodinski, J.D. Kress, R.L. Martin, D.L. Smith, N.N. Barashkov, J.P. Ferraris, Phys. Rev. B54 (1996) 14321; I.M. Dharmadasa, G.G. Roberts, M.C. Petty, Electron. Lett. 16 (1980) 201.
[59] K.K. Ng, Complete Guide to Semiconductor Devices, McGraw-Hill, New York, 1995.
[60] See, for example, Yu.Ya. Gurevich, Yu.V. Pleskov, Z.A. Rotenberg, Photoelectrochemistry, Consultant Bureau, New York, 1980.
[61] H. Dember, Physik. Zeitschr. 32 (1931) 554; H. Dember, Physik. Zeitschr. 32 (1931) 856.
[62] L.J. Richter, R.R. Cavanagh, Progr. Surf. Sci. 39 (1992) 155.
[63] Y.K. Hsieh, H.C. Card, J. Appl. Phys. 65 (1989) 2409.
[64] A.V. Sachenko, Sov. Phys. Semicond. 12 (1978) 1120.
[65] D.R. Frankl, Surf. Sci. 3 (1965) 101.
[66] E.O. Johnson, Phys. Rev. 111 (1958) 153.

[67] D.R. Frankl, E.A. Ulmer, Surf. Sci. 6 (1966) 115.
[68] W.H. Brattain, C.G.B. Garrett, Bell Syst. Tech. J. 35 (1956) 1019; C.G.B. Garrett, W.H. Brattain, Bell Syst. Tech. J. 35 (1956) 1041.
[69] V.M. Buimistrov, A.P. Gorban, V.G. Litovchenko, Surf. Sci. 3 (1965) 445.
[70] G. Brouwer, Philips Res. Repts. 18 (1963) 432.
[71] S.S. De, A.K. Ghosh, T.K. Pattanyak, J. Can. Phys. 69 (1991) 616; 69 (1991) 732.
[72] T.S. Moss, J. Elect. and Control, 1 (1955) 126.
[73] C.-L. Chiang, S. Wagner, IEEE Trans. Elect. Dev. ED-32 (1985) 1722.
[74] D.L. Lile, Surf. Sci. 34 (1973) 337.
[75] V.A. Zuev, V.G. Litovchenko, Phys. Stat. Sol. 16 (1966) 751.
[76] X. Zhang, J. Song, J. Appl. Phys. 70 (1991) 4632.
[77] S.C. Choo, L.S. Tan, K.B. Quek, Sol. State Electr. 35 (1992) 269.
[78] S.C. Choo, L.S. Tan, H.H. See, Sol. State Electr. 36 (1993) 989.
[79] S.R. Dhariwal, B.M. Deoraj, Semicond. Sci. Technol. 8 (1993) 372.
[80] S.C. Choo, Sol. State Electr. 38 (1995) 2085.
[81] C.R. Crowell, S.M. Sze, Sol. State Electr. 9 (1966) 1035.
[82] M.A. Green, J. Shewchun, Sol. State Electr. 16 (1973) 1141.
[83] P. Panayotatos, H.C. Card, Sol. State Electr. 23 (1980) 41.
[84] E.L. Heasell, Sol. State Electr. 24 (1981) 889.
[85] H.J. Pauwels, P. De Vischere, P. Reussens, Sol. State Electr. 21 (1978) 775.
[86] P. De Visschere, Sol. State Electr. 25 (1982) 955.
[87] S.-L. Jang, Sol. State Electr. 34 (1991) 373.
[88] O.V. Konstantinov, B.V. Tsarenkov, Sov. Phys. Semicond. 24 (1990) 1319.
[89] Q. Liu, H.E. Ruda, G.M. Chen, M. Simard-Normandin, J. Appl. Phys. 79 (1996) 7790.
[90] J.P. McKelvey, Solid State and Semiconductor Physics, Harper and Row, New York, 1966.
[91] R.S. Nakhmanson, Solid State Electron. 18 (1975) 617.
[92] R.S. Nakhmanson, Int. J. Electron. 59 (1985) 685.
[93] C. Munakata, S. Nishimatsu, Jpn. J. Appl. Phys. 22 (1983) 1893.
[94] C. Munakata, S. Nishimatsu, N. Honma, K. Yagi, Jpn. J. Appl. Phys. 23 (1984) 1451.
[95] C. Munakata, S. Nishimatsu, Jpn. J. Appl. Phys. 25 (1986) 807.
[96] C. Munakata, Jpn. J. Appl. Phys. 27 (1988) 759.
[97] E. Kamieniecki, J. Appl. Phys. 54 (1983) 6481; E. Kamieniecki, J. Vac. Sci. Technol. 20 (1982) 811.
[98] C.M. Wolfe, N. Holonyak, G.E. Stillman, Physical Properties of Semiconductors, Prentice Hall, New Jersey, 1989.
[99] C.L. Balestra, J. Lagowski, H.C. Gatos, Surf. Sci. 26 (1971) 317.
[100] E.V. Ostroumova, Sov. Phys. Semicond. 3 (1970) 926.
[101] F. Steinrisser, R.E. Hetrick, Surf. Sci. 28 (1971) 607.
[102] J.H. Dinan, L.K. Galbraith, T.E. Fischer, Surf. Sci. 26 (1971) 587.
[103] J. Lagowski, C.L. Balestra, H.C. Gatos, Surf. Sci. 27 (1971) 547.
[104] L. Szaro, Appl. Phys. A29 (1982) 201.
[105] K.Y. Tong, Y.W. Lam, J. Phys. D: Appl. Phys. 9 (1976) L9.
[106] G. Lucovsky, Solid State Commun. 3 (1965) 299.
[107] G. Grimmeiss, L.-Å. Ledebo, J. Phys. C: Solid State Phys. 8 (1975) 2615.
[108] A.L. Musatov, S.V. Geizer, Sov. Phys. Solid State 33 (1991) 69.
[109] J. Lagowski, H.C. Gatos, Surf. Sci. 38 (1973) 252.
[110] J. Lagowski, C.L. Balestra, H.C. Gatos, Surf. Sci. 29 (1972) 203.
[111] K.G. Germanova, L.L. Konstantinov, V.L. Strashilov, Surf. Sci. 128 (1983) 447.
[112] L. Szaro, Surf. Sci. 137 (1984) 311.
[113] I.A. Davydov, L.P. Strakhov, S.L. Tselishchev, Sov. Phys. Semicond. 26 (1992) 89.
[114] L. Szaro, Phys. Stat. Sol. (a)113 (1989) 97.
[115] L. Szaro, Semicond. Sci. Technol. 6 (1991) 875.
[116] M. Leibovitch, L. Kronik, E. Fefer, Y. Shapira, Phys. Rev. B50 (1994) 1739.
[117] A.N. Ishaque, J.W. Howard, M. Becker, R.C. Block, J. Appl. Phys. 69 (1991) 307.

[118] Q. Liu, C. Chen, H. Ruda, J. Appl. Phys. 74 (1993) 7493.
[119] R.M. Esposito, J.J. Loferski, H. Flicker, J. Appl. Phys. 38 (1967) 825.
[120] G. Nadzhakov, S. Balabanov, Sov. Phys. Solid State, 7 (1965) 957.
[121] I.F. Patai, M.A. Pomerantz, J. Franklin Inst. 252 (1951) 239.
[122] W. Thomson (Lord Kelvin), Phil. Mag. 46 (1898) 82.
[123] W.A. Zisman, Rev. Sci. Instrum. 3 (1932) 367.
[124] J.R. Anderson, A.E. Alexander, Aust. J. Appl. Sci. 3 (1952) 201.
[125] J.R. MacDonald, D.E. Edmonson, Proc. IRE 49 (1961) 453.
[126] J. Bonnet, J.M. Palau, L. Soonckindt, L. Lassabatere, J. Phys. E; Sci. Instrum. 10 (1977) 212.
[127] K.A. MacFadyen, T.A. Holbeche, J. Sci. Instrum. 34 (1957) 101.
[128] R.E. Simon, Phys. Rev. 116 (1959) 613.
[129] H. Palevsky, R.K. Swank, R. Grenchik, Rev. Sci. Instrum. 18 (1947) 298.
[130] J.R. Maltby, C.E. Reed, C.G. Scott, J. Phys. E: Sci. Instrum. 5 (1972) 584.
[131] L.B. Harris, J. Fiasson, J. Phys. E; Sci. Instrum. 17 (1984) 788.
[132] S.-M. Huang, R.T. Atanasoski, R.A. Oriani, J. Electrochem. Soc. 140 (1993) 1065.
[133] W.E. Meyerhof, P.H. Miller, Rev. Sci. Instrum. 17 (1946) 15.
[134] A.A. Frost, Rev. Sci. Instrum. 17 (1946) 266.
[135] H.P. Myers, Proc. Phys. Soc. B66 (1953) 493.
[136] H.G. Yamins, W.A. Zisman, J. Chem. Phys. 1 (1933) 656.
[137] E.F. Porter, J. Am. Chem. Soc. 59 (1937) 1883.
[138] S. Rosenfeld, W.M. Hoskins, Rev. Sci. Instrum. 16 (1945) 343.
[139] J.G. Potter, Phys. Rev. 58 (1940) 623.
[140] A.A. Frost, V.R. Hurka, J. Am. Chem. Soc. 62 (1940) 3336.
[141] J.C.P. Mignolet, Disc. Faraday Soc. 8 (1950) 326.
[142] I.D. Baikie, Rev. Sci. Instrum. 60 (1989) 930.
[143] C. Suresh Kumar, A. Subrahmanyam, J. Majhi, Rev. Sci. Instrum. 67 (1996) 805.
[144] K. Besocke, S. Berger, Rev. Sci. Instrum. 47 (1976) 840.
[145] K. Germanova, Ch. Hardalov, V. Strashilov, B. Goergiev, J. Phys. E: Sci. Instrum. 20 (1987) 273.
[146] Y.L. Yousef, A. Mishriki, S. Aziz, H. Mikhail, J. Sci. Instrum. 42 (1965) 873.
[147] E. Weismann, Ch. Petrescu, D. Tarina, J. Phys. E: Sci. Instrum. 1 (1968) 426.
[148] S.C. Fain, L.V. Corbin, J.M. McDavid, Rev. Sci. Instrum. 47 (1976) 345.
[149] J.C. Rivière, Proc. Phys. Soc. B70 (1957) 676.
[150] S. Danyluk, J. Phys. E; Sci. Instrum. 5 (1972) 478.
[151] J. Fiasson, L.B. Harris, J. Phys. E; Sci. Instrum. 10 (1977) 1160.
[152] J.P. Bellier, J. Lecoeur, C. Koehler, Rev. Sci. Instrum. 66 (1995) 5544.
[153] T. Delchar, A. Eberhagen, F.C. Tompkins, J. Sci. Instrum. 40 (1963) 105.
[154] T.K. Bodrova, I.A. Davydov, Yu.V. Protasov, V.T. Seregin, L.P. Strakhov, Inst. Expt. Tech. 29 (1986) 216.
[155] D.P. Woodruff, T.A. Delchar, Modern Techniques of Surface Science, 2nd ed., Cambridge University Press, Cambridge, 1994.
[156] N.A. Surplice, R.J. D'Arcy, J. Phys. E: Sci. Instrum. 3 (1970) 477.
[157] K.B. Johnson, W.N. Hansen, Rev. Sci. Instrum. 66 (1995) 2967.
[158] S. Lundgren, B. Kasemo, Rev. Sci. Instrum. 66 (1995) 3976.
[159] J. Nowotny, M. Sloma, W. Weppner, J. Am. Ceram. Soc. 72 (1989) 564.
[160] P.A. Anderson, Phys. Rev. 88 (1952) 655.
[161] A. Hadjadj, P. Roca i Cabarrocas, B. Equer, Rev. Sci. Instrum. 66 (1995) 5272.
[162] G. Wedler, R. Ruhmann, Appl. Surf. Sci. 14 (1982) 137.
[163] H.H. Kolm, Rev. Sci. Instrum. 27 (1956) 1046.
[164] W. Schaaffs, Z. Angew. Phys. 10 (1958) 424.
[165] E.S. Zanoria, K. Hamall, S. Danyluk, A.L. Zharin, J. Test. Eval. 25 (1997) 233.
[166] T.A. Delchar, G. Ehrlich, J. Chem. Phys. 42 (1965) 2686.
[167] M. Schmidt, M. Nohlen, G. Bermes, M. Böhmer, K. Wandelt, Rev. Sci. Instrum. 68 (1997) 3866.
[168] J. Hölzl, P. Schrammen, Appl. Phys. 3 (1974) 353.

[169] T.L. Ashcraft, J. Riney, N. Hackerman, Rev. Sci. Instrum. 34 (1963) 5.
[170] J.C. Mitchinson, R.D. Pringle, W.E.J. Farvis, J. Phys. E: Sci. Instrum. 4 (1970) 525.
[171] P. Freyer, H.-D. Ohlenbusch, J. Sci. Instrum. 44 (1967) 443.
[172] W.N. Hansen, K.B. Johnson, Surf. Sci. 316 (1994) 373.
[173] T. Fort, R.L. Wells, Surf. Sci. 12 (1968) 46.
[174] S. Yee, R.A. Oriani, M. Stratmann, J. Electrochem. Soc. 138 (1991) 55.
[175] I. Baikie, S. Mackenzie, P.J.Z. Estrup, J.A. Meyer, Rev. Sci. Instrum. 62 (1991) 1326.
[176] F. Rossi, Rev. Sci. Instrum. 63 (1992) 4174.
[177] B. Ritty, F. Wachtel, R. Manquenoille, F. Ott, J.B. Donnet, J. Phys. E: Sci. Instrum. 15 (1982) 310.
[178] B.H. Blott, T.J. Lee, J. Phys. E: Sci. Instrum. 2 (1969) 785.
[179] P.P. Craig, V. Radeka, Rev. Sci. Instrum. 41 (1970) 258.
[180] J.H. Parker, R.W. Warren, Rev. Sci. Instrum. 33 (1962) 948.
[181] R.J. D'Arcy, N.A. Surplice, J. Phys. D; Appl. Phys. 3 (1970) 482.
[182] J.S.W. de Boer, H.J. Krusmeyer, N.C. Burhoven Jaspers, Rev. Sci. Instrum. 44 (1973) 1003.
[183] I. Baikie, E. Venderbosch, J.A. Meyer, P.J.Z. Estrup, Rev. Sci. Instrum. 62 (1991) 725.
[184] H.A. Engelhardt, P. Feulner, H. Pfnür, D. Menzel, J. Phys. E; Sci. Instrum. 10 (1977) 1133.
[185] J. Bonnet, L. Soonckindt, L. Lassabatere, Vacuum, 34 (1984) 693.
[186] S. Saito, T. Soumura, T. Maeda, J. Vac. Sci. Technol. A2 (1984) 1389.
[187] C. Herring, M.H. Nichols, Rev. Mod. Phys. 21 (1949) 185.
[188] M. Wolff, A.E. Guille, D.J. Bell, J. Phys. E: Sci. Instrum. 2 (1969) 921.
[189] R.E. Collins, O.R. French, Rev. Sci. Instrum. 51 (1980) 547.
[190] H. Baumgärtner, U. Hornung, H.-D. Liess, E. Ederle, Archiv Für Elektrotech. 76 (1993) 265.
[191] S. Sakalauskas, G. Dreyfus, J. Lewiner, J. Phys. E: Sci. Instrum. 8 (1975) 837.
[192] F. Rossi, Rev. Sci. Instrum. 63 (1992) 3744.
[193] L.K. Galbraith, T.E. Fischer, Surf. Sci. 30 (1972) 185.
[194] B. Ritty, F. Wachtel, F. Ott, R. Manquenoille, J.B. Donnet, Rev. Sci. Instrum. 51 (1980) 1421.
[195] K. Germanova, L. Nikolov, Ch. Hardalov, Rev. Sci. Instrum. 60 (1989) 749.
[196] J. Baczynski, Rev. Sci. Instrum. 59 (1988) 2471.
[197] J. M. Palau, J. Bonnet, J. Phys. E: Sci. Instrum. 21 (1988) 674.
[198] R.W. Pasco, P.J. Ficalora, Rev. Sci. Instrum. 51 (1980) 246.
[199] Y. Petit-Clerk, J.D. Carette, Rev. Sci. Instrum. 39 (1968) 933.
[200] J.B. Camp, T.W. Darling, R.E. Brown, J. Appl. Phys. 69 (1991) 7126.
[201] I.D. Baikie, G.H. Bruggink, Proc. MRS Symp. 315 (1993) 423.
[202] R. Butz, H. Wagner, Appl. Phys. 13 (1977) 37.
[203] H. Baumgärtner, H.D. Liess, Rev. Sci. Instrum. 59 (1988) 802.
[204] A. Broniatowski, W. Nabhan, B. Equer, G. de Rosny, Mater. Sci. Forum, 207-209 (1996) 149.
[205] R. Mäckel, H. Baumgärtner, J. Ren, Rev. Sci. Instrum. 64 (1993) 694.
[206] H.-D. Liess, R. Mäckel, J. Ren, Surf. Int. Anal., 25 (1997) 855.
[207] H. Baumgärtner, Meas. Sci. Technol. 3 (1992) 237.
[208] W. Nabhan, B. Equer, A. Broniatowski, G.de Rosny, Rev. Sci. Instrum. 68 (1997) 3108.
[209] Bescoke Delta Phi GMBH, Tuchenbleiche 8, D-52428 Jülich, Germany.
[210] KP-6000, McAllister Technical Serivces, West 280 Prarie Avenue, Coeur d'Alene, ID 83815, USA.
[211] Uniscan Instruments, Sigma House, Burlow Road, Buxton, Derbyshire, SK179JB, United Kingdom.
[212] S.R. Morrison, J. Phys. Chem. 57 (1953) 860.
[213] C. Munakata, K. Yagi, T. Warabisako, M. Nanba, S. Matsubara, Jpn. J. Appl. Phys. 21 (1982) 624.
[214] J. Schulz, P. Würfel, W. Ruppel, Phys. Stat. Sol. (b)164 (1991) 425.
[215] K. Kinameri, C. Munakata, K. Mayama, J. Phys. E: Sci. Instrum. 21 (1988) 91.
[216] J. Hlávka, R. Švehla, Rev. Sci. Instrum. 67 (1996) 2588.
[217] A.M. Meshkov, I.A. Akimov, Inst. Expt. Technol. 4 (1964) 674.
[218] J.L. Shohet, K. Nauka, P. Rissman, IEEE Trans. Plasma. Sci. 24 (1996) 75.
[219] V.E. Kozhevin, Sov. Phys. Solid State, 8 (1967) 1979.
[220] C. Munakata, M. Nanba, S. Matsubara, Jpn. J. Appl. Phys. 20 (1981) L137.

[221] C. Munakata, S. Okazaki, K. Yagi, Jpn. J. Appl. Phys. 21 (1982) L555.
[222] C. Munakata, S. Matsubara, J. Phys. D: Appl. Phys. 16 (1983) 1093.
[223] C. Munakata, N. Honma, H. Hayakawa, Jpn. J. Appl. Phys. 23 (1984) 778.
[224] K. Kinameri, C. Munakata, N. Honma, H. Shimizu, Scan. Microsc., 2 (1988) 1237.
[225] K. Kinameri, C. Munakata, T. Abe, Meas. Sci. Technol. 1 (1990) 621.
[226] H. Shimizu, C. Munakata, N. Honma, S. Aoki, Y. Kosaka, Jpn. J. Appl. Phys. 31 (1992) 1817.
[227] N. Honma, H. Shimizu, C. Munakata, Jpn. J. Appl. Phys. 32 (1993) 3639.
[228] H. Shimizu, N. Honma, C. Munakata, M. Ota, Jpn. J. Appl. Phys. 27 (1988) 1454.
[229] C. Munakata, K. Watanabe, Semicond. Sci. Technol. 6 (1991) 612.
[230] H. Shimizu, C. Munakata, Jpn. J. Appl. Phys. 33 (1994) 3335.
[231] H. Shimizu, C. Munakata, Appl. Phys. Lett. 64 (1994) 3598.
[232] SPV station, Semiconductor Diagnostics, 6604 Harney Road, Tampa, FL 33610, USA.
[233] SPV option for the WT-85 lifetime scanner, Semilab – Semiconductor Physics Laboratory Rt., 1327 Budapest, Újpest 3, P.O. Box 18, Hungary.
[234] SCA-2500 surface charge analyzer, SemiTest, 43 Manning Road, Billerica, MA 01821-0812, USA.
[235] SCP-7200 surface charge profiler, QC solutions, 150-U New Boston Street, Woburn, MA 01801, USA.
[236] M. Cardona, L. Ley, in: M. Cardona, L. Ley (Eds), Photoemission in Solids I, Topics in Applied Physics, Vol. 28, Springer, Berlin, 1978.
[237] G. Wlerick, Physica, 20 (1954) 1099.
[238] G.K. Zyrianov, Sov. Phys. Tech. Phys. 3 (1958) 2429.
[239] F. Steinrisser, R. E. Hetrick, Rev. Sci. Instrum. 42 (1971) 304.
[240] M. Henzler, J. Clabes, Jpn. J. Appl. Phys. Supplement 2(2) (1974) 389.
[241] D. Briggs, M. Seah, Practical Surface Analysis, 2nd ed., Wiley, New York, 1990.
[242] Iu. A. Shuba, Sov. Phys. Tech. Phys. 3 (1958) 1311.
[243] W. Pao-k'un, A.N. Arsen'eva-Geil, Sov. Phys. Solid State, 3 (1962) 2637.
[244] J. Wojas, Phys. Stat. Sol. 35 (1969) 903.
[245] P.E. Viljoen, M.S. Jazzar, T.E. Fischer, Surf. Sci. 32 (1972) 506.
[246] I.T. McGovern, R.H. Williams, C.H.B. Mee, Surf. Sci. 46 (1974) 427.
[247] G. Margaritondo, L.J. Brillson, N.G. Stoffel, Solid State Commun. 35 (1980) 277.
[248] R. Schlaf, A. Klein, C. Pettenkofer, W. Jaegermann, Phys. Rev. B48 (1993) 14250.
[249] J.P. Long, H.R. Sadeghi, J.C. Rife, M.N. Kabler, Phys. Rev. Lett. 64 (1990) 1158.
[250] M. Mattern-Klosson, H. Lüth, Surf. Sci. 162 (1985) 610.
[251] F.H. Pollak, H. Shen, Mater. Sci. Eng. R10 (1993) 275.
[252] J. Geurts, Surf. Sci. Rep. 18 (1993) 1.
[253] T. Kanata, M. Matsunaga, H. Takakura, Y. Hamakawa, T. Nishino, J. Appl. Phys. 68 (1990) 5309.
[254] V.L. Alperovich, A.G. Paulish, A.S. Terekhov, Surf. Sci. 331–333 (1995) 1250; V.L. Alperovich, A.G. Paulish, H.E. Scheibler, A.S. Terekhov, Appl. Phys. Lett. 66 (1995) 2122; V.L. Alperovich, A.G. Paulish, H.E. Scheibler, V.I. Tynnyi, A.S. Terekhov, Appl. Surf. Sci. 104–105 (1996) 228.
[255] See, e. g., D.A. Bonnell (Ed.), Scanning Tunneling Microscopy and Spectroscopy, VCH, New York, 1993.
[256] A. Burnham, R.J. Colton, in: D.A. Bonnell (Ed.), Scanning Tunneling Microscopy and Spectroscopy, VCH, New York, 1993.
[257] M.P. Murrell, S.J. O'Shea, J. Barnes, M.E. Welland, C.J. Sofield, Proc. MRS Symp. 386 (1995) 371.
[258] Y. Martin, D.W. Abraham, H.K. Wickramasinghe, Appl. Phys. Lett. 52 (1988) 1103.
[259] J.M.R. Weaver, D.W. Abraham, J. Vac. Sci. Technol. B9 (1991) 1559.
[260] H. Yokoyama, T. Inoue, Thin Solid Films, 242 (1994) 33.
[261] A. Kikukawa, S. Hosaka, R. Imura, Rev. Sci. Instrum. 67 (1996) 1463.
[262] M. Yasutake, Jpn. J. Appl. Phys. 34 (1995) 3403.
[263] H.O. Jacobs, H.F. Knapp, S. Müller, A. Stemmer, Ultramicroscopy, 69 (1997) 39.
[264] R. Steinke, M. Hoffman, M. Böhmisch, J. Eisenmenger, K. Dransfeld, P. Leiderer, Appl. Phys. 64 (1997) 19.
[265] M. Nonnenmacher, M.P. O'Boyle, H.K. Wickramasinghe, Appl. Phys. Lett. 58 (1991) 2921.
[266] A.K. Henning, T. Hochwitz, J. Slinkman, J. Never, S. Hoffmann, P. Kaszuba, C. Daghlian, J. Appl. Phys. 77 (1995) 1888.

[267] T. Hochwitz, A.K. Henning, C. Lewey, C. Daghlian, J. Slinkman, J. Never, P. Kaszuba, R. Gluck, R. Wells, J. Pekarik, R. Finch, J. Vac. Sci. Technol. B14 (1996) 440.

[268] T. Hochwitz, A.K. Henning, C. Lewey, C. Daghlian, J. Slinkman, J. Vac. Sci. Technol. B14 (1996) 457.

[269] A. Kikukawa, S. Hosaka, R. Imura, Appl. Phys. Lett. 66 (1995) 3510.

[270] Y. Leng, C.C. Williams, L.C. Su, G.B. Stringfellow, Appl. Phys. Lett. 66 (1995) 1264.

[271] O. Vatel, M. Tanimoto, J. Appl. Phys. 77 (1995) 2358.

[272] M. Arakawa, S. Kishimoto, T. Mizutani, Jpn. J. Appl. Phys. 36 (1997) 1826; T. Mizutani, M. Arakawa, S. Kishimoto, IEEE Electr. Dev. Lett. 18 (1997) 423.

[273] M. Fujihira, H. Kawate, M. Yasutake, Chem. Lett. (1992) 2223; M. Fujihira, H. Kawate, J. Vac. Sci. Technol. B12 (1994) 1604; M. Yasutake, D. Aoki, M. Fujihira, Thin Solid Films 273 (1996) 279.

[274] M. Fujihira, M. Sakomura, D. Aoki, A. Koike, Thin Solid Films, 273 (1996) 168.

[275] J. Mertz, M. Hipp, J. Mlynek, O. Marti, Appl. Phys. Lett. 64 (1994) 2338.

[276] M. Abe, T. Uchihashi, M. Ohta, H. Ueyama, Y. Sugawara, S. Morita, J. Vac. Sci. Technol. B15 (1997) 1512.

[277] R.J. Hamers, in: D.A. Bonnell (Ed.), Scanning Tunneling Microscopy and Spectroscopy, VCH, New York, 1993.

[278] G.P. Kochanski, R.F. Bell, Surf. Sci. 273 (1992) L435.

[279] R. Möller, S. Akari, C. Baur, B. Koslowski, K. Dransfeld, AIP Conf. Proc. 241 (1992) 314.

[280] M. McEllistrem, G. Haase, D. Chen, R.J. Hamers, Phys. Rev. Lett. 70 (1993) 2471.

[281] G. Haase, private communication, 1997.

[282] D.G. Cahill, R.J. Hamers, J. Vac. Sci. Technol. B9 (1991) 564.

[283] D.G. Cahill, R.J. Hamers, Phys. Rev. B44 (1991) 1387.

[284] D. Gorelik, S. Aloni, J. Eitle, D. Meyler, G. Haase, J. Chem. Phys. 108 (1998) 9877.

[285] D.G. Cahill, R.J. Hamers, Scan. Microsc. 6 (1992) 931.

[286] D.G. Cahill, R.M. Feenstra, J. Vac. Sci. Technol. A11 (1993) 792.

[287] Fig. 37(c) provides a detailed explanation of the synchronized null technique which is briefly explained in [280], courtesy of G. Haase and R.J. Hamers, 1997.

[288] E.V. Ostroumova, Sov. Phys. Semicond. 9 (1975) 992.

[289] W. Mönch, P. Koke, S. Krueger, J. Vac. Sci. Technol. 19 (1981) 313.

[290] B. Adamowicz, J. Szuber, Surf. Sci. 247 (1991) 94.

[291] L. Szaro, J. Misiewicz, Phys. Stat. Sol. (a)118 (1990) 185.

[292] J. Clabes, M. Henzler, Phys. Rev. B21 (1980) 625.

[293] J. Assmann, W. Mönch, Surf. Sci. 99 (1980) 34.

[294] L.L. Jastrzebski, J. Lagowski, RCA Review, 41 (1980) 188.

[295] J. Lagowski, L. Jastrzebski, G.W. Cullen, J. Electrochem. Soc. 128 (1981) 2665.

[296] K. Germanova, Ch. Hardalov, B. Gregov, Phil. Mag. B 57 (1988) 703.

[297] I.D. Baikie, Proc. MRS Symp. 204 (1991) 363.

[298] I.D. Baikie, E. Venderbosch, B. Hall, Proc. MRS Symp. 261 (1992) 149.

[299] W. Liu, W. Yang, T. Li, Y. Liu, Z. Zhu, Thin Solid Films 179 (1989) 309.

[300] R. Zhang, X. Zhang, J. Wang, J. Shen, Thin Solid Films 248 (1994) 102.

[301] J. Yang, W. Yang, Y. Bai, C. Shen, D. Wang, X. Chai, T. Li, C. Li, A. Pan, Thin Solid Films, 284-285 (1996) 477.

[302] M. Büchel, H. Lüth, Surf. Sci. 50 (1975) 451.

[303] B. Goldstein, D.J. Szostak, Surf. Sci. 99 (1980) 235.

[304] V.G. Litovchenko, V.G. Popov, Sov. Phys. Semicond. 16 (1982) 472.

[305] E. Fefer, Y. Shapira, I. Balberg, Appl. Phys. Lett. 67 (1995) 371.

[306] Y. Lubianiker, I. Balberg, E. Fefer, Y. Shapira, J. Non-Cryst. Solids, 198-200 (1996) 309.

[307] B. Wang, D. Wang, Y. Cao, X. Chai, X. Geng, T. Li, Thin Solid Films 284–285 (1996) 588.

[308] Th. Dittrich, P.K. Kashkarov, E.A. Konstantinova, V.Yu. Timoshenko, Thin Solid Films 255 (1995) 74.

[309] Th. Dittrich, H. Flietner, Proc. MRS Symp. 358 (1995) 581.

[310] V. Yu. Timoshenko, P. K. Kashkarov, A. B. Matveeva, E. A. Konstantinova, H. Flietner, Th. Dittrich, Thin Solid Films 276 (1996) 216.

[311] P. K. Kashkarov, E. A. Konstantinova, A. B. Matveeva, V. Yu. Timoshenko, Appl. Phys. A62 (1996) 547.

[312] Z.-H. Yang, P. Zhang, D.-J. Wang, T.-J. Li, J. Vac. Sci. Technol. B15 (1997) 1604.

[313] F. Yan, X.-M. Bao, T. Gao, Solid State Commun. 91 (1994) 341.

[314] B. Wang, D. Wang, L. Zhang, T. Li, J. Phys. Chem. Solids, 58 (1997) 25.
[315] B. Wang, D. Wang, L. Zhang, T. Li, Thin Solid Films 293 (1997) 40.
[316] L. Burstein, Y. Shapira, J. Partee, J. Shinar, Y. Lubianiker, I. Balberg, Phys. Rev. B 55 (1997) R1930.
[317] B. Mishori, Y. Shapira, A. Belu-Marian, M. Manciu, A. Devenyi, Chem. Phys. Lett. 264 (1997) 163.
[318] B. Mishori, E.A. Katz, D. Faiman, Y. Shapira, Solid State Commun. 102 (1997) 489.
[319] J. Lagowski, I. Baltov, H.C. Gatos, Surf. Sci. 40 (1973) 216.
[320] J. Lagowski, H.C. Gatos, Surf. Sci. 45 (1974) 353.
[321] A. Morawski, M.M.G. Slusarczuk, J. Lagowski, H.C. Gatos, Surf. Sci. 69 (1977) 53.
[322] J. Szuber, J. Electron Spectrosc. Relat. Phenom. 53 (1990) 19; J. Szuber, Appl. Surf. Sci. 55 (1992) 143.
[323] L.J. Brillson, J. Vac. Sci. Technol. 17 (1980) 880.
[324] L. Burstein, J. Bregman, Y. Shapira, Appl. Phys. Lett. 57 (1990) 2466; J. Appl. Phys. 69 (1991) 15.
[325] N.L. Dmitruk, V.I. Lyashenko, A.K. Tereshenko, S.A. Spektor, Phys. Stat. Sol. (a)20 (1973) 53.
[326] A. Morawski, J. Lagowski, Phys. Lett. 47A (1974) 219.
[327] J. Lagowski, A. Iller, A. S̀wiatek, Surf. Sci. 49 (1975) 1.
[328] A. Kalnitsky, S. Zukotynski, S. Sumski, J. Appl. Phys. 52 (1981) 4744.
[329] L. Lassabatere, C. Alibert, J. Bonnet, L. Soonckindt, J. Phys. E: Sci. Instrum. 9 (1976) 773.
[330] H. Clemens, W. Mönch, CRC Crit. Rev. Solid State Sci. 5 (1975) 273.
[331] S.C. Dahlberg, Surf. Sci. 59 (1976) 83.
[332] S.C. Dahlberg, J. Vac. Sci. Technol. 13 (1976) 1056.
[333] J. Lagowski, W. Walukiewicz, M.M.G. Slusarczuk, H.C. Gatos, J. Appl. Phys. 50 (1979) 5059.
[334] W. Mönch, H.J. Clemens, S. Görlich, R. Enninghorst, H. Gant, J. Vac. Sci. Technol. 19 (1981) 525.
[335] M. Liehr, H. Lüth, J. Vac. Sci. Technol. 16 (1979) 1200.
[336] H. Lüth, M. Büchel, R. Dorn, M. Liehr, R. Matz, Phys. Rev. B15 (1977) 865.
[337] Z. Czekala-Mukalled, S. Kuzminski, M. Tlaczala, Vacuum 46 (1995) 489.
[338] A.L. Musatov, S. Yu. Smirnov, Surf. Sci. 269/270 (1992) 1048.
[339] A.L. Musatov, S. Yu. Smirnov, Phys. Solid State, 36 (1994) 4.
[340] K. Germanova, Ch. Hardalov, Appl. Phys. A43 (1987) 117.
[341] I.A. Karpovich, B.I. Bednyi, N.V. Baidus, S.M. Plankina, M.V. Stepikhova, M.V. Shilova, Sov. Phys. Semicond. 23 (1989) 1340.
[342] B.I. Bednyi, I.A. Karpovich, N.V. Baidus, P.V. Boldyrevskii, A.S. Stepanov, N.V. Fedoseeva, Sov. Phys. Semicond. 25 (1991) 874.
[343] C. Suresh Kumar, C.S. Gobinath, A. Subrahmanyam, Proc. SPIE, 2733 (1995) 286.
[344] Q. Liu, H.E. Ruda, L.Z. Jedral, I.P. Koutzarov, C.H. Edirisinghe, Proc. SPIE 2403 (1995) 462.
[345] C. Edirisinghe, H.E. Ruda, I. Koutzarov, Q. Liu, L. Jedral, M. G. Boundreau, M. Boumerzoug, J. Brown, P. Maschwer, A. Moore, R. Henderson, Proc. MRS. Symp. 378 (1995) 1007.
[346] I.P. Koutzarov, C.H. Edirisinghe, H.E. Ruda, L.Z. Jedral, Q. Liu, J. Guo-Ping, H. Xia, W.N. Lennard, L. Rodriguez-Fernandez, Proc. MRS. Symp. 421 (1996) 93.
[347] A.L. Musatov, S.V. Geizer, A.D. Korinfskii, Sov. Phys. Semicond. 23 (1989) 1271.
[348] B.I. Bednyi, L.A. Suslov, N.V. Baidus, I.A. Karpovich, Sov. Phys. Semicond. 26 (1992) 1115.
[349] S.M. Thurgate, T.D. Lacuesta, N.R. Huck, Surf. Sci. 219 (1989) 420.
[350] S.M. Thurgate, K. Blight, T.D. Lacuesta, Surf. Sci. 310 (1994) 103.
[351] L. Burstein, Y. Shapira, Semicond. Sci. Technol. 8 (1993) 1724.
[352] Y. Shapira, L.J. Brillson, A. Heller, J. Vac. Sci. Technol. A1 (1983) 766; L.J. Brillson, Y. Shapira, A. Heller, Appl. Phys. Lett. 43 (1983) 174; Y. Shapira, L.J. Brillson, A. Heller, Phys. Rev. B29 (1984) 6824.
[353] S.C. Dahlberg, Surf. Sci. 60 (1976) 231.
[354] Y. Byun, B.W. Wessles, Appl. Phys. Lett. 52 (1988) 1352.
[355] L. Burstein, Y. Shapira, B.R. Bennet, J.A. del Alamo, J. Appl. Phys. 78 (1995) 7163.
[356] M. Leibovitch, P. Ram, L. Malikova, F.H. Pollak, J.L. Freeouf, L. Kronik, B. Mishori, Y. Shapira, A.R. Clawson, C.M. Hanson, J. Vac. Sci. Technol. B14 (1996) 3089.
[357] N. Kinrot, Y. Shapira, M.A. Bica de Moraes, Appl. Phys. Lett. 70 (1997) 3011.
[358] S. Lehr, H. Pagnia, Phys. Stat. Sol. (a)49 (1978) 83.
[359] W. Krystek, F.H. Pollak, Z.C. Feng, M. Schurman, R.A. Stall, Proc. MRS. Symp. 482 (1998) 573.

[360] I. Shalish, L. Kronik, G. Segal, Y. Shapira, Y. Rosenwaks, U. Tisch, J. Salzman, Phys. Rev. B59 (1999) 9748, and additional unpublished results.
[361] J. Lagowski, C.L. Balestra, H.C. Gatos, Surf. Sci. 29 (1972) 213.
[362] S. Simov, M. Kalitzova, E. Nikolova, I. Baltov, Surf. Sci. 59 (1976) 115.
[363] L.J. Brillson, Surf. Sci. 51 (1975) 45.
[364] L.J. Brillson, J. Vac. Sci. Technol. 12 (1975) 249.
[365] M.A. Channon, J.R. Maltby, C.E. Reed, C.G. Scott, J. Phys. D: Appl. Phys. 8 (1975) L39.
[366] J.R. Maltby, C.E. Reed, C.G. Scott, Surf. Sci. 93 (1980) 287.
[367] A. Morawski, R. Banisch, J. Lagowski, Surf. Sci. 69 (1977) 444.
[368] X. Tong, D.-P. Xu, W.-H. Su, L.-Z. Xiao, S.-T. Li, L. Han, AIP Conf. Proc. 309 (1994) 1271.
[369] B. Wang, D. Wang, X. Fu, Y. Cui, T. Li, J. Photochem. Photobiol. A90 (1995) 167.
[370] Y. Rosenwaks, L. Burstein, Y. Shapira, D. Huppert, Appl. Phys. Lett. 57 (1990) 458.
[371] O.F. Vyvenko, I.A. Davydov, V.G. Luchina, S.L. Tselishchev, Sov. Phys. Semicond. 25 (1991) 1050.
[372] L.J. Brillson, J. Vac. Sci. Technol. 15 (1978) 1378.
[373] L.J. Brillson, Phys. Rev. B18 (1978) 2431.
[374] H.C. Gatos, J. Lagowski, R. Banisch, Photogr. Sci. Eng. 26 (1982) 42.
[375] L.J. Brillson, Surf. Sci. 69 (1977) 62.
[376] L.J. Brillson, J. Vac. Sci. Technol. 13 (1976) 325.
[377] L. Szaro, Surf. Sci. 122 (1982) 149.
[378] Yu. A. Cherkasov, P.A. Burov, I.A. Davydov, V.G. Luchina, A.P. Odrinskii, A.I. Rumyantsev, Sov. Phys. Semicond. 23 (1989) 974.
[379] S. Kuzminski, K. Pater, A.T. Szaynok, Surf. Sci. 247 (1991) 90.
[380] L. Kronik, N. Ashkenasy, M. Leibovitch, E. Fefer, Y. Shapira, S. Gorer, G. Hodes, J. Electrochem. Soc. 145 (1998) 1748.
[381] A. Rohatgi, R. Sudharsanan, S.A. Ringel, P.V. Meyers, C.H. Liu, Proc. 20th IEEE Photovoltaic Specialists Conf., IEEE, New York, 1988, p. 1477.
[382] S.A. Ringel, R. Sudharsanan, A. Rohatgi, W.B. Carter, J. Electron. Mater. 19 (1990) 259.
[383] S.A. Ringel, A.W. Smith, M.H. MacDougal, A. Rohatgi, J. Appl. Phys. 70 (1991) 881.
[384] M.S. El-Dessouki, V.A. Attia, Appl. Phys. A45 (1988) 175.
[385] L. Burstein, Y. Shapira, E. Moons, D. Cahen, Appl. Surf. Sci. 74 (1994) 201.
[386] S. Kuzminski, K. Pater, A.T. Szaynok, Surf. Sci. 91 (1980) 707.
[387] S. Kuzminski, A.T. Szaynok, Phys. Stat. Sol. (a) 89 (1985) 623.
[388] S. Kuzminski, A.T. Szaynok, Phys. Stat. Sol. (a) 95 (1986) 279.
[389] S. Kuzminski, A.T. Szaynok, Surf. Sci. 200 (1988) 192.
[390] A.T. Szaynok, Surf. Sci. 213 (1989) 283.
[391] S. Kuzminski, K. Pater, A.T. Szaynok, Surf. Sci. 231 (1990) 36.
[392] S. Kuzminski, K. Pater, A.T. Szaynok, Vacuum 45 (1994) 195.
[393] B. Bieg, S. Kuzminski, Vacuum 45 (1994) 171.
[394] B. Bieg, S. Kuzminski, J. Szatkowski, Vacuum 46 (1995) 481.
[395] S. Kuzminski, K. Pater, A.T. Szaynok, Vacuum 46 (1995) 501.
[396] B. Bieg, S. Kuzminski, A. Morawski, B. Pohoryles, Solid State Phenom. 51–52 (1996) 403.
[397] M.S. El-Dessouki, V.A. Attia, J. Phys. Chem. Solids, 44 (1983) 939.
[398] M.S. El-Dessouki, F. El-Kabbany, V.A. Attia, Annalen der Physik 46 (1989) 615.
[399] J. Lagowski, E.S. Sproles, H.C. Gatos, Surf. Sci. 30 (1972) 653.
[400] J. Lagowski, E.S. Sproles, H.C. Gatos, J. Appl. Phys. 48 (1977) 3566.
[401] J. Lagowski, H.C. Gatos, C.L. Balestra, J. Appl. Phys. 49 (1978) 2821.
[402] D. Gal, J. Beier, E. Moons, G. Hodes, D. Cahen, L. Kronik, L. Burstein, B. Mishori, M. Leibovitch, Y. Shapira, D. Hariskos, R. Klenk, H.-W. Schock, Proc. AIP 353 (1995) 453.
[403] E. Moons, D. Gal, J. Beier, G. Hodes, D. Cahen, L. Kronik, L. Burstein, B. Mishori, Y. Shapira, D. Hariskos, H.-W. Schock, Sol. Ener. Mater. Sol. Cells 43 (1996) 73.
[404] L. Kronik, B. Mishori, E. Fefer, Y. Shapira, W. Riedl, Sol. Ener. Mater. Sol. Cells 51 (1998) 21.
[405] Y. Chen, Y. Cao, Y. Bai, W. Yang, J. Yang, H. Jin, T. Li, J. Vac. Sci. Technol. B15 (1997) 1442.
[406] J. Zhang, D. Wang, Y. Chen, T. Li, H. Mao, H. Tian, Q. Zhou, H. Xu, Thin Solid Films 300 (1997) 208.

[407] N. Mirowska, J. Misiewicz, Semicond. Sci. Technol. 7 (1992) 1332.
[408] L.J. Brillson, C.H. Griffiths, J. Vac. Sci. Technol. 15 (1978) 529.
[409] S.C. Dahlberg, M.E. Musser, J. Chem. Phys. 70 (1979) 5021.
[410] M.E. Musser, S.C. Dahlberg, Surf. Sci. 91 (1980) L23.
[411] M.E. Musser, S.C. Dahlberg, Thin Solid Films 66 (1980) 261.
[412] M.E. Musser, S.C. Dahlberg, Appl. Surf. Sci. 5 (1980) 28.
[413] E. Moons, T. Savenije, A. Goossens, J. Phys. Chem. B101 (1997) 8492.
[414] E. Moons, M. Eschle, M. Grätzel, Appl. Phys. Lett. 71 (1997) 3305.
[415] N. Bachrach-Ashkenasy, L. Kronik, Y. Shapira, Y. Rosenwaks, M.C. Hanna, M. Leibovitch, P. Ram, Appl. Phys. Lett. 68 (1996) 879.
[416] V. Ariel, V. Garber, D. Rosenfeld, G. Bahir, Appl. Phys. Lett. 66 (1995) 2101.
[417] S.M. Eetemadi, R. Braunstein, J. Appl. Phys. 58 (1985) 3856.
[418] H.B. DeVore, Phys. Rev. 102 (1956) 86.
[419] B. Pohoryles, A. Morawski, Surf. Sci. 349 (1996) 155; B. Pohoryles, A. Morawski, Appl. Surf. Sci. 92 (1996) 417; B. Pohoryles, A. Morawski, Mater. Sci. Forum 173–174 (1995) 273.
[420] D.A. Johnson, K. Wadhera, R.A. Puechner, N.S. Kang, G.N. Maracas, D.K. Schroder, Inst. Phys. Conf. Ser. 96 (1989) 409.
[421] Y. Shapira, S.M. Cox, D. Lichtman, Surf. Sci. 50 (1975) 503.
[422] A. Abbate, P. Renicibia, O. Ivanov, G. Masini, F. Palma, P. Das, Mater. Sci. Forum, 173–174 (1995) 221.
[423] L. Aigoui, F.H. Pollak, T.J. Petruzello, K. Shahzad, Solid State Comm. 102 (1997) 877.
[424] Annual Book of ASTM Standards F391-96, American Society for Testing and Materials, Pennsylvania, 1996.
[425] S.S. Li, Appl. Phys. Lett. 29 (1976) 126.
[426] A. Quilliet, M.P. Gosar, J. Phys. Radium 21 (1960) 575.
[427] D.L. Lile, N.M. Davis, Sol. State Electr. 18 (1975) 699.
[428] L. Jastrzebski, O. Milic, M. Dexter, J. Lagowski, D. DeBusk, K. Nauka, R. Witowski, M. Gordon, E. Persson, J. Electrochem. Soc. 140 (1993) 1152.
[429] A.L.P. Rotondaro, T.Q. Hurd, A. Kaniava, J. Vanhellemont, E. Simoen, M.M. Heyns, C. Claeys, G. Brown, J. Electrochem. Soc. 143 (1996) 3014; Electrochem. Soc. Proc. 95-30 (1995) 54.
[430] D. Walz, J.-P. Joly, G. Kamarinos, J. Barla, Electrochem. Soc. Proc. 95-30 (1995) 35.
[431] A. Castaldini, A. Cavallini, E. Gombia, R. Mosca, L. Tarricone, Appl. Surf. Sci. 50 (1991) 485.
[432] A. Castaldini, A. Cavallini, B. Fraboni, B. Mendez, J. Piqueras, J. Appl. Phys. 76 (1994) 987.
[433] L. Tarricone, E. Don, N.M. Pearsall, T.J. Coutts, Solar Cells 7 (1982/83) 281.
[434] T.L. Chu, E.D. Stokes, J. Electron. Mater. 7 (1978) 173.
[435] J. Bailey, J.P. Kalejs, C. Keaveny, Proc. 1st World Conf. on Photovoltaic Energy Conversion, IEEE, New York, 1994, p. 1356.
[436] S.S. Ostapenko, L. Jastrzebski, J. Lagowski, B. Sopori, Appl. Phys. Lett. 65 (1994) 1555; S.S. Ostapenko, L. Jastrzebski, B. Sopori, Semicond. Sci. Technol. 10 (1995) 1494.
[437] P. Edelman, W. Henley, J. Lagowski, Semicond. Sci. Technol. 7 (1992) A22.
[438] M. Bugajski, P. Edelman, K. Ornoch, M. Wesolowski, W. Lewandowski, K. Kucharski, Mater. Sci. Eng. B20 (1993) 186.
[439] F. von Bergmann, C. Fritzsche, H.D. Riccius, Telefunken Z. 37 (1964) 186.
[440] J. Vilms, W.E. Spicer, J. Appl. Phys. 36 (1965) 2815.
[441] S.C. Choo, A.C. Anderson, Sol. State Electr. 13 (1970) 609.
[442] W.E. Phillips, Sol. State Electr. 15 (1972) 1097.
[443] E.Y. Wang, C.R. Baraona, H.W. Brandhorst, Jr., J. Electrochem. Soc. 121 (1974) 973.
[444] E.D. Stokes, T.L. Chu, Appl. Phys. Lett. 30 (1977) 425.
[445] T.L. Chu, E.D. Stokes, J. Appl. Phys. 49 (1978) 2996.
[446] T.L. Chu, E.D. Stokes, Proc. 13th Photovoltaic Specialists Conf., IEEE, New York, 1978, p. 95.
[447] T.L. Chu, E.D. Stokes, S.S. Chu, Solar Cells 1 (1979) 222.
[448] R.O. Bell, G.M. Freedman, Proc. 13th Photovoltaic Specialists Conf., IEEE, New York, 1978, p. 89.
[449] L. Tarricone, E. Gombia, Solar Energy Mater. 2 (1979) 45.
[450] A. Pogany, Proc. 14th Photovoltaic Specialists Conf., IEEE, New York, 1980, p. 410.
[451] L. Gouskov, H. Luquet, L. Soonckindt, A. Oemry, M. Bustani, P.H. Nguyen, J. Appl. Phys. 53 (1982) 7014.
[452] S.J. Fonash, Solar Cell Device Physics, Academic Press, New York, 1981.

[453] T. Wittchen, H.-C. Holstenberg, D. Hünerhoff, Z. J. Min, J. Metzdorf, Proc. 20th Photovoltaic Specialists Conf., IEEE, New York, 1988, p. 1251.
[454] R.Y. Loo, G.S. Kamath, Proc. 20th Photovoltaic Specialists Conf., IEEE, New York, 1988, p. 635.
[455] A.K. Pal, I. Sanyal, S. Ghosh, A. Mondal, S. Chaudhuri, Proc. 1st World Renewable Energy Congress, Pergamon, Oxford, 1990, p. 438.
[456] I. Hwang, D.K. Schroder, Sol. State Electr. 36 (1993) 1147.
[457] J.P. Kalejs, L. Jastrzebski, J. Lagowski, W. Henley, D. Schielein, S.G. Balster, D.K. Schroder, Proc. 12th E.C. Photovoltaic Solar Energy Conf., 1994, p. 52.
[458] S.G. Balster, D.K. Schroder, J. Bailey, J.P. Kalejs, J. Appl. Phys. 77 (1995) 371.
[459] L. Jastrzebski, W. Henley, D. Schielein, J. Lagowski, J. Electrochem. Soc. 142 (1995) 3669.
[460] M.D. Dlamini, Solar Energy Mater. Solar Cells, 43 (1996) 353.
[461] E.R. Weber, S.A. McHugo, H. Hieslmair, Solid State Phenom. 47–48 (1996) 165.
[462] C. Savigni, M. Acciari, S. Binetti, Solid State Phenom. 51–52 (1996) 485.
[463] R. Chakrabarti, A.B. Maity, B. Maiti, J. Dutta, S. Chaudhri, A.K. Pal, Vacuum 47 (1996) 1371.
[464] J. Dresner, D.J. Szostak, B. Goldstein, Appl. Phys. Lett. 38 (1981) 998.
[465] A.R. Moore, Appl. Phys. Lett. 40 (1982) 403.
[466] A.R. Moore, J. Appl. Phys. 54 (1983) 222.
[467] A.R. Moore, D.E. Kane, J. Appl. Phys. 56 (1984) 2796.
[468] A.R. Moore, H.-S. Lin, J. Appl. Phys. 61 (1987) 4816.
[469] M. Hack, J. McGill, W. Czubatyi, R. Singh, M. Shur, A. Madan, J. Appl. Phys. 53 (1982) 6270.
[470] M. Hack, M. Shur, J. Appl. Phys. 55 (1984) 2967.
[471] B. Goldstein, J. Dresner, D.J. Szostak, Phil. Mag. B40 (1982) 63.
[472] T.J. McMahon, R. Konenkamp, Proc. 16th Photovoltaic Specialists Conf., IEEE, New York, 1982, p. 1389.
[473] D.E. Carlson, A.R. Moore, D.J. Szostak, B. Goldstein, R.W. Smith, P.J. Zanzucchi, W.R. Frenchu, Solar Cells 9 (1983) 19.
[474] D.E. Carlson, A. Catalano, R.V. D'Aiello, C.R. Dickson, R.S. Oswald, AIP Conf. Proc. 120, AIP, New York, 1984, p. 330.
[475] K.A. Epstein, N.T. Tran, F.R. Jeffrey, A.R. Moore, Appl. Phys. Lett. 49 (1986) 173.
[476] I. Sakata, T. Ishida, O. Okazaki, T. Saitoh, M. Yamanaka, H. Hayashi, J. Appl. Phys. 61 (1987) 1916.
[477] S.S. Hegedus, H.-S. Lin, A.R. Moore, J. Appl. Phys. 64 (1988) 1215.
[478] H.-S. Lin, Sol. Energy Mater. Solar Cells 30 (1993) 367.
[479] R. Schwartz, D. Slobodin, S. Wagner, Appl. Phys. Lett. 47 (1985) 740.
[480] C.L. Chiang, R. Schwartz, D.E. Slobodin, J. Kolodzey, S. Wagner, IEEE Trans. Electron. Dev. 33 (1986) 1587.
[481] I. Balberg, K.A. Epstein, D. Ritter, Appl. Phys. Lett. 54 (1989) 2461.
[482] C.I. Ukah, J.M. Perz, S. Zukotynski, J. Appl. Phys. 65 (1989) 3617.
[483] J.C. van den Heuvel, R.C. van Oort, M.J. Geerts, Solid State Commun. 69 (1989) 807.
[484] J.C. van den Heuvel, R.C. van Oort, M.J. Geerts, J. Appl. Phys. 68 (1990) 1381.
[485] N.L. Dmitruk, Yu.V. Kryuchnko, V.G. Litovchenko, V.G. Popov, M.A. Stepanova, Phys. Stat. Sol. (a) 124 (1991) 183.
[486] A.M. Goodman, L.A. Goodman, H.F. Gossenberger, RCA Review 44 (1983) 326.
[487] L. Jastrzebski, R. Soydan, H. Elbad, W. Henry, E. Savoye, J. Electrochem. Soc. 137 (1990) 242.
[488] G. Zoth, W. Bergholz, J. Appl. Phys. 67 (1990) 6764.
[489] K. Mishra, M. Banan, J. Moody, S. Chandrasekhar, Proc. SPIE 2337 (1994) 143.
[490] A.C. Ipri, L. Jastrzebski, D. Peters, IEEE Electron Device Lett. 10 (1989) 571; L. Jastrzebski, G. Cullen, R. Soydan, J. Electrochem. Soc. 137 (1991) 303.
[491] W.B. Henley, L. Jastrzebski, N.F. Haddad, J. Non-Cryst. Solids, 187 (1995) 134.
[492] W.B. Henley, L. Jastrzebski, N.F. Haddad, Proc. 31st Reliability Physics Conf., IEEE, New York, 1993, p. 22.
[493] K. Nakao, Y. Matsuda, Y. Inomaki, K. Mizukami, M. Enomoto, Proc. IEEE/UCS/SEMI Int'l Symp. on Semiconductor Manufacturing, IEEE, New York, 1995, p. 64.
[494] H.-J. Schulze, G. Deboy, Proc. SPIE 2638 (1995) 234.
[495] J. Lagowski, P. Edelman, Electrochem. Soc. Proc. 96–13 (1996) 5523.
[496] K. Nauka, Proc. Int. Conf. on Semiconductor Characterization, AIP, 1996, p. 231.
[497] J.J. Rosato, R.M. Hall, T.B. Parry, J.D. Kelly, J.N. Butler, T.D. Jarvis, P.G. Lindquist, in: D.K. Schorder, J.L. Benton, P. Rai-Choudhury (Eds), Symposium on Diagnostic Techniques for Semiconductor Materials and Devices, Electrochemical Society, Pennington, 1994, p. 163.

[498] K. Barla, D. Levy, A. Fleury, J.P. Reynard, L. Kwakman, Proc. SPIE 2637 (1995) 137.
[499] M. Simard-Normandin, Proc. SPIE 2877 (1996) 186.
[500] A. Cacciato, S. Vleeshouwers, S. Evseev, J. Electrochem. Soc. 145 (1998) 701.
[501] W. Henley, D.A. Ramappa, J. Appl. Phys. 82 (1997) 589.
[502] D.A. Ramappa, W. Henley, J. Electrochem. Soc. 144 (1997) 4353.
[503] W. Bergholz, G. Zoth, G. Götz, A. Saliov, Solid State Phenom. 19 (1991) 109.
[504] J. Lagowski, P. Edelman, A.M. Kontkiewicz, O. Milic, W. Henley, M. Dexter, L. Jastrzebski, A.M. Hoff, Appl. Phys. Lett. 63 (1993) 3043.
[505] K. Mishra, Appl. Phys. Lett. 68 (1996) 3281.
[506] A.M. Hoff, T.C. Esry, K. Nauka, Solid State Technol. July 1996, p. 139; J.L. Shohet, K. Nauka, P. Rissman, IEEE Trans. Plasma. Sci. 24 (1996) 75; A.M. Hoff, J. Lagowski, K. Nauka, T.C. Esry, P. Edleman, L. Jastrzebski, Electrochem. Soc. Proc. 96-13 (1996) 544.
[507] J. Lowell, V. Wenner, L. Jastrzebski, Proc. MRS Symp. 315 (1993) 339.
[508] M. Anjum, V. Wenner, J. Lowell, Proc. SPIE 2337 (1994) 165.
[509] J. Lowell, P. Ackmann, S. Brown, J. Sherry, T. Hossain, Proc. SPIE 2725 (1996) 206.
[510] J. Lowell, V. Wenner, L. Jastrzebski, Proc. IEEE/SEMI Int. Conf. on Ultraclean Manufacturing, IEEE, New York, 1994, p. 99.
[511] V. Wenner, J. Lowell, J. Shi, L. Larson, Proc. IEEE/SEMI Int. Conf. on Advanced Semiconductor Manufacturing, IEEE, New York, 1995, p. 309.
[512] V.-T. Quat, W. Eichhammer, P. Siffert, Appl. Phys. Lett. 54 (1989) 1235.
[513] B. Hartiti, A. Slaoui, J.C. Muller, P. Siffert, Appl. Phys. Lett. 63 (1993) 1249.
[514] N. Gay, F. Floret, S. Martinuzzi, L. Roux, J. Arnould, G. Mathieu, Mater. Sci. Eng. B36 (1996) 125.
[515] F.G. Kirscht, Y. Furukawa, W. Seifert, K. Schmalz, A. Bjuczkowski, S.B. Kim, H. Abe, H. Koya, J. Bailey, Mater. Sci. Eng. B36 (1996) 230.
[516] P. Moens, W. Dobbelaere, T. Colpaert, Solid State Phenom. 57–58 (1997) 149.
[517] J.L. Mariani, B. Pichaud, F. Minari, S. Martinuzzi, J. Appl. Phys. 71 (1992) 1284.
[518] A.A. Istratov, C. Flink, H. Hiselmair, T. Heiser, E.R. Weber, Appl. Phys. Lett. 71 (1997) 2121.
[519] C.L. Chiang, S. Wagner, A.A. Ballman, Mater. Lett. 1 (1983) 145.
[520] C.L. Chiang S. Wagner, A.A. Ballman, Appl. Phys. Lett. 43 (1983) 1113.
[521] S. Mora, N. Romeo, L. Tarricone, Nuovo Cimento B60 (1980) 97.
[522] G.J. Storr, D. Haneman, Appl. Surf. Sci. 22/23 (1985) 1098.
[523] G.J. Storr, D. Haneman, J. Appl. Phys. 58 (1985) 1677.
[524] S. Mora, N. Romeo, L. Tarricone, Solid State Commun. 33 (1980) 1147.
[525] E. Placzek-Popko, L. Szaro, Sol. State Electr. 35 (1992) 1451.
[526] A. Jakubowicz, D. Mahalu, M. Wolf, A. Wold, R. Tenne, Phys. Rev. B40 (1989) 2992.
[527] M. Saritas, H.D. McKell, Sol. State Electr. 31 (1988) 835.
[528] R.H. Micheels, R.D. Rauh, J. Electrochem. Soc. 131 (1984) 217.
[529] J. Lagowski, P. Edelman, V. Faifer, SEMI/ASTM Lifetime Characterization Workshop, Santa Clara, 1997.
[530] J. Lagowski, V. Faifer, P. Edelman, Electrochem. Soc. Proc. 96-13 (1996) 512.
[531] O.J. Anttila, S.K. Hahn, J. Appl. Phys. 74 (1993) 558.
[532] W.H. Howland, S.J. Fonash, J. Electrochem. Soc. 142 (1995) 4262.
[533] C. Boit, E. Heindl, Archiv Für Elektrotech. 72 (1989) 141.
[534] E.S. Nartowitz, A.M. Goodman, J. Electrochem. Soc. 132 (1985) 2992.
[535] M.K. Alam, Y.T. Yeow, Sol. State Electr. 24 (1981) 1117.
[536] X. Zhang, G. He, J. Song, Semicond. Sci. Technol. 7 (1992) 888.
[537] B.L. Sopori, R.W. Gurtler, I.A. Lesk, Sol. State Electr. 23 (1980) 139.
[538] V. Faifer, V. Dyudkov, A. Pravdivtsev, D. Skurida, in: Proc. 24th European Solid State Reserach Conf., Editions Frontieres, Gif Sur Yvette, 1994, p. 601.
[539] A.M. Goodman, J. Appl. Phys. 53 (1982) 7561.
[540] J. Lowell, V. Wenner, D. DeBusk, Proc. MRS Symp. 386 (1995) 207.
[541] X. Gao, S. Yee, J. Electrochem. Soc. 140 (1993) 2042.
[542] K. Nauka, D.A. Gomez, J. Electrochem. Soc. 142 (1995) L98.

[543] T.I. Chappell, P.W. Chye, M.A. Tavel, Sol. State Electr. 26 (1983) 33.
[544] M. Nokes, P. Flesher, P. Borden, D. DeBusk, J. Lowell, D. Hill, G. Allen, Proc. SPIE 2337 (1994) 117.
[545] W.H. Howland, S.J. Fonash, J. Electrochem. Soc. 143 (1996) 1958.
[546] A.K. Ghosh, J.I. Haberman, T. Feng, J. Appl. Phys. 55 (1984) 280.
[547] A. Buczkowski, G. Rozgonyi, F. Shimura, K. Mishra, J. Electrochem. Soc. 140 (1993) 3240.
[548] M.L. Polignano, F. Cazzaniga, A. Sabbadini, G. Queirolo, A. Cacciato, A. Di Bartolo, Mater. Sci. Eng. B42 (1996) 157.
[549] J. Lagowski, A.M. Kontkiewicz, L. Jastrzebski, P. Edelman, Appl. Phys. Lett. 63 (1993) 2902.
[550] S.R. Dhariwal, B.M. Deoraj, Solar Energy Mater. Solar Cells 26 (1992) 243; S.R. Dhariwal, B.M. Deoraj, Proc. 8th E.C. Photovoltaic Solar Energy Conf., 1988, p. 1306.
[551] D. Walz, J.-P. Joly, G. Kamarinos, Appl. Phys. A62 (1996) 345.
[552] C.T. Ho, R.O. Bell, F.V. Wald, Appl. Phys. Lett. 31 (1977) 463.
[553] P.J. McElheny, J.K. Arch, S.J. Fonash, Appl. Phys. Lett. 51 (1987) 1611; P.J. McElheny, J.K. Arch, H.-S. Lin, S.J. Fonash, J. Appl. Phys. 64 (1988) 1254.
[554] D. Ritter, E. Zeldov, K. Weiser, J. Appl. Phys. 62 (1987) 4563; Phys. Rev. B38 (1988) 8296.
[555] L.J. Brillson (Ed.), Contacts to Semiconductor Devices, Noyes, New Jersey, 1993.
[556] R. Williams, J. Phys. Chem. Solids 23 (1962) 1057.
[557] J. Shappir, A. Many, Surf. Sci. 14 (1969) 169.
[558] A. Waxman, Solid State Electr. 9 (1966) 303.
[559] K. Okumura, J. Appl. Phys. 45 (1974) 5317.
[560] I. Flinn, D.C. Emmony, Phys. Lett. 6 (1963) 133.
[561] I. Flinn, M. Briggs, Surf. Sci. 2 (1964) 136.
[562] I. Flinn, Surf. Sci. 10 (1968) 32.
[563] R.H. Williams, I.T. McGovern, Surf. Sci. 51 (1975) 12.
[564] V.V. Antoschchuk, V.V. Milenin, V.E. Primachenko, O.V. Snitko, Sov. Phys. Semicond. 11 (1977) 1172.
[565] S.I. Kirillova, M.D. Moin, V.E. Primachenko, S.V. Svechnikov, V.A. Chernobai, I.N. Dubrov, Sov. Phys. Semicond. 26 (1992) 784.
[566] S.I. Kirillova, V.E. Primachenko, G.F. Romanova, P.I. Didenko, V.A. Chernobai, Russian Microelectr. 22 (1993) 157.
[567] V.V. Antoschchuk, V.E. Primachenko, O.V. Snitko, Sov. Phys. Semicond. 20 (1986) 474.
[568] E.F. Venger, S.I. Kirillova, V.E. Primachenko, V.A. Chernobai, Russian Microelectr. 25 (1996) 257.
[569] E.F. Venger, S.I. Kirillova, V.E. Primachenko, V.A. Chernobai, Semiconductors 29 (1995) 121.
[570] S.F. Avramenko, S.I. Kirilova, V.S. Kiselev, V.E. Primachenko, E.F. Venger, V.A. Chrenobai, Semicond. Sci. Technol. 12 (1997) 189.
[571] R.K. Swank, Phys. Rev. 153 (1967) 844.
[572] H. Yamagishi, J. Phys. Soc. Jpn. 25 (1968) 766; 22 (1967) 470.
[573] V.A. Zuev, V.G. Litovchenko, K.D. Glinchuk, N.M. Litovchenko, G.A. Sukach, L.F. Linnik, Sov. Phys. Semicond. 6 (1973) 1662.
[574] B. Adamowicz, Surf. Sci. 231 (1990) 1; B. Adamowicz, S. Kochowski, Surf. Sci. 200 (1988) 172.
[575] B. Aker, S.-Q. Peng, S.-Y. Cai, H. Frtizsche, J. Non-Cryst. Solids 59-60 (1983) 509.
[576] M. Foller, W. Beyer, J. Herion, H. Wagner, Surf. Sci. 178 (1986) 47.
[577] M. Foller, J. Herion, W. Beyer, H. Wagner, J. Non-Cryst. Solids 97-98 (1987) 567.
[578] N.R. Huck, R.C. Smart, S.M. Thurgate, Surf. Sci. 169 (1986) L245.
[579] L.J. Brillson, J. Vac. Sci. Technol. 16 (1979) 1137.
[580] L.J. Brillson, R.S. Bauer, R.Z. Bachrach, J. McMenamin, J. Vac. Sci. Technol. 17 (1980) 476.
[581] L.J. Brillson, R.Z. Bachrach, R.S. Bauer, J. McMenamin, Phys. Rev. Lett. 42 (1979) 397.
[582] L.J. Brillson, D.W. Kruger, Surf. Sci. 102 (1981) 518.
[583] W. Göpel, L.J. Brillson, C.F. Brucker, J. Vac. Sci. Technol. 17 (1980) 894.
[584] P. Edelman, J. Lagowski, L. Jastrzebski, Proc. Conf. Photo-Induced Space Charge Effects in Semiconductors, MRS, Pittsburgh, 1992, pp. 223-8.
[585] P. Edelman, A.M. Hoff, L. Jastrzebski, J. Lagowski, Proc. SPIE 2337 (1994) 154.
[586] A.M. Kontkiewicz, M. Dexter, S. Sen, J. Lagowski, A. Hoff, P. Edelman, L. Jastrzebski, K. Nauka, K. Mishra, T. Hanley, Proc. 5th Int. Conf. on Defect Recognition and Image Processing in Semiconductors and Devices, IOP, Bristol, 1994, p. 385.

[587] K. Nauka, Proc. IEEE Symp. on VLSI Technology, Hawaii, 1994.

[588] K. Nauka, Proc. Int. Workshop on Semiconductor characterization: Present Status and Future Needs, Gaithersburg, MD, USA, AIP, 1996, p. 231.

[589] K. Nauka, Microelectronic Engineering 36 (1997) 351; K. Nauka, M. Cao, F. Assaderaghi, Proc. IEEE Int. SOI Conf., IEEE, New York, 1995, p. 52; J.U. Yoon, G.N. Kim, J.-H. Krska, J.E. Chung, L.P. Allen, K. Goodson, O. Kaeding, K. Nauka, Proc. MRS Symp. 446 (1997) 193.

[590] K. Nauka, J. Lagowski, P. Edelman, Proc. Conf. on Defect Recognition and Image Processing in Semiconductors, Estes Park, CO, USA, 1995; K. Nauka, J. Theil, C. Chi, M. Greene, J.L. Shohet, Proc. 1st Int. Symp. on Plasma Process-Induced Damage, Santa Clara, CA, USA, 1996, p. 34.

[591] K. Nauka, J. Theil, J. Lagowski, L. Jastrzebski, S. Sawtchouk, Proc. 2nd Int. Symp. on Plasma Process-Induced Damage, Monterey, CA, USA, 1997.

[592] J. Lowell, V. Wenner, M. Anjum, Proc. IEEE/SEMI Int. Conf. on Ultraclean Manufacturing, IEEE, New York, 1994, p. 316.

[593] D. DeBusk, J. Lowell, F. Reich, Proc. MRS 386 (1995) 151.

[594] K. Kumar, A.I. Chou, C. Lin, P. Choudhury, J.C. Lee, J.K. Lowell, Appl. Phys. Lett. 70 (1997) 384.

[595] J.S. Jeon, S. Raghavan, J. Lowell, V. Wenner, Proc. SPIE 2337 (1994) 13.

[596] A. Stuber, J. Lowell, Proc. SPIE 2638 (1995) 183.

[597] X. Wang, H.G. Parks, C. Cariss, J. Lowell, Proc. SPIE 2638 (1995) 247.

[598] J. Sherry, J. Lowell, T. Hossain, D. DeBusk, Proc. MRS 428 (1996) 429.

[599] T. Hossain, J. Sherry, P. Burke, S. Ostepenko, L. Jastrzebski, J. Lowell, Proc. VMIC Conf. on CMP for Multilevel Interconnection, 1997.

[600] J. Lowell, J. Vac. Sci. Technol. B14 (1996) 248.

[601] J. Peavey, R. Dawson, J. Lowell, J. Vac. Sci. Technol. A14 (1996) 1156.

[602] Y.W. Lam, J. Phys. D: Appl. Phys. 4 (1971) 1370.

[603] L. Kronik, L. Burstein, Y. Shapira, M. Oron, Appl. Phys. Lett. 63 (1993) 60.

[604] J. Lagowski, A. Morawski, P. Edelman, Jpn. J. Appl. Phys. 31 (1992) L1185.

[605] L. Kronik, L. Burstein, M. Leibovitch, Y. Shapira, D. Gal, E. Moons, J. Beier, G. Hodes, D. Cahen, D. Hariskos, R. Klenk, H.-W. Schock, Appl. Phys. Lett. 67 (1995) 1405.

[606] A. Many, A. Katzir, Surf. Sci. 6 (1967) 279.

[607] R.J. Haas, D.C. Fox, M.J. Katz, J. Phys. Chem. Solids 26 (1965) 1779.

[608] M.J. Katz, K.J. Haas, Surf. Sci. 19 (1970) 380.

[609] B.D. Campbell, H.E. Farnsworth, Surf. Sci. 10 (1968) 197.

[610] A. Ismail, M.T. Chehabeddine, L. Lassabatère, J. Phys. III France 2 (1992) 717.

[611] O.B. Aphek, L. Kronik, M. Leibovitch, Y. Shapira, Surf. Sci. 409 (1998) 485.

[612] B.I. Bednyi, N.V. Baidus, Semiconductors 27 (1993) 620.

[613] S. Kumar, S.C. Agarwal, J. Appl. Phys. 58 (1985) 3798; S. Kumar, S.C. Agarwal, Appl. Phys. Lett. 45 (1984) 575; S. Kumar, S.C. Agarwal, Phil. Mag. B49 (1984) L53.

[614] W.E. Spicer, S. Eglash, I. Lindau, C.Y. Su, P.R. Skeath, Thin Solid Films 89 (1982) 447.

[615] L.J. Brillson, Thin Solid Films 89 (1982) L27.

[616] S. Eglash, W.E. Spicer, I. Lindau, Thin Solid Films 89 (1982) L35.

[617] P. Skeath, I. Lindau, P.W. Chye, C.Y. Su, W.E. Spicer, J. Vac. Sci. Technol. 16 (1979) 1143.

[618] W.E. Spicer, A.M. Green, J. Vac. Sci. Technol. B11 (1993) 1347.

[619] B.I. Bednyi, M.I. Vasilevskii, I.A. Karpovich, Sov. Phys. Semicond. 23 (1989) 223.

[620] B.I. Bednyi, N.V. Baidus, T.V. Belich, I.A. Karpovich, Sov. Phys. Semicond. 26 (1992) 775.

[621] Th. Dittrich, M. Brauer, L. Elstner, Phys. Stat. Sol. (a)137 (1993) K29.

[622] K. Heilig, Surf. Sci. 44 (1974) 421.

[623] L. Kronik, Y. Shapira, J. Vac. Sci. Technol. A11 (1993) 3081.

[624] E. Kamieniecki, Electrochem. Soc. Proc. 90-9 (1990) 273.

[625] E. Kamieniecki, Electrochem. Soc. Proc. 95-20 (1995) 336.

[626] J. Ruzyllo, P. Roman, J. Staffa, I. Kashkoush, E. Kamieniecki, Proc. SPIE 2876 (1996) 162.

[627] E. Kamieniecki, SEMI/ASTM Lifetime Characterization Workshop Santa Clara, 1997.

[628] A. Danel, U. Straube, G. Kamarinos, E. Kamieniecki, F. Tardif, Proc. 5th Int. Symp. on Cleaning Technology in Semiconductor Device Manufacturing, Paris, France, 1997.

[629] A. Danel, T. Lardin, G. Kamarinos, F. Tardif, Electrochem. Soc. Proc. 97-22 (1997) 394.
[630] P. Roman, J. Staffa, S. Fakhouri, M. Brubacker, J. Ruzyllo, K. Torek, E. Kamieniecki, J. Appl. Phys. 83 (1998) 2297.
[631] Y. Yan, Appl. Phys. Lett. 71 (1997) 407.
[632] G. Buchheim, B. Junghans, H. Lippmann, Phys. Stat. Sol. (a)44 (1977) 585.
[633] J.R. Ewing, L.P. Humter, Solid State Electr. 18 (1975) 587.
[634] W. Mindt, H. Gerischer, Surf. Sci. 9 (1968) 449.
[635] J. Shappir, Surf. Sci. 26 (1971) 545.
[636] K. Heilig, Solid State Electr. 21 (1978) 975.
[637] L. Koenders, F. Bartels, H. Ullrich, W. Mönch, J. Vac. Sci. Technol. B3 (1985) 1107.
[638] H. Shimizu, C. Munakata, Semicond. Sci. Technol. 5 (1990) 842.
[639] C. Munakata, H. Shimizu, Semicond. Sci. Technol. 5 (1990) 991.
[640] H. Shimizu, C. Munakata, Semicond. Sci. Technol. 6 (1991) 756.
[641] H. Shimizu, C. Munakata, Jpn. J. Appl. Phys. 31 (1992) 729.
[642] H. Shimizu, C. Munakata, Jpn. J. Appl. Phys. 31 (1992) 2319.
[643] H. Shimizu, C. Munakata, Jpn. J. Appl. Phys. 32 (1993) 3775.
[644] H. Shimizu, C. Munakata, Jpn. J. Appl. Phys. 32 (1993) 3780.
[645] H. Shimizu, C. Munakata, J. Appl. Phys. 73 (1993) 8336.
[646] H. Shimizu, A. Shull, C. Munakata, Proc. SPIE 2877 (1996) 174.
[647] H. Shimizu, J. Electrochem. Soc. 144 (1997) 4335.
[648] W. Jaegermann, Chem. Phys. Lett. 126 (1986) 301.
[649] W. Jaegermann, Ber. Bunsenges. Phys. Chem. 92 (1988) 537.
[650] W. Jaegermann, C. Pettenkofer, Ber. Bunsenges. Phys. Chem. 92 (1988) 1354.
[651] W. Jaegermann, C. Pettenkofer, B.A. Parkinson, Phys. Rev. B 42 (1990) 7487.
[652] T. Mayer, C. Pettenkofer, W. Jaegermann, C. Levy Clement, Surf. Sci. 254 (1991) L423.
[653] T. Mayer, C. Pettenkofer, W. Jaegermann, J. Phys. Condens. Matter. 3 (1991) S161.
[654] M. Sander, W. Jaegermann, H.J. Lewerenz, J. Phys. Chem. 96 (1992) 782.
[655] J.E. Demuth, W.J. Thompson, N.J. DiNardo, R. Imbihl, Phys. Rev. Lett. 56 (1986) 1408.
[656] P. John, T. Miller, T.C. Hsieh, A.P. Shapiro, A.L. Wachs, T.-C. Chiang, Phys. Rev. B 34 (1986) 6704.
[657] G.D. Waddill, C.M. Aldao, C. Capasso, P.J. Benning, Y. Hu, T.J. Wagener, M.B. Jost, J.H. Weaver, Phys. Rev. B 41 (1990) 6092.
[658] G.D. Waddill, T. Komeda, Y.-N. Yang, J.H. Weaver, Phys. Rev. B 41 (1990) 10283.
[659] K. Jacobi, U. Myler, P. Althainz, Phys. Rev. B 41 (1990) 10721.
[660] S. Chang, M. Vitomirov, L.J. Brillson, D.F. Rioux, P.D. Kirschner, G.D. Petit, J.M. Woodall, M.H. Hecht, Phys. Rev. B 41 (1990) 12299.
[661] D. Mao, A. Kahn, M. Marsi, G. Margaritondo, Phys. Rev. B 42 (1990) 3228.
[662] M. Alonso, R. Cimino, K. Horn, J. Vac. Sci. Technol. A9 (1991) 891.
[663] D. Mao, A. Kahn, M. Marsi, G. Margaritondo, J. Vac. Sci. Technol. A9 (1991) 898.
[664] D. Mao, A. Kahn, G. Le Lay, M. Marsi, Y. Hwu, G. Margaritondo, M. Santos, M. Shayegan, L.T. Florez, J.P. Harbison, J. Vac. Sci. Technol. B9 (1991) 2083.
[665] T.U. Kampen, D. Troost, X.Y. Hou, L. Koenders, W. Mönch, J. Vac. Sci. Technol. B9 (1991) 2095.
[666] A. Bauer, M. Prietsch, S. Molodtsov, C. Laubschat, and G. Kaindl, Phys. Rev. B 44 (1991) 4002.
[667] D.A. Evans, T.P. Chen, Th. Chasse, K. Horn, Appl. Surf. Sci. 56–58 (1992) 233.
[668] V. Yu. Aristov, G. Le Lay, L.T. Vinh, K. Hricovini, J.E. Bonnet, Phys. Rev. B 47 (1993) 2138.
[669] P. Chiardia, J.E. Bonnet, M. Fanfoni, C. Goletti, G. Lampel, Phys. Rev. B 47 (1993) 13520.
[670] C.M. Aldao, J.F. Valtueña, I. Izpura, E. Muñoz, Phys. Rev. B 50 (1994) 17729.
[671] A. Hamawi, Phys. Rev. B 50 (1994) 10910.
[672] R. Whittle, A. Murphy, E. Dudzik, I.T. McGovern, A. Hempelmann, C. Nowak, D.R.T. Zahn, A. Cafolla, W. Braun, J. Synchrotron Rad. 2 (1995) 256.
[673] D.A. Evans, D. Wolfframm, D. Gnoth, J. Cairns, A.C. Wright, M. Evans, J. Riley, D. Westwood, D.A. Woolf, Appl. Surf. Sci. 104-105 (1996) 240.
[674] M. Fanfoni, C. Goletti, P. Chiardia, W. Ng, F. Cerrina, Y. Hwu, A. Terrasi, G. Margaritondo, J. Vac. Sci. Technol. A14 (1996) 2433.

[675] X. Yin, H.-M. Chen, F.H. Pollak, Y. Chan, P.A. Montano, P.D. Kirschner, G.D. Petit, J.M. Woodall, Appl. Phys. Lett. 58 (1991) 260; J. Vac. Sci. Technol. A10 (1992) 131.
[676] V.M. Airaksinen, H.K. Lipsanen, Appl. Phys. Lett. 60 (1992) 2110.
[677] N.L. Dmitruk, V.I. Lyashenko, Sov. Phys. Solid State 8 (1966) 457.
[678] T. Sugino, T. Yamada, K. Kondo, H. Ninomiya, K. Matsuda, J. Shirafuji, Jpn. J. Appl. Phys. 31 (1992) L1522.
[679] Y. Sakamoto, T. Sugino, H. Ninomiya, K. Matsuda, J. Shirafuji, Jpn. J. Appl. Phys. 34 (1995) 1417.
[680] T. Sugino, J. Shirafuji, Phys. Stat. Sol. (a)154 (1996) 371.
[681] J. Shirafuji, Y. Sakamoto, A. Furukawa, T. Sugino, Diamond Films Technol. 6 (1996) 311.
[682] E. Fefer, L. Kronik, M. Leibovitch, Y, Shapira, W. Riedl, Appl. Surf. Sci. 104–105 (1996) 61.
[683] J.M. Palau, E. Testemale, L. Lassabatère, J. Vac. Sci. Technol. 19 (1981) 192.
[684] L. Lassabatère, J.M. Palau, E. Vieujot-Testemale, A. Ismail, C. Raisin, J. Bonnet, L. Soonckindt, J. Vac. Sci. Technol. B1 (1983) 540.
[685] A. Ismail, J.M. Palau, L. Lassabatère, Rev. Phys. Appl. 19 (1984) 205.
[686] A. Ismail, A. Ben Brahim, J.M. Palau, L. Lassabatère, Surf. Sci. 162 (1985) 195.
[687] A. Ismail, A. Ben Brahim, J.M. Palau, L. Lassabatère, Surf. Sci. 164 (1985) 43.
[688] A. Ismail, A. Ben Brahim, L. Lassabatère, I. Lindau, J. Appl. Phys. 59 (1986) 485.
[689] A. Ismail, J.M. Palau, L. Lassabatère, J. Appl. Phys. 60 (1986) 1730.
[690] J.M. Palau, L. Soonckindt, A. Ismail, L. Lassabatère, Thin Solid Films 151 (1987) 103.
[691] M. Benkacem, M. Dumas, J.M. Palau, L. Lassabatère, Surf. Sci. 201 (1988) L485.
[692] J.J. Bonnet, A. Doukkali, J. Vac. Sci. Technol. A9 (1991) 2239.
[693] M. Marsi, M.E. Couprie, L. Nahon, D. Garzella, T. Hara, R. Bakker, M. Billardon, A. Delboulbé, G. Indlekofer, A. Taleb-Ibrahimi, Appl. Phys. Lett. 70 (1997) 895; M. Marsi, M.E. Couprie, L. Nahon, D. Garzella, R. Bakker, A. Delboulbé, D. Nutarelli, R. Roux, B. Visentin, C. Grupp, G. Indlekofer, G. Panaccione, A. Taleb-Ibrahimi, M. Billardon, Nucl. Instr. Meth. A393 (1997) 548.
[694] N.J. Halas, J. Bokor, Phys. Rev. Lett. 62 (1989) 1679; J. Bokor, N. Halas, IEEE J. Quant. Electr. 25 (1989) 2550.
[695] A. Kadyshevitch, R. Naaman, R. Cohen, D. Cahen, J. Libman, A. Shanzer, J. Phys. Chem. B101 (1997) 4085.
[696] C. Munakata, N. Honma, H. Itoh, Jpn. J. Appl. Phys. 22 (1983) L103.
[697] N. Honma, C. Munakata, H. Itoh, Jpn. J. Appl. Phys. 23 (1984) L354.
[698] C. Munakata, H. Tamura, N. Honma, M. Ozawa, K. Yagi, Jpn. J. Appl. Phys. 27 (1988) 1770.
[699] N. Honma, C. Munakata, H. Itoh, T. Warabisako, Jpn. J. Appl. Phys. 25 (1986) 743.
[700] N. Honma, C. Munakata, H. Shimizu, Jpn. J. Appl. Phys. 27 (1988) 1322.
[701] N. Honma, C. Munakata, H. Shimizu, Jpn. J. Appl. Phys. 27 (1988) 1498.
[702] R.J. Hamers, D.G. Cahill, Appl. Phys. Lett. 57 (1990) 2031; R.J. Hamers, D.G. Cahill, J. Vac. Sci. Technol. B9 (1991) 514.
[703] C.-L. Chiang, S. Wagner, C.-L. Shieh, Appl. Phys. Lett. 45 (1984) 884.
[704] Z.H. Lu, F. Chatenoud, M.M. Dion, M.J. Graham, H.E. Ruda, I. Koutzarov, Q. Liu, C.E.J. Mitchell, I.G. Hill, A.B. McLean, Appl. Phys. Lett. 67 (1995) 670.
[705] V. Faifer, P. Edelman, A. Kotnkiewicz, J. Lagowski, A. Hoff, V. Dyukov, A. Pravdivtsev, I. Kornienko, Electrochem. Soc. Proc. 95-30 (1995) 73.
[706] R.S. Nakhmanson, Z.Sh. Ovsyuk, L.K. Popov, Solid State Electron. 18 (1975) 627.
[707] W. Goldfarb, Proc. SPIE 2337 (1994) 129; C.M. Kohn, W.C. Goldfarb, Solid State Technol., June 1995, p. 93.
[708] C. Munakata, Semicond. Sci. Technol. 5 (1990) 206.
[709] T. Takahashi, M. Yoshita, Appl. Phys. Lett. 70 (1997) 2162.
[710] F.G. Allen, G.W. Gobeli, Phys. Rev. 127 (1962) 150.
[711] B. Adamowicz, Vacuum 45 (1994) 167; B. Adamowicz, Acta Phys. Pol. A81 (1992) 303.
[712] Y.W. Lam, J. Phys. D: Appl. Phys. 4 (1971) 1370.
[713] K. Heilig, E. Kolbig, J. Reineke, Phys. Stat. Sol. (a)114 (1989) 579.
[714] Th. Dittrich, H. Angermann, H. Flietner, Th. Bitzer, H.J. Lewerenz, J. Electrochem. Soc. 141 (1994) 3595.
[715] O.V. Snitko, Sov. Phys. Solid State 1 (1959) 899.
[716] Y.W. Lam, Jpn. J. Appl. Phys. 12 (1973) 916.
[717] K. Heilig, H. Flietner, J. Reineke, J. Phys. D: Appl. Phys. 12 (1979) 927.
[718] Th. Dittrich, H. Angermann, W. Füssel, H. Flietner, Phys. Stat. Sol. (a)140 (1993) 463.

[719] Th. Dittrich, K. Kliefoth, I. Sieber, J. Rappich, S. Rauscher, V. Yu. Timoshenko, Thin Solid Films 276 (1996) 183.
[720] H. Angermann, Th. Dittrich, H. Flietner, Appl. Phys. A59 (1994) 193.
[721] H. Angermann, K. Kliefoth, W. Füssel, H. Flietner, Microelectr. Eng. 28 (1995) 51.
[722] H. Flietner, Mater. Sci. Forum 185-188 (1995) 73.
[723] H. Angermann, K. Kliefoth, H. Flietner, Appl. Surf. Sci. 104/105 (1996) 107.
[724] H. Angermann, W. Henrion, M. Rebien, K. Kliefoth, D. Fischer, J.T. Zettler, Microelectr. Eng. 36 (1997) 43.
[725] H. Angermann, W. Henrion, M. Rebien, J.T. Zettler, A. Röseler, Surf. Sci. 388 (1997) 15.
[726] Th. Dittrich, S. Rauscher, Th. Bitzer, M. Aggour, H. Flietner, H.J. Lewerenz, J. Electrochem. Soc. 142 (1995) 2411.
[727] S. Rauscher, Th. Dittrich, M. Aggour, J. Rappich, H. Flietner, H.J. Lewerenz, Appl. Phys. Lett. 66 (1995) 3018.
[728] H. Flietner, Surf. Sci. 200 (1988) 463.
[729] Y.W. Lam, E.H. Rhoderick, J. Phys. D: Appl. Phys. 4 (1971) 1376; Y.W. Lam, Electron. Lett. 6 (1970) 153.
[730] R.W.M. Kwok, W.M. Lau, D. Landheer, S. Ingrey, J. Electron. Mater. 22 (1993) 1141.
[731] H. Kobayashi, T. Mori, K. Namba, Y. Nakato, Solid State Commun. 92 (1994) 249.
[732] Y. Mochizuki, M. Mizuta, Appl. Phys. Lett. 69 (1996) 3051.
[733] C.I. Ukah, J.M. Perz, S. Zukotynski, J. Appl. Phys. 67 (1990) 6486.
[734] M. Rennau, A. Beyer, G. Ebest, P. Arzt, Proc. 12th Euro. Photovoltaic Solar Energy Conf. Amsterdam, 1994, p. 489.
[735] H. Shimizu, K. Kinameri, N. Honma, C. Munakata, Jpn. J. Appl. Phys. 26 (1987) 226.
[736] V. Murali, A.T. Wu, A.K. Chatterjee, D.B. Fraser, IEEE Trans. Semicond. Manufact. 5 (1992) 214.
[737] A. Resnick, E. Kamieniecki, A. Phillipossian, D. Jackson, Electrochem. Soc. Proc. 90-9 (1990) 335.
[738] A. Phillipossian, D. Jackson, E. Kamieniecki, A. Resnick, Electrochem. Soc. Proc. 90-9 (1990) 357.
[739] S.A. Ajuria, J.T. Fitch, D. Workman, T.C. Mele, J. Electrochem. Soc. 140 (1993) L113.
[740] A. Phillipossian, J. Electrochem. Soc. 139 (1992) 2956.
[741] L.A. Lipkin, J. Electrochem. Soc. 140 (1993) 2328.
[742] S. Nagalingam, M.-S. Fung, S. Thind, Proc. 1st Int. Symp. on Plasma Process-Induced Damage, Santa Clara, CA, USA, 1996, p. 87.
[743] J. Kato, Y. Maruo, J. Electrochem. Soc. 139 (1993) 1756.
[744] J.M. Grant, T.-Y. Hsieh, Proc. MRS Symp. 342 (1994) 163.
[745] J.M. Grant, L.R. Allen, Proc. SPIE 2091 (1994) 51.
[746] L. Kronik, M. Leibovitch, E. Fefer, L. Burstein, Y. Shapira, J. Electron. Mater. 24 (1995) 379.
[747] W. Kuhlmann, M. Henzler, Surf. Sci. 99 (1980) 45.
[748] C.L. Balestra, J. Lagowski, H.C. Gatos, Surf. Sci. 64 (1977) 457.
[749] S. Kuzminski, A.T. Szaynok, Surf. Sci. 105 (1981) 565.
[750] J. Lagowski, P. Edelman, A. Morawski, Semicond. Sci. Technol. 7 (1992) A211.
[751] H.V. Estrada, Proc. IEEE South East Conf. '92 IEEE, New York, 1992. p. 163
[752] T.P. Ershova, S.G. Ershov, V.E. Zhukov, V.V. Korablev, V.Yu. Tyukin, Sov. Phys. Semicond. 23 (1989) 199.
[753] C. Eiche, W. Joerger, R. Schwarz, K.W. Benz, J. Cryst. Growth 161 (1996) 271.
[754] K. Maeda, M. Uota, Y. Mera, Mater. Sci. Eng. B 42 (1996) 127.
[755] Q. Liu, H.E. Ruda, Phys. Rev. B 55 (1997) 10541.
[756] N. Kasupke, M. Henzler, Surf. Sci. 54 (1976) 111.
[757] M. Bronold, C. Pettenkofer, W. Jaegermann, J. Appl. Phys. 76 (1994) 5800.
[758] B. Kramer, J.T. Wallmark, P. Mark, J. Vac. Sci. Technol. 12 (1975) 713.
[759] B. Goldstein, D. Redfield, D.J. Szostak, L.A. Carr, Appl. Phys. Lett. 39 (1981) 258.
[760] D.J. Szostak, B. Goldstein, J. Appl. Phys. 56 (1984) 522.
[761] C. Munakata, N. Honma, Jpn. J. Appl. Phys. 26 (1981) L856.
[762] O. Lang, V. Tomm, R. Schlaf, C. Pettenkofer, W. Jaegermann, J. Appl. Phys. 75 (1994) 7814.
[763] A.J. Kontkiewicz, A.M. Kontkiewicz, M. Wesolowski, S. Sen, P. Edelman, J. Lagowski, Proc. 4th Int. Conf. on Defect Recognition and Image Processing in Semiconductors and Devices, IOP Conf. Ser. vol. 135, 1993, p. 165.
[764] B. Mishori, M. Leibovitch, Y. Shapira, F.H. Pollak, D.C. Streit, M. Wojtowicz, Appl. Phys. Lett. 73 (1998) 650.
[765] U. Rau, M. Schmitt, D. Hilburger, F. Engelhardt, O. Seifert, J. Parisi, W. Riedl, J. Rimmasch, F. Karg, Proc. 25th IEEE Photovoltaics Specialists Conf., IEEE, New York, 1996, p. 1005.
[766] M. Nonnenmacher, M. O'Boyle, H.K. Wickramasinghe, Ultramicrcscopy 42-44 (1992) 268.
[767] A. Chavez-Pirson, O. Vatel, M. Tanimoto, H. Ando, H. Iwamura, H. Kanbe, Appl. Phys. Lett. 67 (1995) 3069.

[768] M. Tanimoto, O. Vatel, J. Vac. Sci. Technol. B14 (1996) 1547.

[769] O.J. Glembocki, E.S. Snow, C.R.K. Marian, S.M. Prokes, D.S. Katzer, Ultramicrcscopy 42-44 (1992) 764.

[770] P. Blood, J. Appl. Phys. 58 (1985) 2288.

[771] I.A. Karpovich, V.Ya. Aleshkin, A.V. Anshon, T.S. Babushkina, B.N. Zvonkov, I.G. Malkina, Sov. Phys. Semicond. 24 (1990) 1346.

[772] I.A. Karpovich, V.Ya. Aleshkin, A.V. Anshon, N.V. Baidus, L.M. Batukova, B.N. Zvonkov, S.M. Plankina, Sov. Phys. Semicond. 26 (1992) 1057.

[773] V.Ya. Aleshkin, A.V. Anshon, I.A. Karpovich, Semiconductors 27 (1993) 742.

[774] I.A. Karpovich, A.V. Anshon, N.V. Baidus, L.M. Batukova, Yu.A. Danilov, B.N. Zvonkov, S.M. Plankina, Semiconductors 28 (1994) 63.

[775] B.W. Wessles, L.Q. Qian, J. Vac. Sci. Technol. B10 (1992) 1803.

[776] I.A. Karpovich, D.O. Filatov, Semiconductors 30 (1996) 913.

[777] L. Aigoui, T. Holden, F.H. Pollak, N.N. Ledentsov, V.M. Ustinov, P.S. Kop'ev, D. Bimberg, Electrochem. Soc. Proc. 97-11 (1997) 146.

[778] N. Ashkenasy, M. Leibovitch, Y. Shapira, F.H. Pollak, G.T. Burnham, X. Wang, J. Appl. Phys. 83 (1998) 1146.

[779] C. Cameron Miller, S.J. Diol, C.A. Schmuttenmaer, J. Cao, D.A. Mantell, R.J.D. Miller, Y. Gao, J. Phys. D: Appl. Phys. 30 (1997) 1416.

[780] J.K. Arch, S.J. Fonash, J. Appl. Phys. 68 (1990) 591.